Atomistic Calculations of Nanoscale Interface Behavior in FCC Metals

A Dissertation
Presented to
The Academic Faculty

by

Douglas E. Spearot

In Partial Fulfillment
of the Requirements for the Degree
Doctor of Philosophy in Mechanical Engineering

Georgia Institute of Technology
August 2005

© Douglas E. Spearot, 2005

Atomistic Calculations of Nanoscale Interface Behavior in FCC Metals

Approved By:

Dr. David L. McDowell, Co-Advisor
GWW School of Mechanical Engineering
Georgia Institute of Technology

Dr. Min Zhou
GWW School of Mechanical Engineering
Georgia Institute of Technology

Dr. Karl I. Jacob, Co-Advisor
Polymer, Textile & Fiber Engineering
Georgia Institute of Technology

Dr. Mo Li
School of Materials Science & Engineering
Georgia Institute of Technology

Dr. Jianmin Qu
GWW School of Mechanical Engineering
Georgia Institute of Technology

Date Approved: July 12, 2005

ACKNOWLEDGMENTS

There are a number of people who I owe a great deal of appreciation for their contributions to this thesis. First and foremost, I would like to thank my co-advisors, Dr. David McDowell and Dr. Karl Jacob. They have allowed me the freedom to direct this research project according to my own observations, developing in me the ability to think creatively and independently. I also would like to thank both Dr. McDowell and Dr. Jacob for their guidance and advice during my search for an academic position. Second, I would like to thank the members of my Ph.D. thesis reading committee: Dr. Jianmin Qu, Dr. Min Zhou and Dr. Mo Li. Their comments and suggestions over the past several years have no doubt added to the quality of this research.

This research would not be possible without a generous grant from NASA Langley Research Center under the technical supervision of Dr. Ed Glassegen. I would also like to thank Dr. Steve Plimpton at Sandia National Laboratories / Albuquerque, NM for providing the molecular dynamics code used in this research work; Dr. Jon Zimmerman at Sandia National Laboratories / Livermore, CA for serving as my mentor for a summer in the Engineering Summer Sciences Institute and for providing the framework for the energy minimization routine used in this thesis; and Dr. Matt Wolf in the Georgia Tech College of Computing for his assistance (and patience) early in this project as I was learning parallel programming. Calculations in this work were performed on a range of multiprocessor computing systems, including those in the Schools of Mechanical Engineering, Materials Science and the College of Computing at

Georgia Tech and the US Army Engineer Research and Development Center (ERDC) Major Shared Resource Center (MSRC).

There are a number of people at Georgia Tech who have contributed greatly to my experiences over the past several years: Tim Ferguson, Ben Dempsey, Jason Mayeur, Mark Tschopp, Jen Muncy, and many others. Our conversations, both technical and non-technical have enhanced my experience in graduate school. I have no doubt that each of you will find success in your careers and in life. Finally, I would like to thank my family. Your support and encouragement have helped me realize my potential. Michelle Hetrick, I thank you the most for your patience and love.

TABLE OF CONTENTS

LIST OF TABLES

LIST OF FIGURES

NOMENCLATURE

Molecular dynamics / Interatomic potentials

N	Number of atoms
V	System volume
P	System pressure
T	System temperature
$\boldsymbol{\sigma}$	System stress
$\mathbf{F}^{i}$	Force vector for atom i
$\mathbf{r}^{i}$	Position vector for atom i
$\mathbf{p}^{i}$	Momentum vector for atom i
$\mathbf{v}^{i}$	Velocity vector for atom i
$\boldsymbol{\Pi}^{i}$	Stress evaluated at atom i
Ω^{i}	Volume around atom i
L^{i}	Liouville operator for atom i
$\mathbf{r}_{N}$	Set of position vectors for a system of N atoms
U	Potential energy for a system of atoms
$\mathbf{g}_{m}$	Residual of the potential energy for conjugate gradient iteration step m
$\mathbf{d}_{m}$	Conjugate gradient step (search) direction
α	Scalar that minimizes the potential energy in the search direction
μ	Scalar used during nonlinear CG minimization to compute α
β	Scalar used during CG minimization to compute the step direction
m	Atomic mass
Δt	Molecular dynamics timestep
ζ	Isothermal friction coefficient for constant temperature simulations
T_{o}	Temperature of external thermal reservoir
v_{T}	Thermostating rate of for constant temperature molecular dynamics
$\mathbf{R}_{o}$	Center of mass of a system of atoms
$\boldsymbol{\eta}$	Isobaric friction coefficient for constant pressure simulations
$\mathbf{P}_{o}$	Pressure or stress of external isobaric reservoir
k	Boltzmann's constant
v_{P}	Damping rate for constant pressure molecular dynamics
$\mathbf{h}$	Orientation vectors for the boundaries of the simulation cell
r^{ij}	Distance between atoms i and j
λ	Lattice constant
Q	Evolution operator for molecular dynamics integration scheme
$\boldsymbol{\Gamma}$	Multidimensional phase space vector
γ	Scalar factor on additional damping term for NPT equations of motion
G^{i}	Embedding energy contribution to the interatomic energy

φ	Pair interaction contribution to the interatomic energy
$\rho_{\text{ave}}^{\text{j}}$	Spherically averaged background electron density
γ_{US}	Unstable stacking fault energy
γ_{ISF}	Intrinsic stacking fault (ISF) energy
C_{11}, C_{12}, C_{44}	Single crystal elastic stiffnesses

Interface Model / Interface Geometry

Σ	Reciprocal density of coincident lattice sites between crystalline regions
W	Width (X-direction) of the interface model
H	Height (Y-direction) of the interface model
B	Thickness (Z-direction) of the interface model
ε	Strain of interface model
$\dot{\varepsilon}$	Strain rate of deformation
θ	Interface misorientation angle
M	Interface misorientation axis vector
N	Normal vector to the interface plane
ω	Strength of a partial wedge disclination
ν_m	Maximum deviation from a CSL boundary
ν_o	Low angle grain boundary limit = ~15$^{\text{o}}$
e_{i}	Potential energy of atom i
e^{bulk}	Bulk energy
e_{i}^{excess}	Excess energy of atom i due to the presence of the interface
E^{int}	Interface energy
A^{int}	Interface area
N^{int}	Number of atoms in the region around the interface for energy calculation
ω	Rotation vector which defines the strength of a disclination
L_p	Repeating period of the interface
d	Thickness of the interface region
D^{i}	Damage parameter for atom i
$\mathbb{Z}_1^{\text{i}}$	First-order coordination number of atom i
$\mathbb{Z}_{1,\text{th}}$	Threshold first-order coordination number
$\mathbb{Z}_{1,\text{ref}}$	First-order coordination number associated with a perfect lattice
D_{c}	Cumulative measure of damage (nanoporosity parameter)

Interface Separation Laws

ϕ	Cohesive interface separation potential
T	Traction vector on a crack surface
Δ	Displacement jump vector across a crack surface
Δ_{n}	Normal displacement jump across the interface

Δ_t	Tangential displacement jump across the interface
ϕ_o	Work of separation for the interface
δ_n	Characteristic length that normalizes the normal interface displacement
δ_t	Characteristic length that normalizes the tangential displacement
σ_{max}	Maximum interface strength
E_n	Energy of cleavage fracture of the interface
κ_{slide}	Coefficient that provides a weight to each slip system
E_s	Sliding energy for each slip system
E_γ	Energy for sliding along the interface
γ_F	Cleavage surface energy
E_n^*	Universal relation of Rose *et al*. (1983) for normal separation
Δ_{n0}	Equilibrium spacing across the interface at zero normal separation
κ	Rescaling factor to account for ductile separation
κ_R	Scalar function that reflects slip plane orientation and loading conditions
$\mathbf{\Lambda}_q$	Set of internal state variables that prescribes the material state
L	Characteristic length normal to the interface
ρ	Dislocation density within the interface region
$\boldsymbol{\kappa}_{s,i}$	Projects the local stress tensor onto the slip plane in the slip direction
$\boldsymbol{\kappa}_{n,i}$	Projects the stress tensor onto the slip plane normal
$\boldsymbol{\kappa}_{p,i}$	Projects the stress tensor onto the slip plane in the co-slip direction
$\bar{\omega}$	RMS characterization of the interface region
$\omega_{a,i}$	Amplitude of the individual roughness peaks
l	Arbitrary length along the interface plane
χ	Impurity atom parameter
C	Composition parameter
ℓ_c	Total line length of the dislocation cores
V_{int}	Volume of the interface region
$\ell_{y'x}$	Direction cosine between Y' and X directions
$\mathbb{Z}_j$	Total numbers neighbors to a particular atom
c_A^i	Compositional order parameter for type A atoms
c^i	Product of the compositional order parameters
σ_{ideal}	Ideal shear strength defined from *ab initio* calculations
SF	Projection of uniaxial stress onto slip plane in slip direction
NF	Projection of uniaxial stress onto the slip plane normal
PF	Projection of uniaxial stress onto slip plane in co-slip direction
μ	Scalar parameters used to characterize the extent of non-Schmid behavior
ξ	Amplification factor for the nanoporosity measure

SUMMARY

This dissertation focuses on the behavior of homogeneous FCC metallic interfaces on the nanoscale. Specifically, atomistic calculations (molecular statics and molecular dynamics) with embedded-atom method potentials are used to study the fundamental failure processes that occur at a bicrystal interface in Cu and Al as a result of a mechanical deformation. There are four primary objectives to this dissertation. First, molecular statics calculations are used to determine the most appropriate (minimum energy) structure of homogeneous bicrystal interfaces in Cu and Al. Interface structures and energies are reported in this work, with comparison to both theoretical and experimental characterizations of interface configuration. Second, molecular dynamics simulations are performed to provide a characterization of atomic scale inelastic behavior, including both dislocation and void nucleation activities which lead to interfacial failure. Specifically, two 'types' of interfaces are highlighted in this work: a mirror symmetric interface in aluminum and an asymmetrically dissociated interface in copper. Distorted interface structures (after the dislocation nucleation event) are discussed in terms of partial dislocations or disclinations. Third, molecular dynamics simulations are used to investigate potential relationships between interface structure and interface properties or morphology. The orientation of the primary slip planes with respect to the loading direction and the porosity within the interface region are found to be critical factors in defining the strength of the bicrystal interface, for example. Finally, results of the atomistic calculations are utilized to motivate improved forms for

continuum interface separation potentials, ultimately increasing the applicability of these relationships to include cohesive failure in ductile crystalline materials.

CHAPTER I

INTRODUCTION

I.1 Motivation

According to materials scientist/philosopher Cyril Stanley Smith, the structure of materials is best described as a multilevel composition, with strong interaction between levels and certain interplay of perfection and imperfection at all levels (Smith, 1981). This point of view asserts that a clear understanding of material behavior at each length scale is imperative to elucidate the technological or economic value of a material (Olson, 2000). However, most theories of material behavior are based on macroscopic experimental evidence or observation of a naturally occurring process. For example, the kinematic hardening model in continuum plasticity was developed to describe experimental observations of the Bauschinger effect (*cf*. Khan and Huang, 1995). While experimental observations are of tremendous scientific importance, it is highly desirable to develop models that relate the constitutive description of a material to the underlying material microstructure.

The desire to determine structure-property relationships at the atomic level has motivated the field of nanomechanics. Two interests drive this emerging field. First, we seek a fundamental understanding of failure processes and mechanisms that occur at nanometer length scales (McDowell, 2001). For example, it is critical to understand the role of grain boundary interfaces in nanocrystalline materials, as their structure strongly influences many material properties (*cf.* Wolf, 1990; Randle, 1996). In addition, forces

between grain boundaries constrain dislocation emission sources to be predominantly located at the nanocrystalline interfaces (Van Swygenhoven *et al*., 1999a). The second driving interest of nanomechanics is to design or engineer material micro or nanostructures to meet specific mechanical and/or thermal requirements (McDowell, 2001). Here, economic considerations enter, as the ability to control plastic deformation and the related failure processes is extremely important in the design of many metallic engineering components, for example.

Accordingly, this work focuses on modeling the atomic level mechanisms associated with inelastic behavior of homogeneous interfaces on the nanoscale and developing structure-property relationships based on these nanoscale observations. Several experimental studies on polycrystalline samples have indicated that interface structure has an effect on material properties, such as grain boundary energy, mobility, corrosion, crack nucleation and ductility (*cf.* Randle, 1996; Schuh *et al*., 2003 and references therein). Most of the published investigations indicate that there is some correlation between the occurrence of coincident site lattice (CSL) boundaries and material properties; however, the agreement between published results in the literature does not point to a universal relationship. Recall, the CSL methodology may be used to describe the misorientation between crystalline regions (Randle, 1993; Howe, 1997). In general, boundaries with low values of Σ are considered to have better fit along the interface plane, as compared with more general high-angle interfaces. A detailed review of the CSL model and the Σ notation will be provided later in this thesis.

Figure I.1(a) shows the distribution of cracked and uncracked boundaries during low-cycle fatigue of polycrystalline nickel samples from Lim (1987). Interestingly, Lim

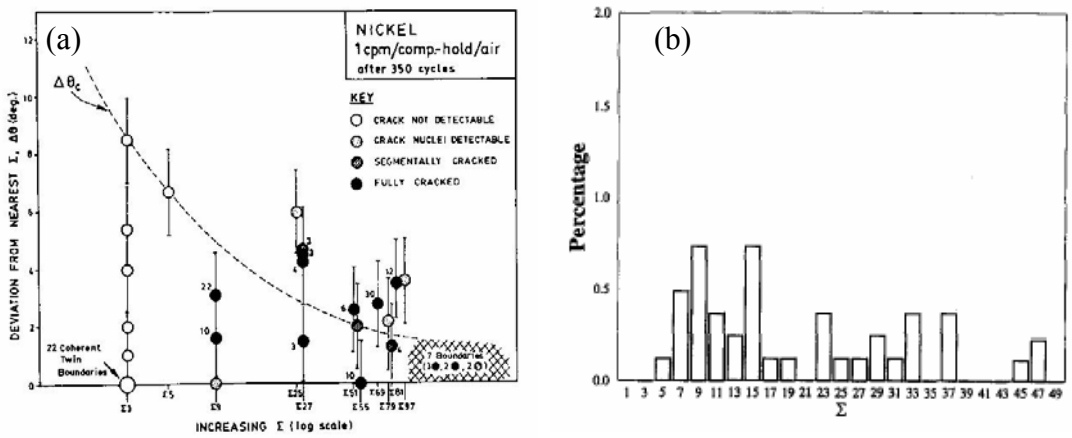

Figure I.1. Effect of grain boundary misorientation on intergranular cracking in (a) nickel from Lim (1987) and (b) nickel based alloy X-750 from Pan *et al*. (1996).

finds that boundaries with low-order CSL character (Σ3 and Σ5) do not crack during the deformation process. In their work, intergranular cracks are induced by impinging slip bands; thus, the resistance of the Σ3 boundary to slip is explained in terms of the ease of dislocation transmission across the coherent twin boundary. Figure I.1(b) shows the distribution of cracked boundaries as a result of stress corrosion from Pan *et al*. (1996). Note that low-angle (Σ1) and Σ3 boundaries (which composed 46% of the original boundary distribution) did not crack. Other experimental studies in the literature on polycrystalline samples of copper (Field and Adams, 1992), for example, have provided similar conclusions regarding the weak relationship between CSL occurrence and cavitation during a mechanical deformation.

Motivated by the experimental observations, the concept of grain boundary engineering was proposed by Watanabe (1984). Here, the goal is to increase the percentage of 'special' boundaries and to reduce the connectivity of 'random' boundaries through material processing techniques. Reducing the connectivity of random boundaries

is particularly important, as polycrystalline samples with a properly oriented continuous path of weak boundaries would be susceptible to failure regardless of the percentage of special CSL interfaces (Watanabe, 1994). Specifically, several authors have shown that the fraction of special boundaries can be increased through sequential cycles of straining and annealing (*cf*. Schuh *et al*., 2003). As a result, enhancements in corrosion resistance (Palumbo and Aust, 1990), creep resistance (Watanabe *et al*., 1991) and crack nucleation and growth resistance under various loading conditions (Watanabe and Tsurekawa, 1999) have been observed experimentally. Of particular effectiveness is the introduction of annealing twins, which are essentially Σ3 coherent interfaces (Gertsman and Tangri, 1995). These twins lead directly to an increase in the fraction of special boundaries and to the reduction of the connectivity of the random boundaries through interaction effects. Further, crack growth may be arrested at triple points that contain at least two Σ3 boundaries.

For nanocrystalline samples, atomistic simulations have been used to investigate potential relationships between interface structure and interface properties (Van Swygenhoven *et al*., 1999b; Caturla *et al*., 2004). In their work, molecular dynamics (MD) simulations are used to deform a nanocrystalline nickel sample composed entirely of either low- or high-angle boundaries. Molecular dynamics is a computation method used to calculate the trajectories (positions and velocities) of individual atoms (*cf.* Allen and Tildesley, 1987; Haile, 1992). The force on a given atom is calculated using an interatomic potential, which is calibrated using a set of experimental or electronic structure data. A detailed review of atomistic methods will be given in Chapter II. Both Van Swygenhoven *et al*. (1999b) and Caturla *et al*. (2004) show that nanocrystalline

nickel samples composed entirely of low-angle boundaries have enhanced dislocation activity and reduced strength as compared with the high-angle samples. For the high-angle samples, most of the deformation is associated with the grain boundaries; while for the low-angle samples, deformation is primarily due to traditional dislocation slip activity within the grain interiors.

I.2 Thesis Objectives and Goals

There are four main objectives to this dissertation: (i) to efficiently determine the minimum energy equilibrated structure of homogeneous copper and aluminum bicrystal interfaces; (ii) to provide a characterization of atomic scale inelastic behavior at an interface, including both dislocation and void nucleation activities which lead to interfacial failure; (iii) to investigate potential relationships between interface structure (occurrence of CSL boundaries) and interface properties; and (iv) to utilize the results of the atomistic calculations to motivate improved forms for continuum interface separation potentials, contributing eventually to a more predictive multiscale model of fracture.

First, molecular statics (MS) calculations are used to determine the minimum energy structure for each interface misorientation considered. Energy minimization is attained using a nonlinear conjugate gradient algorithm (Shewchuk, 1994). It is imperative that the interface structures be posed properly in order to draw definite conclusions regarding the role of individual interface features during the inelastic deformation process. Consequently, this work follows the methodologies developed by Wolf (1990) and Rittner and Seidman (1996) who perform energy minimization

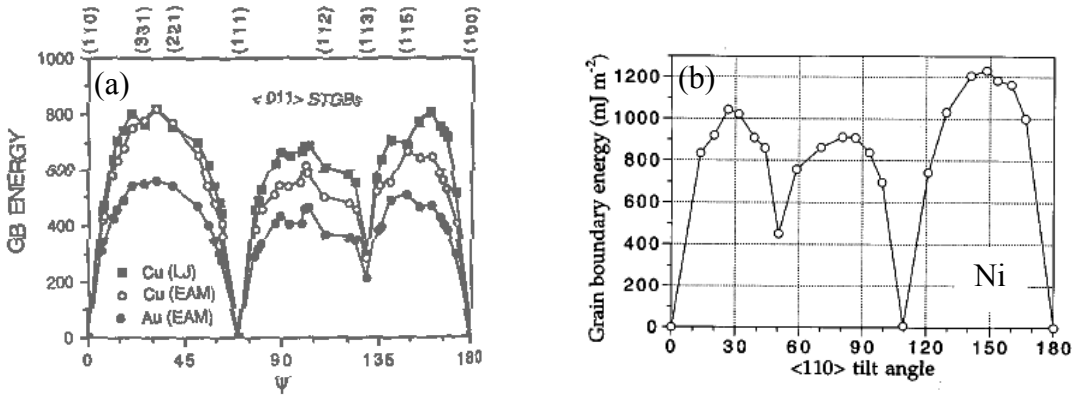

Figure I.2. Grain boundary interface energy as a function of misorientation angle for <110> symmetric tilt interfaces reproduced from (a) Wolf (1990) and (b) Rittner and Seidman (1996).

calculations for a range of face-centered cubic (FCC) materials. Specifically, they showed that a number of initial 'starting configurations' must be used to improve the probability that the energy minimization algorithm finds the global minimum energy configuration. Figure I.2 shows the interface energy as a function of the interface misorientation angle for <110> Cu, Au and Ni interfaces from atomistic simulation results in the literature. Note that the misorientation angle is measured using a different reference crystallographic direction for each graph in Fig. I.2. Large cusps appear in the energy misorientation angle relationship at specific misorientation angles. Interestingly, these misorientation angles correspond to the low-order Σ3 and Σ11 CSL interfaces.

This work represents an advancement over previous energy minimization calculations of interface structure in FCC metallic systems due to the accuracy of the interatomic potential used for these calculations. Note, in Fig. I.2(a), different interatomic potentials for copper yield different results regarding the existence and magnitude of energy cusps. Rittner and Seidman (1996) showed that the value of the

intrinsic stacking fault (ISF) energy can significantly affect the nanoscopic details of the interface structure. More importantly, for low ISF materials, the dislocations that compose the interface may dissociate, leading to an increased thickness for the disordered region at the boundary (Rittner *et al*., 1996). The interatomic potential used in each of the cited energy minimization calculations underestimates the ISF energy of the material (Zimmerman *et al*., 2000). Thus, while the energy minimization calculations presented in the literature lead to a robust method for determining the minimum energy configuration, the structures and energies reported may not be accurate for the FCC material of interest in each article. Calculations in this thesis use an interatomic potential that is rigorously fit to the intrinsic and unstable stacking fault energies, thus providing a more accurate description of the interface structure and energy in both copper and aluminum. The interface structures and energies for a range of tilt Cu and Al misorientations are presented in Chapter III.

Second, molecular dynamics simulations are used to study the atomic scale mechanisms that occur at a bicrystal interface as a result of an applied mechanical deformation. Particular attention is paid to the role of specific interface features during the deformation process and the resulting structure of the interface before and after the dislocation nucleation event. The large majority of molecular dynamics simulations of inelastic deformation in the literature have focused on nanocrystalline samples (Schiøtz *et al*., 1998; 1999; Van Swygenhoven *et al*., 1998; 1999a; 1999b; 1999c; 2001; 2002; 2004; Yamakov *et al*., 2001; 2002; 2003). For example, Van Swygenhoven and colleagues have used displacement vectors and atomic coordination to monitor the nucleation of dislocations and the evolution of the interface structure in nanocrystalline nickel and

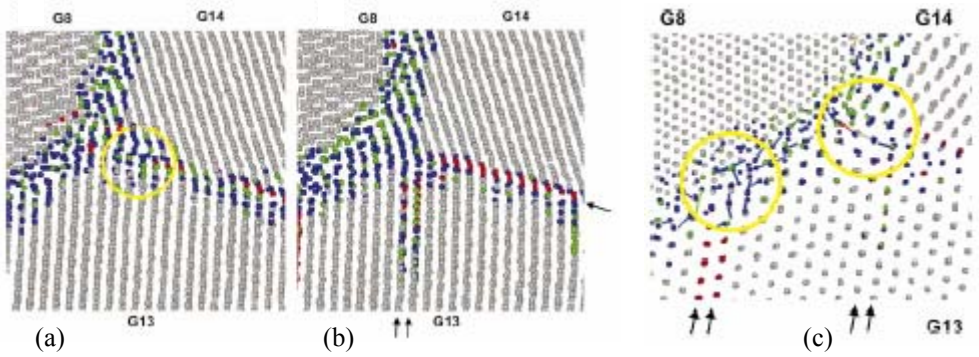

Figure I.3. Nucleation of partial dislocations and associated interface evolution during uniaxial tensile deformation of nanocrystalline nickel from Van Swygenhoven *et al*. (2002); (a) before partial dislocation nucleation, (b) after partial dislocation nucleation, and (c) movement of individual atoms along the interface plane.

copper samples. Figure I.3 shows the nucleation of two partial dislocations from a grain boundary interface near a triple point in nanocrystalline nickel (Van Swygenhoven *et al*., 2002). They observed atomic shuffling and stress-assisted free volume migration along the interface plane prior to the dislocation nucleation event. However, it is unclear in the nanocrystalline simulations what role the accuracy of the initial interface structure plays in their conclusions. Energy minimization is typically not performed prior to the application of a mechanical deformation; instead, the nanocrystalline sample is 'annealed' at room temperature for a brief period of time to equilibrate the structure.

Surprisingly, there is limited atomistic simulation work in the literature that directly addresses the deformation characteristics of bicrystal metallic interfaces. The bicrystal energy minimization calculations (Wolf, 1990; Rittner and Seidman, 1996) do not address inelastic behavior, only the structure and energy of boundaries at 0 K and finite temperature. Chandra and Dang (1999) study the sliding and migration characteristics of several low-order Σ interfaces in aluminum. Sliding is induced by

applying either a displacement or a force to one of the crystalline regions. When subjected to an applied shear force, they showed that grain migration and grain sliding are inherently coupled. In addition, low energy boundaries offered more resistance to shear deformation than higher energy boundaries. The quasicontinuum method has been recently used by Sansoz and Molinari (2004; 2005) to study the deformation of bicrystal models with symmetric Σ boundaries. In tension, failure of the interface occurred through partial dislocation nucleation and grain boundary cleavage. In shear, their worked showed that three different failure modes could exist depending on the initial boundary configuration: grain boundary sliding by atomic shuffling, nucleation of partial dislocations from the bicrytal interface and grain boundary migration. Atomic shuffling was correlated to the presence of the E structural unit, which is associated with the Σ9 (221) interface (Rittner and Seidman, 1996), and appeared to be triggered by the free volume inherent to this structural feature.

In this thesis, molecular dynamics simulations are performed to study the inelastic deformation of bicrytal boundaries in Cu and Al with a range of interface misorientations. This work extends beyond the previous atomistic calculations in the literature that investigate the mechanisms associated with dislocation nucleation using either bicrystal or nanocrystalline geometries by (i) addressing interface evolution and dislocation nucleation at finite temperature (as opposed to 0 K), (ii) considering larger bicrystal samples (by an order of magnitude in some cases) than the previous studies and (iii) by proposing models for the deformed structure of specific interfaces using either partial dislocations or disclinations. The development of proposed models for the deformed interface structure is possible only because energy minimization is performed on the

bicrystal samples prior to the application of a mechanical deformation. As a result, the interface structure is well characterized in terms of structural units and disclinations prior to the dislocation nucleation event. More detail will be provided regarding the disclination-structural unit model representation of interfaces in Chapter III.

Molecular dynamics simulations in this thesis are performed using either 'uniaxial' or 'constrained' tension boundary conditions, which may be considered as limiting cases for deformation in nanoscale systems. Uniaxial tension boundary conditions involve the application of deformation at a constant strain rate normal to the interface plane, while the lateral boundaries are prescribed as stress free (and thus allowed to contract during the deformation process). Constrained tension boundary conditions involve the application of deformation at a constant strain rate normal to the interface plane, while the lateral boundaries are unaltered (and hence will be immobile as a result of the periodic boundary conditions). Thus, these simulations consider stresses parallel to the boundary plane during the tensile deformation process. Both sets of simulations use a mixed set of equations of motion for the atomic trajectories, which are developed as part of this work. Much more detail will be given regarding each boundary condition later in this work.

Third, this thesis addresses potential relationships between nanoscale interface structure and interface properties. As discussed above, both experimental studies on polycrystalline metals and molecular dynamics simulations of inelastic behavior in nanocrystalline samples in the literature showed that grain boundary structure plays a role in the deformation process. In this work, relationships between nanoscale interface structure and interface properties are developed through two measures. First, inelastic

interface properties are plotted as a function of the misorientation angle of the boundary. Important inelastic properties include the peak tensile strength, the displacement associated with peak tensile strength and the tensile work of separation. Interface stress is calculated using the virial definition (*cf.* Allen and Tildesley, 1987) averaged over a small region around the boundary. Second, an approximation of the porosity within the interface region on the nanoscale is developed and correlated to the interface properties. The nanoporosity measurement is developed using the number of first-nearest neighbors to a particular atom and may be adjusted to be sensitive to different types of damage mechanisms.

Finally, motivated by the atomistic calculations performed in this thesis, a framework is proposed to incorporate a characterization of the atomic scale interface structure into a continuum description of separation across an interface, representing a multiscale analysis of ductile interface failure. Previous methods that address connecting material behavior across multiple length scales may be grouped into three categories (Cleri *et al*., 1998): large-scale atomistic simulations, hybrid matching techniques and multi-scale constitutive models. In the multiscale constitutive model approach, a specific constitutive relationship (that describes the atomic process of interest) is used in the area around a defect; while a classical constitutive model (such as linear elasticity) is used to describe material behavior far away from the defect. Thus, atomic information is embedded within the continuum bulk response without prescribing an explicit atomic-continuum coupling.

The critical step in the multiscale constitutive model approach is the selection or development of constitutive equations that mimic atomic scale phenomena. For example,

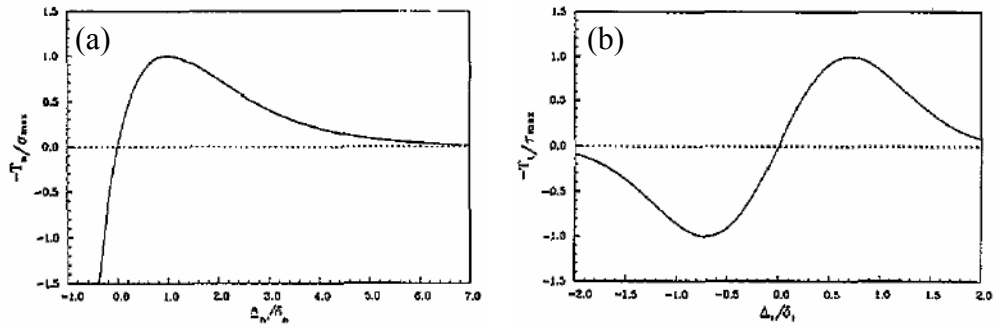

Figure I.4. Phenomenological form of continuum interface separation potentials from Xu and Needleman (1993) for (a) normal and (b) tangential interface separations.

to study the brittle-ductile transition in crystalline solids, Rice (1992) developed a constitutive model for dislocation nucleation at a crack tip, based on the Peierls concept for mobile dislocations (Peierls, 1940); this criterion is useful for understanding whether crack extension may occur via ductile means or cleavage. To model interfacial debonding, Needleman (1987) proposed a phenomenological description of separation across an interface based on the concept of a cohesive process zone at a crack tip (Dugdale, 1960; Barenblatt, 1962). In his approach, the traction vector $\mathbf{T}$ on a crack surface is related to the displacement jump vector $\mathbf{\Delta}$ across that crack surface through a cohesive interface separation potential ϕ. The interface separation potential is designed to serve as an analogue to the atomic separation process. For example, the phenomenological form of the interface separation potential used by Xu and Needleman (1993) is shown in Fig. I.4. Recent work has attempted to define the phenomenological form of the traction-displacement relationship for specific material systems based quantum mechanical calculations (Hao *et al*., 2003) or molecular statics simulations (Grujicic and Lai, 1998). In general, atomic scale calculations typically play two main

roles: (i) to suggest forms for constitutive relationships that mimic atomic scale behavior; and (ii) to evaluate assumptions made regarding material behavior on the nanoscale.

It must be emphasized that the Needleman type cohesive interface separation potentials are based purely on a phenomenological description of interface separation. Thus, these potentials are typically limited to brittle materials, where cleavage fracture is the dominant mode of failure. Interface separation in ductile materials may differ substantially from that shown in Fig. I.4. To model decohesion between ductile metallic constituents, interface separation laws must incorporate dissipative mechanisms, such as dislocation nucleation, that potentially changes the separation energy and maximum strength (Needleman, 1992). Accordingly, recent work (Klein *et al*., 2003; Hao *et al*., 2003) has begun to extend interface separation potentials to ductile constituents. The cohesive relationships in Klein *et al*. (2003) are developed within a thermodynamically consistent framework which is motivated by dislocation mechanics. The length scale over which the failure mechanisms act is extracted through *in-situ* scanning electron microscopy and other experimental evidence (which provide additional details regarding mode-mixity and loading rate effects). The work of Hao *et al*. (2003) is particularly intriguing in that they explicitly account for the effect of dislocation nucleation at the interface in the normal separation relation. The normal components of the gliding induced separations reduce the magnitude of the normal work of separation for the interface. Quantum mechanical calculations are used to determine the parameters required (cleavage surface energy, unstable stacking fault energy) to define the shape of the interface separation laws.

While the above formulations are significant advancements, most current interface separation potentials fail to explicitly account for nanoscale interface details, necessary to distinguish between interfaces and grain boundaries with differing degrees of coherency. The atomistic calculations presented in this thesis are designed to address this issue. Previous work has shown that atomistic calculations are quite capable of providing detailed nanoscale information to guide continuum constitutive relationships (Bozzolo *et al*., 1991; Kaxiras and Duesbery, 1993; Miller and Phillips, 1996, Cleri *et al*., 1998; Grujicic and Lai, 1998, Hao *et al*., 2003). Particularly, the work of Hao *et al*. (2003) represents a significant advancement; however, their methodology is based on separation between a ductile matrix and a rigid inclusion. Dislocation nucleation from the interface is assumed to add directly to the normal interface separation. For interfaces between two ductile components (such as grain boundaries in metals), calculations presented in this thesis will show that dislocation nucleation from the interface does not immediately open voids along the interface plane. The problem of including dislocation emission from interfaces in interfacial separation laws is indeed complex.

I.3 Thesis Structure

Chapter II presents the theory of atomistic simulation. First, the basic assumptions and simplifications of the atomistic method are discussed, including the role of molecular ensemble and periodic boundary conditions in either equilibrium or nonequilibrium simulations. Next, the mathematical details of the nonlinear conjugate gradient method are presented. This method is used to achieve energy minimization

during molecular statics calculations. Section II.3 outlines the fundamentals of the molecular dynamics method. The equations of motion associated with each molecular ensemble are discussed with detailed explanation of the time-reversible velocity-Verlet type integration algorithms used in this work. Two modifications to the isobaric-isothermal equations of motion are also presented. These modifications are necessary to be able to compare the inelastic deformation processes in solids with different crystallographic orientations. Finally, the fundamentals of the embedded-atom method are discussed in Section II.4, with detailed explanation regarding the choice of the Mishin *et al*. (1999; 2001) interatomic potentials for this work. This chapter concludes with results from several simple models that validate the accuracy of both the molecular dynamics code and the Mishin *et al*. interatomic potentials.

Chapter III presents the structures and energies of the Cu and Al interface misorientations considered in this work. First, a review of interface theory, the coincident site lattice methodology and the use of structural units and disclinations in the description of interface structure is presented. This review is designed to introduce the concepts and terminology that will be used throughout this thesis. Next, the details of the energy minimization procedure, the calculation of interface energy and the boundary conditions for each interface model are discussed. The role of the atomic 'overlap' parameter, which controls the spacing and shift of the lattice regions at the interface in the WARP atomistic code, is discussed in detail. In Section III.3, the interface energy as a function of misorientation angle is presented with comparison to that reported in the literature. Finally, the bicrystal interface structures for many low-order CSL boundaries in copper and aluminum are presented with comparison to both theoretical (structural unit

model) and experimental (high-resolution transmission electron microscopy) characterizations of interface structure.

Chapter IV presents molecular dynamics simulations of partial dislocation nucleation from bicrystal interfaces during a uniaxial tensile deformation process. Particular attention is paid to the evolution of the interface structural units in copper and aluminum during the dislocation nucleation event. First, a review of atomistic simulation work in the literature is presented which details the current understanding of atomic scale processes during a mechanical deformation. In this chapter, two types of interface structures are examined in detail, (i) a perfectly mirror symmetric interface in aluminum and (ii) an asymmetrically dissociated interface in copper. During tensile deformation of the symmetric aluminum interface models, both leading and trailing partial dislocations are emitted from the interface. After the nucleation of the trailing partial dislocation, a ledge is created at the intersection of the slip plane and the bicrystal boundary. The structure of this ledge is discussed in terms of disclinations. For the dissociated copper interface, the role of the dissociated structural unit in the deformation processes is examined in detail. Here, the geometric configuration of the ISF facet, which is associated with the asymmetric dissociation of secondary interface dislocations, is shown to promote dislocation activity on secondary slip systems. The evolution of the interface structure is discussed in terms of partial dislocation positions at various stages during the deformation process.

Chapter V presents a quantitative molecular dynamics investigation of potential relationship between interface structure and interface strength using different boundary prescriptions. Here, the two boundary conditions employed may be considered as

limiting cases for deformation in nanoscale systems. Specifically, calculations in this chapter consider multiaxial stress states that occur when lateral confinement of the interface structure is an important consideration. Previous results in the literature on single crystals have shown that the deformation conditions can drastically alter the nanoscale deformation mode (Kitamura *et al*., 1997). In this work, the tensile stress normal to the bicrystal boundary and the porosity within the interface region are monitored throughout the tensile deformation process for each interface considered. An approximation of porosity within the interface region is developed using the first-order coordination number of each atom within the system. Accordingly, a threshold atomic coordination is defined, below which an atom is considered to be completely damaged. The ability of the interface porosity measurement to characterize the evolution of the interface structural units and to correlate the interface strength to the interface structure is discussed in detail.

Chapter VI discusses the potential relationships between atomistic simulations of ductile interface separation and continuum interface separation potentials. First, existing methods in the literature designed to couple descriptions of material behavior over multiple material length scales are briefly reviewed. Particular attention is paid to the work of Needleman (1987), who pioneered the use of continuum interface separation potentials to model interface decohesion. Limitations of the Needleman approach are addressed, including failure to account for dissipative mechanisms (such as dislocation nucleation or structural rearrangement) and failure to include nanoscale interface details, which are necessary to distinguish between interfaces and grain boundaries with differing degrees of coherency. Recent work in the literature (Hao *et al*., 2003; 2004) has

attempted to explicitly account for the effect of dislocation emission on the form of the traction-separation relationship for interfaces between Fe and TiC inclusions in steel. A full discussion of this work is provided in Chapter VI. The applicability of the Hao *et al*. formulation to model interface separation between ductile FCC metallic materials is addressed based on molecular dynamics simulation results in this thesis. Finally, a general model is proposed, based on internal state variable (ISV) theory, which allows for the incorporation of nanoscale interface attributes, such as interface porosity, into a continuum description of interface separation. The ISVs are intended to be derived from MD calculations and relate length scale and orientation parameters associated with the interface structure to the interface separation process. The goal is to obtain a more realistic description of ductile material separation, using nanoscale level details from atomistic simulation results as the building block.

Chapter VII summarizes the significant contributions of this thesis via a bulleted list of accomplishments and provides recommendations for future research directions which build upon the results in this work.

CHAPTER II

THEORY OF ATOMISTIC SIMULATION

II.1 Introduction

Atomistic simulation refers to a suite of computational techniques used to model the interaction and configuration of a system of atoms. In this work, the term 'atomistic simulation' will pertain to both molecular mechanics (statics) and molecular dynamics. Sections II.2 and II.3, respectively, will provide a brief explanation of each method. More detailed and comprehensive reviews are found in books by Allen and Tildesley (1987) and Haile (1992).

Atomistic simulations are commonly classified into two categories: equilibrium and nonequilibrium (Haile, 1992). In equilibrium atomistic simulations, the system is *completely* isolated from its surroundings with a fixed number of atoms, volume and constant total energy. These boundary conditions correspond to the microcanonical (NVE) ensemble in statistical mechanics (Greiner *et al*., 1995). In nonequilibrium atomistic simulations, the system is *allowed to interact* with the surrounding environment through either thermal or physical constraints (such as a thermostat or an applied force). Depending on the equations of motion that describe the system of atoms, these calculations may correspond to the canonical (NVT or NPT) ensemble in statistical mechanics. Note that many different methods exist to specify the interaction between the atomic system and the environment, all of which fall under the general umbrella of nonequilibrium MD methods. Section II.3 will present the differential equations of

motion that correspond to each molecular ensemble. Historically, the use of atomistic calculations to model nonequilibrium behavior, such as crack propagation and fracture, can be traced back to the pioneering work of Ashurst and Hoover (1976).

In the atomistic framework, each atom is represented as a point mass in space while the interatomic potential provides a model for the potential energy of a system of atoms. Commonly, the total potential energy of the system is written solely as a function of the positions of the atomic nuclei. This simplification avoids having to specifically account for the motion and interaction of the individual electrons. Since interatomic forces are conserved, the force on a given atom, $\mathbf{F}^{\mathrm{i}}$, is related to the interatomic potential, U, through the gradient operator, i.e.,

$$\mathbf{F}^{\mathrm{i}} = -\frac{\partial U\left(\mathbf{r}_{\mathrm{N}}\right)}{\partial \mathbf{r}^{\mathrm{i}}} \quad . \tag{II.1}$$

Here, $\mathbf{r}$ is the atomic position vector. In this work, superscripts denote variables assigned to individual atoms, while subscripts denote variables associated with sets of atoms, directions or at specific time steps. Thus, $\mathbf{r}_{\mathrm{N}}$ represents the position vectors for the system of N atoms while $\mathbf{r}^{\mathrm{i}}$ is the atomic position vector for the i^{th} atom. Detailed information regarding the interatomic potential used for calculations in this work is presented in Section II.4.

One of the inherent limitations of the atomistic method is that computational resources often demand that systems are limited to relatively small numbers of atoms. While the study of nanoscale surface effects (which are related to length scale) is

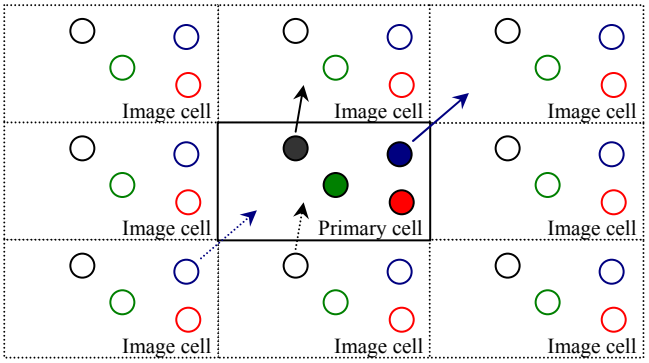

Figure II.1. Two-dimensional illustration of periodic boundary conditions in the atomistic framework.

extremely important, the goal of this work is to examine atomic scale behavior that is representative of what would occur in a bulk sample with micro or nanoscale grain structure. Thus, periodic boundary conditions are used in many of these calculations to eliminate the influence of free surface effects. Fig. II.1 shows a two-dimensional illustration of the use of periodic boundary conditions in the atomistic framework. The primary cell is outlined with solid lines and represents a small portion of material. Atoms that lie within this cell are explicitly modeled using atomistic methods. The bordering 'image' cells, which are outlined with dashed lines in Fig. II.1, represent the infinite repetition of the primary cell in two dimensions. With this methodology, an infinite amount of material is modeled in each direction.

Suppose that the blue atom in the primary cell moves to a point outside of this region during the simulation, as shown with a solid blue arrow in Fig. II.1. The image of this atom will be reflected back into the primary cell on the opposite side with the same momentum, as shown with the dashed blue arrow in Fig. II.1. Note that atoms that lie near the borders of the primary computational cell interact with neighbor atoms across

the periodic boundary. While periodic boundary conditions remove the effects of free surfaces, they impart image constraints on the system which must be taken into consideration when simulating defect behavior with long-range interactions. Such long-range interactions are characteristic of dislocations and asymmetric interfaces, as will be modeled in this work.

The atomistic code used in this thesis was written by Dr. Steve Plimpton at Sandia National Laboratories / Albuquerque, NM. The code is written in FORTRAN90 and uses the MPI message passing libraries to perform parallel calculations with a domain-decomposition technique. The original MD code was capable of performing molecular dynamics simulations in the microcanonical (NVE) and the constant volume canonical (NVT) ensembles. To meet the computational objectives of this project, a number of additional subroutines and algorithms have been written and/or implemented. The two major additions to the atomistic code are (i) the capability to perform molecular statics (energy minimization) calculations and (ii) the ability to perform molecular dynamics simulations in the isobaric-isothermal canonical (NPT) ensemble. The conjugate gradient algorithm used in the molecular statics calculations was originally written by Dr. Jonathan Zimmerman at Sandia National Laboratories / Livermore, CA. This algorithm has been implemented in parallel into the new atomistic code. In addition, a number of smaller modifications have been made to the code that are critical to the analysis provided in this thesis, such as a mixed set of boundary conditions to perform constant strain rate simulations in the framework of the NPT equations of motion and the implementation of algorithms to identify various characteristics of nanoscale defect configurations.

II.2 Molecular Statics

In this work, molecular statics (MS) calculations are used to compute the minimum energy interface structures and excess energies, within a given tolerance. It is critical that the initial interface structures be described accurately to be able to draw definite conclusions regarding the role of individual interface features in the deformation process. A nonlinear conjugate gradient method is used to calculate the atomic positions associated with the minimum potential energy of a system. The following is a brief overview of the algorithms implemented in this work. A more complete review of steepest decent, linear and nonlinear conjugate gradient methods is provided in Shewchuk (1994).

The method of conjugate gradients (CG) is a prominent iterative technique used to solve sparse systems of equations. In general, the CG method may be used to find the minimum of any continuous function $f(x)$ as long as $f(x)$ contains a lower bound and the gradient $f'(x)$ may be computed. Recall from Eq. (II.1) that the negative of the gradient of the potential energy U was defined as the force vector. By definition, the gradient vector points in the direction of the greatest increase of a given function. Thus, the force vector points in the direction of greatest decrease in the potential energy. The minimum of the potential energy is found by setting the gradient equal to zero and solving for the appropriate values of $\mathbf{r}_N$. Energy minimization techniques define the *residual* as the negative of the gradient of the potential energy, i.e.,

$$\mathbf{g}_m = -\frac{\partial U\left(\mathbf{r}_{\mathrm{N}}\right)}{\partial \mathbf{r}_m} \quad . \tag{II.2}$$

Here, m denotes the CG iteration step. Clearly, Eqs. (II.1) and (II.2) are equivalent; thus, the force vector is defined as the residual of the potential energy. An iterative processes is used to update the atomic position vectors,

$$\mathbf{r}_{m+1} = \mathbf{r}_m + \alpha_m \mathbf{d}_m \quad . \tag{II.3}$$

In Eq. (II.3), $\mathbf{d}_m$ is the step (or search) direction and α is a scalar that minimizes the potential energy in the search direction. Note that $\mathbf{d}_m$ is not typically a unit vector. In general, the solution for α requires that the gradient of the potential energy at the point $\mathbf{r}_m + \alpha_m \mathbf{d}_m$ be orthogonal to the search direction, i.e.,

$$\left[U'\left(\mathbf{r}_m + \alpha_m \mathbf{d}_m\right)\right]^T \mathbf{d}_m = 0 \quad . \tag{II.4}$$

In the nonlinear conjugate gradient framework, a line search algorithm is commonly used to solve the above expression, such as the Newton-Raphson or Secant method. Both require that the second derivative of the potential energy exist and be continuous. The Newton-Raphson method attempts a direct calculation of the second derivative of the potential energy to determine α,

$$\alpha_m = -\frac{\left[U'(\mathbf{r}_m)\right]^T \mathbf{d}_m}{\mathbf{d}_m^T \left[U''(\mathbf{r}_m)\right] \mathbf{d}_m} \quad . \tag{II.5}$$

Clearly, both first and second derivatives of the potential energy must be evaluated at each iteration step. Unless $U''(\mathbf{r}_m)$ is a very simple function, this is often computationally expensive. Thus, the algorithm used in this work employs the Secant method to determine the step length. The secant method does not directly compute $U''(\mathbf{r}_m)$; rather, the second derivative of the potential energy is approximated by evaluating the first derivative (negative of the force vector) at points $\alpha = 0$ and $\alpha = \mu$, where μ is a small, nonzero number,

$$\alpha_m = -\mu \frac{\left[U'(\mathbf{r}_m)\right]^T \mathbf{d}_m}{\left[U'(\mathbf{r}_m + \mu \mathbf{d}_m)\right]^T \mathbf{d}_m - \left[U'(\mathbf{r}_m)\right]^T \mathbf{d}_m} \quad . \tag{II.6}$$

The numerator in the above equation contains the inner product between the first derivative of the potential energy (evaluated at the point $\alpha = 0$) and the search direction. The denominator contains the difference between inner products evaluated at $\alpha = \mu$ and $\alpha = 0$. The choice of μ is arbitrary during the first iteration of the Secant method. For each subsequent iteration, the value of μ is set equal to the negative of the previous value of α, i.e., $\mu_{n+1} = -\alpha_n$. Here, n denotes the number of iterations taken in the Secant method.

The definition of the step direction differentiates between different minimization techniques. For example, the method of steepest decent (SD) sets the search direction equal to the residual at each iteration. Thus, successive search directions will always be orthogonal (in a Cartesian sense). Unfortunately, the method of steepest decent is inefficient as the algorithm will step in the same direction a number of times during the energy minimization procedure. Linear and nonlinear conjugate gradient methods use the residual to define the initial search direction only, i.e.,

$$\mathbf{d}_0 = \mathbf{g}_0 = -\frac{\partial U}{\partial \mathbf{r}_0} \quad . \tag{II.7}$$

Using Eq. (II.7) and an appropriate step size, α, the atomic positions may be updated using Eq. (II.3) from $\mathbf{r}_0$ to $\mathbf{r}_1$. Once the new positions are determined, the new residual is calculated in the nonlinear conjugate gradient method directly, i.e., $\mathbf{g}_{m+1} = -\partial U / \partial \mathbf{r}_{m+1}$. To continue the iterative process, each subsequent search direction is constructed from the new residual and the last step direction, i.e.,

$$\mathbf{d}_{m+1} = \mathbf{g}_{m+1} + \beta_{m+1}\mathbf{d}_m \quad . \tag{II.8}$$

In Equation (II.8), the new search direction, $\mathbf{d}_{m+1}$, is built from the last search direction using the scalar β. Clearly, if $\beta = 0$, the new search direction is equal to the new residual and the method of steepest decent is recovered. In the method of conjugate

gradients, the constant β is derived by demanding that successive search directions are U-orthogonal (conjugate), i.e.,

$$\mathbf{d}_{m+1}^{T} U \mathbf{d}_{m} = 0 \quad . \tag{II.9}$$

Equation (II.9) illustrates the common confusion regarding the name of the conjugate gradient method. The gradients themselves are not conjugate and the conjugate directions are not gradients (Shewchuk, 1994). More accurately, conjugate directions are chosen through a Gram-Schmidt conjugation of the residuals. For nonlinear problems (as in atomistic calculations), two estimations are available for β. First, the Fletcher-Reeves formula states,

$$\beta_{m+1}^{FR} = \frac{\mathbf{g}_{m+1}^{T} \mathbf{g}_{m+1}}{\mathbf{g}_{m}^{T} \mathbf{g}_{m}} \quad . \tag{II.10}$$

In the Fletcher-Reeves derivation, β is simply the ratio of the inner products of the residuals for successive iteration steps. The Fletcher-Reeves formula may be used for both linear of nonlinear functions. However, in the nonlinear case, it only converges if the starting point is sufficiently close to the desired minimum. An alternate expression for β comes from the Polak-Ribière formula,

$$\beta_{m+1}^{PR} = \max\left\{ \frac{\mathbf{g}_{m+1}^{T} \left(\mathbf{g}_{m+1} - \mathbf{g}_{m} \right)}{\mathbf{g}_{m}^{T} \mathbf{g}_{m}}, 0 \right\} \quad . \tag{II.11}$$

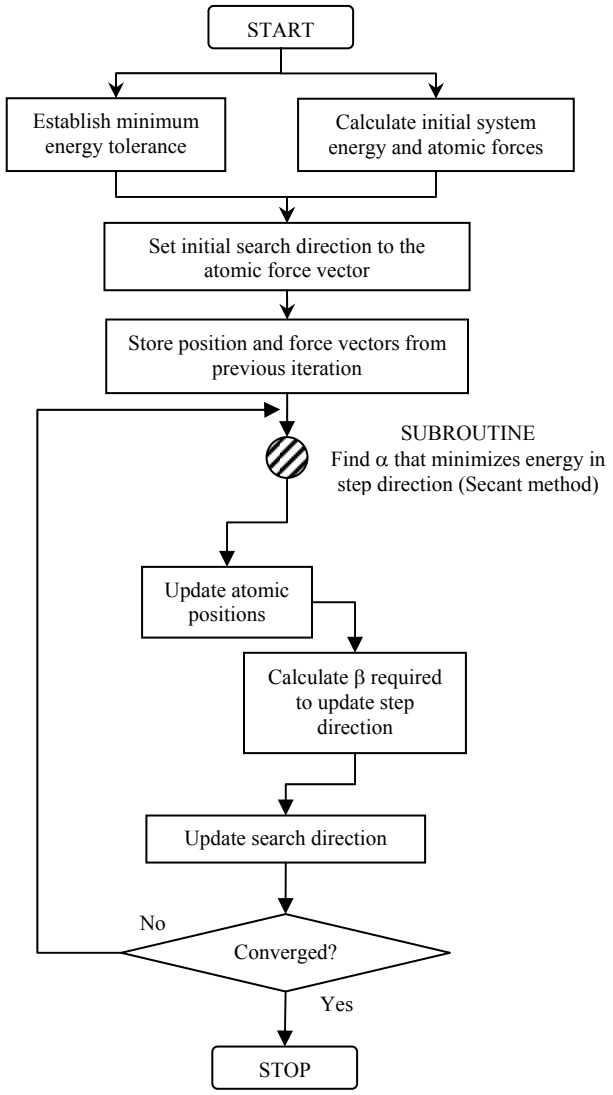

Figure II.2. Flow chart for conjugate gradient algorithm used in the energy minimization calculations.

The Polak-Ribière method assures convergence by requiring that β be non-negative. Setting $\beta = 0$ essentially results in restarting the minimization calculation, as the search direction is then equal to the residual of the potential energy at the given step (Eq. (II.6)). The Polak-Ribière formula is regarded as superior in that it converges more

quickly than the Fletcher-Reeves formula for most nonlinear functions (Shewchuk, 1994). If the function $f(x)$ is an exact quadratic form, for example, the Feltcher-Reeves and Polak-Ribière methods are identical. Since the potential energy of a set of atoms is a highly nonlinear function, the Polak-Ribière formulation is used in this work.

In summary, the combination of properly chosen search directions and step sizes avoids repeated searches by stepping the appropriate distance in each search direction for each CG iteration. Figure II.2 shows a flow chart of the nonlinear conjugate gradient algorithm. Conjugate gradient methods applied to quadratic potential energy functions are guaranteed to converge to the global minimum energy since there is only one minimum. Unfortunately nonlinear CG methods applied to complex potential energy functions do not offer the same convergence assurance. Complex functions potentially contain many local minima. The line search algorithm used to calculate α is dependent on the starting point. Unfortunately, there is no algorithm that guarantees that one will find the global energy minimum every time. Chapter III will detail the methods used in this thesis to increase the probability that the minimum energy interface structure is attained during MS calculations with the nonlinear conjugate gradient algorithm.

II.3 Molecular Dynamics

In this work, molecular dynamics (MD) simulations are performed to study the tensile deformation of grain boundary interfaces on the nanoscale. In the molecular dynamics method, the evolution of atomic positions is described using Newton's 2nd Law of motion,

$$\dot{\mathbf{p}}^{\mathrm{i}} = \mathbf{F}^{\mathrm{i}} = m\dot{\mathbf{v}}^{\mathrm{i}} \tag{II.12}$$

where

$$\dot{\mathbf{r}}^{\mathrm{i}} = \frac{d\mathbf{r}^{\mathrm{i}}}{dt} = \frac{\mathbf{p}^{\mathrm{i}}}{m} \quad . \tag{II.13}$$

Here, m is the mass, $\mathbf{p}^{\mathrm{i}}$ is the momentum and $\mathbf{v}^{\mathrm{i}}$ is the velocity of the i^{th} atom. The 'dot' signifies the first derivative with respect to time. Equations (II.12) and (II.13) represent the equations of motion for a system of atoms that is isolated from the environment. The most widely used method to solve Eqs. (II.12) and (II.13) in molecular dynamics is the velocity-Verlet finite-difference algorithm (Swope *et al*., 1982). This algorithm has many desirable properties because its form is exactly time reversible (which allows the equations of motion to be propagated forward in time without iteration) and symplectic (the volume in phase space is conserved), insuring long simulation time stability and convergence (Martyna *et al*., 1996). Also, the velocity-Verlet algorithm is efficient as it only requires one force evaluation per time step,

$$\mathbf{v}^{\mathrm{i}}\left(t + \frac{\Delta t}{2}\right) = \mathbf{v}^{\mathrm{i}}\left(t\right) + \frac{\Delta t}{2m}\mathbf{F}^{\mathrm{i}}\left(t\right) \tag{II.14}$$

$$\mathbf{r}^{\mathrm{i}}\left(t + \Delta t\right) = \mathbf{r}^{\mathrm{i}}\left(t\right) + \Delta t\mathbf{v}^{\mathrm{i}}\left(t + \frac{\Delta t}{2}\right) \tag{II.15}$$

$$\mathbf{v}^{\mathrm{i}}\left(t + \Delta t\right) = \mathbf{v}^{\mathrm{i}}\left(t + \frac{\Delta t}{2}\right) + \frac{\Delta t}{2m}\mathbf{F}^{\mathrm{i}}\left(t + \Delta t\right) \quad . \tag{II.16}$$

Here, Δt is the molecular dynamics time step for the simulation, which is typically on the order of femptoseconds. In the velocity-Verlet algorithm, the velocity of each atom is first calculated at a half time step forward in time using the current value of the atomic forces. Then, the atomic positions are updated to $t + \Delta t$ using the values of the atomic velocities at the half time step. Next, a force calculation is performed using the updated atomic positions. Finally, the atomic velocities are evolved to the full time step using the updated force vector.

While the study of material behavior in isolated systems has merit, the vast majority of problems in the mechanics and materials science community require that the system interact with the surrounding environment (nonequilibrium molecular dynamics). One way to accomplish this in molecular dynamics is to introduce the concept of an extended system (Andersen, 1980). Essentially, Newton's equations of motion are augmented and coupled to additional differential equations that describe the relationship between the system and environment. Commonly, molecular dynamics calculations are performed at a constant temperature or pressure (or both).

Of course, proper evaluation of the thermodynamic quantities must consider the size of the atomistic system. In statistical mechanics, thermodynamics quantities are introduced using the 'thermodynamic limit,' which states that as the number of atoms goes to infinity, the limit of an intensive thermodynamic quantity (for example) goes to a constant value (Greiner *et al*., 1995). In other words, fluctuations in thermodynamics quantities, such as temperature, are extremely small for a system of atoms with macroscopic dimensions (10^{23}) in steady state. The calculation of temperature would contain significant error if only a small number of atoms are used. The use of periodic

boundary conditions in the atomistic framework serves as an effective way to approximate the thermodynamic limit. As discussed in Section II.1, periodic boundary conditions can be used to approximate an infinite number of atoms within the atomistic framework.

The following sections present a brief overview of the equations of motion and the integration algorithms used in this work for NVT and NPT ensembles. In addition, this thesis introduces modifications to the equations of motion for each ensemble, required to meet the goals of the calculations in this work. Essentially, a mixed set of boundary conditions is developed. More complete reviews on molecular dynamics ensembles are provided in texts by Allen and Tildesley (1987) and Haile (1992); more information on molecular dynamics integrators can be found in Martyna *et al.* (1996).

II.3.1 NVT Molecular Ensemble

To perform calculations in the NVT molecular ensemble, two techniques are commonly used: (i) direct velocity rescaling and (ii) the extended system method. Direct velocity rescaling involves resetting the velocities of the particles at each time step so that the total kinetic energy of the system remains strictly constant (Hoover *et al*., 1982; Evans, 1983). However, this method only reproduces the canonical distribution function for specific restraints. Calculations in this work will use the extended system methodology where the equations of motion for the system are augmented by a 'frictional' coefficient, ζ, which couples the system dynamics to an external temperature reservoir. The first such equations using this methodology for the NVT ensemble were developed by Nosé (1984). Unfortunately, these equations of motion are generally

regarded as difficult to implement into a molecular dynamics code due to a temporal scaling. Hoover (1985) proposed a simplification to Nosé's equations for the NVT ensemble that eliminated the scaling of variables in both time and space,

$$\begin{aligned} \dot{\mathbf{r}}^{\mathrm{i}} &= \frac{\mathbf{p}^{\mathrm{i}}}{m} \\ \dot{\mathbf{p}}^{\mathrm{i}} &= \mathbf{F}^{\mathrm{i}} - \zeta \mathbf{p}^{\mathrm{i}} \\ \dot{\zeta} &= v_T^2 \left(\frac{T}{T_o} - 1 \right) \end{aligned} \quad . \tag{II.17}$$

Here, T_o is the temperature of the thermal reservoir and v_T is the thermostating rate. The thermodynamic 'friction' constant dynamically alters the velocities of the individual atoms such that the temperature of the system is adjusted towards T_o. Although the system of equations in (II.17) is non-Hamiltonian, it does reproduce the canonical distribution function (Hoover, 1985) and conserves the Helmholtz free energy to within a constant (Holian *et al*., 1990).

II.3.2 NPT Molecular Ensemble

To perform molecular dynamics calculations in the NPT ensemble, a number of methods have been developed over the last twenty years using the extended system methodology, including algorithms by Andersen (1980), Parrinello and Rahman (1981), Nosé (1984) and Hoover (1985). Each of these methods allows the periodic system cell to change its size, driven by the imbalance between the internal and desired system pressures or stresses. The Parrinello and Rahman (1981) scheme allows the system to

change its size *and* shape to account for anisotropic behavior or non-hydrostatic loadings. In general, constant pressure algorithms have a close analogy to constant temperature algorithms, as an isobaric 'friction' coefficient is introduced to couple the system pressure or stress to an external reservoir.

Similar to the NVT ensemble, the Hoover (1985) constant pressure equations of motion are typically regarded as the easiest to implement into a molecular dynamics code. However, Melchionna *et al*. (1993) have shown that the Hoover NPT equations of motion do not precisely sample the isobaric-isothermal ensemble, due to the volumetric scaling of the coordinates. Note that the Nosé-Hoover NVT equations of motion do correctly reproduce the NVT ensemble, as they do not include a coordinate scaling (recall Eq. (II.17)). Melchionna *et al.* (1993) suggest a modification to Hoover's equations of motion, which avoids coordinate scaling by shifting the system by the center of mass, $\mathbf{R}_o$, i.e.,

$$\begin{aligned}
\dot{\mathbf{r}}^i &= \frac{\mathbf{p}^i}{m} + \boldsymbol{\eta}\left(\mathbf{r}^i - \mathbf{R}_o\right) \\
\dot{\mathbf{p}}^i &= \mathbf{F}^i - \left(\boldsymbol{\eta} + \zeta\mathbf{I}\right)\mathbf{p}^i \\
\dot{\zeta} &= v_T^2\left(\frac{T}{T_o} - 1\right) \\
\dot{\boldsymbol{\eta}} &= \frac{v_P^2}{NkT_o} V\left(\boldsymbol{\sigma} - \mathbf{P}_o\right) \\
\dot{\mathbf{h}} &= \boldsymbol{\eta}\mathbf{h}
\end{aligned} \quad . \tag{II.18}$$

The isobaric friction coefficient, $\boldsymbol{\eta}$, is a function of the desired pressure or stress, $\mathbf{P}_o$, Boltzmann's constant, k, and the constant pressure damping coefficient, v_P. The

boundaries of the system are defined by a set of vectors, $\mathbf{h}$, that are aligned along the edges of the periodic unit cell. The internal system stress is calculated using the virial definition,

$$\boldsymbol{\sigma} = \frac{1}{V}\left[\frac{1}{2}\sum_{i}\sum_{i\neq j}\frac{U'}{r^{ij}}r_{\alpha}^{ij}r_{\beta}^{ij} - \sum_{i} mv^{i}v^{i}\right] \quad . \tag{II.19}$$

In Eq. (II.19), r^{ij} is the distance between atoms i and j; r_{α}^{ij} and r_{β}^{ij} are the components of the total distance in the α and β directions. The 'prime' denotes the first derivative with respect to atomic position. The kinetic component of the internal pressure is composed of the atomic mass and velocity. Melchionna *et al.* (1993) showed that the equations of motion in (II.18) correctly reproduce the NPT distribution function. Further, since the Melchionna *et al.* equations do not require scaling of the atomic positions or velocities to reproduce the NPT ensemble, they fit easily into the standard framework of a MD code.

II.3.3 Virial Stress

As explained above, stress is calculated in this work using the virial definition. The concept of stress in an atomic system is one that has been argued from different points of view in the literature over the past thirty years (Tsai, 1979; Lutsko, 1988; Cheung and Yip, 1991; Cormier *et al*., 2001; Zhou, 2003; Zimmerman *et al*., 2004). It is important to understand that the expression in Eq. (II.19) is a time and spatially averaged quantity and represents the force per unit area on the surface of a defined volume

containing interacting particles. Mathematically, the virial stress expression in Eq. (II.19) may be decomposed using the volume around a given atom, Ω^{i}, to form a point-wise measure of stress, i.e.,

$$\mathbf{\Pi}^{i} = \frac{1}{\Omega^{i}}\left[\frac{1}{2}\sum_{i}\sum_{i\neq j}\frac{U'}{r^{ij}}r_{\alpha}^{ij}r_{\beta}^{ij} - \sum_{i} m\mathbf{v}^{i}\mathbf{v}^{i}\right] \quad . \tag{II.20}$$

with,

$$\Omega^{i} = \frac{\lambda^{3}}{4} \quad . \tag{II.21}$$

However, the point-wise measure of stress, $\mathbf{\Pi}^{i}$, does not have any physical interpretation unless it is averaged over a representative number of atoms, i.e.,

$$\boldsymbol{\sigma} = \frac{1}{N}\sum_{i=1}^{N}\mathbf{\Pi}^{i} \quad . \tag{II.22}$$

Zimmerman *et al*. (2004) investigate the concept of a 'representative' number of atoms using two expressions for stress in an atomic system (one of which is the stress derived from the virial theorem). They find that for situations of non-zero deformation at finite temperature, fluctuations exist in the virial stress calculation when the summation is performed over small volumes around an arbitrary point within the atomic system. As the size of the averaging region increases, the fluctuations in the stress calculation decrease. They also find that the fluctuations in the stress decrease at a faster rate if both spatial and temporal averaging is performed. Essentially, what Zimmerman *et al*. (2004)

are exploring is the error of the virial stress expression when the calculation is not performed in the thermodynamic limit.

Several authors in the literature have attempted to develop expressions for stress in an atomic system that is defined for a spatial point at an instant of time from the equation for balance of linear momentum for a dynamic continuum (Lutsko, 1988; Zhou, 2003). From this perspective, Zhou (2003) showed that the virial stress expression is unable to handle simple cases of rigid body translation in atomic systems. More importantly, Zhou also showed that the point-wise virial stress expression in Eq. (II.20) violates classical conservation of linear momentum. Zhou argues that in a dynamically deforming atomic system, the stress should be a function of only the force between particles in order to maintain equivalence with the classical definition of the Cauchy stress. Zhou asserts that the kinetic contribution to the stress is already accounted for through the force term and that the kinetic contribution to the point-wise virial stress is incorrect if stress is to be interpreted as a force interaction between material points.

It is beyond the scope of this thesis to provide a full review and discussion of stress calculations in atomic systems. In this work, the kinetic contribution to the virial stress is retained, understanding that there are the possible ambiguities with regard to conservation of linear momentum if the virial expression is used to obtain localized measures of stress. In general, the kinetic energy term is small as compared with the interatomic force term for solid materials (Zhou, 2003). This observation is especially true when calculations are performed at relative low temperatures (10 K and 300 K) and when the system is subjected to an external deformation. Further, in this work, stress is averaged over a large volume around the region of interest to reduce the fluctuations in

the virial stress response (Zimmerman *et al*., 2004). Note that the stresses reported in this work are not time averaged, i.e., they are reported at defined instants in time during the simulation.

II.3.4 Molecular Dynamics Integration Algorithms

There are a number of methods that may be used to numerically integrate the equations of motion for both NVT and NPT ensembles. One such method is the Gear predictor-corrector algorithm (Chapra and Canale, 1988). This method requires iteration over the correction step to maintain a self-consistent solution. As shown previously, the velocity-Verlet integration algorithm may be used to solve the microcanonical equations of motion. Time-reversible integration algorithms have been shown to have improved long-time stability over other integration methods (Tuckerman and Martyna, 1999). In other words, drift in the conserved quantity *will not occur* during the integration over long periods of simulation time. For equilibrium MD (isolated systems), the conserved quantity is the Hamiltonian (total system energy) as implied by the equations of motion Eqs. (II.12) and (II.13). For nonequilibrium MD (system interacting with the environment), the conserved quantity is the Helmholtz free energy, using the NVT equations of motion in (II.17), or the Gibbs free energy, using the NPT equations of motion in (II.18). Further, the use of an explicit time-reversible integration method avoids predictive or iterative corrections over any of the steps to maintain a self-consistent solution, as in the Gear predictor-corrector algorithm. The inelastic deformation of the metallic materials studied in this thesis is path-history dependent (Spearot *et al*., 2005). Use of a time-reversible intergration algorithm should not be

interpreted as violating this sort of path history dependence, as it simply ensures conservation of particular energetic quantities.

The derivation of a time reversible integration algorithm for the NVT and NPT equations of motion is a straight forward extension of the velocity-Verlet time-reversible algorithm for the Hamiltonian equations of motion. Tuckerman *et al.* (1992) and Martyna *et al.* (1996) have shown that time-reversible integration algorithms for MD calculations may be derived with a reversible Trotter expansion of the Liouville operator. Note that the Hoover (1985) and Melchionna *et al.* (1993) equations of motion are non-Hamiltonian because the change in atomic momentum is not solely a function of the atomic positions. Instead, the change in atomic momentum is posed as a function of both the atomic positions and velocities. Using the Hoover equations of motion for the NVT ensemble as a reference, the Liouville operator for a single atom is written as,

$$iL^{\mathrm{i}} = \dot{\mathbf{r}}^{\mathrm{i}} \frac{\partial}{\partial \mathbf{r}} + \mathbf{F}^{\mathrm{i}} \frac{\partial}{\partial \mathbf{p}} - \zeta \mathbf{p}^{\mathrm{i}} \frac{\partial}{\partial \mathbf{p}} + v_T^2 \left(\frac{T}{T_o} - 1 \right) \frac{\partial}{\partial \zeta} \tag{II.23}$$

The system of first-order differential equations in (II.23) can be evolved in time from t to $t + \Delta t$ by applying the evolution operator, $Q(t + \Delta t)$,

$$\mathbf{\Gamma}(t + \Delta t) = Q(t + \Delta t)\mathbf{\Gamma}(t) = \exp\left[iL(t + \Delta t) \right] \mathbf{\Gamma}(t) \quad . \tag{II.24}$$

Here, the multidimensional phase-space vector $\boldsymbol{\Gamma}$ is comprised of the atomic coordinates, atomic velocities the thermodynamic friction coefficient, ζ. The Liouville operator for the atomic system is decomposed as follows,

$$\begin{aligned} iL &= iL_{\mathbf{r}} + iL_{\mathbf{p}} + iL_{\zeta} \\ &= \sum_{\mathrm{i}} \dot{\mathbf{r}}^{\mathrm{i}} \frac{\partial}{\partial \mathbf{r}} + \sum_{\mathrm{i}} \left[\mathbf{F}^{\mathrm{i}} - \zeta \mathbf{p}^{\mathrm{i}} \right] \frac{\partial}{\partial \mathbf{p}} + v_T^2 \left(\frac{T(t)}{T_o} - 1 \right) \frac{\partial}{\partial \zeta} \end{aligned} \quad . \tag{II.25}$$

Then, based on the Trotter factorization, the operator may be written,

$$\begin{aligned} Q(\Delta t) &= \exp(iL\Delta t) = \exp\left[i\left(L_{\mathbf{r}} + L_{\mathbf{p}} + L_{\zeta} \right) \Delta t \right] \\ &\approx \exp\left(iL_{\zeta}\, \Delta t/2 \right) \exp\left(iL_{\mathbf{p}}\, \Delta t/2 \right) \exp\left(iL_{\mathbf{r}} \Delta t \right) \\ &\times \exp\left(iL_{\mathbf{p}}\, \Delta t/2 \right) \exp\left(iL_{\zeta}\, \Delta t/2 \right) \\ &= Q_{\zeta}\left(\Delta t/2 \right) Q_{\mathbf{p}}\left(\Delta t/2 \right) Q_{\mathbf{r}}\left(\Delta t \right) Q_{\mathbf{p}}\left(\Delta t/2 \right) Q_{\zeta}\left(\Delta t/2 \right) \end{aligned} \quad . \tag{II.26}$$

Using the direct translation technique (Martyna *et al.*, 1996), each term in Eq. (II.26) may be applied in succession to the phase-space point $\boldsymbol{\Gamma}$. This step-by-step process is shown in Table II.1. The ~ and ^ over the atomic velocity terms denote intermediate values of the velocity prior to evolving in time. The $Q_{\mathbf{p}}$ operator term is factored into two steps in the derivation without the loss of generality or accuracy. A number of mathematical identities are used to simplify the exponential functions (Tuckerman *et al.*, 1992). The phase space points $\boldsymbol{\Gamma}_a$, $\boldsymbol{\Gamma}_b$, etc. are used as temporary steps between $\boldsymbol{\Gamma}(t)$ and $\boldsymbol{\Gamma}(t+\Delta t)$. The final result in Table II.1 is a velocity-Verlet type

Table II.1. Integration algorithm for the Hoover NVT equations of motion.

Step	Phase Space Evolution	Calculation
(1)		Calculate: $T(t)$
(2)	$\mathbf{\Gamma}_b = Q_\zeta(\Delta t/2)\mathbf{\Gamma}_a$	$\zeta\left(t+\frac{\Delta t}{2}\right) = \zeta(t) + \frac{\Delta t}{2}v_T^2\left(\frac{T(t)}{T_o}-1\right)$
(3)	$\mathbf{\Gamma}_c = Q_{\mathbf{p}}(\Delta t/2)\mathbf{\Gamma}_b$	$\tilde{\mathbf{v}}^{\mathrm{i}}(t) = \mathbf{v}^{\mathrm{i}}(t) * \exp\left(-\frac{\Delta t}{2}\zeta\left(t+\frac{\Delta t}{2}\right)\right)$
(4)		$\mathbf{v}^{\mathrm{i}}\left(t+\frac{\Delta t}{2}\right) = \tilde{\mathbf{v}}^{\mathrm{i}}(t) + \frac{\Delta t}{2m}\mathbf{F}^{\mathrm{i}}(t)$
(5)	$\mathbf{\Gamma}_d = Q_{\mathbf{r}}(\Delta t/2)\mathbf{\Gamma}_c$	$\mathbf{r}^{\mathrm{i}}(t+\Delta t) = \mathbf{r}^{\mathrm{i}}(t) + \Delta t\mathbf{v}^{\mathrm{i}}\left(t+\frac{\Delta t}{2}\right)$
(6)		Calculate: $\mathbf{F}^{\mathrm{i}}(t+\Delta t)$
(7)	$\mathbf{\Gamma}_e = Q_{\mathbf{p}}(\Delta t/2)\mathbf{\Gamma}_d$	$\hat{\mathbf{v}}^{\mathrm{i}}(t+\Delta t) = \mathbf{v}^{\mathrm{i}}\left(t+\frac{\Delta t}{2}\right) + \frac{\Delta t}{2m^{\mathrm{i}}}\mathbf{F}^{\mathrm{i}}(t+\Delta t)$
(8)		$\mathbf{v}^{\mathrm{i}}(t+\Delta t) = \hat{\mathbf{v}}^{\mathrm{i}}\left(t+\frac{\Delta t}{2}\right) * \exp\left(-\frac{\Delta t}{2}\zeta\left(t+\frac{\Delta t}{2}\right)\right)$
(9)		Calculate: $T(t+\Delta t)$
(10)	$\mathbf{\Gamma}_f = Q_\zeta(\Delta t/2)\mathbf{\Gamma}_e$	$\zeta(t+\Delta t) = \zeta\left(t+\frac{\Delta t}{2}\right) + \frac{\Delta t}{2}v_T^2\left(\frac{T(t+\Delta t)}{T_o}-1\right)$

algorithm derived specifically for the Hoover NVT equations of motion. These expressions are simply taken in exact order as the integration algorithm and may be easily implemented into a computer code to perform the calculation.

Similar step-by-step expressions can be derived using the Melchionna *et al.* (1993) equations of motion for the NPT ensemble (Table II.2). A time-reversible integration algorithm for the Melchionna *et al*. (1993) equations of motion has not been presented before in the literature. The Liouville operator for a single atom is written as,

$$\begin{aligned} iL^{\mathrm{i}} = {} & \dot{\mathbf{r}}^{\mathrm{i}}\frac{\partial}{\partial \mathbf{r}} + \boldsymbol{\eta}\mathbf{r}^{i}\frac{\partial}{\partial \mathbf{r}} - \boldsymbol{\eta}\mathbf{R}_{\mathrm{o}}\frac{\partial}{\partial \mathbf{r}} + \mathbf{F}^{\mathrm{i}}\frac{\partial}{\partial \mathbf{p}} - \left(\boldsymbol{\eta}+\zeta\mathbf{I}\right)\mathbf{p}^{\mathrm{i}}\frac{\partial}{\partial \mathbf{p}} \\ & + v_T^2\left(\frac{T}{T_o}-1\right)\frac{\partial}{\partial \zeta} + \frac{v_P^2}{NkT_o}V\left(\boldsymbol{\sigma}-\mathbf{P}_{\mathrm{o}}\right)\frac{\partial}{\partial \eta} + \boldsymbol{\eta}\mathbf{h}\frac{\partial}{\partial \mathbf{h}} \end{aligned} \quad . \tag{II.27}$$

Table II.2. Integration algorithm for the Melchionna NPT equations of motion.

Step	Phase Space Evolution	Calculation
(1)		Calculate: $T(t)$, $\boldsymbol{\sigma}(t)$, $V(t)$, $\mathbf{R}_{\mathrm{o}}(t)$
(2)	$\boldsymbol{\Gamma}_a = Q_{\mathbf{h}}(\Delta t/2)\boldsymbol{\Gamma}(t)$	$\mathbf{h}\left(t+\frac{\Delta t}{2}\right) = \mathbf{h}(t) * \exp\left(\frac{\Delta t}{2}\boldsymbol{\eta}(t)\right)$
(3)	$\boldsymbol{\Gamma}_b = Q_{\boldsymbol{\eta}}(\Delta t/2)\boldsymbol{\Gamma}_a$	$\boldsymbol{\eta}\left(t+\frac{\Delta t}{2}\right) = \boldsymbol{\eta}(t) + \frac{\Delta t}{2}\frac{v_P^2}{NkT_o}V(t)\left(\boldsymbol{\sigma}(t)-\mathbf{P}_{\mathrm{o}}\right)$
(4)	$\boldsymbol{\Gamma}_c = Q_{\zeta}(\Delta t/2)\boldsymbol{\Gamma}_b$	$\zeta\left(t+\frac{\Delta t}{2}\right) = \zeta(t) + \frac{\Delta t}{2}v_T^2\left(\frac{T(t)}{T_o}-1\right)$
(5)	$\boldsymbol{\Gamma}_d = Q_{\mathbf{p}}(\Delta t/2)\boldsymbol{\Gamma}_c$	$\tilde{\mathbf{v}}^{\mathrm{i}}(t) = \mathbf{v}^{\mathrm{i}}(t) * \exp\left(-\frac{\Delta t}{2}\zeta\left(t+\frac{\Delta t}{2}\right)\right) * \exp\left(-\frac{\Delta t}{2}\boldsymbol{\eta}\left(t+\frac{\Delta t}{2}\right)\right)$
(6)		$\mathbf{v}^{\mathrm{i}}\left(t+\frac{\Delta t}{2}\right) = \tilde{\mathbf{v}}^{\mathrm{i}}(t) + \frac{\Delta t}{2m}\mathbf{F}^{\mathrm{i}}(t)$
(7)	$\boldsymbol{\Gamma}_e = Q_{\boldsymbol{\eta}\mathbf{r}}(\Delta t/2)\boldsymbol{\Gamma}_d$	$\tilde{\mathbf{r}}(t) = \mathbf{r}(t) - \frac{\Delta t}{2}\boldsymbol{\eta}\left(t+\frac{\Delta t}{2}\right)\mathbf{R}_{\mathrm{o}}(t)$
(8)		$\tilde{\tilde{\mathbf{r}}}(t) = \tilde{\mathbf{r}}(t) * \exp\left(\frac{\Delta t}{2}\boldsymbol{\eta}\left(t+\frac{\Delta t}{2}\right)\right)$
(9)	$\boldsymbol{\Gamma}_f = Q_{\mathbf{r}}(\Delta t/2)\boldsymbol{\Gamma}_e$	$\hat{\hat{\mathbf{r}}}^{\mathrm{i}}(t+\Delta t) = \tilde{\tilde{\mathbf{r}}}^{\mathrm{i}}(t) + \Delta t\mathbf{v}^{\mathrm{i}}\left(t+\frac{\Delta t}{2}\right)$
(10)	$\boldsymbol{\Gamma}_g = Q_{\boldsymbol{\eta}\mathbf{r}}(\Delta t/2)\boldsymbol{\Gamma}_f$	$\hat{\mathbf{r}}(t) = \hat{\hat{\mathbf{r}}}(t) * \exp\left(\frac{\Delta t}{2}\boldsymbol{\eta}\left(t+\frac{\Delta t}{2}\right)\right)$
(11)		$\mathbf{r}(t) = \hat{\mathbf{r}}(t) - \frac{\Delta t}{2}\boldsymbol{\eta}\left(t+\frac{\Delta t}{2}\right)\mathbf{R}_{\mathrm{o}}(t)$
(12)		Calculate: $\mathbf{F}^{\mathrm{i}}(t+\Delta t)$
(13)	$\boldsymbol{\Gamma}_h = Q_{\mathbf{p}}(\Delta t/2)\boldsymbol{\Gamma}_g$	$\hat{\mathbf{v}}^{\mathrm{i}}(t+\Delta t) = \mathbf{v}^{\mathrm{i}}\left(t+\frac{\Delta t}{2}\right) + \frac{\Delta t}{2m^{\mathrm{i}}}\mathbf{F}^{\mathrm{i}}(t+\Delta t)$
(14)		$\mathbf{v}^{\mathrm{i}}(t+\Delta t) = \hat{\mathbf{v}}^{\mathrm{i}}\left(t+\frac{\Delta t}{2}\right) * \exp\left(-\frac{\Delta t}{2}\zeta\left(t+\frac{\Delta t}{2}\right)\right) * \exp\left(-\frac{\Delta t}{2}\boldsymbol{\eta}\left(t+\frac{\Delta t}{2}\right)\right)$
(15)		Calculate: $T(t+\Delta t)$
(16)	$\boldsymbol{\Gamma}_i = Q_{\zeta}(\Delta t/2)\boldsymbol{\Gamma}_h$	$\zeta(t+\Delta t) = \zeta\left(t+\frac{\Delta t}{2}\right) + \frac{\Delta t}{2}v_T^2\left(\frac{T(t+\Delta t)}{T_o}-1\right)$
(17)		Calculate: $\boldsymbol{\sigma}(t+\Delta t)$, $V\left(t+\frac{\Delta t}{2}\right)$
(18)	$\boldsymbol{\Gamma}_j = Q_{\boldsymbol{\eta}}(\Delta t/2)\boldsymbol{\Gamma}_i$	$\boldsymbol{\eta}(t+\Delta t) = \boldsymbol{\eta}\left(t+\frac{\Delta t}{2}\right) + \frac{\Delta t}{2}\frac{v_P^2}{NkT_o}V\left(t+\frac{\Delta t}{2}\right)\left(\boldsymbol{\sigma}(t+\Delta t)-\mathbf{P}_{\mathrm{o}}\right)$
(19)	$\boldsymbol{\Gamma}(t+\Delta t) = Q_{\mathbf{h}}(\Delta t/2)\boldsymbol{\Gamma}_j$	$\mathbf{h}(t+\Delta t) = \mathbf{h}\left(t+\frac{\Delta t}{2}\right) * \exp\left(\frac{\Delta t}{2}\boldsymbol{\eta}(t+\Delta t)\right)$

This system of first-order differential equations can be evolved in time using the same procedure as in Eqs. (II.23) – (II.26). In this case, the multidimensional phase-space vector $\mathbf{\Gamma}$ is composed of the atomic coordinates, atomic velocities the thermodynamic friction coefficient, ζ, the isobaric friction coefficient, $\boldsymbol{\eta}$, and the simulation cell boundaries, $\mathbf{h}$. Both the $Q_{\eta r}$ and Q_{p} operator terms are factored into two steps, as shown in Table II.2. The velocity-Verlet type algorithm derived for the Melchionna *et al.* (1993) NPT equations of motion may be taken in exact order as the integration algorithm to perform isobaric-isothermal calculations.

II.3.5 Necessary Modifications to the NPT Equations of Motion

Two modifications are made to the Melchionna *et al.* (1993) equations of motion to meet the demands of the calculations in this thesis: (i) introducing an additional damping term on $\boldsymbol{\eta}$ that critically damps the pressure or stress equilibration and (ii) developing a methodology for a mixed set of boundary conditions. The additional damping on the isobaric friction constant is inspired by the molecular dynamics code ParaDyn (which was also written by Dr. Steve Plimpton) and the NPT equations of motion by Feller *et al.* (1995) who showed that the additional boundary 'drag' term reduces the influence of the value of the damping constant, v_P. For solids, it is desirable to have the system equilibrate in a reasonable amount of time without large pressure or stress fluctuations. The mixed set of boundary conditions combines displacement-controlled and stress-controlled boundary prescriptions. Here, the aim is to apply a constant strain rate in one direction, while having the motion of the boundaries transverse

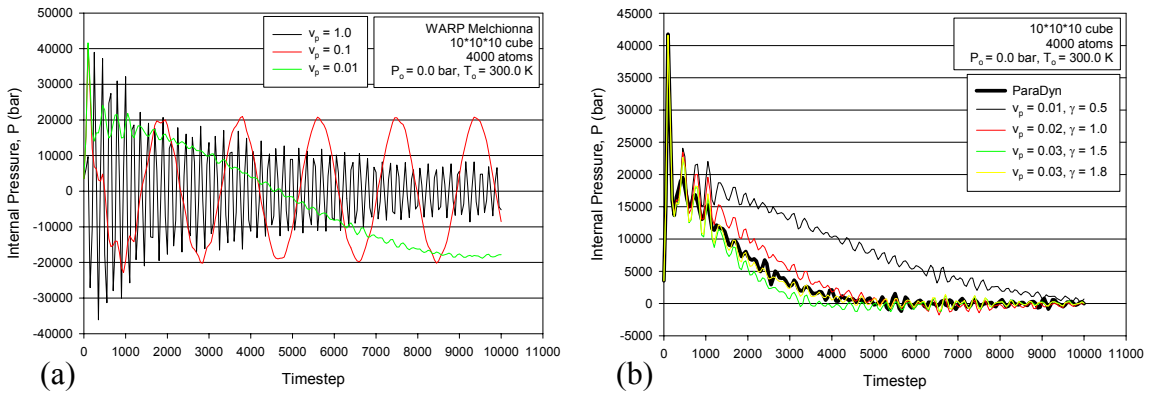

Figure II.3. (a) System pressure versus time step for isobaric-isothermal equilibration using different damping coefficients; (b) system pressure versus time step for isobaric-isothermal equilibration incorporating the additional boundary damping term.

to the loading direction be controlled via the imbalance between the system stress and the desired value.

Figure II.3(a) shows the internal pressure as a function of time step during a molecular dynamics simulation of isobaric-isothermal equilibration to 0 bar and 300 K. The MD simulation contains 4000 atoms in a cubic (10x10x10 lattice units) arrangement with periodic boundary conditions and uses the Mishin *et al.* (2001) embedded-atom method interatomic potential for copper. The copper lattice is constructed using the 0 K lattice constant. As the system is equilibrated to 300 K, the boundaries attempt to expand in each direction, causing a temporary state of compressive pressure (shown with a positive convention in Fig. II.3). Three different values of v_P are chosen for the NPT equilibration. Increasing the value of v_P reduces the time required to reach pressure equilibrium. However, the magnitude of the pressure fluctuations becomes much more significant, which is undesirable from a computational perspective. Although not shown

in Fig. II.3, the magnitude of the isobaric friction coefficient does not alter the thermal equilibration to 300 K.

To eliminate the pressure fluctuations and to minimize the effect of the damping constant on the isobaric equilibration, the Melchionna *et al.* (1993) NPT equations of motion are slightly modified. Specifically, an additional damping term is added that adjusts the boundary acceleration by the current value of the boundary velocity. In the Melchionna *et al.* set of equations, the term that describes the boundary acceleration is,

$$\dot{\boldsymbol{\eta}} = \frac{v_P^2}{NkT_o} V\left(\boldsymbol{\sigma} - \mathbf{P}_o\right) \quad . \tag{II.28}$$

This is evident from the definition of $\boldsymbol{\eta}$,

$$\boldsymbol{\eta} = \frac{\dot{\mathbf{h}}}{\mathbf{h}} \quad . \tag{II.29}$$

Thus, the first order differential equation for the evolution of the isobaric friction parameter is augmented as follows,

$$\dot{\boldsymbol{\eta}} = \frac{v_P^2}{NkT_o} V\left(\boldsymbol{\sigma} - \mathbf{P}_o\right) - \gamma\boldsymbol{\eta} \quad . \tag{II.30}$$

The value of γ should be positive to provide the desired damping effect. The additional damping term is simple to incorporate into the molecular dynamics code

within the framework of the time-reversible integration algorithm described in Table II.2. The utility of the additional damping term is evident from Fig. II.3(b). It is desirable to have the system pressure equilibrate smoothly to the prescribed value (to avoid large steps in the boundary motion which may nucleate defects in metals). Clearly, by adjusting the values of the damping constant and the additional damping term, both the rate at which the system approaches the desired pressure value and the magnitude of the oscillations in the pressure are improved. From Fig. II.3(b), $v_p = 0.03$ and $\gamma = 1.8$ appear to be appropriate choices for the isobaric damping constants at 300 K. However, reasonable variations from these values do not appear to drastically modify the simulation results. Again, the presence of the additional damping term does not affect the equilibration of the system temperature to 300 K.

The ability to deform atomistic models with a constant strain rate is critical to the analysis in this work as the inelastic response of interfaces with different boundary misorientations is compared. To produce inelastic deformation using the Melchionna *et al.* (1993) equations of motion, a pressure or stress, $\mathbf{P}_o$, is prescribed that is larger than the yield stress. Conceivably, each interface model will have a unique yield stress, due to the structure of the boundary and the orientation of the lattice. If a single value of the desired pressure is used for all misorientations, the applied strain rate will be different for each model due to the form of the evolution equation for $\boldsymbol{\eta}$ in Eq. (II.18). Considering that MD strain rates typical range between 10^7 and 10^{10} s^{-1}, minor variations in the strain rate between interface models may produce non-negligible changes in the inelastic response.

Thus, the goal is to extend the periodic cell with a constant strain rate along one direction, while maintaining that the motion of the periodic cell boundaries in the other directions be controlled through the equations of motion in Eq. (II.18), i.e., by the imbalance between the system and desired values of stress through the isobaric friction constant $\boldsymbol{\eta}$. Recent work by Frederiksen *et al.* (2004) subjects a nanocrystalline atomistic sample to a strain by uncoupling the unit cell vector along the loading direction from the dynamics (equations of motion) and extending the unit vector manually according to a desired strain rate. They showed that the mixed set of boundary conditions allows for the simulation of combined dislocation activity and nanoscale crack growth. However, the details of the decoupling are not specifically reported.

The critical variable in the development of a mixed set of boundary conditions is $\mathbf{h}$, which describes the length and orientation of the boundaries of the periodic cell. Suppose that the rate of change of the periodic cell, $\dot{\mathbf{h}}$, is prescribed in the loading direction. Then, the magnitude of the isobaric friction constant in the loading direction may be calculated using the definition in Eq. (II.29). The isobaric friction constants in the directions transverse to the load are calculated as usual from the fourth relationship in Eq. (II.18). The combined $\boldsymbol{\eta}$ can then be inserted into the differential equations for the position and momentum to calculate the atomic evolution. Note that the rate of change of the periodic cell, $\dot{\mathbf{h}}$, is in units of Å/ps, which is not strain rate. Thus, if $\dot{\mathbf{h}}$ were specified in the input file, models with different heights would require different values of $\dot{\mathbf{h}}$ to stipulate that the strain rates be consistent. A more efficient method is to specify the strain rate explicitly in the input file, then have the molecular dynamics program calculate the necessary $\dot{\mathbf{h}}$ after isobaric-isothermal equilibration,

$$\dot{\mathbf{h}} = \dot{\varepsilon}\mathbf{h}_e \quad . \tag{II.31}$$

Here, $\dot{\varepsilon}$ is the desired strain rate and $\mathbf{h}_e$ is the size of the periodic cell after isothermal and/or isobaric equilibration. In summary, the added control over the position of the periodic simulation cell boundaries in the loading direction allows for direct comparison of interface models with different lattice orientations. In addition, this method allows for the simulation of void nucleation because the motion of the boundary in the loading direction is no longer a function of the internal system pressure.

II.4 Interatomic Potentials

Historically, four classes of interatomic potentials are defined: pair potentials, cluster potentials, pair functionals and cluster functionals. Each class corresponds to an increasing level of complexity in the potential energy approximation. For pair potentials, such as the Lennard-Jones 12-6 potential (Lennard-Jones, 1924a; 1924b), the force between two atoms is a function of only the distance between those two atoms. The position of neighboring atoms does not influence the strength of the bond. On the other hand, cluster potentials consider both the distance between atoms and the angles between sets of atoms in the force calculation. A complete review of interatomic potentials can be found in Carlsson (1990). The following will only discuss one example of a pair functional: the embedded-atom method.

II.4.1 The Embedded-Atom Method

Daw and Baskes (1983; 1984) developed the embedded-atom method (EAM) to describe atomic bonding in face-centered cubic (FCC) metallic systems. The EAM is analogous to previous quasiatom (Stott and Zaremba, 1980) or effective-medium (Nørskov, 1982) theories in that each atom is viewed as an embedded impurity in the bulk of other atoms. To approximate the potential energy of a set of atoms, the EAM includes both pair interactions between nuclei of atoms i and j and the embedding energy as a function of the local background electron density around i^{th} atom,

$$U = \sum_i G^i\left(\rho^j_{ave}\left(r^{ij}\right)\right) + \frac{1}{2}\sum_{i,j(j\neq i)} \varphi\left(r^{ij}\right) \quad . \tag{II.32}$$

Here, G^i is the embedding energy function, ρ^j_{ave} is the spherically averaged background electron density due to neighbors of the i^{th} atom, φ is the pair interaction and r^{ij} is the distance between atoms i and j. The embedding energy is assumed to depend solely on the local background electron density provided by the surrounding atoms and its lower derivatives, which alleviates the need for a volume-dependent energy term (*cf.* Johnson, 1972). The background electron density is calculated using a linear superposition of the densities from the neighboring atoms, i.e.,

$$\rho^j_{ave}\left(r^{ij}\right) \equiv \sum_{j\neq i} \rho^j_{ave}\left(\mathbf{r}^i - \mathbf{r}^j\right) \quad . \tag{II.33}$$

This summation is performed over local atoms within a specified cut-off distance. The cut-off distance typically includes at least first and second nearest neighbors. Since the background electron density is a local quantity, the embedded-atom method is applicable for examining systems with crystalline defects, such as dislocations and grain boundaries. The EAM is known as a semi-empirical approximation because the embedding energy, background electron density and pair interaction functions are tailored to match certain material properties from *ab initio* calculations and experimental observations. Typical material properties include the lattice constant, bulk modulus, elastic constants, vacancy formation energy and sublimation energy (*cf*. Foiles *et al.*, 1986). Interatomic potentials developed more recently are fit to additional structural properties, such as the stacking fault energy (*cf*. Mishin *et al*., 1999; 2001).

An important assumption in the derivation of the EAM expression is that the electron cloud around each atom is spherical in shape. Thus, it is assumed that bond orientation is not important in the description of the potential energy. This approximation is valid for FCC crystal structures with either nearly empty or nearly full d-bands (Daw, 1989); however, the EAM fails to describe systems where directional bonding is important, such as BCC, HCP and nonmetallic materials. Cluster functionals, are capable of extending the applicability of pair functionals to the angular dependent space. For example, Baskes (1992) has developed the modified embedded-atom method (MEAM) to include a measure of the directionality of atomic bonding. The MEAM has shown that it is capable of producing accurate numerical results for BCC and nonmetallic systems, even though the concept of a local embedding function is not rigorously defined in angular dependent bonding systems.

II.4.2 Mishin *et al.* EAM potentials

The Mishin *et al*. EAM interatomic potentials for aluminum (1999) and copper (2001) are used in this work. These potentials are fitted (with varying weights) to:

- The lattice constant
- The cohesive energy
- The elastic constants
- The vacancy formation energy
- Phonon frequencies
- (110), (100) and (111) surface energies
- Energies of HCP, BCC and diamond cubic structures
- The intrinsic stacking fault energy

Calculations in this section will show that the EAM interatomic potentials of Mishin *et al.* for both aluminum (1999) and copper (2001) are the most appropriate choice for the work presented in this dissertation. Specifically, it is critical that the interatomic potential used in this work accurately model the formation and structure of dislocations in FCC metals. As discussed in Chapter I, Van Swygenhoven and colleagues (Van Swygenhoven *et al.*, 2004; Froseth *et al*., 2004) argue the importance of both the intrinsic and unstable stacking fault energies on the nucleation of full dislocations from nanoscale grain boundary interfaces. In essence, the entire generalized stacking fault (GSF) energy curve (Zimmerman *et al*., 2000) must be accurately

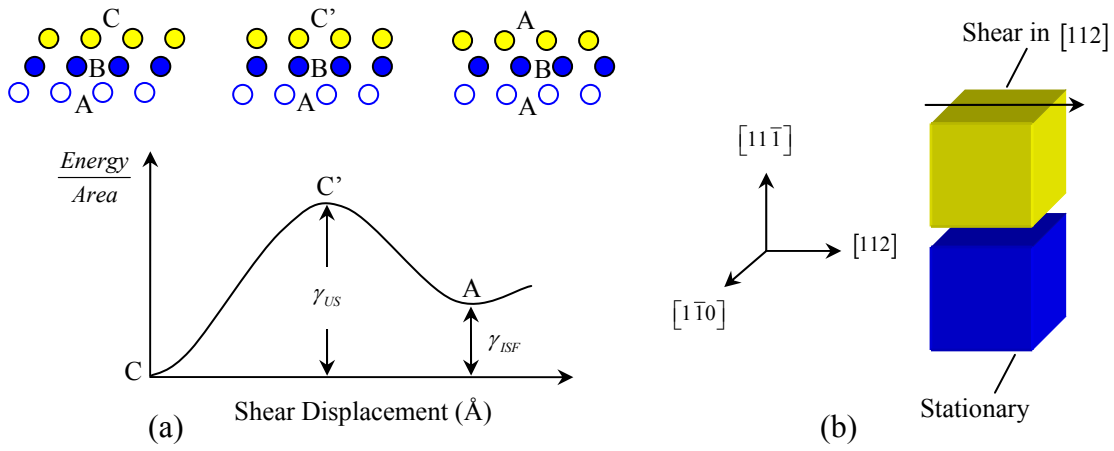

Figure II.4. (a) Schematic of the generalized stacking fault (GSF) energy curve and (b) schematic of the GSF energy curve calculation.

reproduced by the chosen interatomic potential. A schematic of a typical GSF energy curve is shown in Fig. II.4(a). Shear occurs between two {111} planes in the <112> direction, breaking the ABCABC stacking sequence. The unstable stacking fault energy, γ_{US}, is defined as the magnitude of the peak of the GSF curve. The intrinsic stacking fault energy, γ_{ISF}, is taken as the energy of the first local minimum beyond GSF energy peak. Rice (1992) showed that the unstable stacking fault energy is an important parameter in the characterization of dislocation nucleation. The intrinsic stacking fault energy is an important parameter that describes the spacing between partial dislocations in FCC metals (Hirth and Lothe, 1982). Note that the Mishin *et al*. potentials are not fit to the unstable stacking fault energy.

The GSF energy curve calculations of Zimmerman *et al.* (2000) are reproduced to validate the energy minimization algorithm and to select an appropriate interatomic potential for copper and aluminum. A schematic of the simulations geometry is shown in Fig. II.4(b). A block of atoms, approximately 10x20x10 lattice units on each side, is

constructed with the specified orientation. Periodic boundary conditions are applied in the [112] and $[1\bar{1}0]$ directions to eliminate in influence of free surfaces on the stacking fault calculation. The block of atoms is sectioned between two $(11\bar{1})$ planes, as shown in Fig. II.4(b). Note, the gap shown between the two lattice regions in Fig. II.4(b) is only for illustrative purposes; the undeformed configuration (position C in Fig. II.4(a)) is a perfect lattice. A uniform shear displacement is applied to the top block of atoms in the [112] direction. The bottom block remains stationary during the simulation.

Both relaxed and unrelaxed shear calculations are performed at 0 K. In the unrelaxed calculations, the two lattice regions are sheared rigidly, i.e., atomic displacement is not allowed in the $[11\bar{1}]$ direction. In the relaxed calculations, molecular statics (0 K) simulations are performed after each shear step to determine the movement of the atoms in the $[11\bar{1}]$ direction at the fault plane necessary to minimize the system potential energy. The generalized stacking fault energy curve is calculated by monitoring the energy of each atom in the vicinity of the fault created during the shearing process. The difference in the energy between the distorted and undeformed (bulk energy) states is used to calculate the critical points along the GSF curve, γ_{US} and γ_{ISF}.

Figures II.5(a) and II.4(b) show the GSF energy curves for each of the copper and aluminum potentials evaluated. Two copper EAM potentials (Foiles *et al*., 1986; Mishin *et al*., 2001) and five aluminum EAM potentials are tested (Jacobsen *et al*., 1987; Voter and Chen, 1987; Ercolessi and Adams, 1994; Mishin *et al*., 2001; Li, 2003). More aluminum EAM potentials were tested than copper potentials due to the wide variation in the calculated GSF energy curve, as can be seen in Fig. II.5(b). Note, each of the

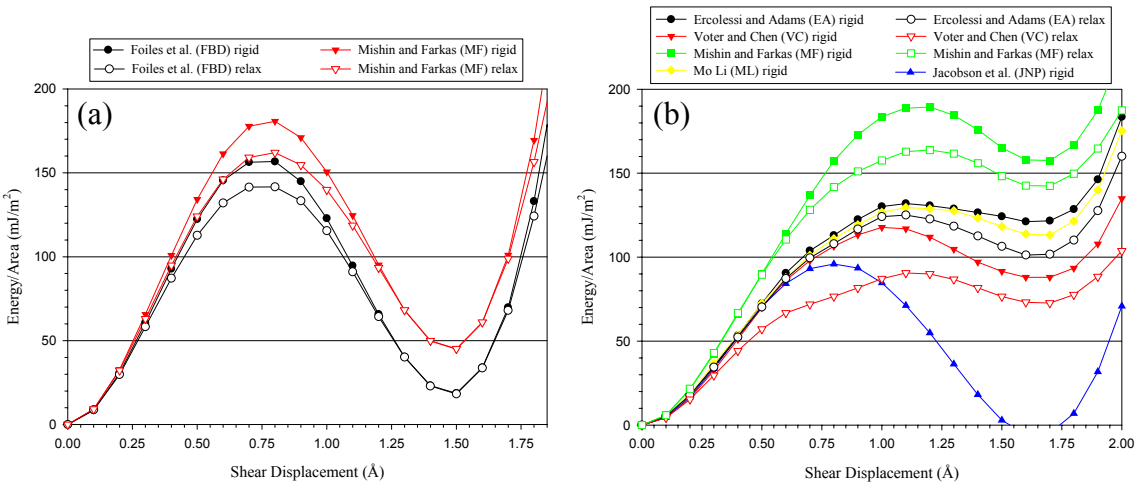

Figure II.5. (a) GSF curves for copper EAM potentials tested; (b) GSF curves for aluminum potentials tested. Both relaxed and unrelaxed calculations are shown.

interatomic potentials examined in this work uses a different set of property data and likely different 'weights' assigned to each property during the fitting procedure.

In copper, each of the potentials tested shows a similar form for the GSF energy curve. The Mishin *et al.* (2001) copper EAM potential predicts slightly higher values for both the intrinsic and unstable stacking fault energies than the potential of Foiles *et al.* (1986). Specifically, the values predicted for γ_{US} and γ_{ISF} using the Mishin *et al.* (2001) copper EAM potential are 162.0 mJ/m^2 and 45.0 mJ/m^2, respectively, which are in agreement with the reported values from tight-binding calculations (Mehl *et al.*, 2000) and experimental observations (Carter and Ray, 1977). Electronic structure calculations using density functional theory predict a slightly higher value for the unstable stacking fault energy of copper at 210 mJ/m^2 (Zimmerman *et al.*, 2000). This value of the unstable stacking fault is for an unrelaxed configuration and is not drastically different

from the unrelaxed stacking fault energy of 180 mJ/m^2 using the Mishin *et al.* copper potential

The calculated GSF curves for aluminum show a much wider variation than those in copper. Aluminum is more difficult to model with the EAM methodology because of the mildly directional nature of its interatomic bonding. Aluminum borders between metallic and nonmetallic elements on the periodic table; thus, directional bonding is more prevalent, violating one of the assumptions of the embedded-atom method. Regardless, using the aluminum EAM potential by Mishin *et al*., the stacking fault energies are calculated as $\gamma_{US} = 163.8$ mJ/m^2 and $\gamma_{ISF} = 142.4$ mJ/m^2. The stable stacking fault energy compares favorably with experimental observations by Murr (1975). Unrelaxed calculations using density function theory predicts a value of 213 mJ/m^2 for the unstable stacking fault energy (Hartford *et al*., 1998), which again is slightly higher than the value of 190 mJ/m^2 from EAM calculations in this work. In summary, the Mishin *et al.* EAM potentials appear to be more accurate than the other EAM potentials tested for the dislocation properties critical to this thesis.

To further validate the Mishin *et al.* EAM potentials and the molecular dynamics code, simulations are designed to calculate the elastic stiffness (C_{11} and C_{12}) and Young's modulus in the [100], [110] and [111] crystallographic directions. Figure II.6 schematically describes the two sets of simulations performed to determine these constants. Deformation is performed in the Y-direction for each simulation using the equations of motion for the NPT ensemble. In Fig. II.6(a), the boundaries in the X- and Z-directions are artificially constrained ($v_P = 0$) so that the displacement (or strain) in

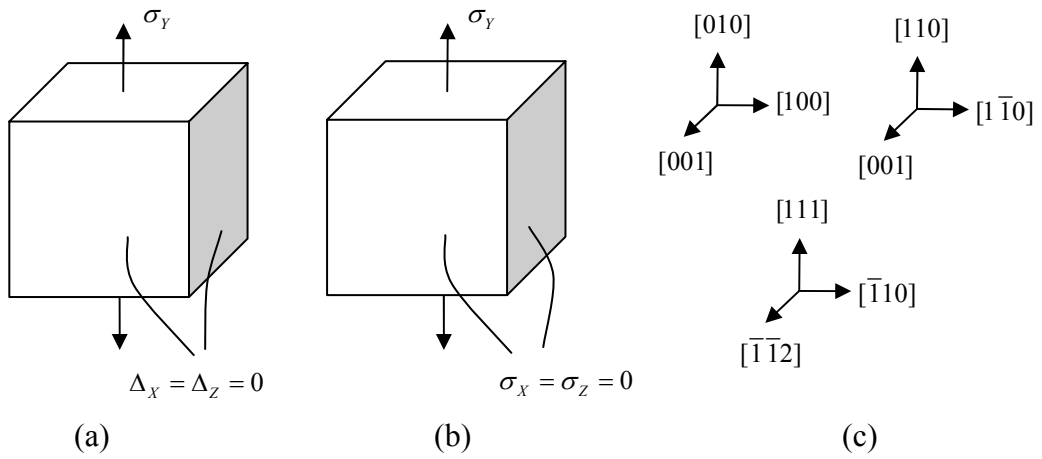

Figure II.6. (a) Displacement of the X- and Z- boundaries is restricted; (b) boundaries are allowed to move so that the stress in the X- and Z- directions is equal to zero; (c) lattice orientations studied in this example.

these directions is equal to zero. Thus, the set of elastic equations to describe the response of a homogeneous cubic crystal (in Voigt notation),

$$\begin{bmatrix} \sigma_1 \\ \sigma_2 \\ \sigma_3 \\ \sigma_4 \\ \sigma_5 \\ \sigma_6 \end{bmatrix} = \begin{bmatrix} C_{11} & C_{12} & C_{12} & 0 & 0 & 0 \\ C_{12} & C_{11} & C_{12} & 0 & 0 & 0 \\ C_{12} & C_{12} & C_{11} & 0 & 0 & 0 \\ 0 & 0 & 0 & C_{44} & 0 & 0 \\ 0 & 0 & 0 & 0 & C_{44} & 0 \\ 0 & 0 & 0 & 0 & 0 & C_{44} \end{bmatrix} \begin{bmatrix} \varepsilon_1 \\ \varepsilon_2 \\ \varepsilon_3 \\ \varepsilon_4 \\ \varepsilon_5 \\ \varepsilon_6 \end{bmatrix} \tag{II.34}$$

reduces to,

$$\begin{aligned} \sigma_1 &= C_{12}\varepsilon_2 = \sigma_3 \\ \sigma_2 &= C_{11}\varepsilon_2 \end{aligned} \quad . \tag{II.35}$$

Table II.3. Elastic constants from MD simulation and experiment.

	C11 (GPa)	C12 (GPa)	E [100] (GPa)	E [110] (GPa)	E [111] (GPa)
Simulation	172.9	125.4	69.4	117.9	187.4
Experiment*	168.4	121.4	66.7	130.0	191.1

*Experimental data from Hertzberg (1996)

Thus, the elastic constants C_{11} and C_{12} may be determined by measuring the slope of the appropriate stress-strain relation. In Fig. II.6(b) the boundaries of the simulation cell are allowed to move so that the stress in the X- and Z-directions is equal to zero. Thus, a uniaxial tension simulation is performed. Here, the slope of the stress-strain relation is Young's modulus in the appropriate direction. Three different orientations are considered, as shown in Fig. II.6(c). Simulations are performed with the Mishin *et al.* (2001) EAM potential for copper. All calculations are performed at a temperature of 300 K.

Numerical results for the elastic constant calculations are shown in Figs. II.7(a) and II.7(b) and compared to experimental values in Table II.3. Stress is calculated using the virial definition (Eq. (II.19)), while strain is derived from the positions of the periodic boundaries, $\mathbf{h}$. While some nonlinearity is evident, the elastic constants calculated from the initial slope of the MD simulations are all within acceptable accuracy of the experimental values. The largest deviation between simulation and experiment is for the calculation of Young's modulus in the [110] direction at approximately 9%. Magnitudes of elastic stress and strain on the order of 5-8 GPa and 5-9%, respectively, are typical for molecular dynamics simulations of perfect crystalline behavior. Previous molecular dynamics calculations of elastic deformation of single crystal nickel in the [100] direction

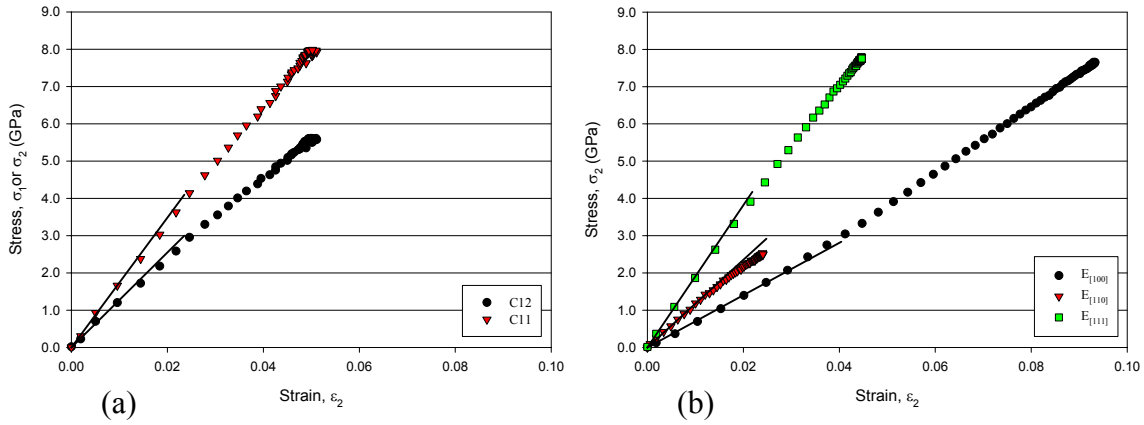

Figure II.7. (a) Calculation of elastic constants from the stress-strain relationship for simulations in which the strain in the nonloading directions is constrained to zero; (b) calculation of Young's modulus in [100], [110] and [111] directions from a uniaxial stress-strain relationship.

with stress free boundary conditions (*cf.* Kitamura *et al.*, 1997) are in qualitative agreement with that reported in Fig. II.7.

CHAPTER III

BICRYSTAL INTERFACE STRUCTURES AND ENERGIES

III.1 Introduction

Interfaces between crystal lattices may be classified into two categories based on their composition: homophase and heterophase (Howe, 1997). The set of homophase interfaces includes grain boundaries in pure metals, twins and stacking faults. The face-centered cubic (FCC) metallic interfaces studied in this thesis are all considered homophase interfaces. The degree of coherency of each boundary varies based on the misorientation angle of the interface and the nanoscale translations that exist to minimize the interface energy. The coherency of low-angle grain boundaries may be described through dislocation based models (Read and Shockley, 1950). Here, the degree of coherency is directly related to the spacing between misfit dislocations along the interface plane. As the misorientation angle of the interface is increased beyond 15^{o}, the cores of the interface dislocations begin to overlap, requiring a different description of the interface structure. The coherency of high-angle boundaries may be described through the structural unit model (Sutton and Vitek, 1983a) or coincident site lattice theory (Randle, 1996), both of which are discussed in greater detail later in this section.

For reference, heterophase boundaries may be subdivided into three categories: fully coherent, semicoherent and incoherent (Howe, 1997). In general, the degree of coherency in heterophase boundaries may be characterized by the lattice mismatch between crystalline regions. Fully coherent heterophase interfaces exist between

materials with nearly identical crystallographic structure, but with different elemental composition. Cahn-Hilliard (1958) interface theory provides one method to model this type of boundary. Semicoherent heterophase interfaces are characterized by a small discrepancy in the lattice parameter between the two crystalline regions. The lattice misfit is accommodated by a periodic array of dislocations at the interface. Incoherent heterophase interfaces are those with no obvious correspondence of atomic planes across the boundary. Here, significant mismatch in the lattice parameter (>30%) and possible differences in the bonding character (covalent versus metallic, for example) prevent any local atomic relaxation at the boundary.

In general, interfaces between crystal lattices have five macroscopic degrees of freedom (Randle, 1993; 1996; Howe, 1997). Four degrees of freedom are accounted for by two orientation vectors, while the fifth is defined by an interface angle. Using the misorientation scheme notation, an interface is fully characterized by a misorientation angle, θ, a misorientation axis vector, $\mathbf{M}$, and the normal vector to the interface plane, $\mathbf{N}$. Figure III.1 shows a schematic of the misorientation scheme. Boundaries for which the normal to the interface plane is perpendicular to the misorientation axis ($\mathbf{M} \perp \mathbf{N}$) are defined as 'tilt' interfaces, as shown in Fig. III.1(a). Similarly, boundaries for which the normal to the interface plane is parallel to the misorientation axis ($\mathbf{M} \parallel \mathbf{N}$) are defined as 'twist' interfaces. In general, grain boundaries in actual polycrystals may have both tilt and twist character, as shown in Fig. III.1(b). Although pure tilt boundaries compose a very small portion of the total set of interface angle/axis combinations, they are often observed experimentally, suggesting that they may be energetically favorable as compared with general high-angle interfaces (Sutton and Balluffi, 1987).

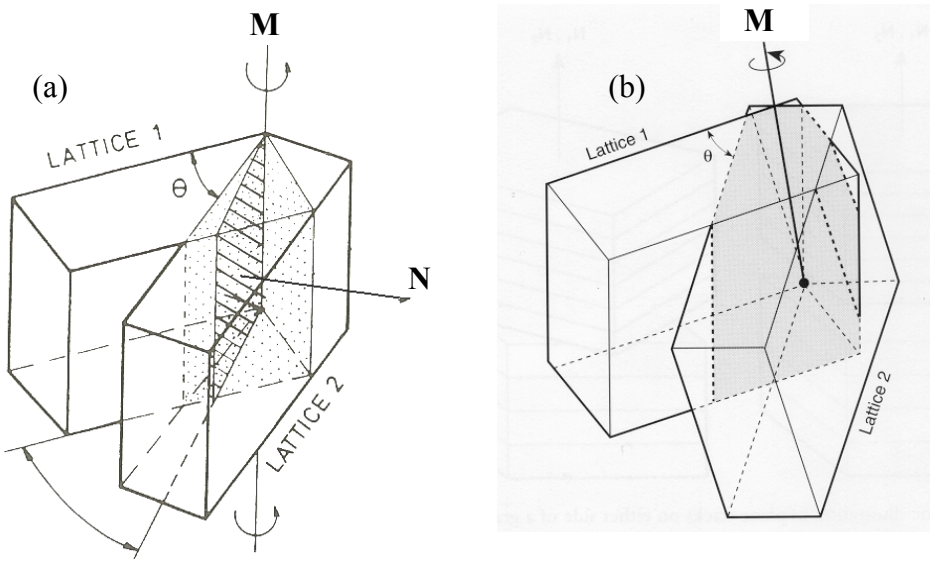

Figure III.1. Schematic representation of the grain boundary misorientation scheme for (a) tilt boundaries and (b) general boundaries. Reproduced from Randle (1996).

In addition, interfaces between crystal lattices have three microscopic degrees of freedom associated with the mutual nanoscale translation of the opposing lattice regions parallel and perpendicular to the interface plane. These translations exist to minimize the interface energy for a given misorientation. The three interface microscopic degrees of freedom do not need to be prescribed in this work, as they are resolved naturally during the energy minimization procedure described in Section III.2.

A small subset of interfaces are considered geometrically 'special' in the sense that the opposing lattice regions fit more closely across the interface plane (Randle, 1993; 1996; Howe, 1997). To illustrate this concept, Fig. III.2 shows a two-dimensional schematic of two interpenetrating lattices. The two lattice regions, A and B, are rotated relative to one another around a common origin. Specific angle/axis combinations will result in an array of coincidence lattice points. This array of lattice points is known as the

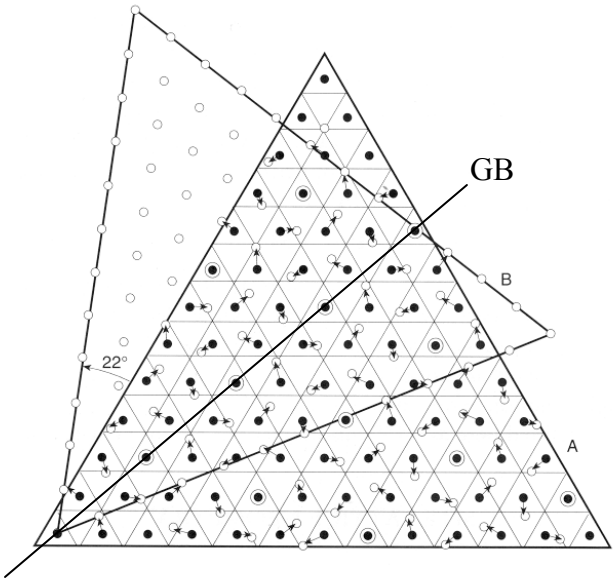

Figure III.2. Schematic of a Σ7 coincident site lattice (CSL) model. 1 in 7 lattice sites are coincident between the two lattice regions. Reproduced from Randle (1996).

coincident site lattice (CSL) and is illustrated in Fig. III.2 where filled and open circles overlap. The inverse density of coincident lattice points is defined as Σ. The CSL methodology may be considered as a shorthand notation used to describe specific misorientation angle/axis combinations. More importantly, boundaries with low values of Σ typically have special geometric characteristics. The CSL Σ notation is used to describe specific angle/axis combinations throughout this thesis.

In Fig III.2, lattice region B is rotated 22^{o} around the <111> axis with respect to lattice region A. At this orientation, 1 in 7 lattice points is coincident between lattice regions A and B; thus, an interface with this angle/axis combination is known as a Σ7 interface using the CSL methodology. The tilt boundary that would result from a symmetric rotation of each lattice region is drawn through the densest line of coincident sites, as shown in Fig. III.2. Other tilt boundaries are certainly possible through

asymmetric rotations of the two lattice regions. Twist boundaries are also possible by considering the plane of rotation in Fig. III.2 as the boundary (the interface normal and misorientation axes would be parallel in this case).

The CSL notation is an important tool to characterize the interface structure because the pattern of coincident atomic sites leads directly to a definable periodic structure at the interface. Atomistic simulations by Sutton and Vitek (1983a; 1983b; 1983c; Wang *et al*., 1984) using a pair-potential showed that interfaces in FCC metals may be viewed as a linear combination of 'structural units.' This concept became known as the structural unit model (SUM). Each structural unit is associated with a 'favored' boundary for a given misorientation axis. For the <001> misorientation axis, Wang *et al.* (1984) found that the favored boundaries are the Σ1 (110) (perfect lattice), Σ5 (210), Σ5 (310) and the Σ1 (100) (perfect lattice) interfaces. The structural units associated with each of these boundaries were denoted A-D, respectively. The Σ5 interface is the lowest order Σ boundary for the <001> misorientation axis. However, Sutton and Vitek surprisingly found that favored interfaces did not always correspond to the lowest value of Σ for a given misorientation axis. For the <110> misorientation axis, Sutton and Vitek (1983a) reported that favored boundaries exist at the Σ27 (115) and Σ11 (113) interfaces. Several other Σ boundaries exist around the <110> misorientation axis that have a lower Σ value. Rittner and Seidman (1996) evaluated the entire range of <110> misorientations and found that the favored boundaries are the Σ1 (001) (perfect lattice), Σ27 (115), Σ11 (113), Σ3 (111), Σ9 (221) and the Σ1 (110) (perfect lattice) interfaces. The structural units associated with each of these boundaries were denoted A-E (both Σ1 'interfaces'

were defined as A structural units). Note that the Σ3 (112) interface is not found to be a favored boundary, even though it has a high density of coincident lattice sites.

There are, however, several limitations to the structural unit model. First, it is difficult to identify structural units with three-dimensional character, as is commonly the case with twist boundaries. Second, the SUM has limited applicability for interfaces with mixed tilt and twist characteristics or if a high index misorientation axis is examined (Sutton and Balluffi, 1990). While only four structural units are required to characterize <001> tilt boundaries, for high index misorientation axes the number of independent structural units becomes extremely large. Third, the SUM fails to describe interfaces with delocalized structural units. Rittner and colleagues (Rittner and Seidman, 1996; Rittner *et al*., 1996) showed that for materials with low stacking fault energies, the interface dislocations tend to dissociate, leading to short intrinsic stacking fault (ISF) facets that extend from the interface plane. Rittner and Seidman (1996) also revealed that if the delocalization of the interface is severe, the structural units may not change continuously between two favored boundaries. Here, several variations of a given structural unit may be required to describe the interface geometry. Molecular statics simulations presented in Section III.3.2 will show several examples of each type of interface. Despite the limitations of the SUM, Rittner and Seidman (1996) showed that boundaries with highly dissociated structural units still have a definable repeating structure over the length of the interface, i.e., the interface structure is not random or amorphous.

Disclinations have also been proposed as a method to describe the structure of interfaces in crystalline materials (Li, 1972; Shih and Li, 1975). A disclination is a

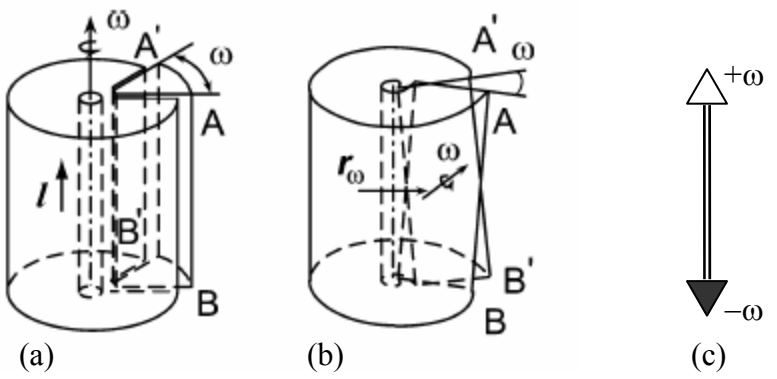

Figure III.3. Schematic of defect structure for (a) wedge disclination (b) twist disclination and (c) wedge disclination dipole.

rotational defect that has a close analogy to a dislocation. Figures III.3(a) and III.3(b) show schematics of wedge and twist disclinations. The strength of a disclination is characterized by the magnitude of the rotation vector, ω. The orientation of the rotation axis with respect to the disclination core differentiates between disclination types. Disclinations for which the rotation axis is parallel to the disclination core are defined as wedge disclinations, whereas disclinations for which the rotation axis is perpendicular to the disclination core and defined as twist disclinations.

Unlike dislocations, the stress field around a disclination diverges; thus, dislcinations are commonly observed in dipole or quadrupole formations which effectively 'screen' the divergent stress field (Romanov, 1993). An example of a partial wedge disclination dipole is shown in Fig. III.3(c). Two partial wedge disclinations (illustrated as triangles), which are equal in strength but opposite in magnitude, are positioned in close proximity. The spacing between partial disclinations is defined as the dipole 'arm' length. In general, Li's (1972) work extended beyond the traditional dislocation based grain boundary theories (Read and Shockley, 1950), which were

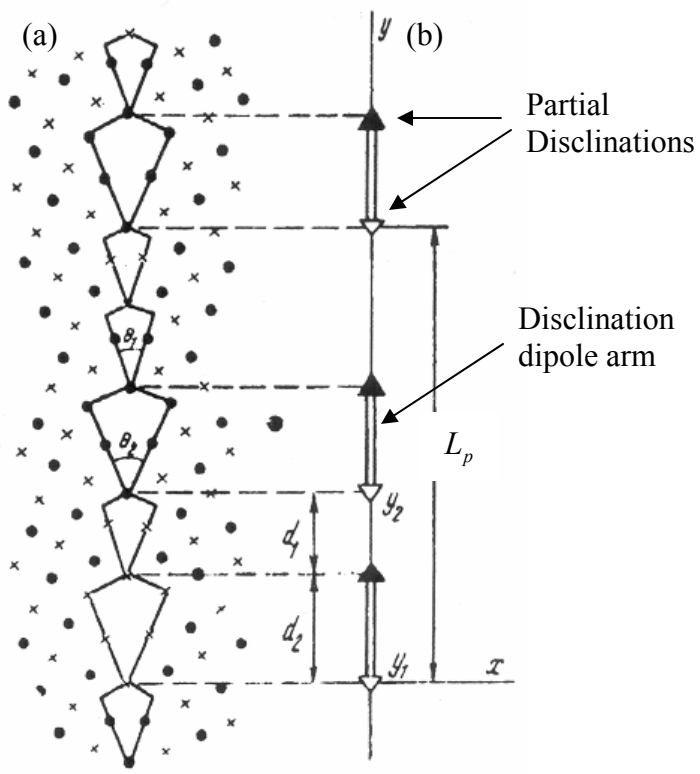

Figure III.4. Disclination structural unit model representation of a grain boundary interface composed of A and B structural units. Reproduced from Valiev *et al.* (2002).

limited to low-angle grain boundaries (<15^{o}). At higher angles, the cores of the interface dislocations become too densely packed to accommodate individual distinction.

More recent work has combined the structural unit model with Li's disclination based description of interfaces to model the structure and energy of high-angle grain boundaries (Gertsman *et al*., 1989; Valiyev *et al*., 1990; Nazarov *et al*., 2000; Bachurin *et al*., 2003). As discussed above, certain high-angle boundaries may be modeled as a linear combination of structural units. Boundaries that are not considered favored in the SUM representation of interfaces consist of alternating regions of different structural units, each of which has a defined misorientation angle characteristic of a favored boundary, as

shown in Fig. III.4(a). Thus, at the junction between two different structural units, there is a local change in the rotation of the lattice. The disclination-structural unit model (DSUM) identifies this junction as a partial wedge disclination, as shown in Fig. III.4(b). The strength of each partial wedge disclination is calculated from the misorientation angle associated with each structural unit, $\omega = \pm(\theta_2 - \theta_1)$. The length of the disclination dipole arm is equivalent to the size of one of the structural units, which is related to the repeating period of the interface, L_p. Commonly, the minority structural unit (structural unit that appears less frequently) is represented as the disclination dipole. Note that if angle of the interface, θ, was equal to either θ_1 or θ_2 the interface would be considered favored and consist only of one type of structural unit. Thus, favored high-angle boundaries can not be described in terms of disclination dipoles.

III.2 Energy Minimization Procedure and Boundary Conditions

Molecular statics calculations with a nonlinear conjugate gradient algorithm (described in Chapter II) are used to refine the initial interface structures. Recall that one of the primary goals of this work is to quantify the role of specific interface features in the inelastic response of the interface. Thus, it is critical that the initial interface structures be described accurately to meet the computational objectives of this work. For example, while previous molecular dynamics work has identified the nucleation of both partial and full dislocations during a deformation process (Van Swygenhoven *et al.*, 1998; 1999a; 2001), the influence of different structural units on dislocation nucleation is not well understood in the literature. Very recent work by Sansoz and Molinari (2004;

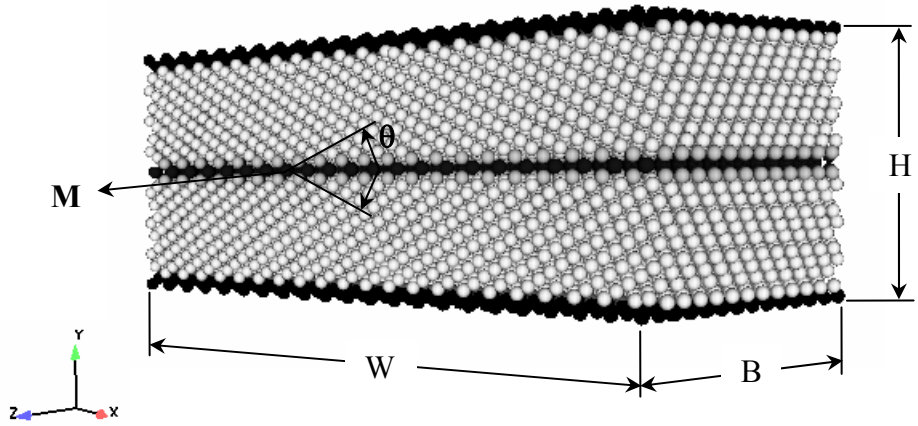

Figure III.5. Bicrystal interface model used to determine the interface structure at 0 K.

2005) using the quasicontinuum method has investigated the sliding behavior of several <110> interfaces. They find that the E structural unit, which is associated with the Σ9 {221} interface (Rittner and Seidman, 1996), plays a strong role in triggering the shuffling of atoms along the interface plane.

III.2.1 Interface Model Geometry

The tilt bicrystal interface model used for the energy minimization calculations is shown in Fig. III.5. The interface misorientation is created by a symmetric tilt rotation, θ, of opposing lattice regions around a misorientation axis, **M**. For calculations in this work, the interface misorientation axis is taken as either the [001], $[1\bar{1}0]$ or [111] crystallographic directions. The [001] and $[1\bar{1}0]$ axes are aligned with the global Z-direction to study tilt boundaries whereas the [111] axis is aligned with the global Y-direction to study twist interfaces. The interface misorientation angle is measured using the [100] direction as the reference (0^o) for the [001] tilt boundaries, the $[\bar{0}01]$ direction

Table III.1. Interface misorientations studied with M = [001].

Axis M	Angle θ (deg)	Σ	Boundary Plane	Axis M	Angle θ (deg)	Σ	Boundary Plane
[001]	4.24	365	{27 1 0}	[001]	48.9	73	{11 5 0}
[001]	5.21	485	{22 1 0}	[001]	50.0	137	{15 7 0}
[001]	7.15	257	{16 1 0}	[001]	51.1	325	{23 11 0}
[001]	9.53	145	{12 1 0}	[001]	51.9	941	{39 19 0}
[001]	11.4	101	{10 1 0}	[001]	53.1	5	{210}
[001]	14.3	65	{8 1 0}	[001]	54.3	1921	{39 20 0}
[001]	16.3	25	{7 1 0}	[001]	55.1	673	{23 12 0}
[001]	19.7	545	{23 4 0}	[001]	56.1	289	{15 8 0}
[001]	20.6	125	{11 2 0}	[001]	57.2	157	{11 6 0}
[001]	21.6	457	{21 4 0}	[001]	60.1	241	{19 11 0}
[001]	22.6	13	{5 1 0}	[001]	60.9	389	{17 10 0}
[001]	23.5	601	{24 5 0}	[001]	61.9	17	{5 3 0}
[001]	24.2	205	{14 3 0}	[001]	62.9	445	{18 11 0}
[001]	25.6	509	{22 5 0}	[001]	64.0	89	{8 5 0}
[001]	26.0	89	{13 3 0}	[001]	64.6	505	{19 12 0}
[001]	27.0	661	{25 6 0}	[001]	65.5	277	{14 9 0}
[001]	28.1	17	{4 1 0}	[001]	66.4	965	{26 17 0}
[001]	29.1	389	{27 7 0}	[001]	67.4	13	{3 2 0}
[001]	29.9	241	{15 4 0}	[001]	68.4	457	{25 17 0}
[001]	33.4	109	{10 3 0}	[001]	69.4	125	{13 9 0}
[001]	34.2	185	{13 4 0}	[001]	70.4	433	{17 12 0}
[001]	35.1	397	{19 6 0}	[001]	73.7	25	{4 3 0}
[001]	35.9	1277	{34 11 0}	[001]	75.7	65	{9 7 0}
[001]	36.9	5	{3 1 0}	[001]	77.3	41	{5 4 0}
[001]	37.9	1145	{32 11 0}	[001]	79.6	61	{6 5 0}
[001]	38.9	325	{17 6 0}	[001]	82.4	113	{8 7 0}
[001]	40.0	137	{11 4 0}	[001]	84.0	181	{10 9 0}
[001]	41.1	73	{8 3 0}	[001]	85.0	265	{12 11 0}

as the reference for the $[1\bar{1}0]$ tilt boundaries and the $[11\bar{2}]$ direction as the reference for the [111] twist boundaries. Note that other crystal directions are sometimes taken in the literature to define the reference angle (Wang *et al*., 1984). In general, the most precise method to specify the interface misorientation is to specify both the angle and the crystallographic boundary plane.

Table III.1 summarizes the 56 tilt interface misorientations that are considered around the [001] misorientation axis for the energy minimization calculations. Table III.2 summarizes the 62 interface misorientations that are evaluated around the $[1\bar{1}0]$

misorientation axis. Table III.3 summarizes the 14 interface misorientations that are evaluated around the [111] twist axis. Fewer interface misorientations are required around the [111] twist axis due to the symmetry of the {111} boundary plane. The distribution of interface orientations in this work is chosen using the following methodology. As discussed in Chapter I, certain CSL boundaries have improved or special material properties as compared with more general interfaces (Randle, 1996). Historically, the question of how close an interface needs to be to a special orientation has been answered with geometric arguments; however, there is some disagreement in the literature. Originally, Brandon (1966) proposed the following relationship,

$$\nu_m = \nu_o \Sigma^{-1/2} \quad . \tag{III.1}$$

In Eq. (III.1), ν_m is the maximum deviation from a CSL boundary for the interface to still be considered special and ν_o is taken as the low angle grain boundary limit, 15^o. Unfortunately, the Brandon criterion predicts overlapping between two neighboring CSL regions. For example, the above equation would predict improved properties for every interface between $\Sigma 5$ (310) 36.9^o and $\Sigma 17$ (510) 28.1^o boundaries. Other authors have proposed that ν_m be proportional to Σ^{-1} (Ishida and McLean, 1973), $\Sigma^{-2/3}$ (Warrington and Grimmer, 1974) or $\Sigma^{-5/6}$ (Palumbo and Aust, 1990). Each of these dependencies avoids the overlapping effect seen with the Brandon criterion. The distribution of interface orientations in this work (Tables III.1 – III.3) is chosen using the Palumbo and Aust (1990) approximation for the maximum deviation from a low-order CSL boundary (defined here as those boundaries with a Σ value less than 20).

Table III.2. Interface misorientations studied with M = [1$\bar{1}$0].

Axis M	Angle θ (deg)	Σ	Boundary Plane	Axis M	Angle θ (deg)	Σ	Boundary Plane
[1$\bar{1}$0]	5.1	513	{1 1 32}	[1$\bar{1}$0]	93.4	17	{3 3 4}
[1$\bar{1}$0]	8.1	201	{1 1 20}	[1$\bar{1}$0]	103.7	131	{9 9 10}
[1$\bar{1}$0]	10.1	129	{1 1 16}	[1$\bar{1}$0]	104.7	193	{11 11 12}
[1$\bar{1}$0]	12.4	171	{1 1 13}	[1$\bar{1}$0]	105.7	617	{14 14 15}
[1$\bar{1}$0]	16.1	51	{1 1 10}	[1$\bar{1}$0]	106.5	1009	{18 18 19}
[1$\bar{1}$0]	20.0	33	{1 1 8}	[1$\bar{1}$0]	109.5	3	{1 1 1}
[1$\bar{1}$0]	26.5	19	{1 1 6}	[1$\bar{1}$0]	112.5	937	{18 18 17}
[1$\bar{1}$0]	36.1	187	{3 3 13}	[1$\bar{1}$0]	113.4	561	{14 14 13}
[1$\bar{1}$0]	37.2	491	{5 5 21}	[1$\bar{1}$0]	114.5	171	{11 11 10}
[1$\bar{1}$0]	37.8	1217	{8 8 33}	[1$\bar{1}$0]	115.7	113	{9 9 8}
[1$\bar{1}$0]	38.9	9	{1 1 4}	[1$\bar{1}$0]	125.6	153	{11 11 8}
[1$\bar{1}$0]	40.1	1089	{8 8 31}	[1$\bar{1}$0]	126.4	123	{7 7 5}
[1$\bar{1}$0]	40.8	411	{5 5 19}	[1$\bar{1}$0]	127.3	249	{10 10 7}
[1$\bar{1}$0]	42.2	139	{3 3 11}	[1$\bar{1}$0]	129.5	11	{3 3 2}
[1$\bar{1}$0]	47.0	201	{4 4 13}	[1$\bar{1}$0]	131.5	291	{11 11 7}
[1$\bar{1}$0]	48.1	433	{6 6 19}	[1$\bar{1}$0]	132.3	153	{8 8 5}
[1$\bar{1}$0]	49.0	1161	{10 10 31}	[1$\bar{1}$0]	133.0	201	{13 13 8}
[1$\bar{1}$0]	50.5	11	{1 1 3}	[1$\bar{1}$0]	137.1	187	{9 9 5}
[1$\bar{1}$0]	52.0	1041	{10 10 29}	[1$\bar{1}$0]	138.3	387	{13 13 7}
[1$\bar{1}$0]	53.1	361	{6 6 17}	[1$\bar{1}$0]	139.5	601	{23 23 12}
[1$\bar{1}$0]	54.4	153	{4 4 11}	[1$\bar{1}$0]	141.1	9	{2 2 1}
[1$\bar{1}$0]	65.5	171	{5 5 11}	[1$\bar{1}$0]	142.5	697	{25 25 12}
[1$\bar{1}$0]	66.8	323	{7 7 15}	[1$\bar{1}$0]	143.5	499	{15 15 7}
[1$\bar{1}$0]	67.9	641	{10 10 21}	[1$\bar{1}$0]	144.4	267	{11 11 5}
[1$\bar{1}$0]	68.5	1067	{13 13 27}	[1$\bar{1}$0]	153.5	19	{3 3 1}
[1$\bar{1}$0]	70.5	3	{1 1 2}	[1$\bar{1}$0]	160.0	33	{4 4 1}
[1$\bar{1}$0]	72.5	1121	{14 14 27}	[1$\bar{1}$0]	163.9	51	{5 5 1}
[1$\bar{1}$0]	73.1	683	{11 11 21}	[1$\bar{1}$0]	166.6	73	{6 6 1}
[1$\bar{1}$0]	74.1	353	{8 8 15}	[1$\bar{1}$0]	169.9	129	{8 8 1}
[1$\bar{1}$0]	75.3	193	{6 6 11}	[1$\bar{1}$0]	171.9	201	{10 10 1}
[1$\bar{1}$0]	86.6	17	{2 2 3}	[1$\bar{1}$0]	174.9	513	{16 16 1}

Calculations are focused on the low-order CSL boundaries (Σ3, Σ5, Σ7, Σ9, Σ11, Σ13, Σ17 and Σ19) and those grain boundaries with misorientations close to (using the Palumbo and Aust criteria) those low-order CSL orientations.

In Fig. III.5, the interface model width, W, and thickness, B, are specified to properly enforce periodic boundary conditions in the X- and Z-directions for these calculations. The size of the interface model in the X-direction includes a minimum of 4

Table III.3. Interface misorientations studied with M = [111].

Axis M	Angle θ (deg)	Σ	Boundary Plane	Axis M	Angle θ (deg)	Σ	Boundary Plane
[111]	9.43	111	{1 1 1}	[111]	38.2	7	{1 1 1}
[111]	13.2	57	{1 1 1}	[111]	42.1	93	{1 1 1}
[111]	17.9	31	{1 1 1}	[111]	44.8	129	{1 1 1}
[111]	21.8	21	{1 1 1}	[111]	46.8	19	{1 1 1}
[111]	26.0	237	{1 1 1}	[111]	49.6	5	{1 1 1}
[111]	27.8	13	{1 1 1}	[111]	52.7	61	{1 1 1}
[111]	32.2	39	{1 1 1}	[111]	60.0	3	{1 1 1}

interface periods, which is assumed to be sufficient to not restrict the refinement of the interface structure. Similar methodologies are taken in the previous energy minimization calculations (Wolf, 1990). In the case of low-order CSL boundaries, where fewer structural units are required to describe the interface geometry, many interface periods are used. The thickness of the Z-direction is taken as $B=12\lambda$ for calculations on interfaces built around the [001] axis and $B=11.31\lambda$ for calculations on interfaces constructed around the $[1\,\bar{1}0]$ axis, where λ is the lattice constant of the selected material (3.615 Å for copper or 4.050 Å for aluminum). For [111] twist boundaries, the thickness of the interface region includes at least 4 interface periods, in accordance with the size of the interface model in the X-direction.

The Y-direction is specified using non-periodic boundary conditions, which introduces free surfaces into the calculation. The atoms that compose these boundaries are constrained such that the surface of the model in the +/- Y-direction remains planar during the energy minimization process. However, these surfaces are not fixed; they are allowed to translate both parallel and perpendicular to the interface, allowing for expansion at the interface or asymmetric translations of the structural units. The use of

nonperiodic boundary conditions in the Y-direction also introduces image forces into the system. Image forces are additional forces exerted on dislocations in the lattice due to free and rigid surfaces (Hirth and Lothe, 1982). For example, a dislocation will be attracted towards a free surface. The stress field for a symmetric tilt boundary, such as that studied in this thesis, decreases exponentially away from the interface. Thus, the height of the interface model selected for the energy minimization calculations will have minimal effect on the prediction of the interface structures. Nonetheless, the bicrystal interface is positioned exactly midway between the system boundaries, to avoid any possible unbalanced image forces. Note, once a full dislocation is emitted from the interface, the stress field of the resulting boundary is considered long-range and larger interface model heights must be used. These concerns will be addressed in Chapter IV.

III.2.2 Calculation of Interface Energy

To calculate the energy of each bicrystal interface, the excess energy of each atom due to the presence of the interface must be determined,

$$e_{\mathrm{i}}^{excess} = e_{\mathrm{i}} - e^{bulk} \quad . \tag{III.2}$$

Here, e_{i} is the potential energy of the i$^{\mathrm{th}}$ atom and e^{bulk} is the energy of an atom in a bulk environment (away from all defects). The bulk energy is calculated from the interatomic potential as $e_{CU}^{bulk} = -3.54\,\mathrm{eV}$ (Mishin *et al*., 2001) and $e_{AL}^{bulk} = -3.36\,\mathrm{eV}$ (Mishin *et al*., 1999). Recall that energy minimization calculations are performed at 0 K; thus, there is no kinetic contribution to the total energy of each atom. The energy of the

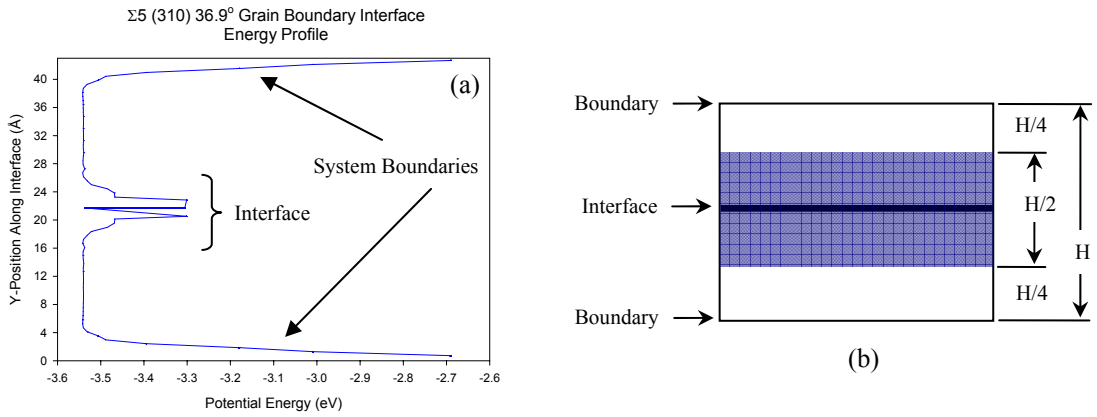

Figure III.6. (a) Potential energy profile of a Σ5 (310) bicrystal interface; (b) schematic illustration of the minimum region around the interface used to calculate the interface energy.

interface, E^{int}, can be calculated by summing the excess energy of each atom within the interface region and dividing by the interface area,

$$E^{\text{int}} = \frac{1}{A^{\text{int}}} \sum_{N^{\text{int}}} e_{\text{i}}^{excess} \quad . \tag{III.3}$$

Here, A^{int} is the interface area, calculated using the periodic dimensions of the interface model in the X- and Z-directions. The summation in Eq. (III.3) is not to be performed over all atoms within the interface model. The number of atoms in the summation, N^{int}, is determined by gauging the thickness of the region for which the presence of the interface contributes to the energy of each atom. Figure III.6(a) shows the potential energy profile in the Y-direction of a copper Σ5 (310) 36.9° interface model. Three prominent deviations from the bulk energy are apparent in Fig. III.6(a), one

corresponding to the interface and the other two corresponding to the system boundaries in the +/- Y-direction.

In Fig. III.6(a), the thickness of the region that is affect by the interface does not extend far into either lattice region. Thus, to calculate the interface energy, the criteria illustrated in Fig. III.6(b) is used. Atoms that lie within H/4 of the bicrystal interface in the +/- Y-direction are used in the energy calculation. With this convention, atoms that are influenced by the nonperiodic boundaries will not be included in the interface energy calculation. Calculations in this chapter will show that the Σ5 interface in copper, which is used in Fig. III.6(a), is nearly mirror symmetric about the interface plane. Not all interfaces examined in this work have this type of structure. Some interfaces have a dissociated structure, which involves the asymmetric dissociation of secondary interface dislocations (Rittner and Seidman, 1996). The length of the dissociated structural unit potentially extends beyond the cutoff distance for the energy calculation, illustrated in Fig. III.6(b) (Rittner *et al*., 1996). In these cases, the interface energy is calculated several times, using systematically larger regions around the interface. The appropriate region is determined once the change in the interface energy between regions is less than 2% of the total interface energy.

III.2.3 Energy Minimization Procedure

Previous energy minimization calculations using bicrystal geometries (Wolf, 1990; Rittner and Seidman, 1996) have shown that a number of initial starting 'positions' must be used to increase the probability that the global minimum energy configuration is attained. This is accomplished by systematically removing atomic layers at the interface

(using the atomic 'overlap' command in the WARP atomistic code) and allowing the energy minimization procedure to rearrange the interface atoms as necessary. Specifically, the atomic overlap command will remove one atom from a pair of atoms that are positioned inside of a defined distance during the interface construction process. For MD simulations of nanocrystalline geometries (*cf.* Van Swygenhoven *et al*., 1998a; Schiotz *et al*., 1998; Yamakov *et al*., 2002) a constant overlap value is chosen for all interfaces, regardless of the misorientation angle (typically at 2.0 Å). It is unlikely that a single atomic overlap parameter is capable of describing the minimum energy structure of all interfaces. Thus, in this work an optimization study is performed to determine the appropriate atomic overlap parameter for each interface angle/axis combination considered. Here, the interface energy is evaluated using a range of atomic overlap values between $0.34*\lambda$ and $0.69*\lambda$.

Figures III.7(a) and III.7(b) show the interface energy versus atomic overlap distance for bicrystal interfaces with misorientations centered around the $\Sigma5$ (310) 36.9^{o} and $\Sigma5$ (210) 53.1^{o} orientations in copper. Figures III.7(a) and III.7(b) clearly show that each grain boundary interface has a brief range of atomic overlap values that corresponds to a minimum energy interface configuration. There does not appear to be a universal atomic overlap value that results in the minimum energy structure for each misorientation considered. This observation is consistent for both Cu and Al boundaries. Thus, each interface must be evaluated individually to insure that the minimum energy configuration is attained in each case.

Unfortunately, it is impossible to be absolutely certain that the energy minimization procedure has produced the global minimum energy configuration (Wolf,

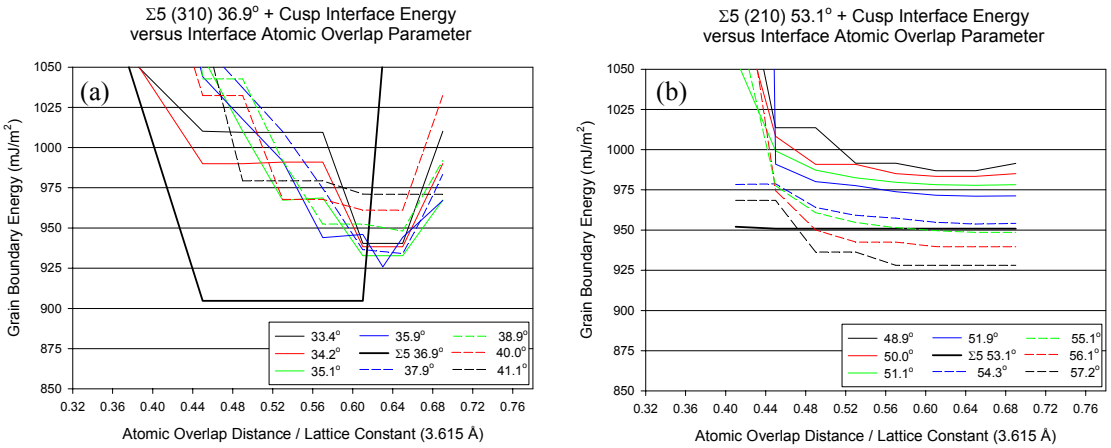

Figure III.7. (a) Potential energy of near and exact Σ5 (310) bicrystal interface models as a function of atomic overlap parameter; (b) potential energy of near and exact Σ5 (210) bicrystal interface models as a function of atomic overlap parameter.

1990). Thus, in Section III.3.2 an additional measure of certainty is provided by comparing the bicrystal interface structures refined using the above procedure to high-resolution transmission electron microscopy (HRTEM) images and electronic structure calculations of metallic interfaces in the literature.

III.3 Energy Minimization Results

III.3.1 Interface Energy

Figure III.8 shows the bicrystal interface energy versus the interface misorientation angle for [001] boundaries in both copper and aluminum. The energy of the aluminum Σ5 (310) 36.9° interface is calculated as 465 mJ/m^2, while the energy of the aluminum Σ5 (210) 53.1° interface is calculated as 494 mJ/m^2. Both values are very close to the values reported by Mishin *et al.* (1999) of 467 mJ/m^2 and 495 mJ/m^2,

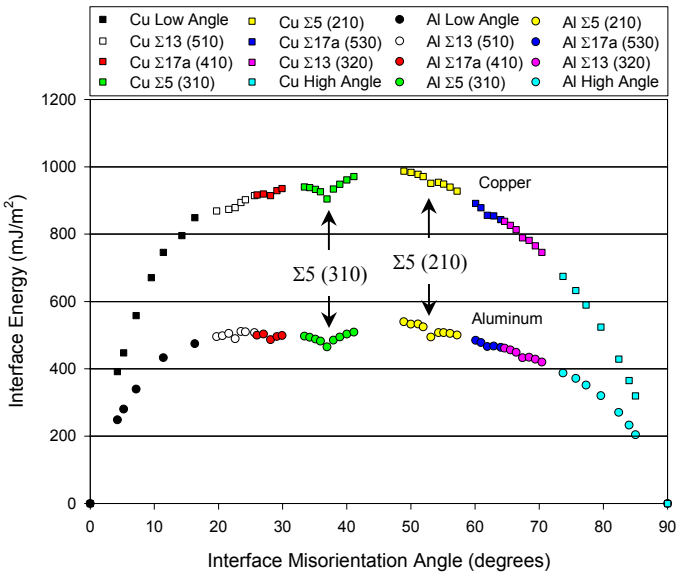

Figure III.8. Bicrystal interface energy for copper and aluminum tilt [001] interface models.

respectively. For both copper and aluminum, small 'cusps' appear in the energy-misorientation angle relationship at specific misorientations, which correspond to low-order CSL grain boundaries. In Fig. III.8, small energy cusps appear at the Σ5 (310) 36.9° and Σ5 (210) 53.1° boundaries. Note that each of these boundaries is considered favored in the structural unit model for the [001] misorientation axis. Other low-order Σ boundaries show only minor reductions in the interface energy, corresponding to small inflection points in the energy curve. Figure III.8 also shows a slight asymmetric character. While the interface energy appears to reach a maximum value between each of the Σ5 boundaries (approximately around 45°), the energy-misorientation angle relationship does not possess mirror symmetry across the 45° centerline. Similar observations have been made for other FCC metals (Cu, Ni and Au) by Wolf (1990).

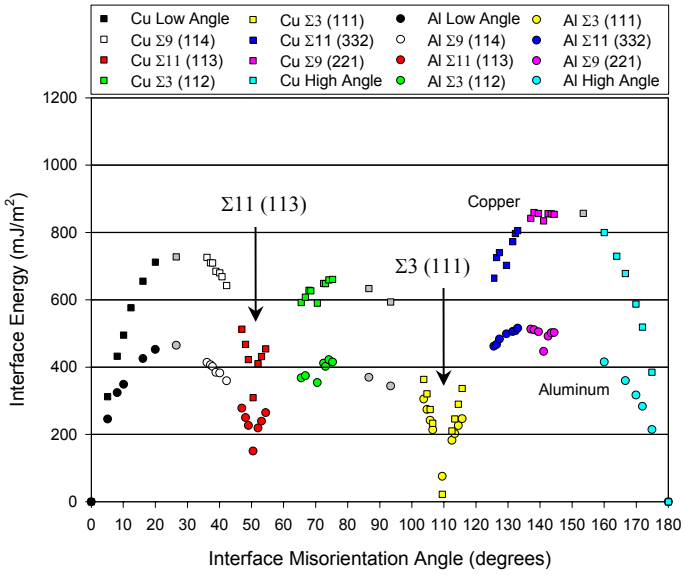

Figure III.9. Bicrystal interface energy for copper and aluminum tilt $[1\,\bar{1}0]$ interface models.

Figure III.9 shows the bicrystal interface energy versus the interface misorientation angle for $[1\,\bar{1}0]$ boundaries in copper and aluminum. Interfaces created around this misorientation axis show a significantly more pronounced cusp behavior than boundaries around the [001] misorientation axis. In both copper and aluminum, prominent 'cusps' appear in the energy-misorientation angle relationship at the Σ3 (111) 109.5° and Σ11 (113) 50.5° boundaries. The energy of the Σ3 (111) 109.5° boundary is calculated as 22 mJ/m^2 in copper and 75 mJ/m^2 in aluminum. Other low-order Σ boundaries show only a small reduction in the interface energy. Figure III.9 shows a pronounced asymmetric character. While the Σ3 (111) 109.5° and Σ11 (113) 50.5° boundaries have very low interface energies, their reciprocal boundaries, Σ3 (112) 70.5° and Σ11 (332) 129.5°, have much larger interface energies by comparison.

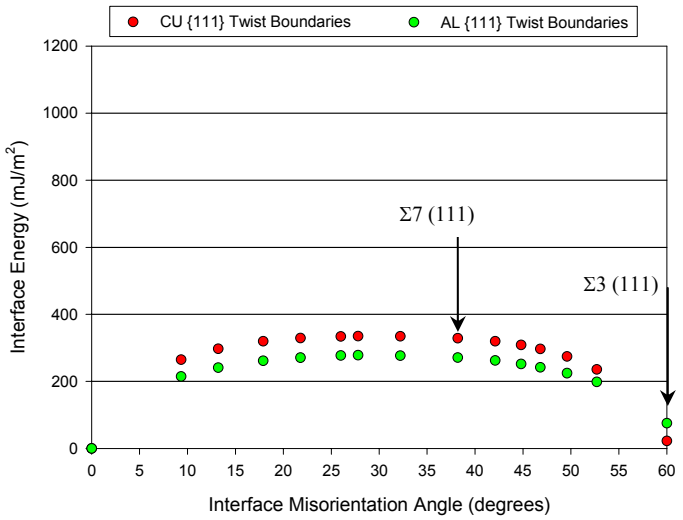

Figure III.10. Bicrystal interface energy for copper and aluminum twist [111] interface models.

Figure III.10 shows the bicrystal interface energy versus the interface misorientation angle for [111] twist boundaries in both copper and aluminum. The energy of the copper Σ3 (111) 60.0° interface is calculated as 22 mJ/m^2, while the energy of the aluminum Σ3 (111) 60.0° interface is calculated as 75 mJ/m^2. Both of these values are in agreement with the values report in Fig. III.9 for the Σ3 (111) boundaries. For both copper and aluminum, a cusp appears in the energy-misorientation angle relationship at the Σ3 (111) 60.0° interface, which correspond to the lowest-order CSL interface for this twist misorientation. However, note that a cusp does not occur at other low-order CSL interfaces, such as Σ7 or Σ13. Similar observations have been made previously in the literature for copper by Wolf (1989). In general, the interface energy for [111] twist boundaries is significantly lower than that for [001] or $[1\,\bar{1}0]$ tilt boundaries.

III.3.2 Interface Structure

Figure III.11 shows a detailed view of the Σ5, Σ13 and Σ17a interface structures in copper. Recall that each of these interfaces is created by a symmetric rotation around the [001] misorientation axis. The viewing direction is along the [001] crystallographic direction (Z-axis) and atom positions are projected into the X-Y plane for clarity. Snapshots of the atomic configurations at the interface are taken after the 0 K energy minimization procedure. Atoms are shaded by their respective {001} atomic plane in order to identify the interface structural units. In addition, the centrosymmetry parameter (Kelchner *et al*., 1998) is used to assist in the identification of the structural units, especially in cases where the interface structure is complex. The centrosymmetry parameter is a scalar measure designed to identify atoms in defect configurations.

The Σ5 (310) 36.9^{o} interface in Fig. III.11(a) is composed of C type structural units along the entire length of the interface. Similarly, the Σ5 (210) interface in Fig. III.11(b) is composed entirely of B' structural units. The B' structural unit is a slightly modified version of the B structural unit originally proposed by Sutton and Vitek (1983a) that is shown via molecular dynamics calculations to have a slightly lower energy in FCC materials (Bachurin *et al*., 2003). Bicrystal boundaries with non-favored misorientations are composed of two (or more) different types of structural units. For example, the structure of the Σ13 (510) boundary in Fig. III.11(c) is composed of one C unit and two D units per interface period, with the SUM notation |CDD|. The vertical 'bars' denote one period of the interface structure. Similarly, the Σ13 (320) boundary in Fig. III.11(d) is composed of two A units and two B' units per interface period, with the SUM notation |AB'.AB'|. Here, the 'dot' signifies that the structural unit has shifted from the {001}

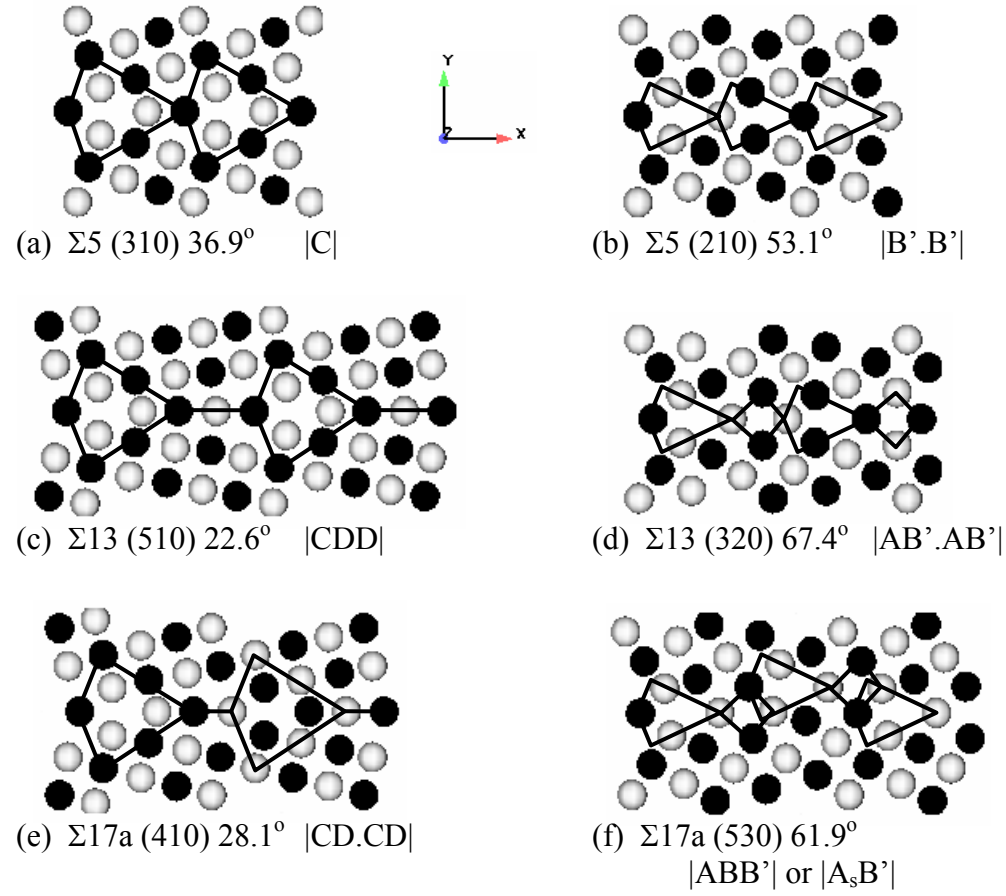

Figure III.11. Bicrystal interface structures for copper [001] interface models. The structural unit model notation is given.

lattice plane to the neighboring {002} plane. Sutton and Vitek (1983a) define this type of structure as being 'centered'.

The Σ17a (530) interface in Fig. III.11(f) shows a slightly different behavior. The minimum energy configuration of this boundary is not mirror symmetric about the interface plane, as in the case with the other low-order CSL boundaries in Fig. III.11. The energy of this boundary in copper is calculated as 856 mJ/m^2. Two possible representations are available to describe the interface structure: |ABB'| or $|A_sB'|$, the

latter of which is shown in Fig. III.11(f). The A_s structural unit includes a step or facet in the interface plane between B' structural units. For this boundary, the SUM is only loosely applicable because different variations of traditional structural units begin to appear, which are not associated with the favored boundaries. By using a different starting position (overlap value) in the energy minimization calculation, a mirror symmetric Σ17a (530) interface may be created. This interface has an |AB'B'| structure, which is in agreement with the theoretical prediction using the SUM. However, the energy of this interface is calculated as 906 mJ/m^2, which is higher than that of the faceted boundary. Thus, the structure for the Σ17a (530) interface shown in Fig. III.11(f) is considered the appropriate structure for this misorientation.

Figure III.12 shows a detailed view of the Σ3, Σ9, Σ11 and Σ17b interface structures in copper. Each of these interfaces is created by a symmetric rotation around the $[1\,\bar{1}0]$ misorientation axis. The viewing direction is along this same axis, which is aligned with the Z-direction. Similar to Fig. III.11, snapshots of the atomic configurations at the interface are taken after the 0 K energy minimization procedure. The structure of each interface is identified by shading atoms by their respective {110} atomic plane through the thickness of the interface model and by using the centrosymmetry parameter (Kelchner *et al*., 1998). The structural units outlined are based on those proposed in the literature by Rittner and Seidman (1996), who used an EAM potential for nickel for their energy minimization calculations.

Three of the boundaries presented in Fig. III.12 are considered favored in the structural unit model representation of interfaces. The Σ3 (111) 109.5^o coherent twin boundary in Fig. III.12(b) is composed entirely of D structural units with centered

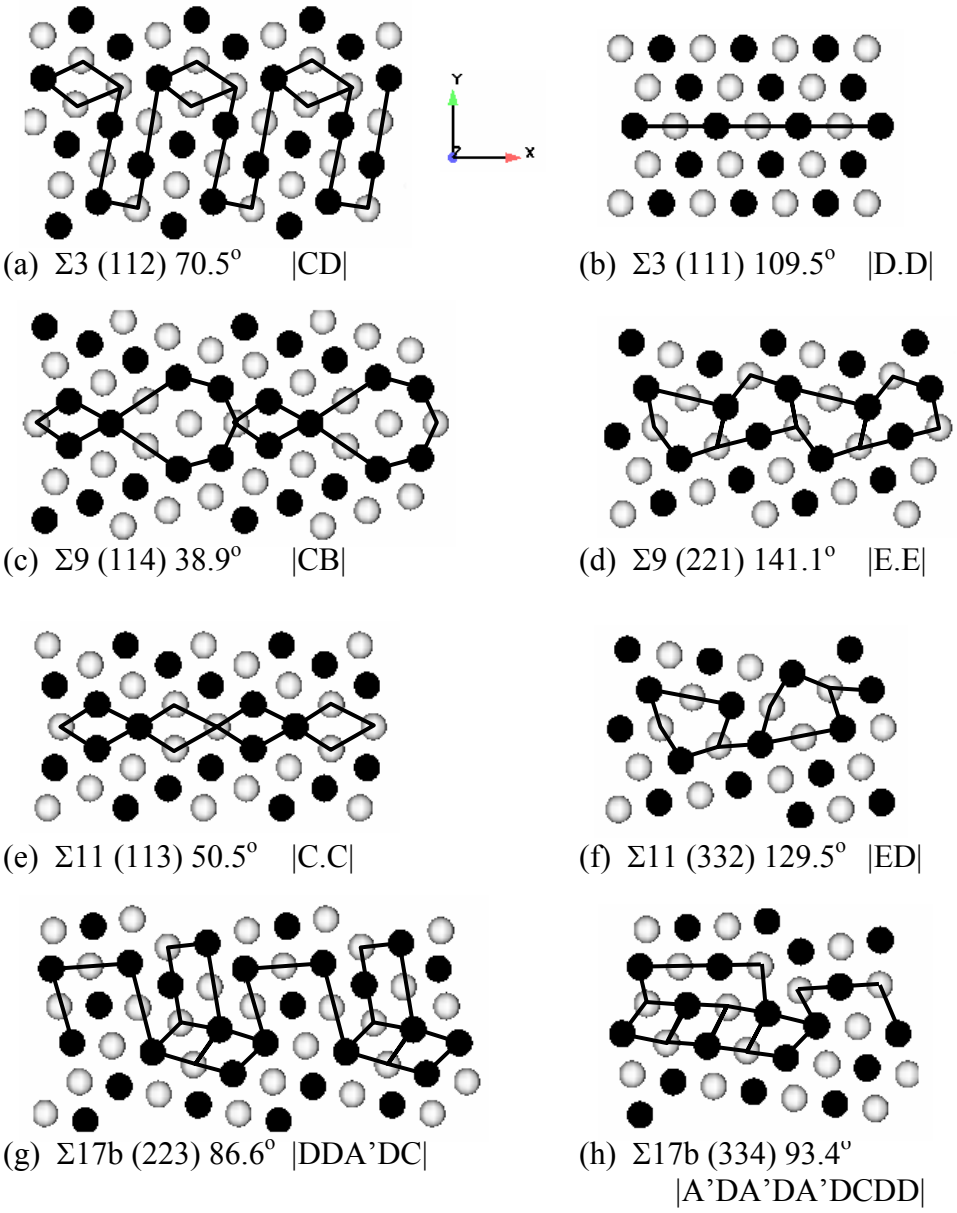

Figure III.12. Bicrystal interface structures for copper $[1\,\bar{1}0]$ interface models. The structural unit model notation is given.

interface structure. Similarly, the Σ11 (113) 50.5° and the Σ9 (221) 141.1° interfaces are composed entirely of C and E structural units, respectively. Recall from the introduction that the E structural unit has been correlated with the incidence of atomic shuffling during

a shear deformation (Sansoz and Molinari, 2004; 2005). Sansoz and Molinari proposed that the free volume inherent to this structural feature is responsible for triggering the atomic shuffling event.

In general, many of the bicrystal interface structures presented in Fig. III.12 can be characterized by the structural unit model, even though the interface structures are not all mirror symmetric about the interface plane. For example, the Σ9 (114) 38.9^{o} interface in Fig. III.12(c) contains one C and one B structural unit per interface period. Similarly, the Σ11 (332) 129.5^{o} interface is composed of one E and one D structural unit. However, three boundaries in Fig. III.12 show a dissociated interface structure. For example, the Σ3 (112) interface in Fig. III.12(a) is composed of both C and D type structural units. The C type structural unit is representative of the Σ11 (113) 50.5^{o} interface. The D type structural unit is associated with the Σ3 (111) 109.5^{o} twin boundary. This structural unit lies at the termination of an intrinsic stacking fault (ISF) that extends from the bicrystal interface. The delocalized structure occurs as a result of the asymmetric dissociation of secondary interface dislocations (Rittner *et al.*, 1996). The Σ17b interface structures in Fig. III.12 show a highly dissociated structure. Here, intrinsic stacking fault facets of various lengths and widths are formed during the energy minimization process. In addition, at least three structural units are identified using the centrosymmetry parameter, including the A structural unit, which should not exist for this misorientation according to the SUM. Thus, the structural unit model fails to characterize boundaries with dissociated structure because the SUM is unable to predict the length, width or spacing or delocalized structural units. However, images in Fig. III.12 and results in the literature

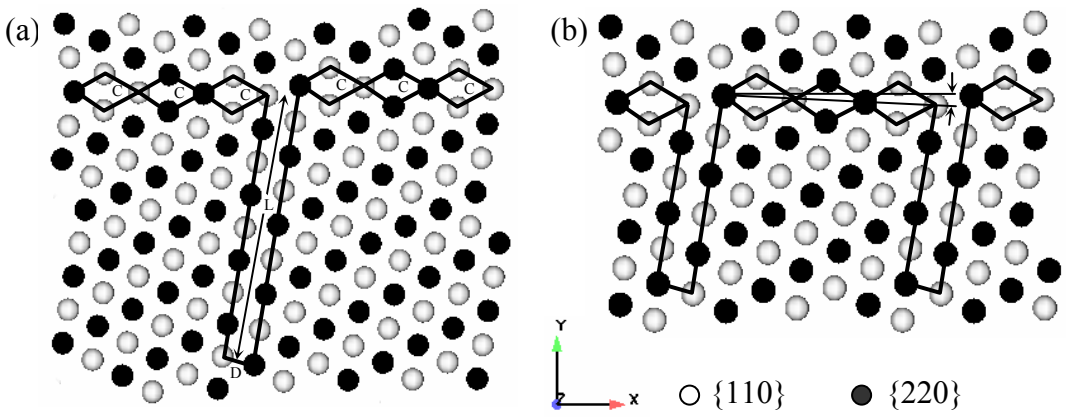

Figure III.13. Bicrystal interface structures for dissociated (a) 53.1° and (b) 59.0° copper $[1\bar{1}0]$ interface models.

(Rittner and Seidman, 1996) clearly show that even highly delocalized bicrystal interfaces can still be defined in terms of a repeating structure.

The observation of intrinsic stacking fault facets that extend from the interface plane is particularly intriguing, because these facets could potentially play a strong role in the deformation process (since they are in essence pre-nucleated partial edge dislocations). Figure III.13 shows a detailed view of the interface structures for 53.1° and 59.0° <110> misorientations in copper after energy minimization. Note that neither of these boundaries is considered favored in SUM notation. Figure III.13 provides additional evidence that ISF facets can be formed during the energy minimization procedure. As explained above, this occurs due to the asymmetric dissociation of secondary interface dislocations. The ISF facet occurs on the $(11\bar{1})$ slip plane in the lower lattice region in Figs. III.13(a) and III.13(b). Rittner and colleagues (Rittner and Seidman, 1996; Rittner *et al*., 1996) define the termination of each ISF facet as the D structural unit, which is associated with the Σ3 (111) 109.5° coherent twin interface. The remainder of the boundary is composed of C structural units, which are associated with

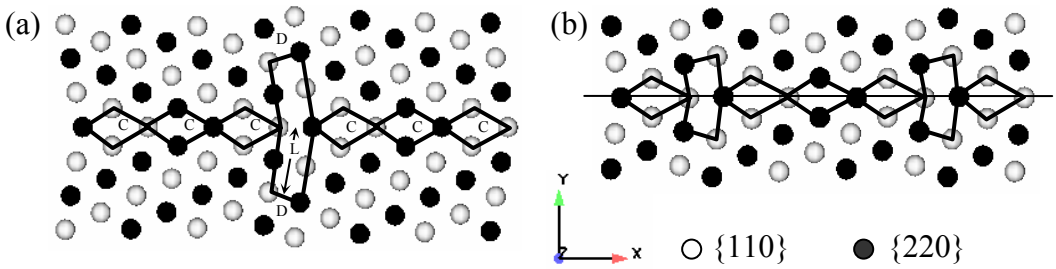

Figure III.14. Bicrystal interface structures for dissociated (a) 53.1° and (b) 59.0° aluminum [1 $\bar{1}$0] interface models.

the Σ11 (113) 50.5° favored interface (Fig. III.12). To accommodate the ISF facet, the C structural units are tilted downward relative to the positive X-axis, as shown in Fig. III.13(b). The spacing between ISF facets decreases as the misorientation angle of the interface is increased between 53.1° and 59.0°. Specifically, the 53.1° boundary has 11 C units for each dissociated D unit, while the 59.0° interface has only 3 C units for each dissociated D unit. The interface structures in Figs. III.13(a) and III.13(b) are in qualitative agreement with those presented by Rittner *et al*. (1996) for nickel.

Rittner and Seidman (1996) also showed that interface structures can vary significantly between materials with appreciably different ISF energies for the misorientation range between 0° and 50.5° around the <110> misorientation axis. Specifically, Rittner and Seidman showed that delocalized structural units do not occur in materials with high stacking fault energies. Each of the interface structures presented in their work showed a mirror symmetric interface configuration for the high ISF energy material. As a result, they concluded that the structural unit model representation of high-angle interfaces becomes more applicable for materials with high ISF energy.

Figures III.14(a) and III.14(b) show that the ISF facet that extends from the 53.1° or 59.0° interfaces is significantly shorter in aluminum, a material with higher stacking fault energy. Further, in aluminum the dissociation of secondary interface dislocations is mirror symmetric on opposing {111} slip planes. Specifically, the facet occurs on the $(11\bar{1})$ slip plane in the lower lattice region and on the (111) slip plane on the upper lattice region. Similar to copper, the termination of the ISF facet is identified as the D structural unit, with the remainder of the boundary composed of C structural units, as shown in Fig. III.14(a). The spacing between each dissociated facet decreases as the misorientation angle of the interface is increased over the range considered. The same ratio of C:D interface structural units occurs in both copper and aluminum. In aluminum, the C structural units are not distorted by the dissociation of secondary dislocations, i.e., the entire interface is mirror symmetric about the boundary plane, as shown in Fig. III.14(b).

Performing energy minimization calculations over the entire range of <001> and <110> boundaries using the Mishin *et al*. (1999) EAM potential for aluminum, Figs. III.15 and III.16 show the same low-order CSL bicrystal interface misorientations that are presented previously in Figs. III.11 and III.12. Specifically, Fig. III.15 shows a detailed view of the Σ5, Σ13 and Σ17a interface structures in aluminum. Coincidently, all of the aluminum interface structures presented in Fig. III.15 are identical to those presented in Fig. III.11. The higher stacking fault energy of aluminum does not appear to significantly affect the interface structures for the low-order CSL boundaries created around the <001> misorientation axis. As before, the Σ5 (310) interface is composed entirely of C structural units along the length of the interface. Similarly, the Σ5 (210)

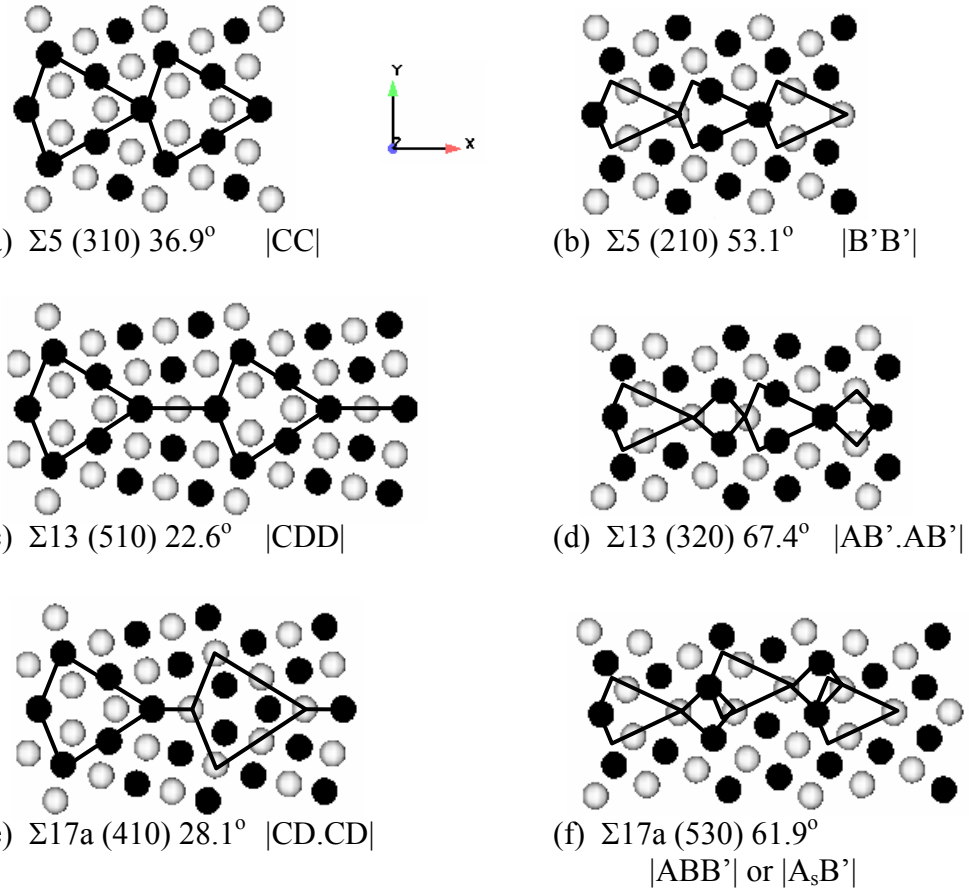

Figure III.15. Bicrystal interface structures for aluminum [001] interface models. The structural units and SUM notation are given.

interface is composed entirely of B' structural units. Of particular interest is the stepped Σ17 (530) interface in Fig. III.15(e). Identical to that in copper, this boundary does not have a mirror symmetric interface structure. Accordingly, two descriptions based on the interface structure are possible, |ABB'| or |A_sB'|. The energy of the Σ17a (530) boundary in aluminum shown in Fig. III.15(e) is calculated as 465 mJ/m^2. If a different starting position is used, resulting in a mirror symmetric Σ17a (530) interface with an |AB'B'|

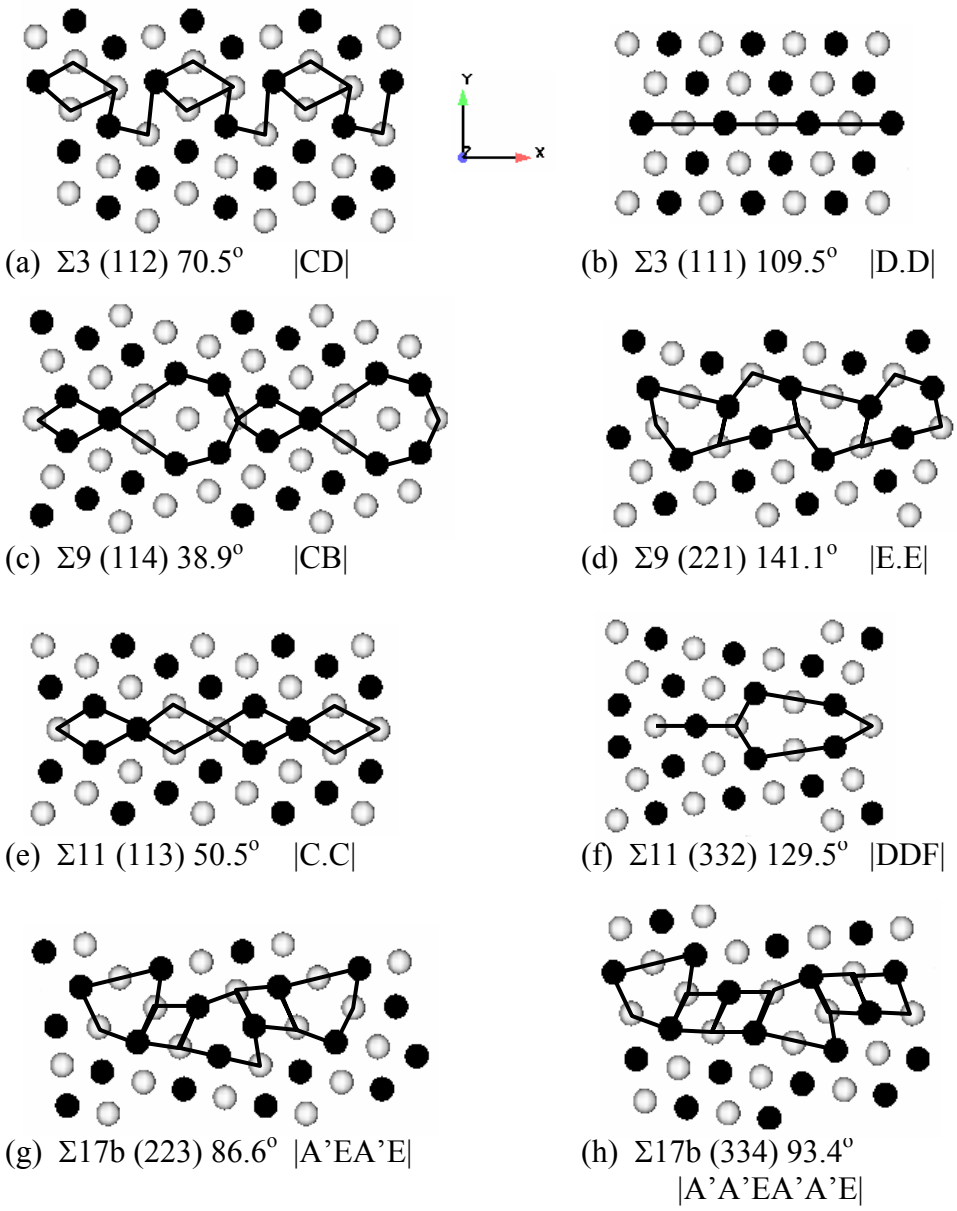

Figure III.16. Bicrystal interface structures and SUM notation for aluminum [$1\bar{1}0$] interface models.

structure, the interface energy is calculated as 493 mJ/m^2. Thus, the appropriate structure for this boundary is again the stepped interface because it has lower interface energy.

Figure III.16 shows a detailed view of the Σ3, Σ9, Σ11 and Σ17 interface structures in aluminum. Clearly, many of interface structures presented in aluminum in

Fig. III.16 are different than those in Fig. III.12. This is due to the difference in intrinsic stacking fault energies between copper and aluminum. It is unclear exactly why the ISF energy affects the interface structure more severely for the $[1\bar{1}0]$ misorientation axis than for the [001] misorientation axis; however, it likely has to do with the orientation of the interface with respect to the favored slip systems. The favored boundaries in Fig. III.16, Σ3 (111), Σ9 (221) and Σ11 (113), are identical to those presented for copper. For example, the Σ11 (113) interface is composed of C type structural units along the entire length of the interface. Similarly, the Σ3 (111) interface is composed entirely of D structural units.

Four of the interface structures presented in Fig. III.16 are remarkably different than those for the same interface misorientation in copper: Σ3 (112), Σ17b (223), Σ17b (334) and Σ11 (332). In agreement with copper, the aluminum Σ3 (112) interface in Fig. III.16(a) shows that short stacking fault facets are nucleated between C structural units. However, the length of each of the ISF facets is much shorter in aluminum than in copper, which is in agreement with the results shown in Fig. III.13. For both of the Σ17b interface misorientations, the stacking faults that are prominent in copper do not appear in aluminum. Instead, the E structural unit is observed, separated by different numbers of A' structural units depending on the misorientation angle. This result is surprising since in copper the E structural unit does not appear until the misorientation angle of the interface is increased beyond 109.5^{o}. Again, the SUM fails to describe this situation, as the structural units change discontinuously over the misorientation range. The structure of each of the Σ17b interfaces is remarkably similar to the Σ11 (332) interface in copper (Fig. III.12(f)), the primary different being that the 'connection' between E units is made

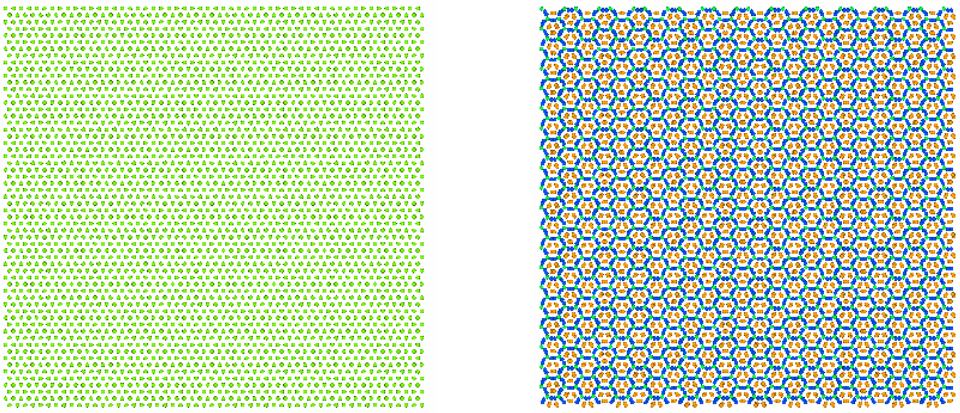

(a) Σ3 (111) 60.0° (b) Σ7 (111) 38.2°

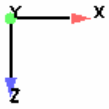

Figure III.17. Bicrystal interface structures for copper [111] twist terface models. Atoms are colored by the centrosymmetry parameter.

via the A' unit instead of the D structural unit. For the Σ11 (332) interface in aluminum, a new structural unit is identified, which has been labeled as F. The structure of this interface is mirror symmetry about the boundary plane with a calculated energy of 499 mJ/m^2. While the mirror symmetric interface structure appears to be inappropriate as compared with the primarily asymmetric interface structures presented for other misorientations in Fig. III.16, the energy of an asymmetric boundary composed of E and D structural units (similar to that in copper) would have an energy of 516 mJ/m^2. Thus, the identification of the previously undefined structural unit is warranted.

Figures III.17(a) and III.17(b) show a detailed view of the Σ3 and Σ7 interface structures in copper, respectively. Recall that both of these interfaces is created by a symmetric twist rotation around the [111] misorientation axis. The viewing direction is along the [111] crystallographic direction (Y-axis) and atom positions are projected into the X-Z plane for clarity. Snapshots of the atomic configurations at the interface are

taken after the 0 K energy minimization procedure. Atoms are colored by the centrosymmetry parameter (Kelchner *et al*., 1998), while atoms that are in a perfect FCC environment are removed in order to identify the interface structure. For twist interfaces, the identification of structural units along the interface plane is more complicated than for tilt interfaces; thus, no attempt is made to classify the individual structure features of the interface, as is presented in Figs. III.11 – III.16.

For the Σ3 (111) 60.0^{o} interface in Fig. III.17(a), the centrosymmetry parameter identifies a single {111} atomic layer at the interface as being in a distorted environment. In general, the twist Σ3 interface structure is identical to the Σ3 coherent twin interface presented in Fig. III.12(b). On the other hand, for the Σ7 (111) 38.2^{o} interface in Fig. III.17(b), the centrosymmetry parameter identifies several atomic layers at the boundary. Here, the [111] twist misorientation creates a three-dimensional pattern of atoms with varying degrees of local distortion. Similar three-dimensional patterns of distortion are observed for each of the twist interfaces examined in this work. Recall that pure twist boundaries may be represented as a network of screw dislocations along the interface plane (Hirth and Lothe, 1982).

Finally, the interface structures that are presented in Figs. III.11 through III.16 are verified against high resolution transmission electron microscope (HRTEM) images or electronic structure (first-principles) calculations results in the literature. Unfortunately, a very small number of the boundaries in this work have been characterized using HRTEM. Regardless, Fig. III.18 shows several HRTEM images for bicrystal boundaries in copper and aluminum as compared with molecular statics calculations in this work. Four boundaries are examined based on the available results in the literature: the Σ5

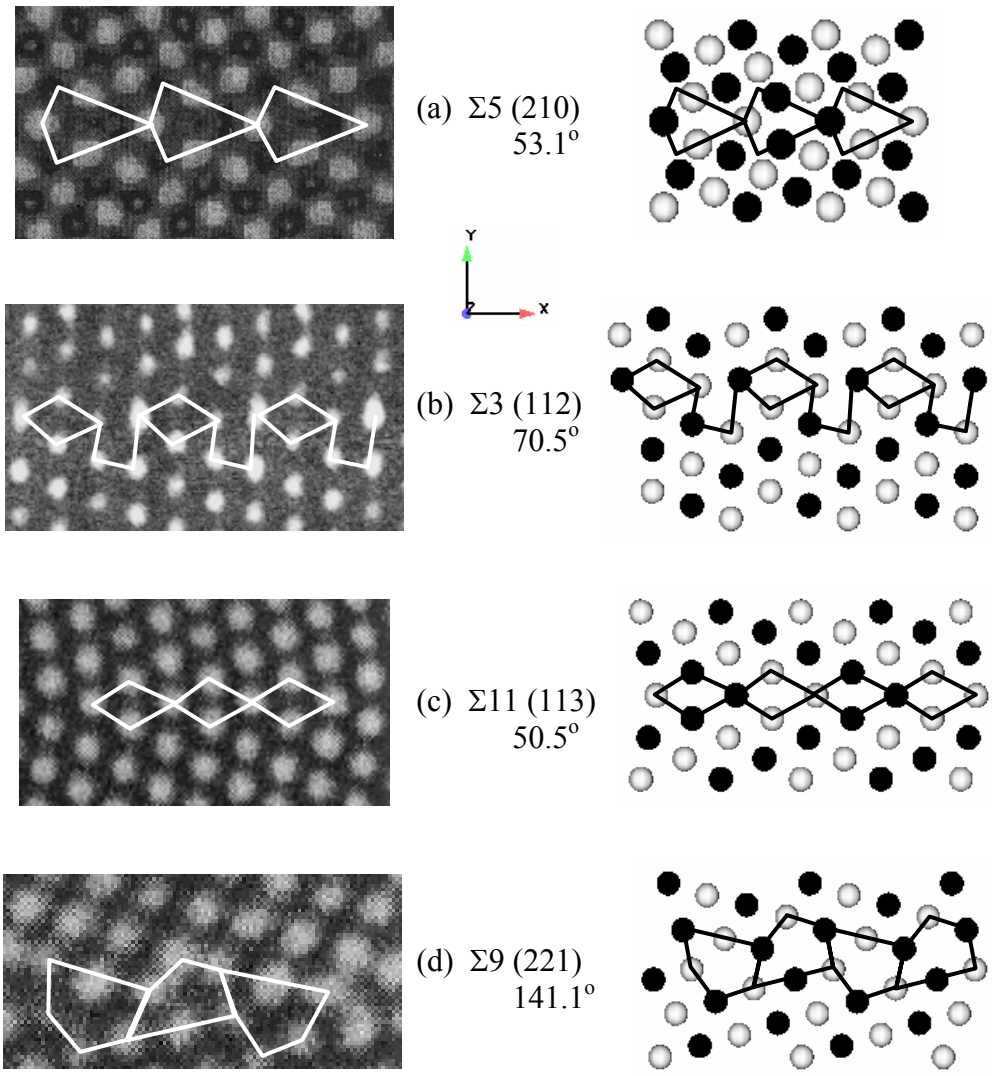

Figure III.18. Comparison of predicted bicrystal interface structures using energy minimization and HRTEM images for a selection of interface misorientations in copper and aluminum.

(210) interface in copper (Grigoriadis *et al*., 1999), the Σ3 (112) interface in aluminum (Medlin *et al*., 1993), the Σ11 (113) interface in aluminum (Mills *et al*., 1992) and the Σ9 (221) interface in aluminum (Mills *et al*., 1992). Clearly, the interface structures predicted in this work using molecular statics calculations are in agreement with the reported HRTEM images.

It must be reemphasized that the boundary conditions used during the energy minimization procedure are extremely critical to the success of these calculations. Additional calculations are performed (although not shown in this work) where the boundaries in the +/- Y-direction are held fixed, i.e., the simulation cell boundaries are not allowed to translate parallel or perpendicular to the interface plane during the energy minimization. These boundary conditions suppress any lattice expansion or rigid body translation that may occur between crystal regions during the energy minimization procedure. As a result, mirror symmetric interface structures are predicted for nearly all misorientations examined with these boundary conditions. This is clearly inappropriate based on the evidence presented in Fig. III.18. The boundary planes must be allowed to translate both parallel and perpendicular to the interface plane during the energy minimization procedure in order to produce accurate interface structures.

CHAPTER IV

DISLOCATION NUCLEATION FROM BICRYSTAL INTERFACES

IV.1 Introduction

The last decade has witnessed considerable progress towards understanding the atomic scale mechanisms associated with inelastic deformation in nanocrystalline metals. A substantial contribution has come from the computational materials science community through the use of atomistic simulations. As discussed in Chapter II, Atomistic simulation is an effective tool to monitor nanoscale mechanisms in a range of material systems. In particular, atomistic simulation has been used to model the nucleation of partial dislocations from interfaces in face-centered cubic (FCC) metals using bicrystal (Sansoz and Molinari, 2004; 2005) and nanocrystalline geometries (Yamakov *et al*., 2001; 2002; 2003; Van Swygenhoven *et al*., 1998; 1999a; 2001; 2002; 2004; Derlet *et al*. 2002; 2003). The work of Sansoz and Molinari (2004; 2005), which was discussed early in this thesis, represented a significant advancement because they were able to correlate individual failure mechanisms to the presence of a certain structural unit. Specifically, atomic shuffling occurred during a shear deformation only for interfaces that contained the E structural unit, which is associated with the Σ9 (221) interface (recall Fig. III.11). Results in the literature typically do not provide such detailed information regarding the role of individual interface features in the deformation process. MD calculations of inelastic deformation in nanocrystalline FCC metals have shown that once the grain size is reduced below approximately 10 nm, the deformation is dominated by grain boundary

processes, such as atomic migration or grain boundary sliding. For grain sizes above approximately 10 nm, the deformation of nanocrystalline metals is a result of both atomic scale grain boundary processes and dislocation activity within the grains. In these samples, the grain boundaries serve as sources for dislocation nucleation.

Recently, there has been some debate in the literature regarding the existence of full dislocations in nanocrystalline grains during the deformation process. Initial work by Van Swygenhoven and coworkers (1999a; 2001) in nanocrystalline pure nickel and copper with a grain size of approximately 12 nm showed that the leading (first) partial dislocation could be emitted from a grain boundary. In their work, the first partial dislocation would sweep across the nanosize grain and become absorbed into the opposing interface. The trailing (second) partial dislocation was not emitted from the grain boundary; as a result, an extended intrinsic stacking fault (which was typically longer than the equilibrium spacing between partial dislocations) remained within the grain. Through detailed analysis of the grain boundary structure (Van Swygenhoven *et al*., 1999a; 2002; Derlet *et al*., 2003) the nucleation of the first partial dislocation in nanocrystalline metals was shown to be assisted by local atomic shuffling within the interface and stress-assisted free volume migration. Van Swygenhoven and coworkers suggested that the nucleation of the first partial dislocation and the associated atomic rearrangement along the interface was sufficient to lower the grain boundary energy such that the emission of the second partial dislocation was unnecessary.

MD simulations by Yamakov *et al*. (2001; 2002; 2003) showed that the trailing partial dislocation may be emitted from grain boundary interfaces in aluminum. Aluminum was chosen for their simulations with the hypothesis that the higher intrinsic

stacking fault energy (as compared with copper and nickel), which leads to a shorter stacking fault width, would facilitate the emission of the second partial dislocation. Yamakov *et al.* used a columnar microstructure with a thickness of only 10 $(1\bar{1}0)$ atomic planes in order to simulate larger nanoscale grain sizes. They identified the stacking fault width as a critical length scale parameter necessary to describe the cross-over between extended partial dislocation and full dislocation deformation regimes in nanocrystalline metals. However, more recent work by Van Swygenhoven and coworkers (Van Swygenhoven *et al*., 2004; Froseth *et al*., 2004) has argued that interpreting the cross-over between deformation regimes in terms of only the intrinsic stacking fault energy is insufficient. They emphasized that the entire generalized stacking fault curve (Zimmerman *et al*., 2000) must be taken into consideration and proposed that the ratio of the unstable and intrinsic stacking fault energies is more appropriate to describe the observed dislocation activity in nanocrystalline samples. If this ratio is close to unity, full dislocations are anticipated during the deformation process; conversely, if this ratio is high, extended partial dislocations are expected within the nanocrystalline grains.

In this chapter, the atomic scale mechanisms associated with dislocation nucleation from tilt interfaces in aluminum and copper are studied using molecular dynamics simulations. Whereas most previous MD work has used 2D and 3D nanocrystalline geometries, work in this thesis examines the nucleation of full dislocation loops from well-defined high-angle interfaces using a bicrystal configuration. Calculations are performed on two distinct sets of interfaces. First, a $\Sigma 5$ (310) 36.9^{o} interface and two interfaces with misorientations close to the $\Sigma 5$ (310) interface are examined in aluminum. Energy minimization calculations show that these boundaries

have a mirror symmetric interface structure. Second, three interfaces with dissociated structure (recall Chapter III) in copper are examined to evaluate the role of the dissociated structural unit on the inelastic deformation process. After an isobaric-isothermal equilibration procedure, molecular dynamics simulations are used to deform the interface models in uniaxial tension at a constant strain rate. The primary goal of this work is to map the evolution of the interface structure during the dislocation nucleation process. We do not consider absorption of partial dislocations into an interface or dislocation-dislocation interactions after multiple nucleation events. Molecular dynamics calculations will show how the dislocation emission process irreversibly alters the interface structure.

IV.2 Partial Dislocations in FCC metals

It is well accepted that inelastic deformation in crystalline metals is predominantly due to the nucleation, motion and interaction of dislocations (Hirth and Lothe, 1982; Hull and Bacon, 2001). Consequently, material properties are strongly dependent on the ease at which dislocations are formed under an externally applied stress. Before introducing the boundary conditions and the results for the molecular dynamics simulations in this chapter, a brief review of dislocation structures in face-centered cubic (FCC) metals is useful for the reader to fully appreciate the significance of the dislocation nucleation mechanisms observed in this work. More complete reviews of the theory of dislocations can be found in texts by Hirth and Lothe (1982) and Hull and Bacon (2001).

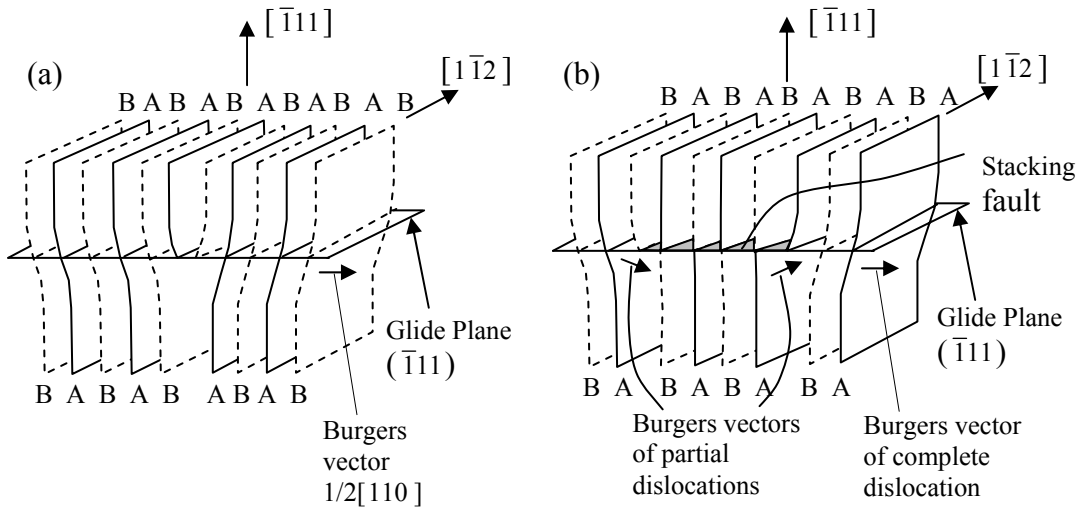

Figure IV.1. Schematic representation of (a) a perfect dislocation and (b) Shockley partial dislocations in a FCC lattice. Reproduced from Hull and Bacon (2001).

Dislocation motion (commonly termed as 'slip') in FCC systems, occurs on the {111} family of crystallographic planes in the <110> family of directions. An example of the slip process has been seen previously in Chapter III with the nucleation of partial dislocations resulting in dissociated interface structures in low intrinsic stacking fault energy materials. In a perfect crystalline lattice, a FCC metal incorporates a two-fold ABAB stacking sequence in the <110> directions and a three-fold ABCABC stacking sequence in the <111> directions. Conceptually, the 'perfect' edge dislocation is depicted in Fig. IV.1(a). This dislocation involves the addition (or removal) of two atomic half-planes perpendicular to the {111} slip plane. The stacking sequence is maintained in both <111> and <110> directions except at the dislocation core, where the two extra planes of atoms terminate.

However, perfect dislocations in FCC metals are rarely observed as shown in Fig. IV.1(a). Commonly, it is energetically favorable for the perfect dislocation to split into

two halves, which are known as Shockley partial dislocations, as shown in Fig. IV.1(b). The resulting structure includes an intrinsic stacking fault, which lies between the two partial dislocations where the stacking sequence of the lattice is distorted. For FCC structures, the stacking fault occurs between two {111} planes and alters the stacking sequence in the <111> directions from three-fold ABCABC symmetry to non-symmetric ABCBCA, for example. The FCC lattice is shifted into a hexagonal close-packed (HCP) stacking sequence across the stacking fault. The resulting structure has a higher energy than that of the perfect lattice with three-fold symmetry. This energy is common termed the intrinsic stacking fault energy, as previously discussed in Chapter II.

Recall that in Chapter II, the Mishin *et al*. EAM interatomic potentials for aluminum (1999) and copper (2001) were chosen because they were capable of accurately modeling the intrinsic and unstable stacking fault energies as compared with that which is measured experimentally or derived using electronic structure (*ab initio*) calculations. Thus, in the molecular dynamics calculations presented in this section, it is expected that the nucleation mechanisms, the dislocation structures (separation distance between partials of both edge and screw type) and nucleation stress levels will all be accurate for the interface misorientations considered.

IV.3 Bicrystal Interface Model Boundary Conditions

In this thesis, bicrystal interface models are developed using a combination of molecular statics (mechanics) and molecular dynamics simulations. An example interface model for the calculations performed in this chapter is shown in Fig. IV.2. The

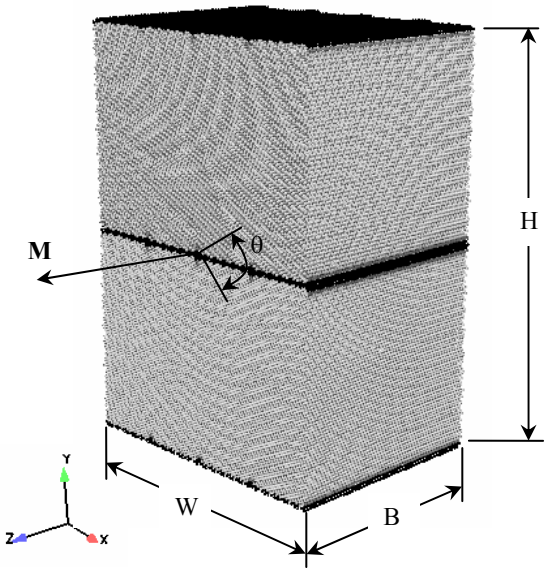

Figure IV.2. Bicrystal interface model examined in this thesis. The interface is created by a symmetric tilt rotation of opposing lattice regions around a specific misorientation axis.

interface misorientation is created by a symmetric rotation, θ, of opposing lattice regions around a misorientation axis, **M**. Table IV.1 summarizes the interface misorientations examined in this chapter. Two sets of calculations are performed. In the first set, calculations are focused around the Σ5 (310) 36.9^{o} boundary in aluminum, which has a high density of coincident atomic sites across the interface plane (Sutton and Vitek, 1983a). Two other interface misorientations are chosen, 33.4^{o} and 41.1^{o}, to study the behavior of tilt boundaries which are close but not exactly at a CSL boundary. These boundaries are considered to have a more general interface structure. In the second set of calculations, the role of the dissociated structural unit (recall Chapter III) during the inelastic deformation process is evaluated. Three interface misorientations are studied, 53.1^{o}, 54.4^{o} and 59.0^{o}. Energy minimization calculations in Chapter III showed that

Table IV.1. Bicrystal interface misorientations examined in this chapter.

Interface Misorientation	CSL Σ Notation		Structural Unit Representation	Size X,Y,Z (nm)	Number of atoms
Aluminum					
33.4°	109	{10 3 0}	|CCCD.CCCD|	25.4, 25.4,16.2	622,080
36.9°	5	{3 1 0}	|C.C|	28.2, 20.5, 16.2	559,680
41.1°	73	{8 3 0}	|CCB'.CCB'|	24.2, 20.7, 16.2	486,080
Copper					
53.1°	361	{6 6 17}	|CCCCCCCCCCCD|	19.3, 27.5, 14.3	641,984
54.4°	153	{4 4 11}	|CCCCCCCD|	25.3, 17.9, 14.3	542,080
59.0°	33	{2 2 5}	|CCCD|	20.6, 20.8, 14.3	512,736

boundaries with misorientations that lie within this range have a dissociated structure. Here, each boundary has a different spacing between ISF facets (i.e., a different number of C structural units as shown in Table IV.1). Calculations in this work will investigate how this spacing influences the nucleation of interface dislocations.

The interface model dimensions and number of atoms are also presented in Table IV.1. For all calculations, periodic boundary conditions are used in all directions (X, Y and Z); thus, the bicrystal interface model dimensions are defined accordingly to properly enforce this boundary prescription. For the calculations that focus on the Σ5 interface, the minimum dimension (Z-direction) of the interface model includes 80 (001) atomic planes. For calculations designed to study dissociated interfaces, the thickness of each interface model is taken as B=39.59λ, where λ is the lattice constant defined from the interatomic potential as 3.615 Å for copper (Mishin *et al*., 2001). The thickness of the interface model includes 112 atomic planes in the Z-direction. The chosen model dimensions in the Z-direction are presumed to be sufficient to not affect the 3D dynamics of dislocation nucleation. MD calculations of deformation in single crystals (with same

sample size) confirm this assumption as dislocation loops are nucleated on the favorable slip systems according to a Schmid factor analysis. Further, the thickness of the interface model is doubled (while maintaining the same X and Y dimensions) for one set of tensile deformation calculations with the 53.1^{o} boundary at 10 K. Although not explicitly shown in this thesis, results are essentially identical with regard to dislocation patterning and nucleation stress.

The use of periodic boundary conditions in the Y-direction introduces a second interface into the model, which in turn gives rise to forces on dislocations. The stress field for a symmetric tilt boundary, such as that studied in this work, decreases exponentially away from the interface (Hirth and Lothe, 1982). The spacing between interfaces, H/2, is sufficiently large to minimize effects on nucleation of the first dislocation. However, as these calculations will show, the nucleation of dislocations causes distortion in the interface structure. This is particularly true in the case of disassociated interface, where partial dislocation emission is inherent to the interface structure. If the interface distortion is idealized as a single dislocation positioned at the nucleation point (Hurtado *et al*., 1995), the magnitude of the shear stress on the active slip planes due to the distorted boundary at a distance H/2 away from the interface is less than 8% of the ideal shear strength in aluminum derived from first-principles calculations (Ogata *et al*., 2002). Accordingly, we consider the dimensions of the periodic model suitable for the study of dislocation nucleation phenomena at early stages.

After the minimum energy configuration is attained, the interface model is equilibrated using molecular dynamics in the isobaric-isothermal ensemble at a pressure of 0 bar and a temperature of either 10 K or 300 K. The nucleation of dislocations at both

temperatures is examined in Section IV.3. In this work, the Melchionna *et al.* (1993) equations of motion for the NPT ensemble govern the dynamics of the system. Upon completion of the equilibration process, molecular dynamics calculations are used to deform each interface model in uniaxial tension, which is applied in the Y-direction normal to the interface plane (recall Fig. IV.1). The mixed set of boundary conditions, introduced in Chapter II, is used for these calculations. A constant strain rate of $1x10^9$ s^{-1} is introduced by decoupling the vector that describes the dimensions of the periodic cell from the equations of motion in the Y-direction and extending the length of this vector during the simulation. Essentially, the rate of change of the periodic cell length, $\dot{\mathbf{h}}$, is prescribed in the Y-direction in accordance with a desired strain rate. The motions of the boundaries in the X- and Z-directions are calculated from the current and prescribed system stresses using the Melchionna *et al*. (1993) equations of motion. For all simulations in this chapter, the X- and Z-direction boundaries are specified as stress-free. Simulations of tensile deformation are carried out at temperatures of 10 K and 300 K.

IV.4 Nucleation of Interface Dislocations

IV.4.1 [001] Boundaries in Aluminum

Molecular dynamics simulations are used to study the process of dislocation nucleation from bicrystal interfaces. Figure IV.3 shows the uniaxial tensile deformation of the Σ5 (310) 36.9^o interface model in aluminum at 10 K. Figures IV.3(a)-(d) are colored according to the centrosymmetry parameter (Kelchner *et al*., 1998), which is a scalar quantity designed to identify defects such as interfaces, dislocations and stacking

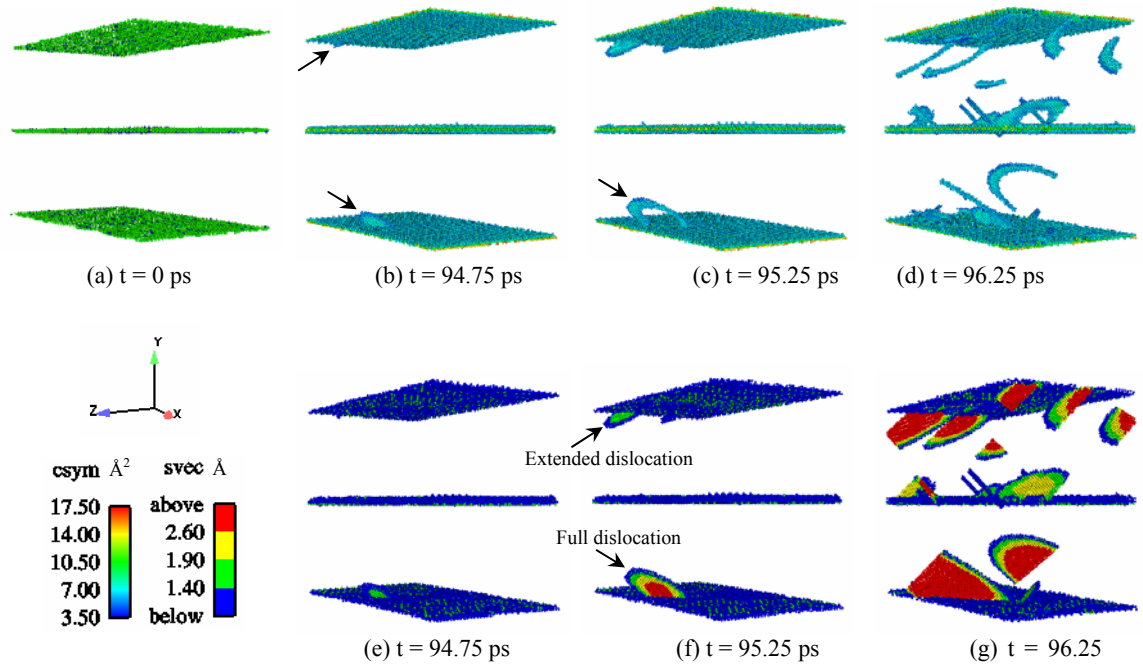

Figure IV.3. Nucleation of full dislocation loops during uniaxial tension of the Σ5 (310) 36.9° interface model at 10 K; (a)-(d) atoms are colored by the centrosymmetry parameter and (e)-(g) atoms are colored by the atomic slip vector.

faults. In Figs. IV.3(a)-(d), atoms with a centrosymmetry parameter close to zero are removed to facilitate viewing of the defect structures. Figures IV.3(e)-(g) show atomic positions at the same time step as Figs. IV.3(b)-(d); however, atoms are colored by the magnitude of the atomic slip vector (Zimmerman *et al.*, 2001). The atomic slip vector will identify atoms that have been displaced relative to their reference neighbors, even if they reside in a perfect FCC environment. This includes both stacking fault (partial slip) regions and regions of full slip. In this work, the atomic slip vector is calculated using the isobaric-isothermal equilibrium positions of the atoms as the reference configuration.

In Figs. IV.3(b)-(d), full dislocation loops are clearly nucleated from the bicrystal interface during tensile deformation. Initially, partial dislocations are nucleated from the

interface, indicated by arrows in Fig. IV.3(b). In the lower lattice region, slip occurs on the $(111)[\bar{1}01]$ and $(11\bar{1})[101]$ slip systems, which are the most favorable slip systems according to a Schmid factor analysis. Likewise, the most favorable slip systems are activated in the upper lattice region. The tensile stress required to nucleate the first partial dislocation at 10 K from the Σ5 (310) boundary is calculated as 5.74 GPa. For the given orientation, this corresponds to a critical resolved shear stress of approximately 2.81 GPa, which is comparable to the ideal shear strength of aluminum obtained from first-principles calculations of 2.84 GPa (Ogata *et al*., 2002). Thus, our calculations appear to give reasonable values for the nucleation stress. It is noted that Ogata *et al*. also showed that other stress components influence the calculated value of the critical shear stress.

In Fig. IV.3(c), the leading partial dislocations have moved further away from the interface, leaving behind an intrinsic stacking fault. The trailing partial dislocation has been emitted for the defect marked with an arrow, resulting in a dislocation loop. As deformation proceeds, several dislocation loops are emitted from each interface in Fig. IV.3(d). At this point, dislocations have been passed through the periodic boundaries and dislocation interaction effects become important. In Figs. IV.3(c) and IV.3(d), the width of the stacking fault ribbon of the dislocation loops appears to be greater in one direction than the other. The thicker direction corresponds to the edge component of the dislocation loop. Byun (2003) showed that at equilibrium, the stacking fault widths of edge and screw dislocations will differ, even though the intrinsic stacking fault energy is the same. Byun reported that the equilibrium intrinsic stacking fault width of an edge dislocation is approximately twice that of a screw dislocation. However, the intrinsic

stacking fault width can depend on applied stresses, particularly in materials with low intrinsic stacking fault energies. Byun (2003) showed that as the intrinsic stacking fault energy is increased to 100 mJ/m^2, the influence of applied stresses on the partial dislocation spacing becomes minimal. In this work, the intrinsic stacking fault energy of aluminum predicted by the interatomic potential is 146 mJ/m^2; thus, the separation distance between partial dislocations is not expected to vary far from the equilibrium spacing. Figure IV.3(d) shows that our calculations are in agreement with this result.

In Figs. IV.3(e)-(g), atoms with an atomic slip vector magnitude less than half of the Burgers vector for a partial dislocation, $\lambda/\sqrt{6}$, are removed for clarity. Dislocations at two distinct points during the nucleation process are identified in Fig. IV.3(f). The dislocation within the upper lattice region shows an extended formation, as the trailing partial dislocation has not yet been emitted from the interface. Atoms that are shaded green have an atomic slip vector magnitude that ranges between 1.5 and 1.8 Å, which encompasses the theoretical value for partial slip of 1.65 Å for aluminum. The dislocation within the lower lattice region has emitted the trailing partial dislocation and has formed a dislocation loop. Full slip has occurred in the wake of the trailing partial dislocation as atoms that are shaded red have an atomic slip vector magnitude between 2.8 and 3.0 Å, which again encompasses the theoretical value of 2.86 Å. In Figs. IV.3(f) and IV.3(g), atoms that are shaded blue and yellow indicate transitions between perfect lattice, intrinsic stacking fault and full slip regions, i.e., the positions of the leading and trailing partial dislocations.

The structure of the Σ5 (310) 36.9^o interface at two critical points during the dislocation nucleation process is shown in Fig. IV.4. Here, six {001} atomic planes are

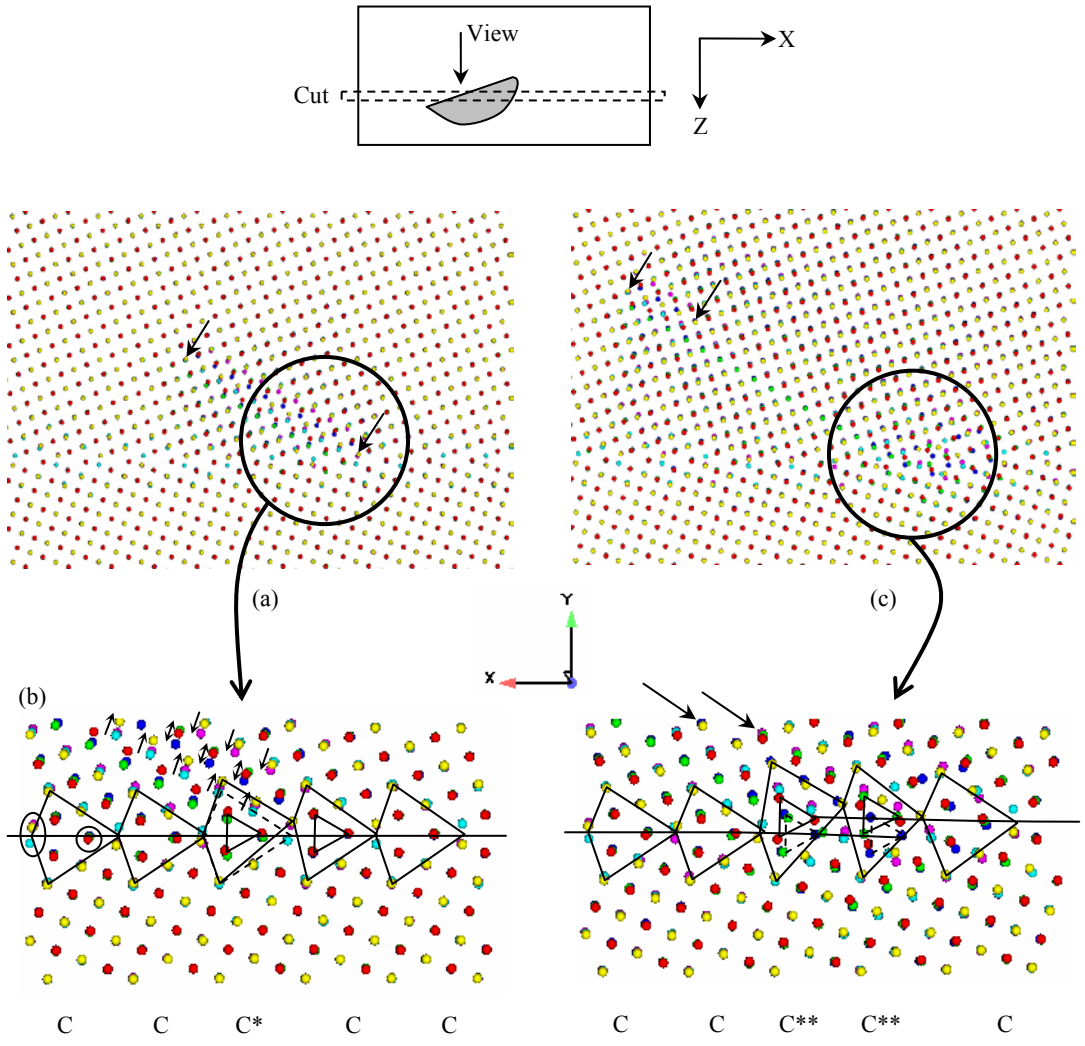

Figure IV.4. Detailed view of the interface structure of the Σ5 (310) 36.9° boundary during dislocation emission at 10 K. Atoms are colored by their respective atomic {001} plane through the thickness of the interface model.

cut from the thickness of the interface model *through* the dislocation loop identified in Fig. IV.3(c) to illustrate the dislocation nucleation process. This dislocation loops lies in the $(11\bar{1})[101]$ slip system. Atoms are colored by their respective {001} plane and projected into the X-Y plane. For reference, recall the original structure of the Σ5 (310) 36.9° interface in Chapter III. Prior to dislocation nucleation, this boundary has an

ABAB stacking sequence in the Z-direction. In Fig. IV.4(a), only the first partial dislocation has been emitted from the interface. This is clearly identified by a shift in the atomic layers at the point of dislocation nucleation. Atoms that once aligned perfectly in an ABAB stacking sequence have been displaced relative to one another. The length of the extended partial dislocation at this time step is approximately 31.6 Å (which is longer than the equilibrium partial dislocation spacing in aluminum) and is shown with arrows in Fig. IV.4(a). Figure IV.4(b) shows a detailed view of the dislocation nucleation point. First, notice that interface expansion during the uniaxial deformation allows some atoms to migrate in the direction of the load. However, the atom that is coincident between lattice regions remains stationary. The dislocation slip process involves atoms that were originally identified as belonging to the structural units. One of the structural units (in the second layer of atoms) is irreversibly deformed as a result of the partial dislocation slip, labeled as C*. The C structural units surrounding this defect unit appear to be only slightly modified to accommodate the slip process. The centerline of the interface is shown in Fig. IV.4(b). Even though the structural units are being deformed by the slip process, the interface still remains planar after the emission of the first partial dislocation.

As deformation continues in Fig. IV.4(c), the second partial dislocation is emitted from the interface, creating a dislocation loop. The loop itself is not visible in this view; however, it is clear that the second partial has been emitted because the atomic layers associated with full slip have aligned on top of each other. The positions of the leading and trailing partial dislocations are marked with arrows in Fig. IV.4(c) with a separation of approximately 10.8 Å. Figure IV.4(d) shows a detailed view of the interface after the emission of the trailing partial dislocation. Two deformed structural units are identified

along the interface plane, labeled as C**. The C** deformed unit appears only after the emission of the second partial dislocation and involves a small step or ledge within the interface plane. The shape of the C** unit is similar to that of the C* structural unit; however, additional slip from the trailing partial dislocation has further amplified the asymmetric expansion. The ledge has a peak magnitude in the Y-direction of approximately 1.8 Å and appears to be irreversible, because it involves atoms that are associated with the full slip event. The remainder of the interface accommodates the development of this ledge by smoothly shifting in opposite directions on either side of the dislocation nucleation point, as shown in Fig. IV.4(d). For the C** structural unit shown on the left in Fig. IV.4(d), the ledge occurs between the first and third atomic layers; in contrast, the ledge occurs between the third and fifth atomic layers for the C** structural unit shown on the right. This indicates that the ledge exists within the interface plane at an angle to the viewing direction. Specifically, the ledge occurs at the intersection of the slip plane and the interface. The angle depends on to the orientation of the slip plane relative to the misorientation axis.

Figure IV.5 shows the nucleation of dislocations from the 33.4^{o} and 41.1^{o} aluminum boundaries at 10 K. In Figs. IV.5(a) and IV.5(c), atoms are colored by the centrosymmetry parameter. Clearly, full dislocation loops are nucleated for both misorientations. The tensile stress required to nucleate the first partial dislocation at 10 K from the 33.4^{o} and 41.1^{o} boundaries is calculated as 5.92 and 5.46 GPa, respectively. These tensile stress magnitudes correspond to critical resolved shear stresses of approximately 2.88 and 2.69 GPa, respectively. Figures IV.5(b) and IV.5(d) show a detailed view of the structure of each interface after the emission of the trailing partial

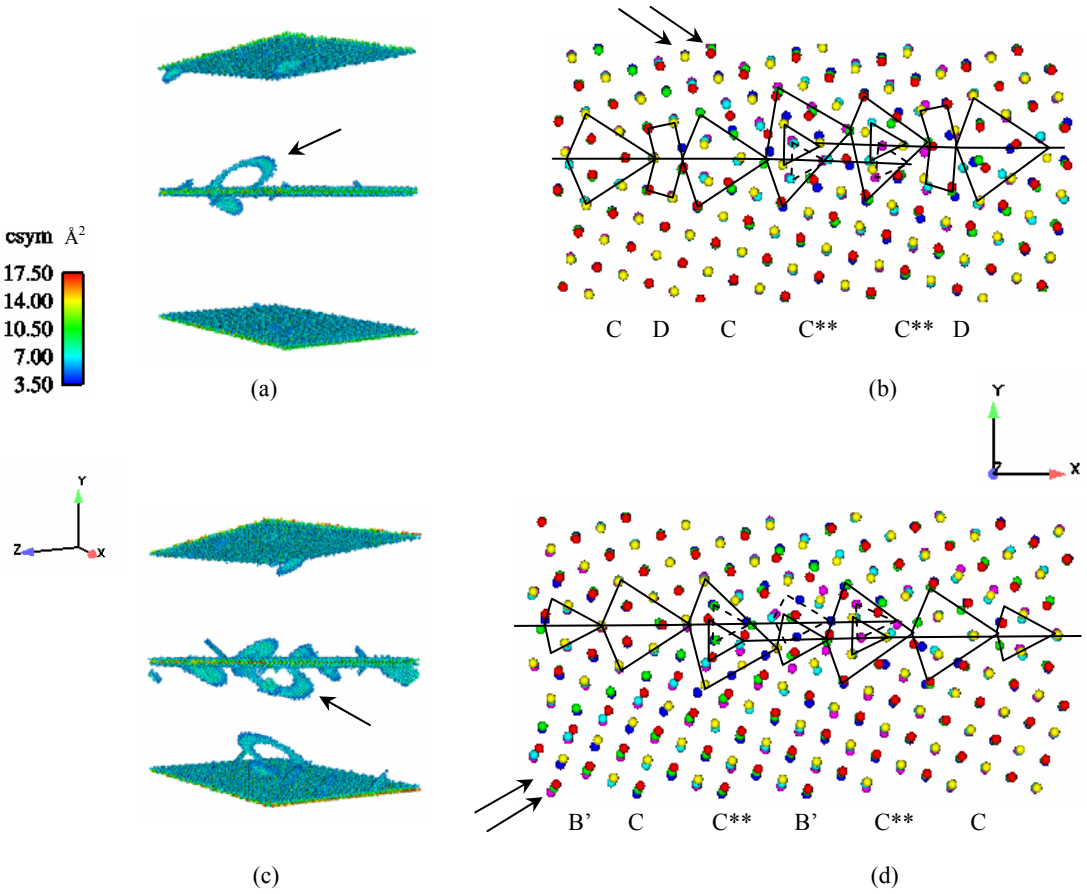

Figure IV.5. Detailed analysis of 33.4° and 41.1° interface structures after full dislocation nucleation at 10 K. Atoms are colored by their respective atomic {001} plane through the thickness of the interface model.

dislocation. Here, atoms are colored by their respective {001} atomic plane, similar to that in Fig. IV.4. Again, six {001} atomic planes are cut from the thickness of the interface model through the dislocation loop to identify the distorted structure of the interface.

Similar to the Σ5 (310) interface, the slip process in each of the general tilt boundaries involves atoms that are originally identified as belonging to the structural units. For the 33.4° interface in Fig. IV.5(b), slip occurs predominantly at the C units,

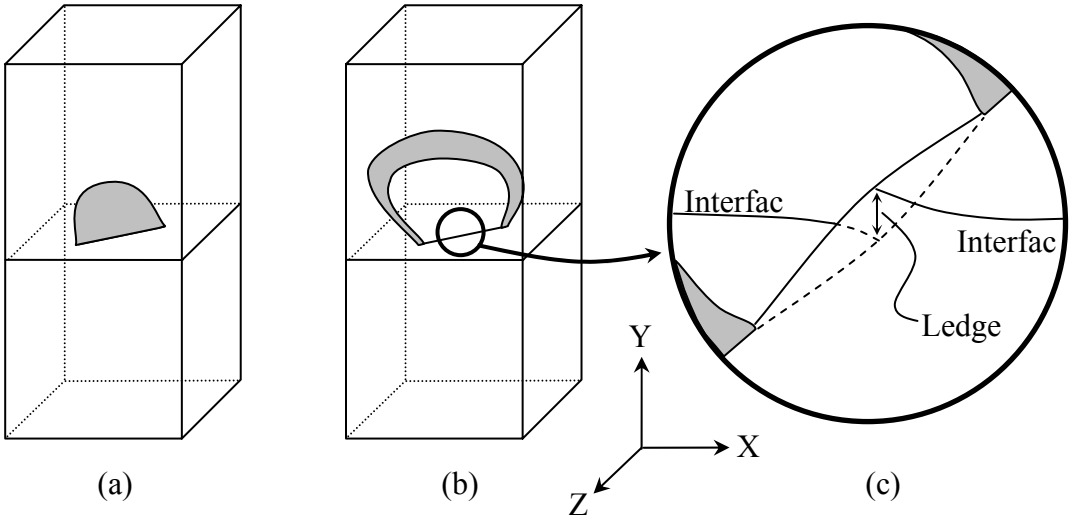

Figure IV.6. Schematic of the dislocation nucleation process: (a) after emission of the first partial dislocation, (b) after emission of the trailing partial dislocation creating a dislocation loop and (c) resulting interface structure showing formation of a ledge.

creating two C** deformed units after the nucleation of the trailing partial dislocation. As with the Σ5 boundary, the C** deformed units involve an irreversible ledge at the intersection of the slip plane and the interface. The magnitude of this step in the Y-direction ranges between 1.3-1.7 Å, depending on the position along the interface. Similarly, for the 41.1^{o} boundary in Fig. IV.5(d), full dislocation nucleation causes a small ledge within the interface plane after the emission of the trailing partial dislocation. Again, this ledge appears to be irreversible, because it involves atoms that are associated with the full slip event. Here the slip event occurs across the junction between C and B' structural units, i.e., the position of the partial wedge disclination.

Figures IV.4 and IV.5 show molecular dynamics evidence of a ledge in the bicrystal interface after the emission of the second partial dislocation. This ledge occurs at the intersection of the plane of the dislocation loop and the boundary, which occurs at a

defined angle (based on the active slip plane) to the viewing direction. It is noted that while Figs. IV.4 and IV.5 illustrate the slip process by monitoring the motion of atoms within the X-Y plane, there is also a component of slip that occurs in the Z-direction. Regardless, additional analysis has confirmed that a ledge occurs within the interface plane at the intersection of the slip plane and the interface for any cut through the defect structure. The magnitude of the ledge appears to be at a maximum towards the center of this intersection. Based on the molecular dynamics evidence, Fig. IV.6 shows a schematic of the dislocation nucleation process and the resulting interface ledge after the emission of the full dislocation.

Finally, Fig. IV.7 shows the dislocation nucleation process for the Σ5 (310) aluminum boundary at a temperature of 300 K. Figures IV.7(a) and IV.7(c) are colored by the centrosymmetry parameter. Atoms with a centrosymmetry parameter close to zero are removed to facilitate viewing of the defect structures. Clearly, thermal vibrations prevent a completely unobstructed view. A full dislocation loop is nucleated during uniaxial tensile deformation. Similar to the previous examples at 10 K, an extended partial dislocation is first emitted from the interface, shown with an arrow in Fig. IV.7(a). Slip occurs on the $(\bar{1}1\bar{1})/[\bar{1}01]$ slip system initially; however, further deformation will nucleate dislocations on the other favored slip system in both lattice regions. The length of this extended dislocation reaches approximately 37.6 Å from the center of the interface before the trailing partial dislocation is emitted in Fig. IV.7(c). The tensile stress required to nucleate the first partial dislocation at 300 K from the Σ5 (310) boundary is calculated as 4.28 GPa. This value is lower than that of the 10 K simulation due to the temperature dependence of the yield stress.

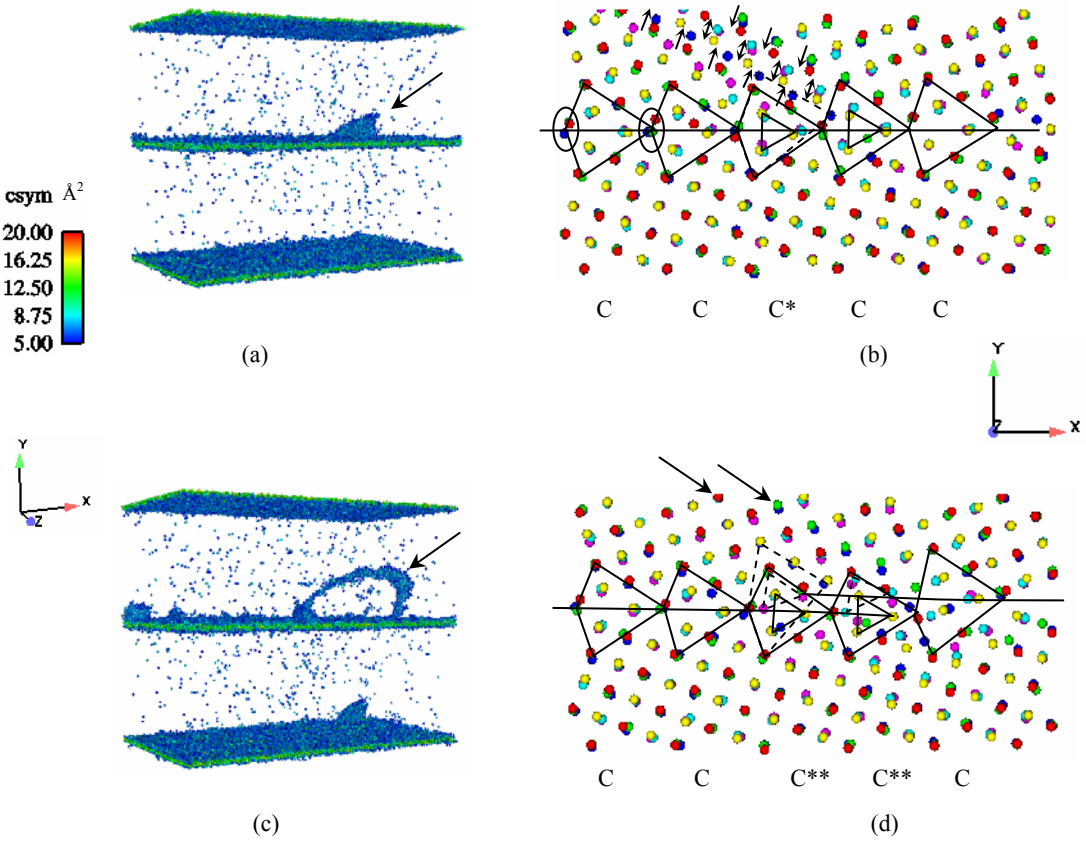

Figure IV.7. Nucleation of full dislocation loops during uniaxial tension of the Σ5 (310) 36.9° interface model at 300 K; (a)-(d) atoms are colored by the centrosymmetry parameter and (e)-(g) atoms are colored by the atomic slip vector.

In Figs. IV.7(b) and IV.7(d), atoms are colored by their respective {001} plane in the Z-direction and projected into the X-Y plane, similar to that in Figs. IV.4 and IV.5. In Fig. IV.7(b), only the first partial dislocation has been emitted from the interface. Many of the same phenomena observed at 10 K are also evident at 300 K. First, expansion of the interface region allows some atoms to migrate in the loading direction within the interface plane (circled in Fig. IV.7(b)). Second, the slip process involves atoms that belong to the structural units. As before, one of the C structural units is

irreversibly distorted as a result of the partial dislocation slip, labeled as C*. In Fig. IV.7(b), the C* deformed unit occurs in the fifth plane through the cut. The C structural units above and to each side of this distorted unit are only slightly modified to accommodate the slip process. Fig. IV.7(d) shows the interface structure after the emission of the second partial dislocation from the interface. Two C** structural units are formed during the deformation process, creating a ledge similar to that formed in the simulations at 10 K. The peak magnitude of the ledge is approximately 1.7 Å, which is comparable to that observed in the low temperature simulations.

Two phenomena observed during these calculations above necessitate additional discussion: (i) the interface structural units are directly involved in the dislocation nucleation process, and (ii) a small ledge forms at the intersection of the dislocation loop and the interface after the emission of the trailing partial dislocation. Both phenomena are shown to irreversibly modify the interface structural units. Previous molecular dynamics work on nanocrystals by Van Swygenhoven *et al*. (2004) has shown that atomic shuffling along the grain boundary occurs prior to the emission of the first partial dislocation. The atomic migration locally rearranges the interface to assist in the nucleation process. Calculations in this work at both 10 K and 300 K do not show atomic shuffling prior to the emission of the first partial dislocation. Instead, the interface structural units are directly involved in the dislocation nucleation process. The shuffling observation in nanocrystalline materials is likely due to the orientation of the load with respect to the interface, resulting in both tensile and shear stress components. Furthermore, triple points in the nanocrystalline samples provide the free volume required for atomic migration. The bicrystal geometry used in this work more closely

relates to grain boundary behavior in materials with larger grain sizes than that simulated in the nanocrystalline work of Van Swygenhoven and colleagues. Specifically, the effects of triple points and other irregularities that cause local stress concentrations are not considered.

Recall from Chapter III that the structure of high-angle interfaces may be described using the disclination-structural unit model (Valiyev *et al*., 1990; Gertsman *et al*., 1989). In this framework, the junction between different structural units is identified as a partial wedge disclination. The difference in the angle between neighboring structural units defines the strength of the partial wedge disclination. The minority structural unit is taken by convention as the disclination dipole. Molecular dynamics results in this work show that dislocation emission irreversibly distorts the grain boundary structure at the nucleation site. Hurtado *et al.* (1995) consider two models for the altered grain boundary structure following dislocation emission. The first model considers the creation of a disclination dipole (with opposite orientation to the dipoles that compose the interface) at the nucleation site. The length of the created dipole is assumed to be the same as that of the interface dipoles. The second model assumes the introduction of a dislocation at the nucleation site with the same burgers vector and opposite orientation as the dislocation that is emitted into the lattice.

Figure IV.8 shows a proposed disclination dipole model based on our molecular dynamics results for an idealization of the deformed Σ5 (310) bicrystal interface structure. Recall that the original structure of the Σ5 (310) interface involved a uniform distribution of C structural units, i.e., no net disclination dipoles were present in the undeformed configuration. Figure IV.8(a) shows the shape of the structural components

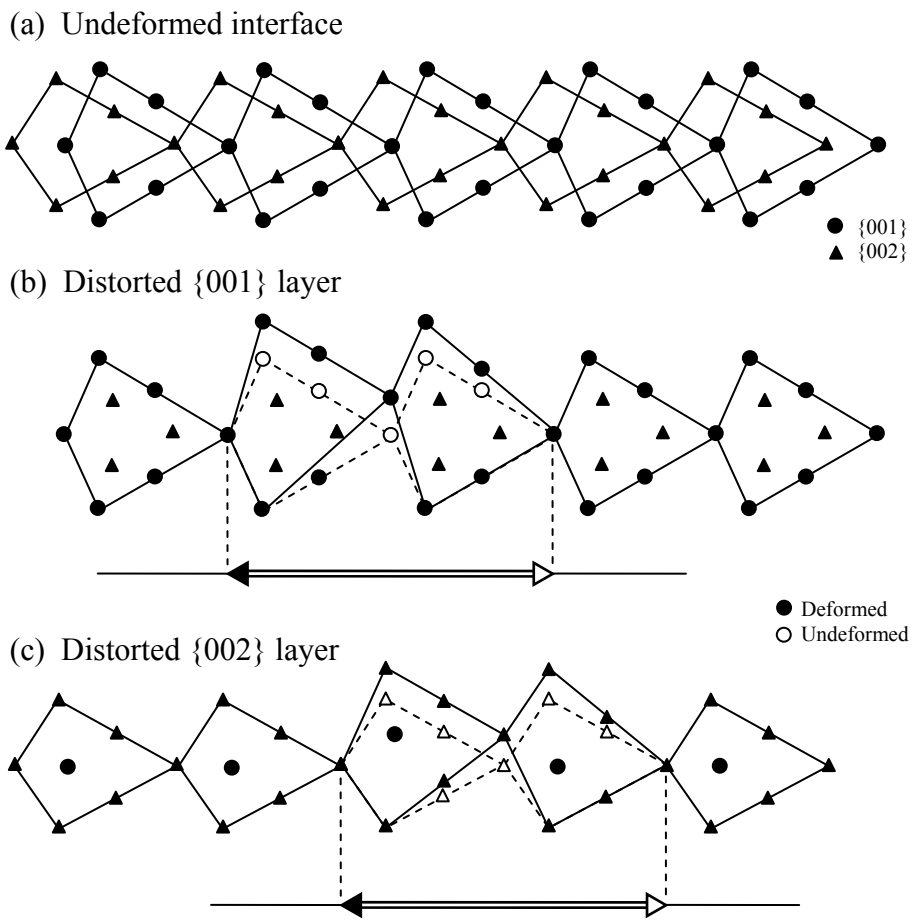

Figure IV.8. Proposed disclination dipole model for the distorted Σ5 (310) interface after full dislocation nucleation; (a) reference (undeformed configuration), (b) distorted {001} atomic layer with disclination dipole representation and (c) distorted {002} atomic layer with disclination dipole representation.

that exist in the {001} and {002} planes prior to deformation. The nucleation of a full dislocation from the interface is accompanied by a local lattice rotation, leading to the asymmetric expansion of two C structural units as shown in Figs. IV.8(b) and IV.8(c). Thus, the distorted interface can be represented as a series of staggered disclination dipoles that span the interface ledge at the nucleation site. The strength of the each disclination dipole is equal to the difference between the angle of the C and C**

structural units, which is calculated from molecular dynamics as approximately 10^{o}-12^{o}. The spacing between partial disclinations is equal to the length of two C** segments, calculated from molecular dynamics as approximately 12.7 Å, which is essentially identical to the theoretical length of two C segments, $\sqrt{10}\lambda$. It is noted that the deformed configurations in Figs. IV.8(b) and IV.8(c) are 'idealized' to show that only two structural units are deformed by the slip process. In reality, a few structural units on either side of the dislocation nucleation point are slightly modified to smoothly accommodate the ledge at the intersection of the slip plane and the interface.

Representing the ledge in the distorted interface using a disclination dipole is in accordance with the work of Nazarov *et al.* (2000) who studied zig-zag interface arrangements in covalently bonded materials. Although the axis of the C** units is not aligned along the interface plane (i.e., the lattice rotation is not symmetric about the interface), the junction between C and C** units may still be described with a disclination dipole that is oriented parallel to the interface. If additional structural units existed between the C** units, such as the B' unit in Fig. IV.7(d), then two dipoles may be required to represent the interface structure, each of which is oriented at an angle to the interface plane (Nazarov *et al*., 2000). Based on the proposed disclination dipole model, the total energy of the distorted boundary will have contributions from the surface energy of the undeformed C structural units, the disclination cores, and the elastic energy of the disclination dipoles (Valiyev *et al*., 1990; Gertsman *et al*., 1989). The elastic energy of the disclination dipoles must include both the elastic self energy and the energy of interaction between the dipoles that are staggered across the interface ledge.

IV.4.2 Dissociated <110> Interfaces in Copper

Molecular dynamics simulations are used to study the process of dislocation nucleation from bicrystal interfaces with dissociated structure. Figure IV.9 shows the 53.1^{o} interface model in copper at 10 K and 300 K subjected to a uniaxial tensile deformation normal to the interface plane. All images in Fig. IV.9 are color rendered according to the centrosymmetry parameter (Kelchner *et al*., 1998). Atoms with a centrosymmetry parameter close to zero are removed to facilitate viewing of the defect structures. A detailed characterization of the interface structure during the tensile deformation process is presented in Fig. IV.10. The specific points of interest are circled and labeled A-D in Fig. IV.9. In Fig. IV.10, atoms are shaded by their respective {110} atomic plane. Atoms that are outlined are identified via the centrosymmetry parameter as being in defect configurations.

When subjected to a tensile deformation, Figs. IV.9(b) and IV.9(f) show that the bicrystal interface structure evolves prior to the dislocation nucleation event. Specifically, tensile deformation applied normal to the interface plane causes the ISF facet to become shorter in length. In Fig. IV.10(a), at an interface model strain of 5.0%, the length of the intrinsic stacking fault facet is approximately 40% of that presented in Chapter III, Fig. III.12(a). Additional tensile strain causes partial edge dislocations to be nucleated from the bicrystal interfaces, as shown in Figs. IV.9(c) and IV.10(b). Initially, a partial edge dislocation is nucleated from the interface at the intersection of the ISF facet and the bicrystal boundary. The core of the partial dislocation is not shown in Fig IV.10(b), only the extrinsic stacking fault (ESF) that extends from the partial dislocation

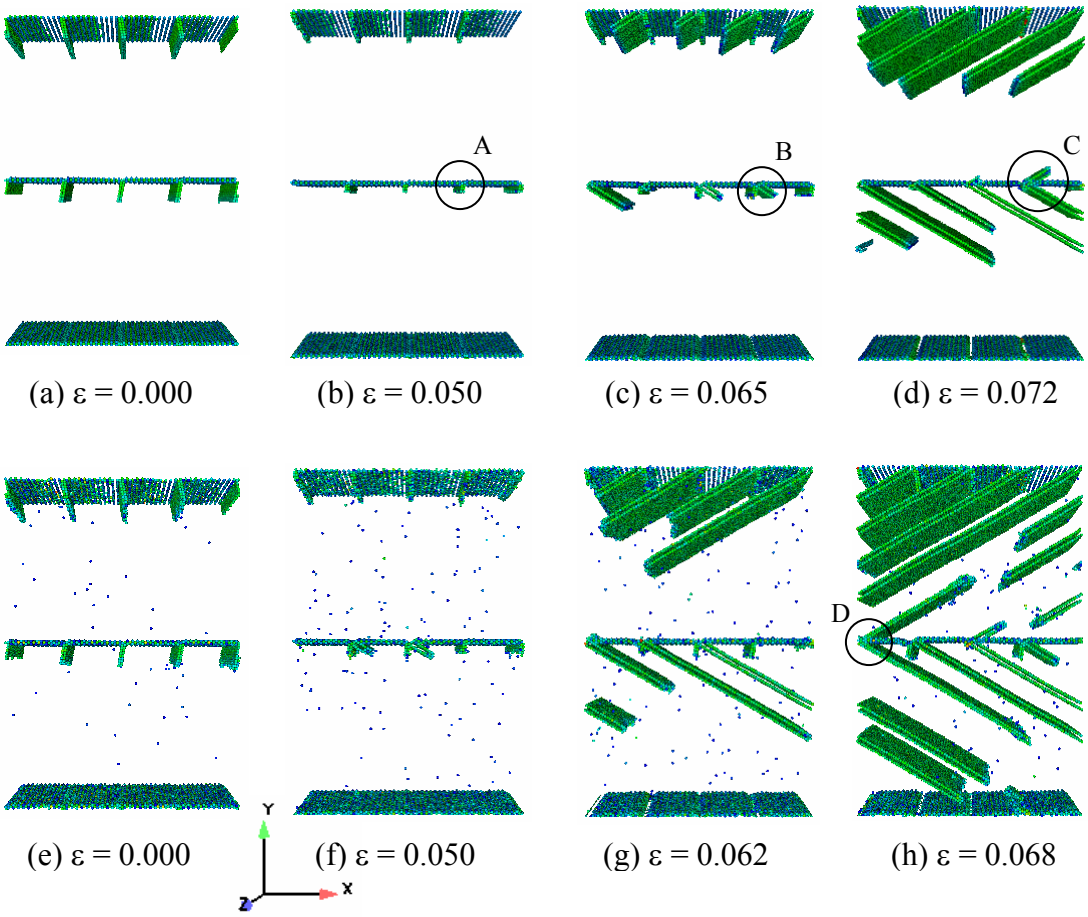

Figure IV.9. Uniaxial tensile deformation of the 53.1° copper interface model at (a)-(d) 10 K and (e)-(h) 300 K. Dislocations are nucleated from the intersection of the ISF facet and the bicrystal boundary.

core back to the interface. Because dislocation nucleation involves the entire slip plane through the thickness of the interface model, the ABAB stacking sequence in the Z-direction is preserved. In the upper lattice region, slip occurs initially on the $(11\bar{1})$ plane, which is a secondary slip plane according to the Schmid factor. Likewise, the secondary (111) slip plane is activated in the lower lattice region. This indicates that the ISF facet

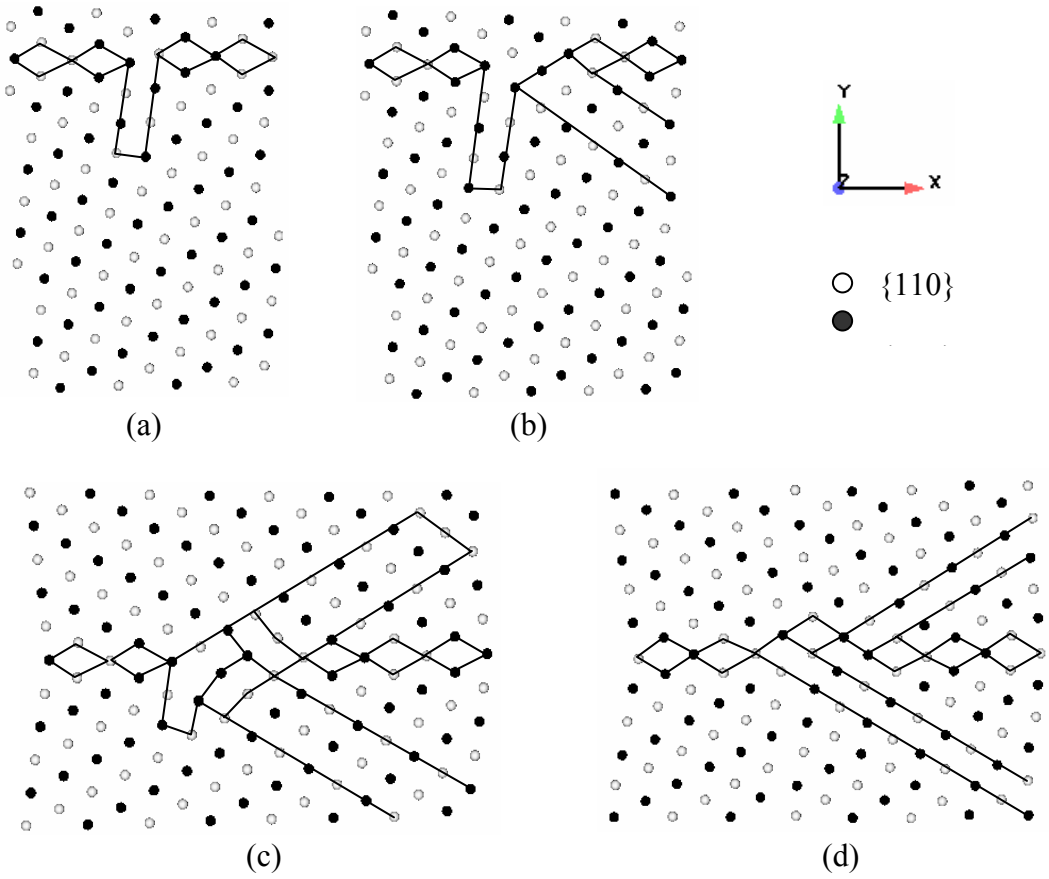

Figure IV.10. Detailed examination of the 53.1° copper interface structure during the uniaxial tensile deformation process. Images (a)-(d) correspond to circled regions in Fig. IV.9.

promotes slip activity on the secondary slip systems. This result is due to the configuration of the ISF facet which potentially acts as a stress riser.

The tensile stress required to nucleate the first partial dislocation from the 53.1° interface is calculated as 6.94 GPa at 10 K and 5.29 GPa at 300 K. For the given loading direction and activated slip system, this corresponds to critical resolved shear stresses of approximately 2.50 GPa and 1.91 GPa, respectively, which compare favorably with the ideal shear strength of copper obtained from first-principles calculations as 2.16 GPa

(Ogata *et al*., 2002). Thus, our simulations give reasonable values for the nucleation stress. However, it is noted that the critical resolved shear stresses obtained in these calculations are not considered ideal by the definition in Ogata *et al*. (2002). In our calculations, stresses exist normal to the slip planes that can influence the yield behavior, although the magnitude of these stresses does not appear to play a dramatic role for these specific interface misorientations.

Continued tensile strain leads to the nucleation of partial edge dislocations from the ISF facet into the opposing lattice region, as shown in Figs. IV.9(d) and IV.9(h). The additional dislocation nucleation is accompanied by a second decrease in the length of the ISF facet, which is shown in Fig. IV.10(c). As the leading partial edge dislocations glide away from the interface, Fig. IV.9(h) shows that the ESF will transform into an ISF. This indicates that one trailing partial dislocation is nucleated from each side of the interface during the tensile deformation process. At this point, the ISF facet has become completely absorbed by the interface to facilitate this final transition, as shown in Fig. IV.10(d). Although not shown in Fig. IV.9, this transition will occur during simulations at both 10 K and 300 K. In copper, the leading partial edge dislocations remain connected to the interface by an intrinsic stacking fault. Throughout the entire deformation process, the interface structural units away from the dislocation nucleation site are largely unaffected.

Figures IV.11(a)-(c) show the uniaxial tensile deformation of the 54.4^{o} boundary in copper at 300 K while Figs. IV.11(d)-(e) show the deformation of the 59.0^{o} interface model in copper at 300 K (simulations at 10 K provide similar conclusions for each misorientation). Images in Fig. IV.11 are color rendered according to the

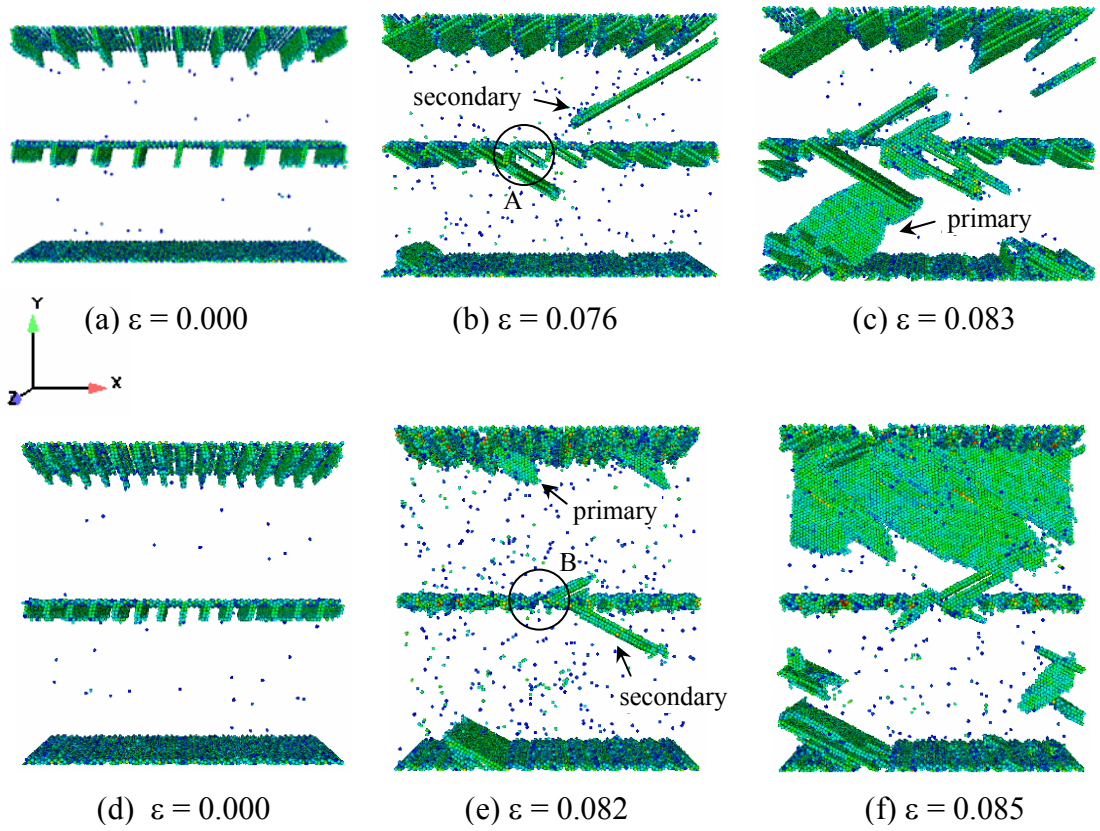

Figure IV.11. Uniaxial tensile deformation of the (a)-(c) 54.4° copper interface model and (d)-(f) 59.0° copper interface model. The deformation mode is influenced by the spacing between ISF facets.

centrosymmetry parameter while atoms with a centrosymmetry parameter close to zero are removed to facilitate viewing of the defect structures. When subjected to a uniaxial tensile deformation, Figs. IV.11(b) and IV.11(e) show that the interface structure initially evolves prior to the emission of dislocations. Similar to the 53.1° example, the length of each ISF facet decreases during the early stages of tensile deformation. As deformation continues, dislocations are nucleated from each interface on multiple slip planes. Analysis shows that the sequence of dislocation nucleation events and the activated slip planes change as the misorientation angle is increased from 53.1° to 59.0°.

Specifically, for the 54.4° misorientation, Fig. IV.11(b) shows that dislocations are initially nucleated from the interface at the intersection of the ISF facet and the bicrystal boundary. In the upper lattice region, slip occurs initially on the $(11\bar{1})$ slip plane, which is a secondary slip system according to the Schmid factor. Likewise, the secondary (111) slip plane is initially activated in the lower lattice region. The tensile stress required to nucleate the first partial dislocation from the 54.4° interface at 300 K is calculated as 6.56 GPa. For the given loading direction and activated slip system, this corresponds to a critical resolved shear stress of approximately 2.32 GPa. As deformation continues, partial dislocations are observed on the $(\bar{1}11)$ and $(\bar{1}1\bar{1})$ slip planes, which are the primary slip planes according to a Schmid factor analysis (and lie at an angle to the viewing direction).

For the 59.0° interface misorientation, Figs. IV.11(e) and IV.11(f) show a slightly different behavior as compared with the 53.1° or 54.4° examples. Here, partial dislocations are nucleated from the interface nearly simultaneously on both the primary and secondary slip systems. Each slip system is marked with an arrow in Fig. IV.11(e). The tensile stress required to nucleate the first partial dislocation from the 59.0° interface at 300 K is calculated as 7.60 GPa. For the given loading direction and the secondary slip system, this corresponds to a critical resolved shear stress of approximately 2.54 GPa.

Images in Figs. IV.9 and IV.11 indicate that as the misorientation angle of the interface is increased from 53.1° to 59.0°, leading to a decrease in the spacing between ISF facets (Table IV.1), the failure mode changes from one that is dominated by dislocation nucleation on secondary slip systems at the ISF facet to that which is a

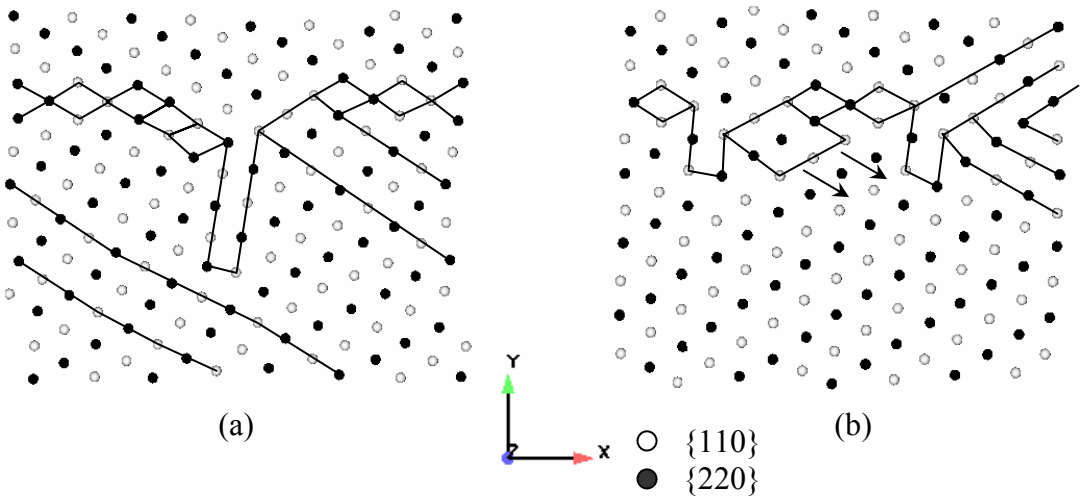

Figure IV.12. Detailed examination of the interface structure during the uniaxial tensile deformation process of the 54.4° and 59.0° copper interface models. Images (a) and (b) correspond to circled regions in Fig. IV.11.

mixture of dislocation nucleation on both primary and secondary slip systems. Figure IV.12 shows a detailed characterization of the copper interface structure during the tensile deformation process for both 54.4° and 59.0° boundaries. These images, combined with those in Fig. IV.10, elucidate the interface mechanisms that lead to a change in the dislocation activity from secondary to primary slip systems. The two specific points of interest in Fig. IV.12 are circled in Fig. IV.11.

Figure IV.12(a) shows that for the 54.4° interface there is a close interaction between the ISF facet and the ESF associated with the nucleated partial dislocation. Both the ESF and the ISF facet are distorted due to this interaction, which arises as a result of the reduced separation distance between dissociated structural units, as compared with the 53.1° misorientation. Regardless, the spacing between ISF facets is still sufficient to allow the nucleated partial dislocation to pass into the lattice region. This is not the case with the 59.0° boundary, as shown in Fig. IV.12(b). Here, the spacing between ISF facets

critically inhibits the nucleation of partial edge dislocations on the secondary slip planes. Specifically, the ISF facet blocks the motion of the nucleated partial edge dislocation, as shown with arrows in Fig. IV.12(b). Consequently, additional interface structural rearrangement is required, facilitating dislocation activity on the primary slip systems.

Energy minimization calculations in Chapter III show that materials with different intrinsic stacking fault energies may have different interface structures for the same misorientation angle. These calculations are in qualitative agreement with those in the literature. Results in the literature also show that the ISF energy can influence the nucleation of dislocations from interfaces in nanocrystalline materials, as discussed in the introduction of this chapter. Images in Fig. IV.13 show the nucleation of dislocations from the 53.1^{o}, 54.4^{o} and 59.0^{o} boundaries in aluminum at 10 K. Calculations are performed at 10 K to determine the initially activated slip system in the absence of thermal vibrations. In all three cases, dislocation nucleation occurs nearly simultaneously on both primary and secondary slip systems and originates from the dissociated structural unit. Apparently, the very short ISF facets in aluminum (recall Chapter III, Fig. III.13) are still sufficient to promote some dislocation activity on the secondary slip systems. The images presented in Fig. IV.13 show that there are two main differences between the dislocation activities in aluminum compared with that in copper. First, the majority of the dislocation motion in aluminum occurs on the primary slip systems. Partial edge dislocations are nucleated on the secondary planes; however, they appear to reach a limit where their motion is inhibited by the dislocation activity on the primary systems. Only dislocations on primary systems sweep from one interface to the other. Second, full dislocation loops are nucleated during the deformation process in aluminum. The

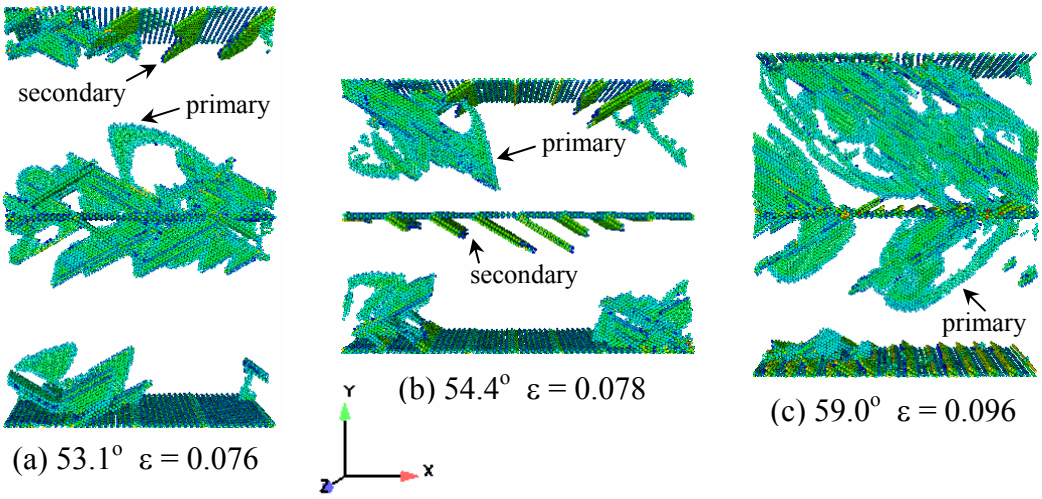

(a) 53.1° ε = 0.076 (b) 54.4° ε = 0.078 (c) 59.0° ε = 0.096

Figure IV.13. Uniaxial tensile deformation of the (a) 53.1°, (b) 54.4° and (c) 59.0° aluminum interface model at 10 K. Dislocations are nucleation on both primary and secondary slip systems.

dislocation loops have both edge and screw character and occur on the primary slip systems, as shown with arrows in Fig. IV.13. In copper, the trailing partial dislocation is emitted only to transform the extrinsic stacking fault to an intrinsic stacking fault, as explained earlier in Fig. IV.9(d).

Based on the molecular dynamics result presented above, Fig. IV.14 shows a schematic of the evolution of an asymmetrically dissociated interface under the application of a uniaxial tensile deformation. Specifically, images in Fig. IV.14 characterize the positions of partial edge dislocations at critical stages during the tensile deformation process. Here, it is assumed that the ISF facets are sufficiently far apart that interaction effects (such as those in Fig. IV.12) do not play a strong role. Figure IV.14(a) shows the initial interface structure, with an ISF facet on the $(11\bar{1})$ slip plane. Tensile stress applied normal to the interface planes causes the ISF to become shorter in length

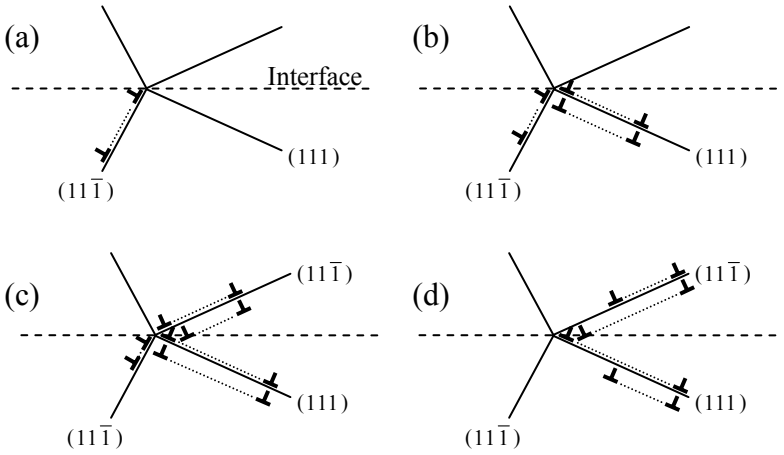

Figure IV.14. Schematic of the dislocation nucleation process during tensile deformation from an interface with an asymmetric dissociated structure.

and promotes dislocation nucleation on the (111) slip plane, as shown in Fig. IV.14(b). Initially, the emitted dislocation is connected back to the interface via an extrinsic stacking fault. Additional tensile strain leads to dislocation nucleation on the secondary slip plane in the opposing crystal region, as shown in Fig. IV.14(c). Initially, dislocations in both lattices are connected back to the interface via an ESF. Finally, the ISF facet is completely absorbed by the interface and the extrinsic stacking faults are transformed into intrinsic stacking faults by the emission of trailing partial dislocations from the interface, as shown in Fig. IV.14(d).

Figure IV.15 illustrates in greater detail the discrete transitions that the ISF facet experiences during the tensile deformation process. MD data from the 53.1^{o} interface model in copper at 10 K is used in Fig. IV.15 to provide a reference with regard to the strain level associated with each transition. However, note that these strain levels are not

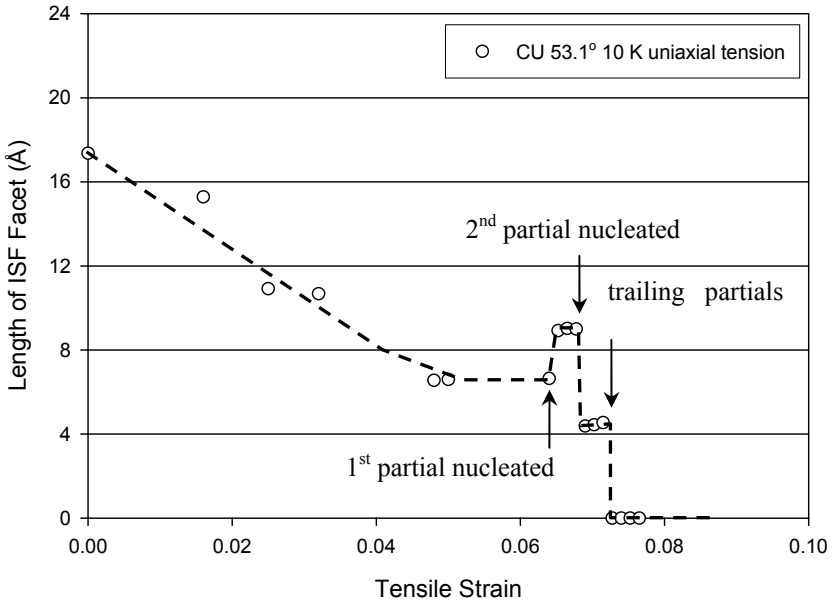

Figure IV.15. Intrinsic stacking fault facet length as a function of tensile strain for the 53.1° interface misorientation in copper illustrating the discrete transitions that the ISF facet experiences during the deformation process.

universal; calculations at different temperatures or for different misorientations will result in different magnitudes of strain associated with each dislocation nucleation event.

Initially, the length of the ISF facet is reduced by the applied tensile deformation, until it reaches a constant magnitude around 5% strain. The first dislocation nucleation event occurs at a tensile strain of 6.4% and surprisingly results in a slight increase in the length of the ISF facet. It is unclear if this slight increase in length is inherent to the dislocation nucleation process, or if the increase in length is due to an attraction between the nucleated partial dislocation and the ISF facet (similar to that in Fig. IV.12(a)). Additional tensile deformation results in the nucleation of a partial dislocation at a strain of 7.03% into the opposing lattice region, which causes a decrease in the length of the ISF facet. Finally, at a strain of 7.27%, trailing partial dislocations are nucleated from the interface. At this point, the ISF facet is completely absorbed into the bicrystal boundary.

The interface transformations described above are remarkably similar to that discussed by Baskes *et al*. (1998) concerning the stress dependence of a lock formation consisting of a stair rod dislocation in nickel. The stair rod dislocation is the sessile product of two partial edge dislocations on intersecting {111} slip planes (Hirth and Lothe, 1982). The parallels between deformation in our simulations and those of Baskes *et al*. are logical due to the similarities between the stair rod dislocation and the dissociated structural unit. Specifically, Baskes *et al*. (1998) considered a stair rod symmetrically located between two Shockley partial edge dislocations. In our work, the termination of the ISF facet accounts for one of the partial dislocations, while the other partial dislocation is initially positioned at the interface (Fig. IV.14(a)).

Baskes *et al*. (1998) show that the stair rod goes through several transitions, associated with the sequential nucleation of partial dislocations from the lock. First, the separation distance between each Shockley partial dislocation and the stair rod is reduced. Next, one of the Shockley partial dislocations passes through the lock to a position on the other side of the stair rod, with an extrinsic stacking fault. For increased stress, one of the partial dislocations escapes the stair rod lock, transforming the extrinsic stacking fault into an intrinsic stacking fault. Finally, the other Shockley partial dislocation passes through the stair rod resulting in a symmetric formation of extrinsic and intrinsic stacking faults in either side of the lock. While, the sequence of nucleation events is slightly different, the structural similarities between the dislocation configurations described in this work and those in Baskes *et al*. (1998) are evident.

CHAPTER V

BICRYSTAL INTERFACE STRENGTH AS A FUNCTION OF INTERFACE STRUCTURE

V.1 Introduction

Analysis in Chapter IV provided a detailed description of different physical mechanisms associated with the nucleation of dislocations from bicrystal interfaces subjected to a uniaxial tensile deformation. Descriptions of the deformed interface structures after the dislocation nucleation event were provided in terms of partial dislocations or disclinations. In this chapter, analysis of the MD simulation results shifts towards the investigation of potential relationships between interface properties and interface structure. Specifically, the tensile stress normal to the bicrystal boundary and the porosity within the interface region are monitored throughout the deformation process. The ability of the interface porosity measurement to characterize the evolution of the interface structural units and to correlate the interface strength to the interface structure is discussed in detail. Two different boundary prescriptions are employed, which may be considered as limiting cases for deformation in nanoscale systems. Specifically, calculations in this chapter consider multiaxial stress states that occur when lateral confinement of the interface structure is an important consideration. More detail will be provided regarding each boundary prescription in Section V.2.

Interface strength is determined by calculating the stress within a defined region around the interface during the tensile deformation process (using the virial definition in

Section II.3.3). The stress normal to the interface plane is plotted as a function of the interface displacement for each bicrystal interface model considered. This methodology is chosen to maintain analogy with the form of interface separation relations (Needleman, 1987), which will be discussed in greater detail in Chapter VI. Several authors have used atomistic simulation techniques to calculate stress-strain or stress-displacement relationships for single crystal, bicrystal and nanocrystalline geometries (*cf*. Kitamura *et al.*, 1997; Schiøtz *et al*., 1998; 1999; Heino *et al*., 1998; Horstemeyer and Baskes, 1999; Gall *et al.*, 2000; Komanduri *et al*., 2001; Horstemeyer *et al*., 2001a; 2001b; 2002; Sansoz and Molinari, 2004; 2005). These works employed a range of different boundary prescriptions, including both periodic and nonperiodic borders with stress- or displacement-based deformation conditions. For example, Horstemeyer *et al*. (2001a; 2001b; 2002) subjected single crystal samples of nickel to a fixed-end shear deformation. Nonperiodic boundary conditions were used in the directions parallel and perpendicular (in plane) to the shear deformation. Periodic boundary conditions were employed through the thickness of the single crystal sample. With these boundary conditions, the calculations of Horstemeyer *et al*. focused on the influence of sample size (length scale) on the shear deformation response. The nonperiodic boundaries served as the nucleation point for dislocations during the shear deformation.

Calculations in this work are performed using periodic boundary conditions in all directions. Unfortunately, there are many important considerations regarding the use of different deformation prescriptions for periodic boundaries that are not well addressed in the literature. Kitamura *et al*. (1997) provided some insight regarding the consequence of different periodic boundary conditions on the inelastic response of single crystal samples

of nickel deformed in tension. In their work, periodic boundary conditions are applied in the directions transverse to the load. Simulations are then performed using either zero-stress (uniaxial tension) or zero-strain (constrained tension) conditions in these directions. Kitamura *et al*. (1997) reported that the zero-strain constraint placed on the boundaries transverse to the loading direction lead to very high tensile yield stresses and severely limited inelastic deformation, which in turn promoted cleavage fracture. This is in agreement with calculations in Gall *et al*. (2000), who studied tensile fracture of an aluminum-silicon interface using constrained periodic boundary conditions. On the other hand, simulations using the zero-stress condition transverse to the applied load in Kitamura *et al*. (1997) showed a much lower tensile yield stress and significant dislocation activity by comparison. Void nucleation is not observed even for very large strains (beyond 50%). Calculations in this work will evaluate the effect of uniaxial and constrained tension boundary conditions on the inelastic deformation of bicrystal interface models.

Very few authors in the literature have attempted to directly correlate interface strength with interface structure using atomistic techniques. Sansoz and Molinari (2004; 2005) used the quasicontinuum method with atomic resolution around the interface region to attempt to quantify the relationship between interface structure and maximum shear strength. As discussed in Chapter I, Sansoz and Molinari studied the inelastic response of bicrystals with <110> tilt misorientations under tension and shear. In tension, failure of the interface occurred through partial dislocation nucleation and grain boundary cleavage. In shear, three different failure modes are observed depending on the

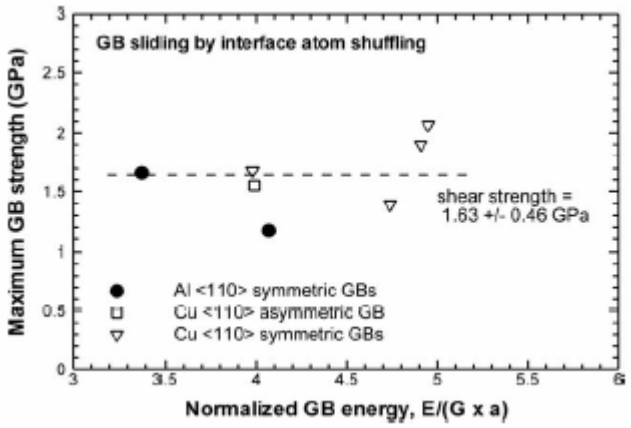

Figure V.1. Maximum interface strength as a function of interface energy for symmetric tilt boundaries. Reproduced from Sansoz and Molinari (2005).

initial boundary configuration: grain boundary sliding by atomic shuffling, nucleation of partial dislocations from the bicrystal interface and grain boundary migration.

Unfortunately, Sansoz and Molinari did not find any discernible trend between maximum shear strength and interface structure. Specifically, they reported maximum shear strengths that range discontinuously over the range of misorientations considered from 1.03 GPa to 5.41 GPa in copper and 0.63 GPa to 3.50 GPa in aluminum. The relationship between maximum interface shear strength and grain boundary energy reported by Sansoz and Molinari (2005) for boundaries which deform primarily by atomic shuffling is shown in Fig. V.1. Although an average maximum grain boundary shear strength of 1.63 GPa is reported, the data shows significant scatter; thus, Sansoz and Molinari concluded that interface energy does not appear to be a viable method to correlate interface structure and interface strength. In addition, their results showed that the structural unit model does not provide a definite means to characterize the interface strength as a function of interface structure (although they do not discuss this explicitly in

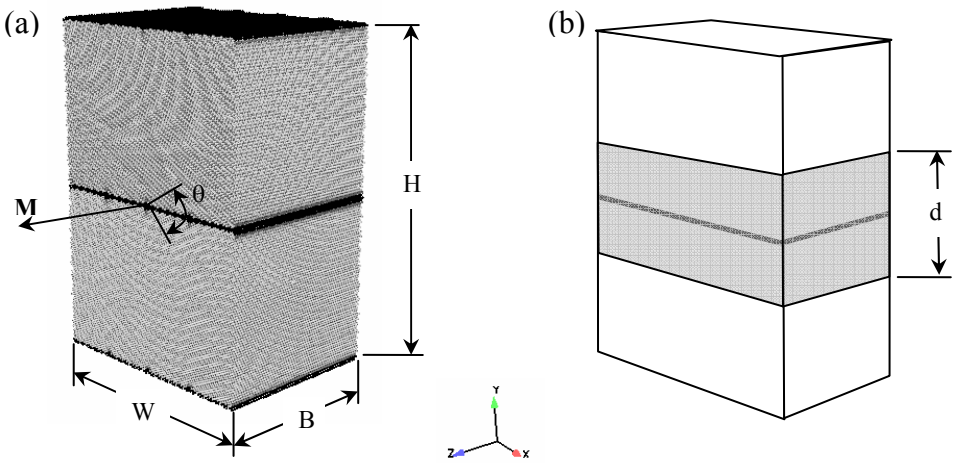

Figure V.2. Bicrystal interface model examined in this thesis. The interface is created by a symmetric tilt rotation of opposing lattice regions around a specific misorientation axis.

their work). In their results, the Σ27 (115) and Σ11 (113) favored boundaries (recall Chapter III) showed high levels of maximum shear strength for both copper and aluminum. However, the Σ9 (221) and Σ3 (111) favored boundaries were among the weakest interfaces considered in their work for deformation in shear.

V.2 Bicrystal Interface Model Boundary Conditions

Identical to the calculations performed in Chapter IV, bicrystal interface models in this chapter are developed using a combination of molecular statics (mechanics) and molecular dynamics simulations. The initial bicrystal interface structures are obtained using molecular statics calculations. Then, after the bicrystal interface model is equilibrated to the desired temperature and pressure in NPT ensemble (Melchionna *et al*., 1993), molecular dynamics simulations are used to subject the interface model to a

mechanical deformation. An example interface model for the calculations performed in this chapter is shown in Fig. V.2(a). The interface misorientation is created by a symmetric rotation, θ, of opposing lattice regions around a misorientation axis, **M**. Stress, displacement and porosity are calculated over a defined region around the interface, as shown in Fig. V.2(b). This region includes the interface in the center of the model and extends to the periodic boundaries in both the X- and Z-directions. The size of this 'interface region' is determined using results from the energy minimization calculations presented in Chapter III. Here, the thickness of the interface region is chosen as $d = 12\lambda$. Again, λ is the lattice constant of either copper or aluminum. Note that the stress-displacement response calculated over the defined interface region will include some lattice effect. Thus, single crystal calculations are also presented in this chapter, using the same boundary conditions and dimensions as the bicrystal models, to evaluate the role of lattice orientation on the calculated interface properties. In total, each atomistic model contains between 450,000 and 750,000 atoms.

Two different boundary conditions are used in this work. Specifically, molecular dynamics simulations are performed using either 'uniaxial' or 'constrained' tension boundary conditions, as schematically illustrated in Fig. V.3. These boundary conditions are very similar to those used by Kitamura *et al*. (1997) to study the effect of boundary prescription on tensile deformation of nickel single crystal models. Uniaxial tension boundary conditions involve the application of a deformation at a constant strain rate normal to the interface plane, while the boundaries in the lateral (X and Z) directions are prescribed as stress free. The boundaries in the lateral directions are allowed to expand or contract during the deformation process, as shown in Fig. V.3(a). The dashed lines

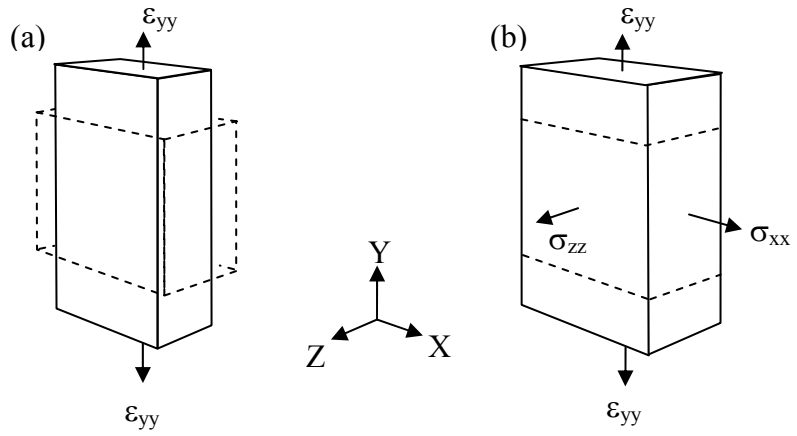

Figure V.3. Schematic illustration of the boundary prescription for (a) uniaxial tensile deformation and (b) constrained tensile deformation.

represent the initial shape of the interface model, while the solid lines represent the deformed shape. Specifically, the time rate of change of the dimensions of the periodic cell is prescribed in the Y-direction in accordance with a desired strain rate of $1x10^{9}$ s^{-1}. The motions of the boundaries in the X- and Z-directions are determined from the current and prescribed system stresses using the Melchionna *et al.* (1993) equations of motion. Throughout deformation, the temperature is maintained approximately at 300 K.

Constrained tension boundary conditions involve the application of deformation at a constant strain rate normal to the interface plane while the boundaries in the lateral directions are prescribed with a zero strain condition ($\varepsilon_{xx} = \varepsilon_{zz} = 0$). Note, the lateral boundaries are not 'fixed' or 'rigid,' they are rendered immobile by not allowing the periodic simulation cell to contract during the deformation process, as shown in Fig. V.3(b). As a result, these calculations consider stresses parallel to the interface plane during the tensile deformation process. To deform the interface model, the time rate of change of the dimensions of the periodic cell is prescribed in the Y-direction in

accordance with the desired strain rate, identical to that used for uniaxial tension boundary conditions. Again, the system temperature is maintained approximately at 300 K throughout deformation.

V.3 Calculation of Nanoporosity

Sansoz and Molinari (2005) showed in their work that neither the interface energy nor the CSL methodology is sufficient to correlate interface structure and interface strength. Perhaps a more appropriate correlation exists through a measure of interface damage. On the atomic level, a measure of the number of broken bonds within the system is most appropriate to define damage. Although other parameters, such as dislocation density, may depict a degree of rearrangement, they do not contain the same information as a measure of bond breakage. In this work, a measure of damage is developed by examining the first-order coordination number of each atom, $\mathbb{Z}_1^i$. The first-order coordination number corresponds to the number of first-nearest neighbors around a particular atom. For example, atoms in a perfect FCC crystalline arrangement have a first-order coordination number of 12. Atoms with $\mathbb{Z}_1^i$ less than that of the perfect crystal arrangement are defined as 'damaged' in that they have partially ineffective bonding or that they lie at newly created free surfaces. Using this concept, an expression for the damage parameter on a per atom basis is formulated, i.e.,

$$D^i = 1 - \left\langle \frac{\mathbb{Z}_1^i - \mathbb{Z}_{1,th}}{\mathbb{Z}_{1,ref} - \mathbb{Z}_{1,th}} \right\rangle \quad . \tag{V.1}$$

Here, $\mathbb{Z}_{1,\mathrm{ref}}$ is the first-order coordination number associated with a perfect crystalline lattice and $\mathbb{Z}_{1,\mathrm{th}}$ is the threshold first-order coordination number required for an atom to be considered completely damaged ($D^i = 1$). In this work, $\mathbb{Z}_{1,\mathrm{th}} = 8$. This threshold value may be loosely associated with the first-order coordination of an atom sitting directly on a free surface. Obviously, the true coordination of an atom in such a position will vary slightly due to the orientation of the surface or undulations in the fracture faces. Equation (V.1) allows the i^{th} atom to have partial damage ($0 \le D^i \le 1$) depending on its local environment. Angle brackets define that atoms with $\mathbb{Z}_1^i < \mathbb{Z}_{1,\mathrm{th}}$ have $D^i = 1$ and atoms with $\mathbb{Z}_1^i > \mathbb{Z}_{1,\mathrm{ref}}$ have $D^i = 0$. By averaging the point-wise damage measure over a set of atoms around the interface, a cumulative measure of damage D_c may be defined as

$$D_c = \frac{1}{N'}\left[\sum_{i=1}^{N'} D^i\right] = \frac{1}{N'}\left[\sum_{i=1}^{N'}\left(1 - \left\langle \frac{\mathbb{Z}_1^i - \mathbb{Z}_{1,\mathrm{th}}}{\mathbb{Z}_{1,\mathrm{ref}} - \mathbb{Z}_{1,\mathrm{th}}} \right\rangle\right)\right] \quad . \tag{V.2}$$

In general, N' is the total number of atoms within the interface region minus the number of atoms that are perceived as damaged because they sit initially at free surfaces (nonperiodic boundaries). For calculations in this thesis, periodic boundary conditions are used in all directions; thus, N' is simply the number of atoms in the interface region. Numerically, Eq. (V.2) may be evaluated at each timestep from the atomic positions and

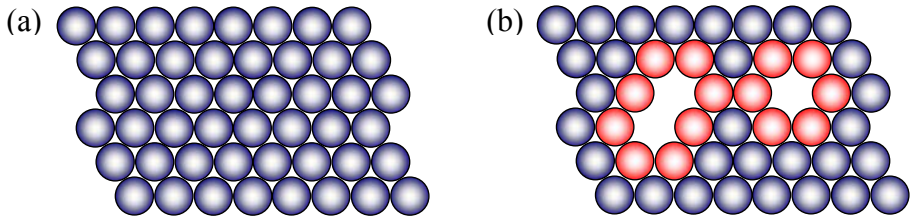

Figure V.4. Schematic representation of the nanoporosity calculation. Atoms shaded blue have perfect atomic coordination, while atoms shaded red lie at or near free volume within the system.

requires no preconceived knowledge or prescription of a critical damage associated with complete fracture.

From a macroscopic perspective, the cumulative damage relation in Eq. (V.2) corresponds approximately to a measure of the free volume or porosity within an atomic system. Figure V.4(a) shows a 2D schematic illustration of a perfect lattice where each atom has perfect atomic coordination. In this example, each atom has $\mathbb{Z}_1^i = \mathbb{Z}_{1,\text{ref}}$; thus, D_c equals zero for a perfect lattice. On the other hand, Fig. V.4(b) shows a 2D schematic illustration of a lattice with voids of different shape and size. Atoms that lie at or near voids are considered damaged by Eq. (V.1) and thus the distorted lattice in Fig. V.4(b) will have a nonzero D_c. Previous atomistic studies have shown that atoms at high-angle grain boundary interfaces (for example) have a statistical variation of first-order coordination numbers (Van Swygenhoven and Caro, 1998), indicating the presence of initial porosity within the interface structure. All of the bicrystal interfaces examined in this work, except for the perfectly coherent Σ3 (111) interface, will include some initial porosity at zero normal separation. Thus, the cumulative damage measure in Eq. (V.2) potentially serves as a means to characterize the initial coherency of high-angle

boundaries. In addition, monitoring the form of the nanoporosity evolution during the tensile deformation process potentially allows for a classification of deformation in high-angle interfaces with different 'types' initial structures, e.g., favored versus dissociated. It is noted that there is some slight overlap between the nanoporosity parameter and a measure of dislocation density as atoms at dislocation cores within the lattice may contribute to both measures. However, the initial bicrystal interface models are dislocation free in the crystal regions between the boundaries; thus, the overlap between different measures to quantify defect contribution should be minimal.

V.4 Tensile Deformation of Bicrystal Interface Models

V.4.1 [001] Cu Tilt Interfaces

V.4.1.1 Uniaxial tensile deformation

Figures V.5(a) and V.5(b) show the tensile stress-displacement response for copper bicrystal interface models subjected to a uniaxial tensile deformation for a range of <100> tilt misorientations. Tensile stress and displacement are calculated over a region around the bicrystal interface, as defined in Section V.2. In Fig. V.5, the maximum tensile stress corresponds to the nucleation of partial dislocations, in agreement with results for uniaxial tension of nickel single crystals by Kitamura *et al*. (1997). In this work, the bicrystal interface serves as the source for partial dislocations. Figures V.6(a) and V.6(b) show the maximum tensile stress and the critical resolved shear stress in the {111}<112> system, respectively, during uniaxial tensile deformation of copper <100> interface models as a function of the misorientation angle of the interface. For

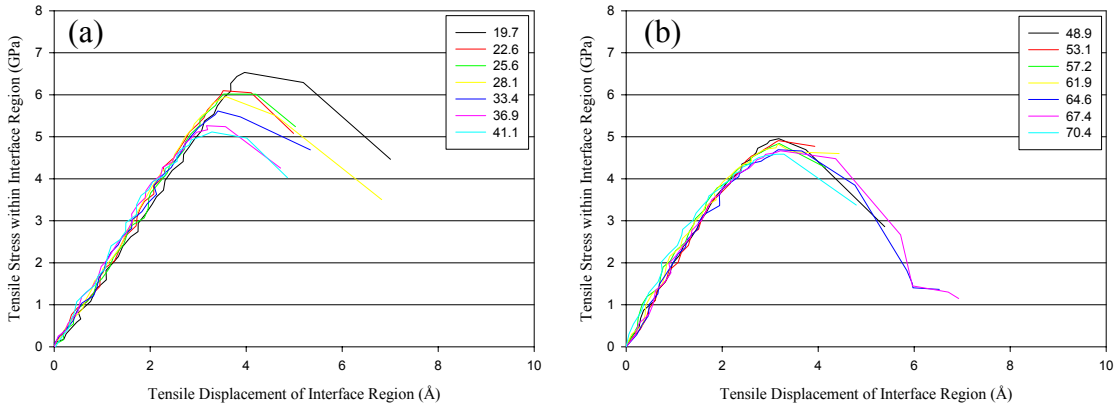

Figure V.5. Tensile stress versus tensile displacement of the interface region during uniaxial tension of <001> tilt bicrystal interface models in copper.

comparison, several single crystal calculations are also reported in Fig. V.6 to determine the importance of the lattice orientation on the magnitude of the peak tensile strength. With these boundary conditions, it appears that the orientation of the lattice with respect to the load is a critically important parameter required to model the strength of the interface. The relationship between interface strength and interface misorientation angle follows a form very similar to that of the single crystal models. Note that the resolved shear stress required for dislocation emission for single crystal models is always greater than that for the bicrystal interface models. This provides addition evidence that the interface is the root of failure in these calculations.

Figure V.7 shows images of the Σ5 (310) 36.9^{o} interface model in copper at 300 K subjected to uniaxial tension boundary conditions. All images are colored according to the centrosymmetry parameter (Kelchner *et al*., 1998) which is a scalar quantity designed to identify atoms in defect configurations. In Fig. V.7, atoms with a centrosymmetry parameter close to zero are removed to facilitate viewing of the defect structures. Images

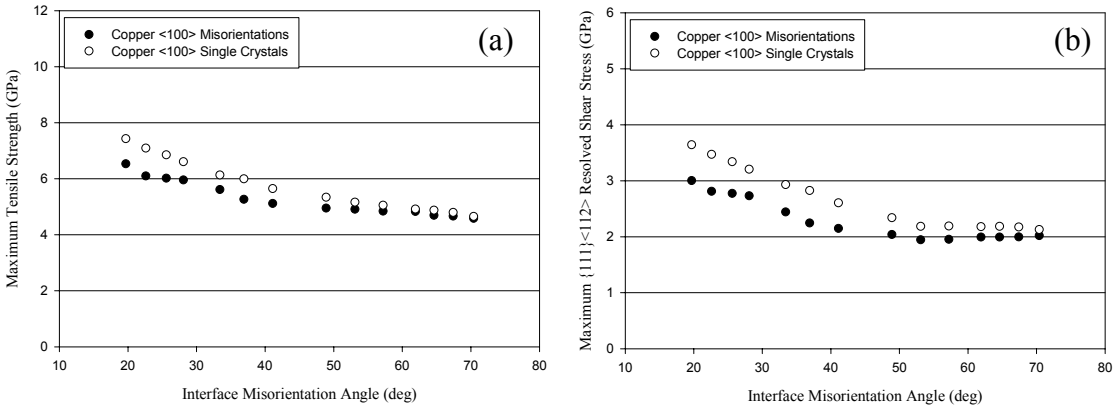

Figure V.6. (a) Maximum tensile strength and (b) {111}<112> critical resolved shear stress as a function of orientation during uniaxial tension for bicrystal interface models and single crystal models in copper.

in Fig. V.7 indicate that partial dislocations with both edge and screw character are nucleated from the bicrystal interface as a result of the applied mechanical deformation. Specifically, the centrosymmetry parameter identifies the intrinsic stacking fault that connects the partial dislocation core back to the interface. For these simulations, the trailing partial dislocation is not nucleated from the interface, contrary to simulations in Chapter IV for a Σ5 (310) 36.9^{o} interface in aluminum. This observation is in agreement with that of Van Swygenhoven *et al*. (2004) who argue that extended partial dislocations are the predominant mode of failure for materials that have γ_{US}/γ_{ISF} much greater than one (as is the case with copper). Analysis of the defect configurations in Fig. V.7 reveals that partial dislocations are nucleated nearly simultaneously on both the (111) and $(11\bar{1})$ slip planes in the lower lattice region and on both the $(\bar{1}11)$ and $(\bar{1}1\bar{1})$ slip planes in the upper lattice region. Thus, interface failure occurs via activation of two slip systems, which is in agreement with that predicted using a Schmid factor analysis (*cf.* Hosford,

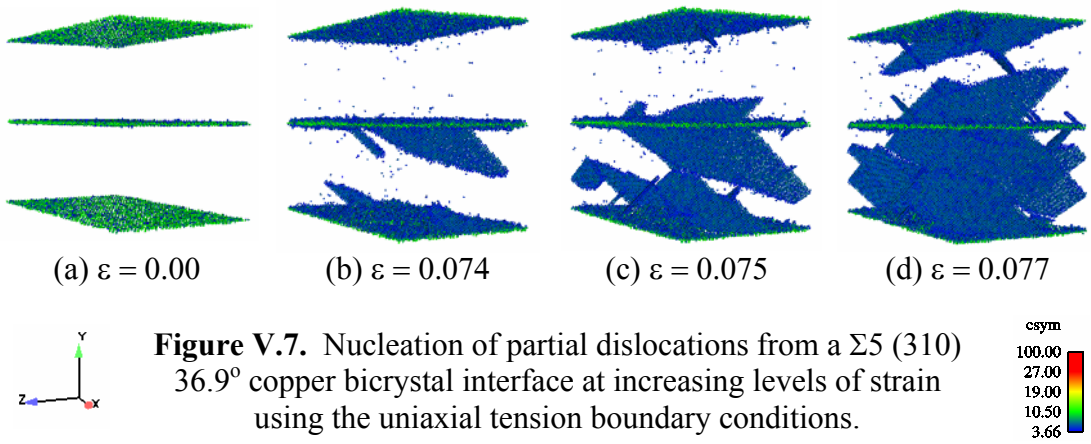

Figure V.7. Nucleation of partial dislocations from a Σ5 (310) 36.9° copper bicrystal interface at increasing levels of strain using the uniaxial tension boundary conditions.

1993). In general, each of the interface misorientations examined in this work has at least two slip systems activated during the tensile deformation process.

The critical resolved shear stress in the {111}<112> system is plotted for each misorientation in Fig. V.6(b). The CRSS for both single crystal and interface models decreases smoothly as the misorientation of the lattice is increased from 0° to 90° around the <100> misorientation axis. Thus, while the primary slip systems are activated in each case, as indicated in Fig. V.7, the relationship between the critical resolved shear stress and the lattice orientation shows definite non-Schmid behavior. The evolution of the CRSS as a function of orientation is likely due to the magnitude of other (non-glide direction) stress components acting on the slip plane. Experiments by Nagata and Yoshida (1972) showed that the critical resolved shear stress of copper single crystals subjected to a uniaxial *static* tension was essentially independent of the crystal orientation (Schmid behavior). However, for *dynamic* loading conditions (>10^3 s^{-1}), the critical resolved shear stress exhibited a mild dependence on the crystal orientation. Specifically, crystals with orientations close to <001> (0°) had a higher critical resolved shear strength than crystals oriented near <011> (90°), in agreement with that shown in Fig. V.6(b).

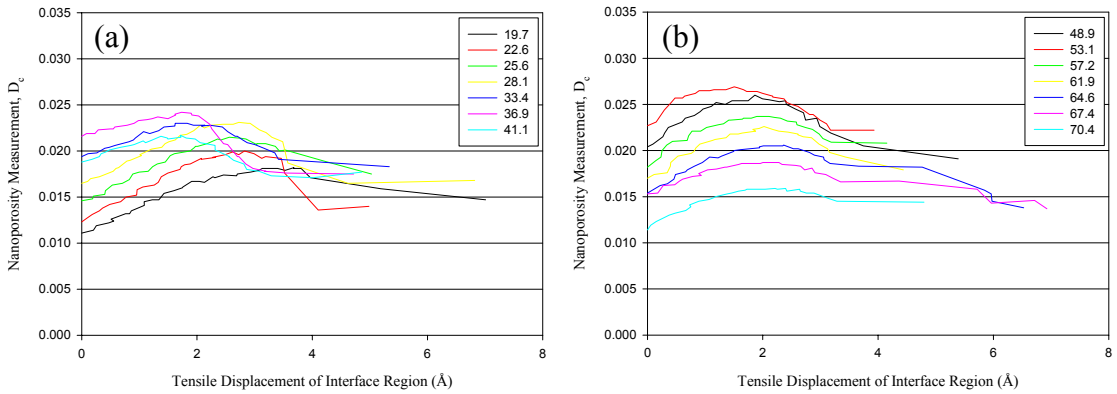

Figure V.8. Interface nanoporosity versus tensile displacement of the interface region during uniaxial tension of <001> tilt bicrystal interface models in copper.

First principles calculations by Ogata *et al*. (2002) also show that non-glide stresses acting on the slip plane can play a role in the calculated critical resolved shear stress.

Phenomenological theories to address the influence of non-glide stresses on the yield of single crystals have been developed by Qin and Bassani (1992), Dao and Asaro (1993) and Steinmann *et al*. (1998). While these theories are aimed at describing non-Schmid behavior in body-centered cubic (BCC) or intermetallic alloys with $L1_2$ structure, these models generally predict that the yield stress for dislocation nucleation is reduced by the presence of tensile stresses normal to the slip plane. For the orientations considered in this section, the magnitude of the tensile stress normal to the slip plane increases as the orientation of the model is increased from 0^o to 90^o around the <001> axis. This increase in the tensile stress normal to the slip plane contributes to the decrease in the magnitude of the CRSS. For example, the magnitude of the tensile stress normal to the slip plane in the 70.4^o misorientation is nearly 50% larger than that in the 19.7^o misorientation.

The evolution of the nanoporosity measure during uniaxial tensile deformation of the copper <100> bicrystal interface models is shown in Figs. V.8(a) and V.8(b). The nanoporosity measure is calculated using Eq. (V.2) and is averaged over the same region as the stress and the displacement. From Fig. V.8, the nanoporosity measure appears to be a unique way to initially differentiating between interfaces with different misorientations. The boundaries with the lowest porosity are those with misorientations closest to the low-angle (dislocation) regimes. The nanoporosity measure shows a similar evolution for each of the <001> boundaries examined in copper. In general, the porosity within the interface region initially increases during elastic deformation. At a given tensile displacement, the porosity within the interface region begins to decrease. For certain boundaries, like the $\Sigma 5$ (310) 36.9^{o} interface, this critical displacement occurs prior to the tensile displacement associated with the peak tensile strength. In this case, the reduction in the interface porosity is associated with a coarsening of the interface region around the interface plane. This is seen in Fig. V.7(b), as the thickness of the interface (as identified via the centrosymmetry parameter) in the center of the model is larger than that in Fig. V.7(a). The interface coarsening effectively improves the local coherency of the interface for certain interfaces. On the other hand, as the misorientation of the interface is reduced towards the [001] orientation (0^{o}), the displacement associated with the maximum porosity and the displacement associated with the peak tensile strength begin to coincide. Here, the coarsening of the interface plane is less prevalent for these boundaries due to the periodic regions of perfect lattice (D structural unit) along the interface plane (Chapter III; Sutton and Vitek, 1983a). While the nanoporosity measure is capable of initially differentiating between boundaries, porosity does not

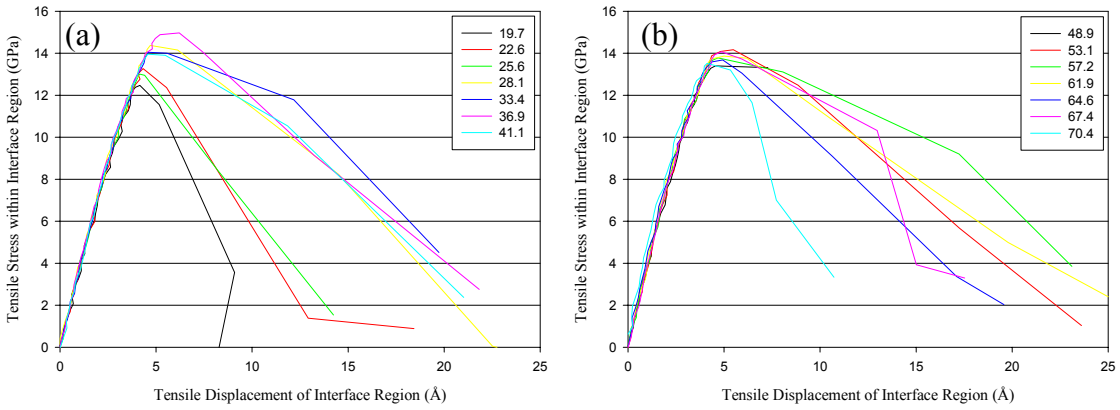

Figure V.9. Tensile stress versus tensile displacement of the interface region during constrained tension of <001> tilt bicrystal interface models in copper.

appear to be the primary mechanism that affects the magnitude of the peak tensile strength. Since the maximum tensile stress of the interface model is associated with the nucleation of dislocations on the primary slip systems, the orientation of the lattice is apparently the most important factor in the description of the interface strength.

V.4.1.2 Constrained tensile deformation

Figures V.9(a) and V.9(b) show the tensile stress-displacement response for copper bicrystal interface models subjected to a constrained tensile deformation for a range of <100> tilt misorientations. Tensile stress and displacement are calculated over a region around the bicrystal interface, as defined in Section V.2. In Fig. V.9, the peak tensile stress corresponds to the nucleation of partial dislocations from the bicrystal interface. The tensile stress required for dislocation emission in significantly higher with the constrained tension boundary conditions due to the tensile stresses that develop transverse to the loading direction during the deformation process.

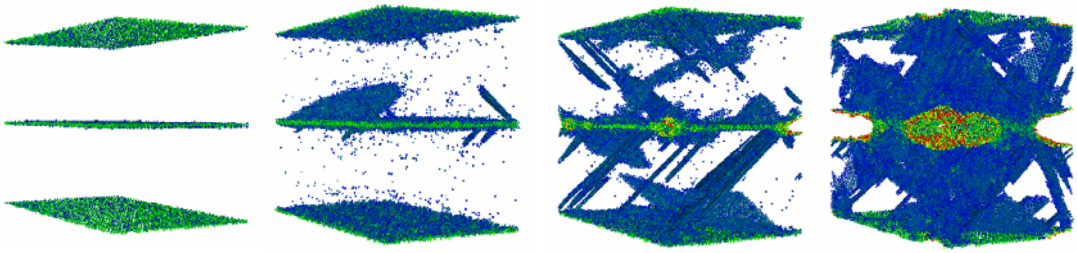

Figure V.10. Nucleation of partial dislocations from a Σ5 (310) 36.9° copper bicrystal interface at increasing levels of strain using the constrained tension boundary conditions.

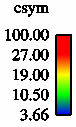

Apparently, the constrained tension deformation condition also promotes the nucleation of voids along the interface plane after the peak tensile stress has been reached, as shown in Fig. V.10 for a Σ5 (310) 36.9° interface model in copper at 300 K. All images in Fig. V.10 are colored according to the centrosymmetry parameter (Kelchner *et al*., 1998). Again, atoms with a centrosymmetry parameter close to zero are removed to facilitate viewing of the defect structures. Note that the interface models shown Fig. V.7 and Fig. V.10 are oriented in an identical manner. Images in Fig. V.10 indicate that partial dislocations with both edge and screw character are nucleated from the bicrystal interface as a result of the applied mechanical deformation. Analysis of the defect configurations in Fig. V.10 reveals that partial dislocations are nucleated nearly simultaneously on the (111) and $(11\bar{1})$ slip planes in the lower lattice region and on the $(\bar{1}11)$ and $(\bar{1}1\bar{1})$ slip planes in the upper lattice region. Thus, the activated slip planes appear to be independent of the applied boundary conditions, i.e., dislocations are nucleated in the same slip systems regardless of whether uniaxial tension or constrained tension deformation conditions are prescribed.

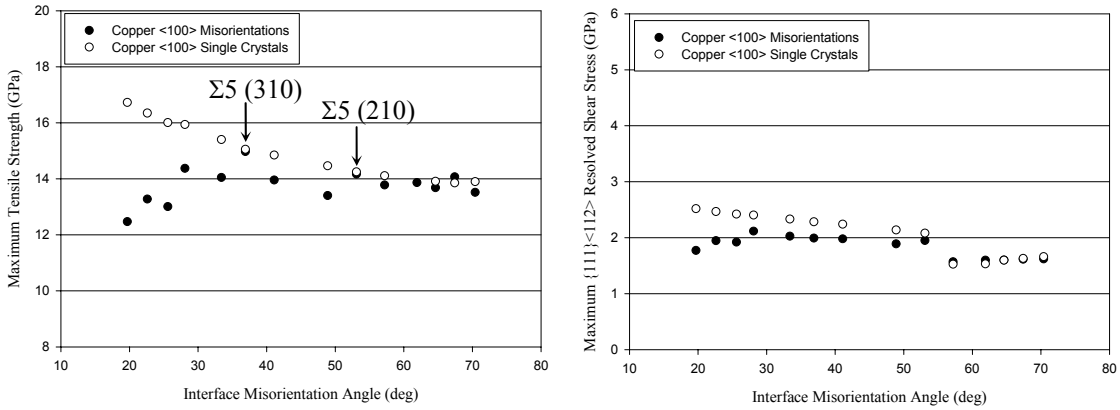

Figure V.11. (a) Maximum tensile strength and (b) {111}<112> critical resolved shear stress as a function of orientation during constrained tension for bicrystal interface models and single crystal models in copper.

Voids are nucleated along the interface when deformation is performed using the constrained tension boundary conditions, as shown in Figs. V.10(c) and V.10(d). Void nucleation occurs after several partial dislocations have been emitted from the interface. The nucleated voids grow and coalesce during the deformation process, eventually leading to complete separation of the interface. Recall that failure of the interface is dominated solely by partial dislocation slip activity when the model is subjected to a uniaxial tensile deformation. This appears to be the primary difference between the two boundary prescriptions. The multiaxial state of tensile stress, which arises due to the constraints placed on the boundaries of the simulation cell transverse to the load, leads to a more brittle mode of failure as compared with the uniaxial tensile deformation. This observation was also noted by Kitamura *et al*. (1997) for single crystals.

Figure V.11 shows the maximum tensile stress and the {111}<112> critical resolved shear stress calculated during constrained tensile deformation of the copper <100> interface models as a function of the misorientation angle of the interface. For

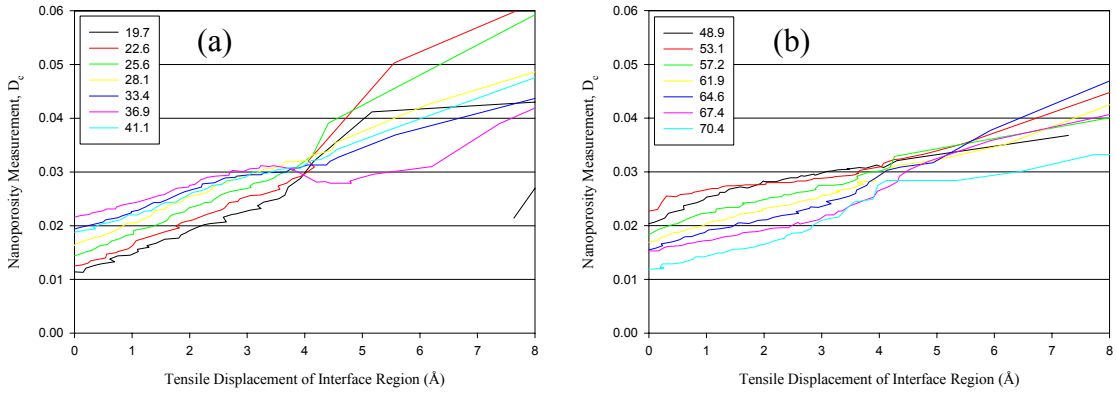

Figure V.12. Interface nanoporosity versus tensile displacement of the interface region during constrained tension of <001> tilt bicrystal interface models in copper.

comparison, several single crystal calculations are also reported in Fig. V.11, to evaluate the role of lattice orientation on the magnitude of the peak tensile strength. First, it is clear that the relationship between maximum tensile strength and interface misorientation angle for single crystals follows a trend very similar to that observed using the uniaxial tension boundary conditions. The maximum tensile strength decreases smoothly as the orientation of the lattice is increased from 0^o to 90^o around the <100> axis. On the other hand, the relationship between interface strength and misorientation angle is remarkably different for the bicrystal interface models. Here, local peaks are observed in the interface strength versus misorientation angle relationship, as shown in Fig. V.11(a). These peaks correspond to two low-order CSL boundaries ($\Sigma 5$ and $\Sigma 13$). Thus, in copper the tensile strength of the interface appears to show a modest increase at low-order CSL boundaries when lateral confinement of the interface region is an important factor.

Note that some non-Schmid effects are observed for constrained tensile deformation of single crystal models in Fig. V.11(b). However, the magnitude of the

non-Schmid behavior is not as significant as that shown with uniaxial tension boundary conditions. Also the CRSS calculated with the constrained tension boundary conditions is less than that calculated using uniaxial tension boundary conditions. This difference is related to the increased tensile stresses normal to the slip plane in the constrained case. The abrupt drop at the 57.2° boundary in Fig. V.11(b) is due to a change in the character of the partial dislocation activity. Dislocation activity remains on the $(11\bar{1})[101]$ slip system for each orientation (for example); however, the activated partial dislocation direction changes from $(11\bar{1})[2\bar{1}1]$ to $(11\bar{1})[112]$ as the misorientation angle is increased above 53.1°

The evolution of the nanoporosity measure during constrained tensile deformation of the copper <100> bicrystal interface models is shown in Figures V.12(a) and V.12(b). The nanoporosity measure is calculated using Eq. (V.2) and is averaged over the same region as the stress and the displacement. The evolution of the nanoporosity measure is quite different using the constrained tension boundary conditions as compared with that shown in Fig. V.8. In general, the porosity within the interface region shows a positive trend over the course of the tensile deformation process. This indicates the formation and growth of voids within the interface region. Some boundaries, such as the Σ5 (310) 36.9° interface, show either a brief decrease in the porosity or a plateau region prior to reaching the displacement associated with the peak tensile strength. This observation is associated with an elastic coarsening of the interface region. At a displacement of approximately 4.0 Å, a switch occurs in Fig. V.12(a) in the ordering of the boundaries. This switch is related to the ease at which voids are created after the nucleation of dislocations. For the 19.7° boundary, for example, the nucleation of dislocation and the formation of void

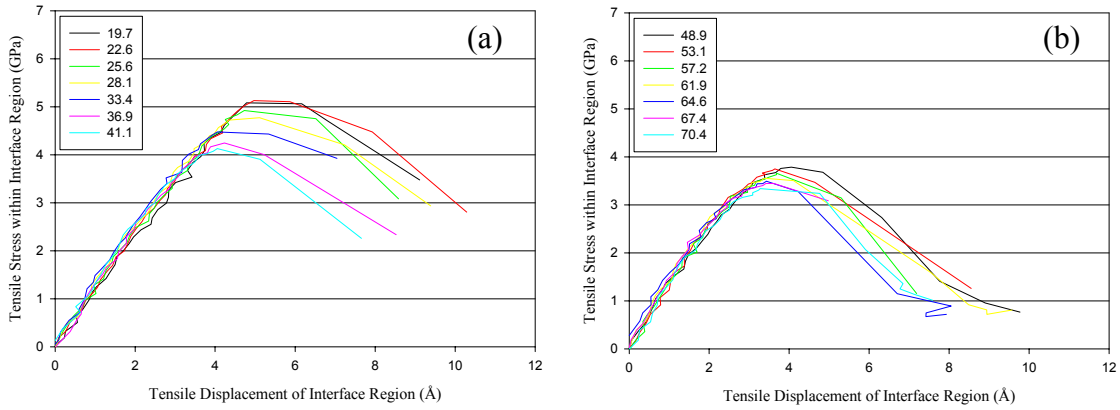

Figure V.13. Tensile stress versus tensile displacement of the interface region during uniaxial tension of <001> bicrystal interface models in aluminum.

happen simultaneously resulting in a sharp increase in the nanoporosity, whereas for the Σ5 (310) 36.9° boundary, there is a brief amount of time between dislocation emission and void nucleation, as shown in Fig. V.10. Note that the nanoporosity measure shows that the Σ5 (310) 36.9° boundary contains the least amount of porosity after the peak tensile stress has been achieved, which in turn is related to the increase in the tensile strength of this particular interface, seen in Figs. V.9 and V.11.

V.4.2 [001] Al Tilt Interfaces

V.4.2.1 Uniaxial tensile deformation

Figures V.13(a) and V.13(b) show the tensile stress-displacement response for aluminum bicrystal interface models subjected to a uniaxial tensile deformation for a range of <100> tilt misorientations. Tensile stress and displacement are calculated over a region around the bicrystal interface, as defined in Section V.2. In Fig. V.13, the maximum tensile stress corresponds to the nucleation of partial dislocations, in agreement

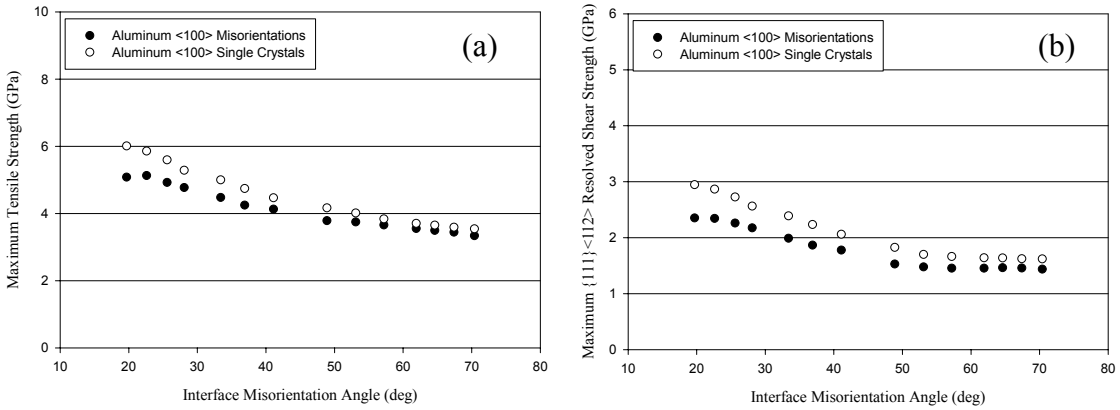

Figure V.14. (a) Maximum tensile strength and (b) {111}<112> critical resolved shear stress as a function of orientation during uniaxial tension for bicrystal interface models and single crystal models in aluminum.

with that in Section V.4.1.1 for copper and with results for uniaxial tension of nickel single crystals in Kitamura *et al*. (1997). In this work, the bicrystal interface serves as the source for partial dislocations, as shown previously in Fig. IV.4 for an aluminum Σ5 (310) 36.9^{o} boundary. Note that the maximum tensile stress required for dislocation nucleation in aluminum is slightly lower than that reported for copper.

Figure V.14 shows the maximum tensile stress and the critical resolved shear stress in the {111}<112> slip system during uniaxial tensile deformation of the aluminum <100> tilt interface models as a function of the misorientation angle of the interface. For comparison, several single crystal calculations are also reported for aluminum in Fig. V.14. Again, Figure V.14(a) shows that the orientation of the lattice with respect to the load is a critically important parameter required to predict the strength of the interface using the uniaxial tension boundary conditions. The relationship between interface strength and interface misorientation angle follows a form very similar to that of the single crystal models.

Recall images of the Σ5 (310) 36.9° bicrystal interface in aluminum during uniaxial tension deformation at 10 K and 300 K presented in Chapter IV. Images in Fig. IV.4, for example, indicate that full dislocation loops with both edge and screw character are nucleated from the aluminum bicrystal interface as a result of the applied mechanical deformation. Analysis of the defect configurations revealed that full dislocation loops are nucleated on both the (111) and $(11\bar{1})$ slip planes in the lower lattice region and on both the $(\bar{1}11)$ and $(\bar{1}1\bar{1})$ slip planes in the upper lattice region. These slip planes correspond to the primary slip systems as predicted using a Schmid factor analysis (*cf.* Hosford, 1993).

Accordingly, the critical resolved shear stress in the primary {111}<112> system is plotted for each aluminum misorientation in Fig. V.14(b). Similar to that shown in copper, the CRSS decreases smoothly as the misorientation of the lattice is increased from 0° to 90° around the <100> axis. Thus, while the primary slip systems are activated in each case, the relationship between the critical resolved shear stress and the lattice orientation shows a non-Schmid behavior, comparable to that observed with copper <001> tilt misorientations. The difference in the CRSS for each orientation is likely due to the magnitude of other (non-glide direction) stress components acting on the slip plane and the magnitude of the applied strain rate. First principles simulations by Ogata *et al.* (2002) also show that non-glide stresses within the slip plane can play a role in the calculated critical resolved shear stress in aluminum. In their work, compressive stress applied normal to the slip plane resulted in a hardening behavior in aluminum; thus, it is reasonable to assume that tensile stresses normal to the slip plane lead to a reduction in the CRSS. For example, the magnitude of the tensile stress normal to the slip plane

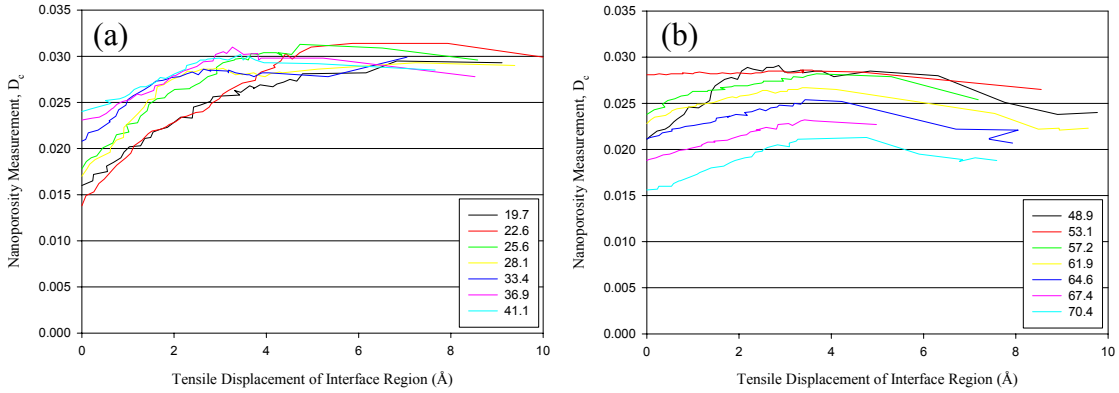

Figure V.15. Interface nanoporosity versus tensile displacement of the interface region during uniaxial tension of <001> bicrystal interface models in aluminum.

increases as the orientation of the model is increased between [001] to [011] orientations, which again likely contributes to the decrease in the magnitude of the CRSS.

The evolution of the nanoporosity measure during uniaxial tensile deformation of the aluminum <100> bicrystal interface models is shown in Figures V.15(a) and V.15(b). The nanoporosity measure is calculated using Eq. (V.2) and is averaged over the same region as the stress and the displacement. Similar to that observed in copper, the nanoporosity measure appears to be a unique way to initially differentiating between interfaces with different misorientations. The boundaries with the lowest porosity are those with misorientations closest to the low-angle [001] and [011] orientations. On the other hand, the nanoporosity measure shows a different evolution in aluminum than that observed in copper for the <100> tilt boundaries. In general, the porosity within the interface region increases to a constant value during the deformation process. Only a few boundaries show a slight decrease in the porosity within the interface region after the nucleation of dislocations. Thus, in aluminum, the coarsening effect that is observed in

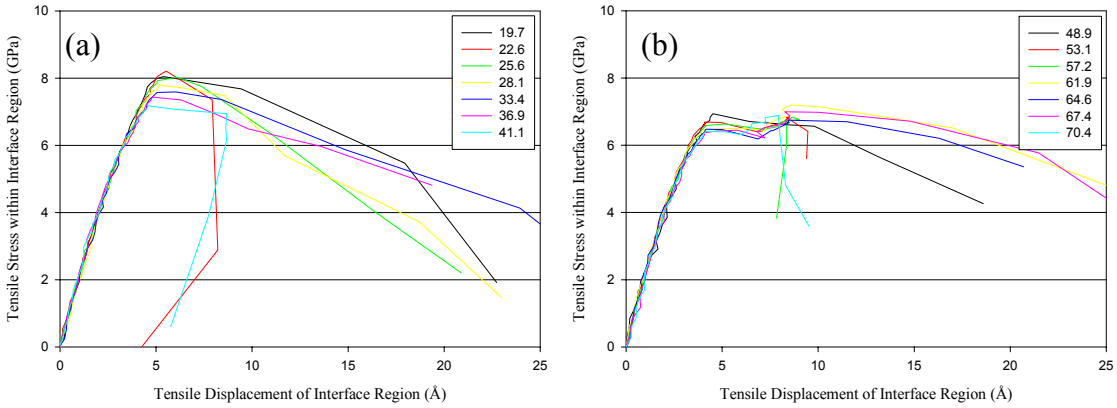

Figure V.16. Tensile stress versus tensile displacement of the interface region during constrained tension of <001> bicrystal interface models in aluminum.

copper does not appear to affect the nanoporosity measurement. While the nanoporosity measure appears to be capable of initially differentiating between boundaries, porosity does not appear to be the primary mechanism that affects the magnitude of the interface strength. Again, the orientation of the individual lattice regions, which is directly related to the relative availability of certain slip systems, drives the deformation response.

V.4.2.2 Constrained tensile deformation

Figures V.16(a) and V.16(b) show the tensile stress-displacement response for aluminum bicrystal interface models subjected to a constrained tensile deformation for a range of <100> tilt misorientations. Tensile stress and displacement are calculated over a region around the bicrystal interface, as defined in Section V.2. Here, the magnitude of the peak tensile strength is significantly larger than that shown in Fig. V.13 due to the stresses that develop transverse to the load during the deformation process. However, the peak stresses reported in Fig. V.16 are still lower than those in copper with constrained

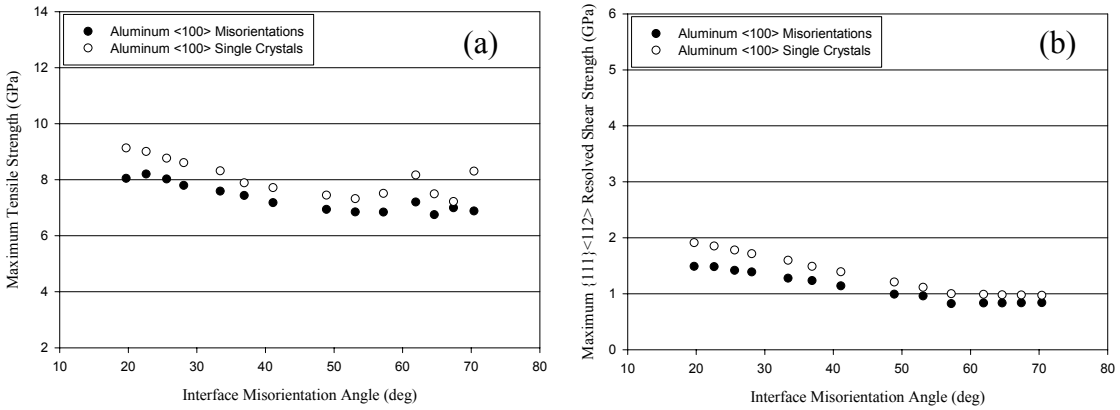

Figure V.17. (a) Maximum tensile strength and (b) {111}<112> critical resolved shear stress as a function of orientation for bicrystal interface models and single crystal models in aluminum subjected to constrained tension boundary conditions.

tension boundary conditions. In Fig. V.16(a), the peak tensile stress corresponds to the nucleation of partial dislocations from the bicrystal interface which is followed by the nucleation of voids along the interface plane. In Fig. V.16(b), two peaks are observed in the tensile stress-displacement relationship. The first peak is associated with the nucleation of partial dislocations from the bicrystal interface, while the second peak is associated with the nucleation of voids along the interface plane. The observation of void nucleation and growth using constrained tension boundary condition is in agreement with molecular dynamics simulations in copper in the Section V.4.1.2.

Figure V.17 shows the maximum tensile stress and the {111}<112> critical resolved shear stress recorded during constrained tensile deformation of the copper <100> interface models as a function of the misorientation angle of the interface. For comparison, several single crystal calculations are also reported in Fig. V.17 to evaluate the role of lattice orientation on the magnitude of the peak tensile strength. First, it is clear that the relationship between maximum tensile strength and interface misorientation

angle for single crystals follows a trend very similar to that observed using the uniaxial tension boundary conditions. In general, the maximum tensile strength decreases as the misorientation angle is increased, although some scatter is observed in the data for misorientations above 61.9^{o}. Contrary to that observed in copper, the relationship between interface strength and interface misorientation angle follows a form similar to the single crystal models. Local peaks are not observed in the interface strength versus misorientation angle relationship at the low-order CSL boundaries ($\Sigma 5$ and $\Sigma 13$). Thus, confinement of the interface region during the tensile deformation process appears to affect copper and aluminum interface models differently. While this conclusion is mildly surprising, Ogata *et al*. (2002) showed that dislocation nucleation processes in copper and aluminum were inherently different, particularly in the way that non-glide stresses affect the resolved shear strength. This difference in nucleation character potentially contributes to the observations reported in Fig. V.17.

The evolution of the nanoporosity measure during constrained tensile deformation of the aluminum <100> bicrystal interface models is shown in Figures V.18(a) and V.18(b). The nanoporosity measure is calculated using Eq. (V.2) and is averaged over the same region as the stress and the displacement. The evolution of the nanoporosity measure is quite different using the constrained tension boundary conditions as compared with that observed for the uniaxial case. In general, the porosity within the interface region increases continuously during the tensile deformation process. This indicates void formation and growth occurs during the applied mechanical deformation. At a displacement of approximately 5.0 Å (displacement associated with peak tensile strength), a switch occurs in Fig. V.18(a) in the ordering of the boundaries. This switch

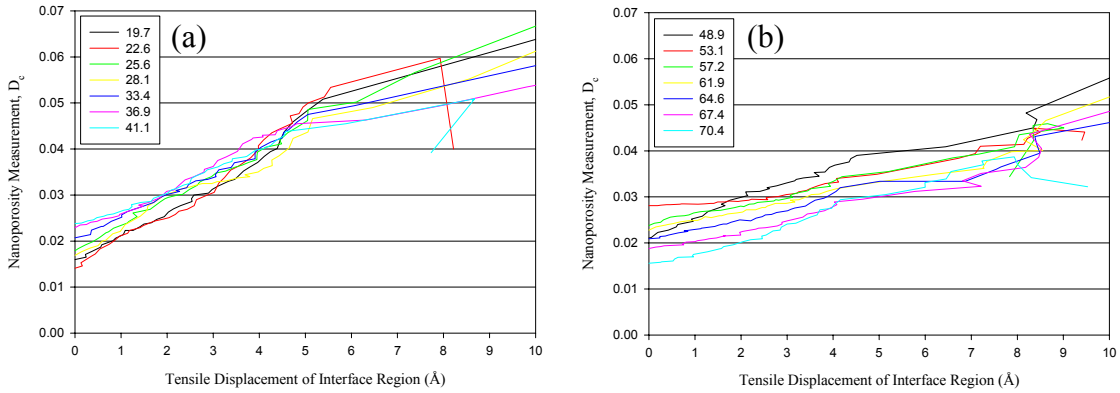

Figure V.18. Interface nanoporosity versus tensile displacement of the interface region during constrained tension of <001> bicrystal interface models in aluminum.

is related to the ease at which voids are created after the nucleation of dislocations, similar to that observed in copper. For the Σ5 (310) 36.9^o boundary, for example, there is a brief duration of time between dislocation emission and void nucleation. On the other hand, for the 19.7^o boundary, dislocation and void nucleation happen nearly simultaneously resulting in a distinct increase in the nanoporosity. In general for both copper and aluminum, as the misorientation angle of the <100> interface is reduced towards 0^o, the delay time between dislocation nucleation and void nucleation events decreases. Further, for the <100> boundaries, the nanoporosity measure appears to be more applicable in copper with regard to differentiation and characterization of the interface structure evolution than in aluminum.

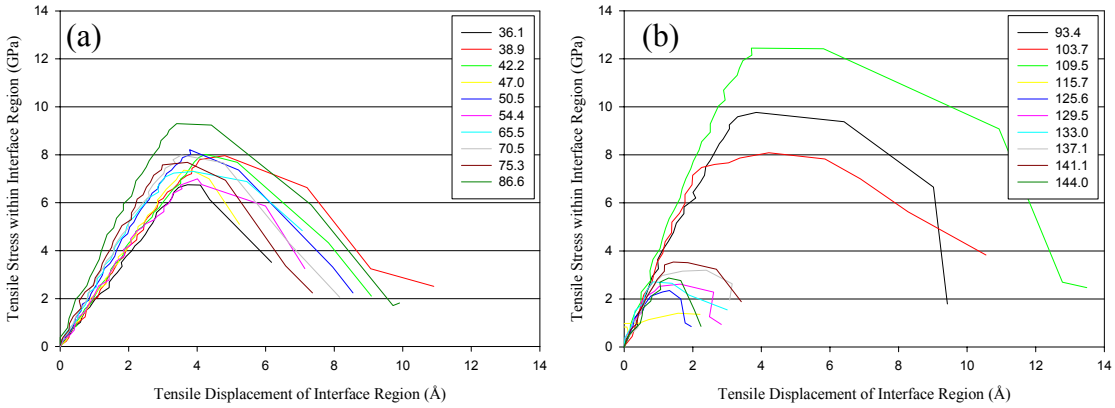

Figure V.19. Tensile stress versus tensile displacement of the interface region for <110> copper bicrystal interface models subjected to a uniaxial tensile deformation.

V.4.3 [1$\bar{1}$0] Cu Tilt Interfaces

V.4.3.1 Uniaxial tensile deformation

Figures V.19(a) and V.19(b) show the tensile stress-displacement response for copper bicrystal interface models subjected to a uniaxial tensile deformation for a range of <110> tilt misorientations. Tensile stress and displacement are calculated over a region around the bicrystal interface, as defined in Section V.2. The peak tensile stress corresponds to the nucleation of partial dislocations. This observation is in agreement with the molecular dynamics simulation results presented in Section V.4.1 for copper <100> tilt misorientations and with results for uniaxial tension of nickel single crystals in Kitamura *et al*. (1997). Here, the interface serves as the source for dislocations in all cases except the Σ3 (111) coherent twin boundary. For this interface, dislocations are nucleated homogeneously within each lattice.

Clearly, the interface structure plays a role in the tensile deformation response as the maximum tensile stress and the displacement associated with the peak tensile stress

both vary significantly for each <110> tilt misorientation considered. Figure V.19(b) shows that the coherent Σ3 (111) 109.5^{o} interface has the highest tensile strength as compared with the other misorientations presented. Recall that this observation is contrary to that found by Sansoz and Molinari (2005) for deformation in shear. The Σ3 boundary has a high propensity to migrate when subjected to tangential deformation. A large abrupt decrease is observed in the tensile strength and the tensile work of separation as the misorientation angle of the interface is increased beyond 109.5^{o}. Here, the character of the interface structure and the orientation of the primary slip systems with respect to the load both contribute to this significant drop in the interface strength. Specifically, boundaries with <110> misorientations less than 109.5^{o} deform via partial dislocation nucleation on either of two slip planes, with one slip direction active within each slip plane. On the other hand, boundaries with misorientations greater than 109.5^{o} deform by dislocation emission on one slip plane only, with two directions active within that slip plane, i.e., coplanar slip systems. In addition, many boundaries in this range of <110> misorientations contain the E structural unit. Sansoz and Molinari (2005) reported that the E structural unit has increased free volume as compared with the other structural features for the <110> misorientation axis. In their work, the increased free volume inherent to the E structural unit triggered a change in the shear deformation mode.

Figure V.20 shows images of dislocation nucleation from two example <110> copper boundaries with misorientations greater than 109.5^{o}. Specifically, Figs. V.20(a) and V.20(b) show the initial (equilibrated to 0 bar and 300 K) and distorted configurations of the 115.7^{o} boundary, respectively. Figures V.20(c) and V.20(d) show the initial and distorted structures of the Σ9 (221) 141.1^{o} interface, respectively. Atoms

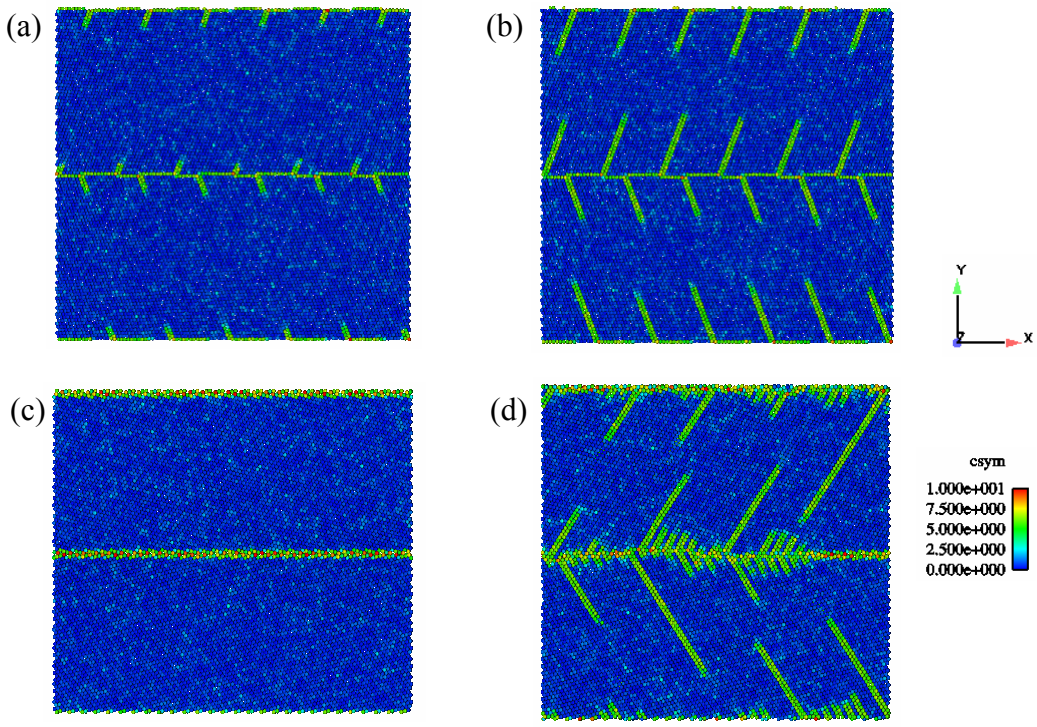

Figure V.20. Initial and deformed copper interface models showing the nucleation of partial dislocations from (a) and (b) a 115.7° <110> interface; (c) and (d) a Σ9 (221) 141.1° interface.

are colored by the centrosymmetry parameter (Kelchner *et al*., 1998) and projected into the X-Y plane for clarity. The 115.7° copper boundary consists entirely of D structural units (similar to that of the coherent Σ3 boundary); however, one of the D structural units is dissociated and lies at the termination of an intrinsic stacking fault (ISF) facet that extends from the interface plane, similar to that shown in Chapter IV. Further, the interface structure involves a small step or ledge at a periodic distance along the interface plane. The ISF facet is emitted on the $(11\bar{1})$ slip plane in the lower lattice region, which is the primary slip plane for loading normal to the 115.7° interface. For reference, the structural unit model predicts that the 115.7° boundary should be composed of both E and D structural units (with the E structural unit in the place of the dissociated structural unit).

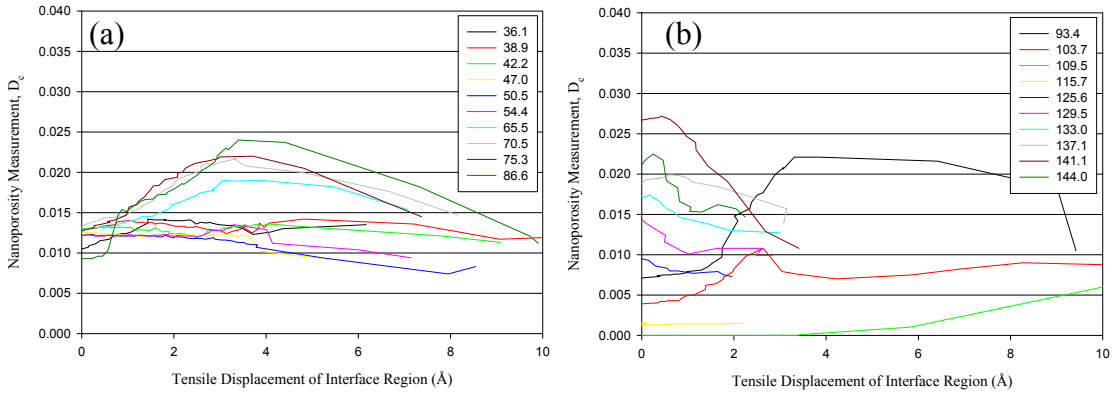

Figure V.21. Interface nanoporosity versus tensile displacement of the interface for <110> copper interface models subjected to a uniaxial tensile deformation.

Figure V.20(b) shows that failure of the 115.7° interface occurs via partial dislocation nucleation and motion on the primary slip plane. Essentially, the ISF facets simply glide away from the interface when subjected to the uniaxial tensile deformation.

The 141.1° boundary in Fig. V.20(c) consists entirely of E structural units in agreement with the structural unit model representation of interfaces (Wang *et al.*, 1984). Figure V.20(d) shows that dislocations are nucleated from the interface on the primary slip planes, similar to that which occurs for the 115.7° boundary. For example, in the lower lattice region the $(11\bar{1})$ slip plane is activated with slip occurring in both [101] and [011] directions. Note, the orientation of the image in Fig. V.20(d) gives the impression that the entire slip plane through the thickness of the interface model is activated during the tensile deformation process. While this eventually becomes true, as partial dislocations glide away from the interface during the coplanar slip process, the dislocations are initially nucleated over discrete sections of the interface. This provides

additional confirmation that the thickness, B, of the interface model used in these calculations does not significantly influence the dislocation nucleation event.

The evolution of the nanoporosity measure during uniaxial tensile deformation of the copper <110> bicrystal interface models is shown in Figures V.21(a) and V.21(b). The nanoporosity measure is calculated using Eq. (V.2) and is averaged over the same region as the stress and the displacement. Clearly, the initial interface structure affects the form of the porosity evolution within the interface region. First, the nanoporosity measure for boundaries with <110> misorientations less than 54.4^o remains relatively constant during the uniaxial tensile deformation process. Second, for boundaries with misorientations between 54.4^o and 109.5^o, the porosity within the interface region initially increases prior to the dislocation nucleation event and then decreases after the interface model has reached its critical strength. Recall from Chapter III that these boundaries commonly have a dissociated structure which involves several variations of different interface structural units (as defined in Wang *et al*., 1984) and stacking fault facets that span multiple lattice planes on non-primary slip systems. The structural evolution and dislocation nucleation process for these interfaces is highly complicated and involves interactions between different interface features over multiple length scales, as shown with the 59.0^o copper interface in Chapter IV. Third, for boundaries with misorientations above 125.6^o the porosity within the interface region decreases nearly immediately after the model is subjected to a tensile deformation. This decrease is associated with the nucleation of several short intrinsic stacking fault facets, from the E structural unit as shown in Fig. V.20(d), analogous to the coarsening effect seen for <100> copper boundaries. The formation of the ISF facets improves the coherency of the

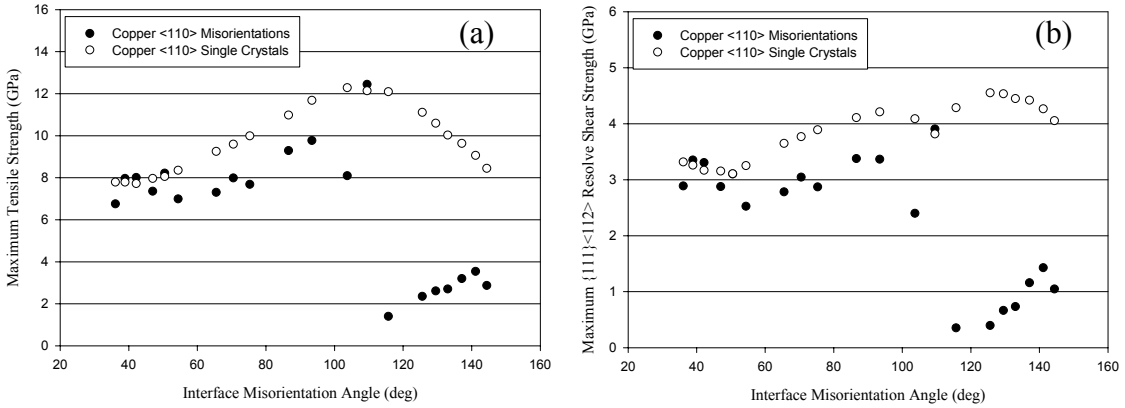

Figure V.22. (a) Maximum tensile strength and (b) {111}<112> critical resolved shear stress as a function of orientation for bicrystal interface models and single crystal models in copper subjected to uniaxial tension boundary conditions.

boundary by reducing the free volume at the point where they are attached. Interfaces which have a larger number of E structural units show a greater decrease in the rate of porosity reduction in Fig. V.21. Finally, note that the Σ9 (221) 141.1^{o} boundary, which is composed entirely of E structural units, has the highest initial interface porosity. This observation is in agreement with the conclusions in Sansoz and Molinari (2005).

While the nanoporosity measure appears to be capable of differentiating between dissimilar groups of boundaries, porosity does not appear to be the only mechanism that affects the magnitude of the peak tensile strength. Figure V.22(a) shows the maximum tensile stress during uniaxial tensile deformation of the copper <110> interface models as a function of the misorientation angle of the interface. For comparison, several single crystal calculations are also reported to determine the role of the lattice orientation on the magnitude of the peak tensile strength. These results reemphasize the abrupt drop in the maximum tensile strength for <110> boundaries with misorientations above 109.5^{o}. The nanoporosity measure on its own does not appear capable of capturing this effect

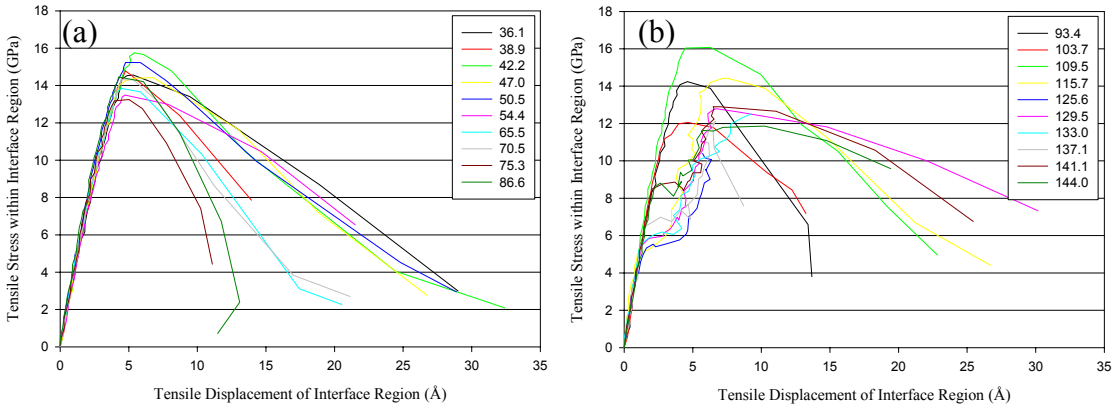

Figure V.23. Tensile stress versus tensile displacement of the interface region for <110> copper bicrystal interface models subjected to constrained tensile deformation.

completely. For example, the Σ9 (221) 141.1° boundary has an initial porosity nearly twice that of the Σ11 (332) 129.5° boundary; however, the maximum tensile strength of the Σ9 boundary is slightly larger than that of the Σ11 boundary. Additional measures may be required, such as a gradient of porosity, to characterize the interaction between different structural features.

V.4.3.2 Constrained tensile deformation

Figures V.23(a) and V.23(b) show the tensile stress-displacement response for copper bicrystal interface models subjected to constrained tensile deformation for a range of <110> misorientations. The calculated maximum tensile strength for each <110> boundary is significantly larger using the constrained tension boundary conditions than using the uniaxial tension boundary conditions reported in Fig. V.19. This observation is a direct result of the tensile stresses that develop parallel to the interface plane during the deformation process, resulting in a multiaxial state of tensile stress. Here, the peak

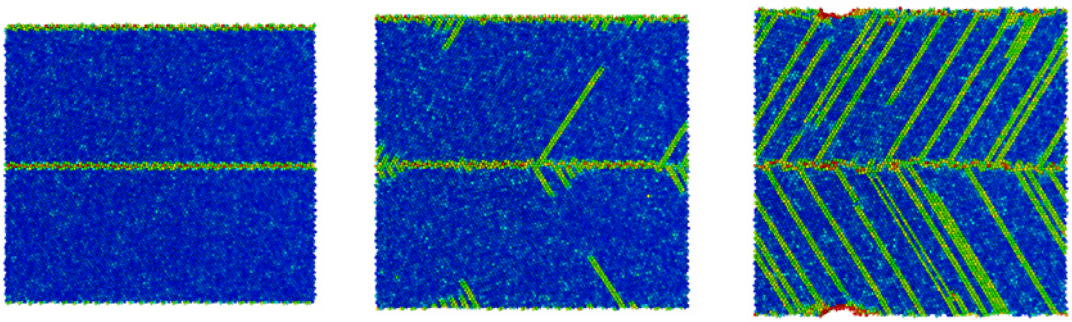

(a) (b) (c)

Figure V.24. Nucleation of dislocations and voids from a Σ9 (221) 141.1° copper interface. Atoms are colored by the centrosymmetry parameter.

tensile stress corresponds to either the nucleation of dislocations or the nucleation of voids within the bicrystal interface model. For example, for each of the misorientations presented in Fig. V.23(a), the maximum tensile stress corresponds to the nucleation of dislocations from the interface, which is quickly followed by the nucleation of voids along the interface plane. However, for boundaries with <110> misorientations greater than 109.5°, such as the Σ9 (221) 141.1° interface shown in Fig. V.24, two distinct peaks are observed. The first (smaller) peak is associated with the nucleation of dislocations from the interface on the primary coplanar slip systems. The second (ultimate) peak corresponds to the nucleation of voids along the interface plane. Here, dislocations are nucleated well before the peak tensile strength is reached due to the orientation of the lattice and the presence of the E structural unit. Similar to the calculations which used uniaxial tension boundary conditions, Fig. V.23(b) shows that the coherent Σ3 (111) 109.5° interface has the largest tensile strength as compared with the other misorientations. However, recall that for this boundary, the interface does not serve as

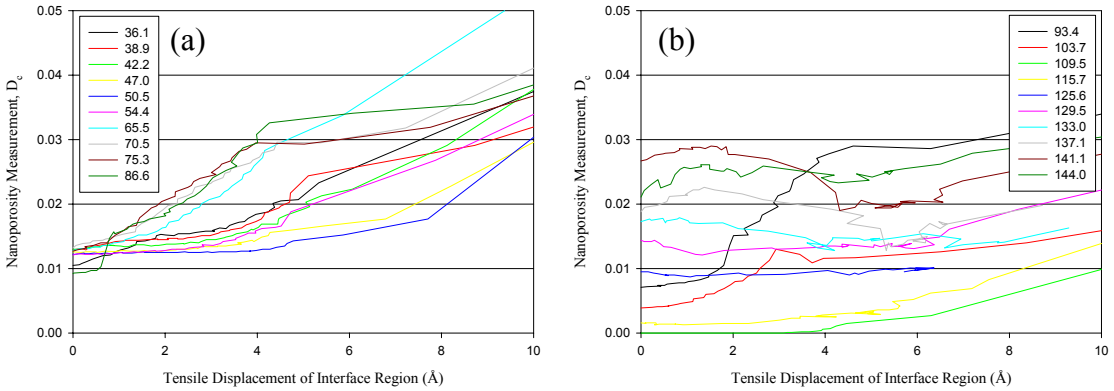

Figure V.25. Interface nanoporosity versus tensile displacement of the interface for <110> copper interface models subjected to constrained tensile deformation.

the source for dislocations, i.e., the peak stress is associated with the homogeneous nucleation of dislocations in each lattice region.

The evolution of the nanoporosity measure during constrained tensile deformation of copper <110> bicrystal interface models is shown in Figs. V.25(a) and V.25(b). Similar to the uniaxial calculations, dissimilar groups of interface structural units evolve differently during the deformation process. Recall that with uniaxial tension boundary conditions, the nanoporosity measure remained relatively constant for boundaries with <110> interface misorientations less than 54.4^o. In Fig. V.25(a), with the constrained tension boundary conditions, the nanoporosity measure shows a noticeable increase after the tensile displacement associated with the maximum tensile stress has been reached (around 4.5 to 5.0 Å). This indicates the development of voids (free volume) within the interface region during the tensile deformation process (images of the deformed interface models confirm this conclusion). Similarly, for boundaries with misorientations between 54.4^o and 109.5^o, the porosity within the interface region increases continuously during

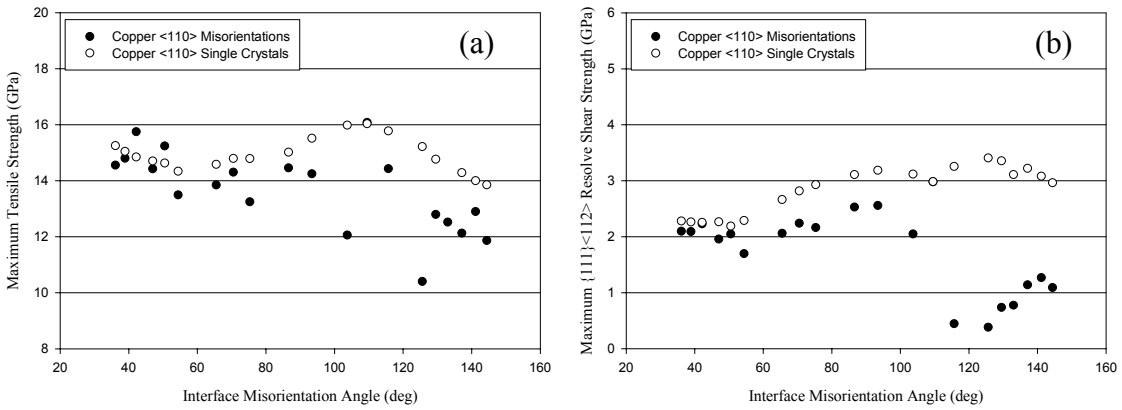

Figure V.26. (a) Maximum tensile strength and (b) {111}<112> critical resolved shear stress as a function of orientation for bicrystal interface models and single crystal models in copper subjected to constrained tension boundary conditions.

the tensile deformation process, whereas in the uniaxial case, the porosity measure decreased after the displacement associated with the maximum tensile strength. The nanoporosity measure for bicrystal boundaries with misorientations above 125.6^{o} shows either a small decrease of an initial plateau region, prior to the dislocation nucleation event. This behavior can be attributed to the nucleation of short ISF facets from the E structural units along the interface plane. However, once the displacement associated with the ultimate tensile strength is reached, the porosity within the interface region for these boundaries begins to increase, indicating the formation of voids as shown in Fig. V.24(c).

Figure. V.26 shows the maximum tensile strength and the critical resolved shear strength in the {111}<112> slip system during constrained tensile deformation of the copper <110> interface models as a function of the misorientation angle of the interface. For comparison, several single crystal calculations are performed to determine the role of the lattice orientation on the peak tensile strength. Here, a modest drop in the peak

tensile strength for boundaries with <110> misorientations greater than 109.5^{o} is observed using the constrained tension boundary conditions, contrary to that observed in the uniaxial case. This discrepancy is a result of the two distinct peaks in the stress-displacement relationship for these boundaries. The ultimate strength is related to the nucleation of voids from the interface. Thus, even though dislocations are nucleated at an early stage of deformation for the Σ9 (221) 141.1^{o} interface, for example, the stress within the interface region continues to increase until voids are formed along the interface plane. The abrupt drop in the dislocation nucleation stress is observed Fig. V.26(b), which shown the CRSS in the {111}<112> slip system. Finally note that for many boundaries, the peak tensile strength of the interface is not drastically different than that of the corresponding single crystal model even though for each of these models (except the perfectly coherent Σ3 boundary) the interface serves as the nucleation point for dislocations in the system.

V.4.4 [1$\bar{1}$0] Al Tilt Interfaces

V.4.4.1 Uniaxial tensile deformation

Figures V.27(a) and V.27(b) show the tensile stress-displacement response for aluminum bicrystal interface models subjected to a uniaxial tensile deformation for a range of <110> misorientations. Again, stress and displacement are calculated over a region around the bicrystal interface, as defined in Section V.2. For these boundary conditions in aluminum, the peak tensile stress corresponds to the nucleation of extended partial dislocations or full dislocation loops. Extended partial dislocations are commonly observed when coplanar slip is the dominant failure mechanism, whereas full dislocation

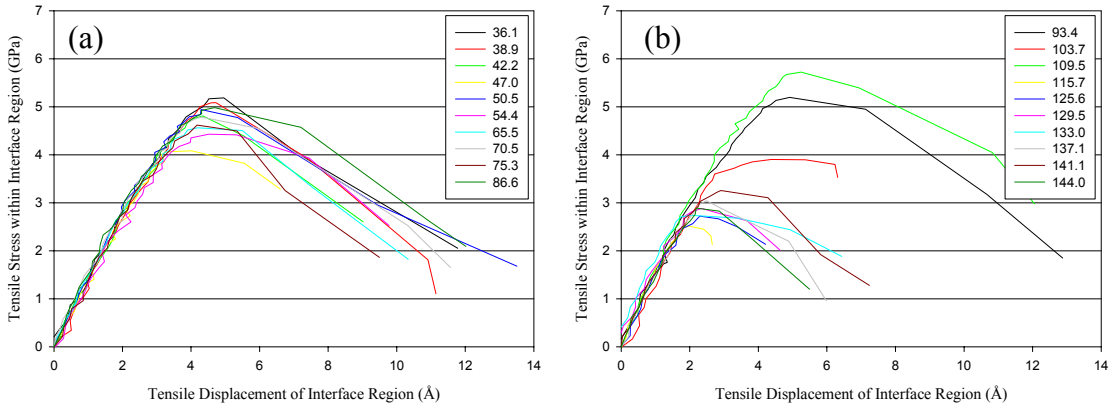

Figure V.27. Tensile stress versus tensile displacement of the interface region for <110> aluminum bicrystal interface models subjected to uniaxial tensile deformation.

loops are observed for all other interface misorientations. In general, the results reported for aluminum in Fig. V.27 show many of the same general trends as discussed in Section V.4.3.1 for copper. For example, the coherent Σ3 (111) 109.5^{o} interface has the highest tensile strength as compared with the other misorientations presented. Further, a noticeable decrease is observed in the tensile strength and tensile work of separation as the misorientation angle of the interface is increased beyond 109.5^{o}. However, the magnitude of this decrease is not nearly as significant in aluminum as that shown in Fig. V.19(b) for copper. In aluminum, the difference between the maximum tensile strength of the 109.5^{o} and 115.7^{o} boundaries is approximately 3.5 GPa, whereas in copper the difference between maximum tensile strength of the two boundaries is on the order of 10 GPa. Again, the difference in the interface character (presence of the E structural unit) and the geometry of the activated slip systems for interfaces with misorientations greater than 109.5^{o} both contribute to this drop in the tensile strength.

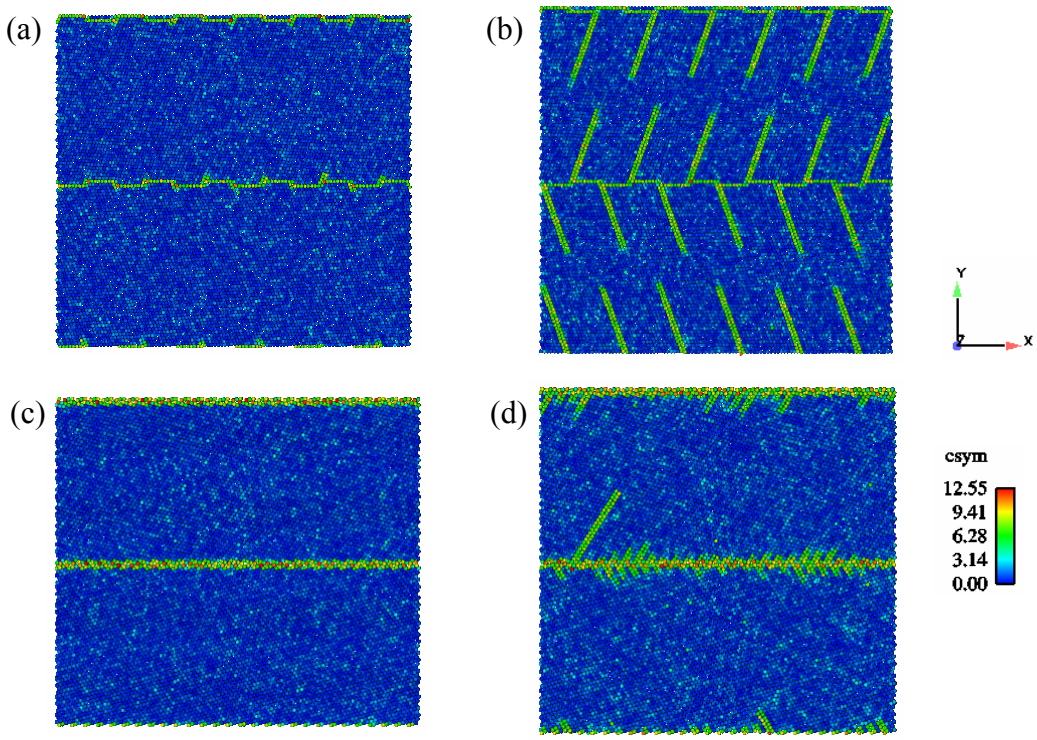

Figure V.28. Initial and deformed aluminum interface models showing the nucleation of partial dislocations from (a) and (b) a 115.7^{o} interface; (c) and (d) a Σ9 (221) 141.1^{o} interface subjected to uniaxial tensile deformation.

Figure V.28 shows the nucleation of partial dislocations from two aluminum <110> boundaries with misorientations greater than 109.5^{o}. Specifically, Figs. V.28(a) and V.28(b) show the nucleation of partial dislocations from a 115.7^{o} boundary, while Figs. V.28(c) and V.28(d) show the emission of partial dislocations from a Σ9 (221) 141.1^{o} interface. Atoms are colored by the centrosymmetry parameter (Kelchner *et al.*, 1998) and projected into the X-Y plane for clarity. After isobaric-isothermal equilibration, the 115.7^{o} boundary in Fig. V.28(a) is composed of both E and D structural units. The steps along the interface plane mark the positions of the E structural units. A few of the E structural units show a slightly dissociated structure; however, distinct intrinsic stacking fault facets (such as those easily identified for the same misorientation

in copper) are not observed. The steps along the interface plane are separated by a series of D structural units, which are associated with the coherent Σ3 (111) twin boundary. Dislocations are nucleated directly from the steps in the interface plane when subjected to a uniaxial tensile deformation. The resulting dislocation structure in Fig. V.28(b) is very similar to that shown for copper in Fig. V.20(b). Apparently, the extent that the leading partial dislocations can glide away from the interface without emitting the trailing partial dislocation in a coplanar slip orientation is much greater than that for individual slip systems, such as that shown in Chapter IV for the Σ5 (310) boundary. Eventually the trailing partial dislocations will be nucleated from the interface in aluminum.

Nucleation of the trailing partial dislocations on coplanar slip systems is observed (although not explicitly shown) for the Σ9 (221) 141.1^{o} boundary in Fig. V.28(c). This boundary consists entirely of E structural units in agreement with that predicted by the SUM (Wang *et al*., 1984). When subjected to a uniaxial tensile deformation, dislocations are nucleated directly from the interface, as shown in Fig. V.28(d). In the lower lattice region, the $(11\bar{1})$ slip plane is activated with slip occurring in both (101) and (011) directions. These are the primary slip systems for lattice orientation and loading direction. The structural rearrangement of the interface region and the initial dislocation activity for the 141.1^{o} boundary in aluminum looks very similar to that in copper shown in Fig. V.20(d). Short ISF facets are emitted along the entire length of the interface from the E structural units. Again, the orientation of the image in Fig. V.20(d) gives the impression that the entire slip plane through the thickness of the interface model is instantly activated during the tensile deformation process. Initially, dislocations are nucleated over discrete sections of the interface. Thus, the thickness of the interface

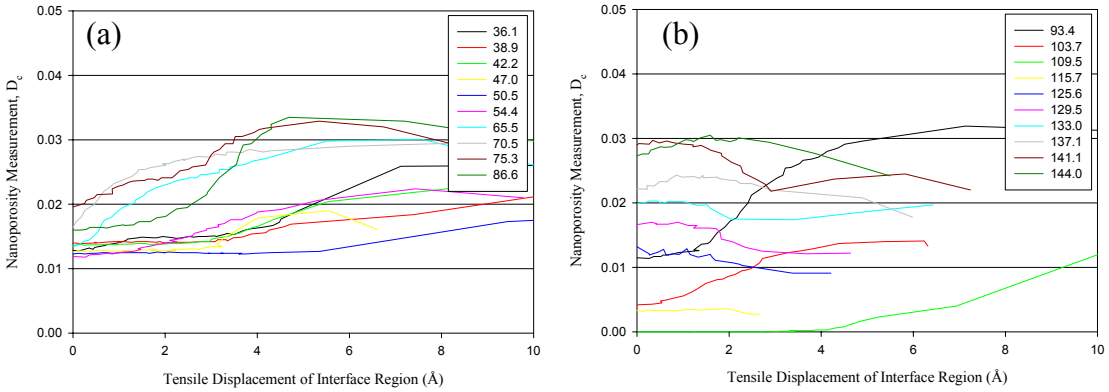

Figure V.29. Interface nanoporosity versus tensile displacement of the interface for <110> aluminum interface models subjected to uniaxial tensile deformation.

model is appropriate to model the 3D aspects of the dislocation nucleation process. As the partial dislocations glide in their respective slip directions, the entire slip plane will eventually become activated.

The evolution of the nanoporosity measure during uniaxial tensile deformation of aluminum <110> bicrystal interface models is shown in Figures V.29(a) and V.29(b). The nanoporosity measure is calculated using Eq. (V.2) and is averaged over the same region as the stress and the displacement. Similar 'groups' of interface misorientations may be defined in aluminum as were identified in copper regarding porosity evolution during uniaxial tensile deformation. First, for boundaries with <110> misorientations less than 54.4^o, the nanoporosity measure remains relatively constant prior to reaching the displacement associated with peak tensile strength, then increases slightly after the nucleation of partial dislocations. Second, for boundaries with misorientations between 54.4^o and 109.5^o, the porosity within the interface region increases immediately upon application of the uniaxial tensile deformation, then either decreases slightly or remains

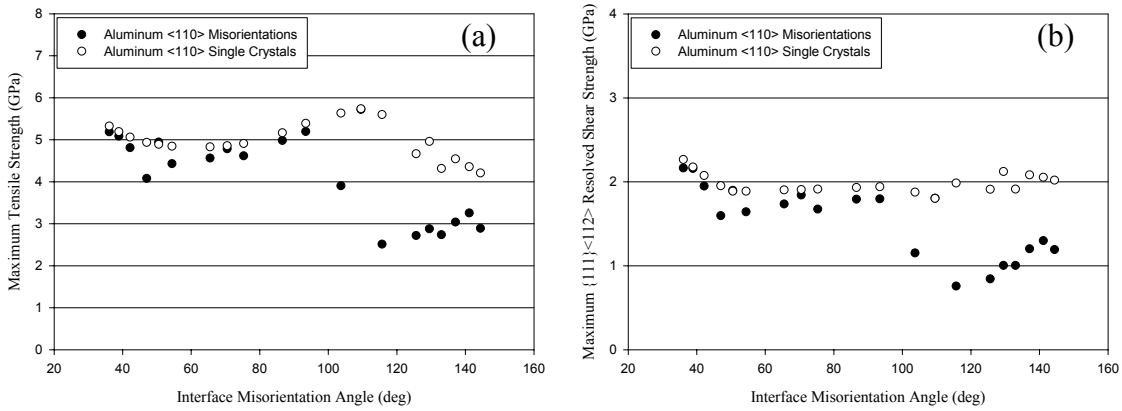

Figure V.30. (a) Maximum tensile strength and (b) {111}<112> critical resolved shear stress as a function of orientation for bicrystal interface models and single crystal models in aluminum subjected to uniaxial tension boundary conditions.

at a constant magnitude after the interface has reached its critical strength. For boundaries in this misorientation range, the evolution of the nanoporosity measure indicates that some structural rearrangement of the interface occurs prior to partial dislocation nucleation. Recall from Chapter III that some of these boundaries have a dissociated structure (even in aluminum), which involves stacking fault facets on non-primary slip planes. Third, for bicrystal boundaries with misorientations above 125.6^{o}, the nanoporosity measure for these boundaries decreases almost immediately when subjected to the tensile deformation. This decrease is associated with the emission of the short ISF facets from the E structural units, which effectively improve the local coherency of the boundary. This rearrangement mechanisms is readily apparent in Fig. V.28(d).

Figure V.30(a) shows the maximum tensile stress reached during uniaxial tensile deformation of the aluminum <110> interface models as a function of the misorientation angle of the interface. For comparison, several single crystal calculations are reported to

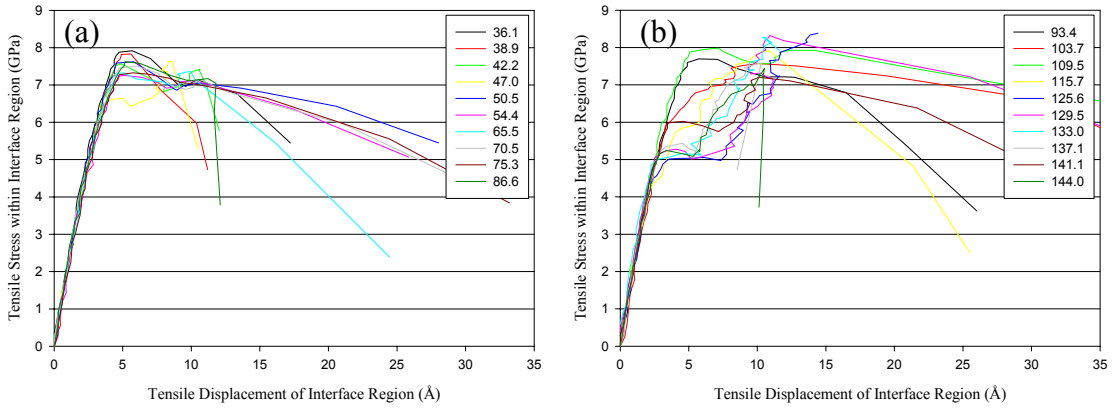

Figure V.31. Tensile stress versus tensile displacement of the interface region for <110> aluminum bicrystal interface models subjected to constrained tensile deformation.

determine the role of the lattice orientation on the magnitude of the peak tensile strength in aluminum. Similar to that shown in copper, there clearly is a large drop in the maximum tensile strength for boundaries with <110> misorientation angles above 109.5°. The nanoporosity measure is capable of capturing some of this effect, as these boundaries typically had the largest initial porosity within the interface region. However, porosity on its own does not appear capable of completely characterizing the interface response. For example, the Σ9 (221) 141.1° boundary has the largest initial porosity; however, the maximum tensile strength of the Σ9 boundary is slightly larger than that of other boundaries with similar <110> misorientations which deform via dislocation nucleation on coplanar slip systems.

V.4.4.2 Constrained tensile deformation

Figures V.31(a) and V.31(b) show the tensile stress-displacement response for aluminum bicrystal interface models subjected to constrained tensile deformation for a

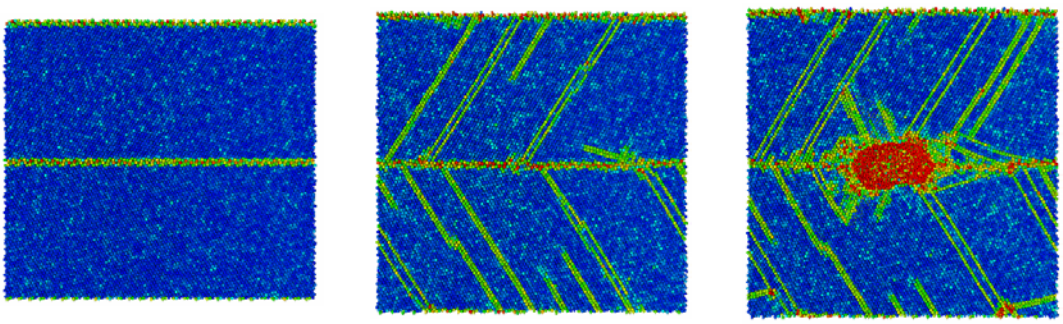

(a) (b) (c)

Figure V.32. Nucleation of dislocations and voids from a Σ9 (221) 141.1° aluminum interface subjected to constrained tension. Atoms are colored by the centrosymmetry parameter.

range of <110> misorientations. Again, the maximum tensile stresses are significantly larger using the constrained boundary conditions than those with uniaxial tension boundary conditions due to the additional tensile stresses that develop parallel to the interface plane during the deformation process. Similar to that in copper, the peak tensile stress in Fig. V.31 corresponds to either the nucleation of dislocations or the nucleation of voids from the bicrystal interface, depending on the character of the interface structure. For example, for boundaries with misorientations greater than 109.5°, such as the Σ9 (221) 141.1° interface shown in Fig. V.32, two distinct peaks are observed. The first (smaller) peak is associated with the nucleation of dislocations from the interface, while the second (ultimate) peak corresponds to the nucleation of voids along the interface plane. In Fig. V.32(c), voids are nucleated along the bicrystal boundary during the constrained tensile deformation process after several dislocations have been nucleated into each lattice region.

The evolution of the nanoporosity measure during constrained tensile deformation of aluminum <110> bicrystal interface models is shown in Figs. V.33(a) and V.33(b).

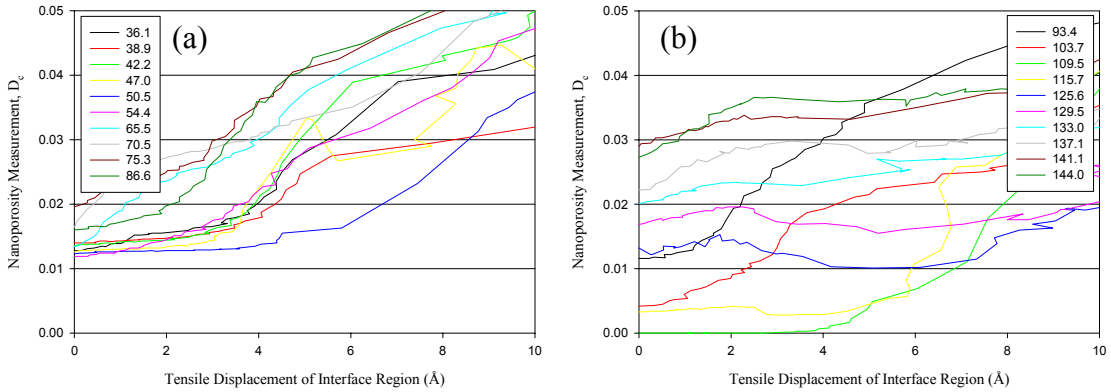

Figure V.33. Interface nanoporosity versus tensile displacement of the interface for <110> aluminum interface models subjected to constrained tensile deformation.

Again, dissimilar interface structural units evolve differently during the constrained tensile deformation process. For boundaries with <110> misorientations less than 54.4^o with the constrained tension boundary conditions, the nanoporosity measure shows an increase which coincides with the displacement associated with the maximum tensile stress. This indicates that the development of voids (free volume) accompanies the nucleation of dislocations within the interface region during the deformation process (images of the deformed interface models confirm this observation). For boundaries with misorientations between 54.4^o and 109.5^o, the porosity within the interface region increases continuously during the tensile deformation process. Recall that in the uniaxial case, the porosity measure decreased after the displacement associated with the maximum tensile strength had been reached. The nanoporosity measure for bicrystal boundaries with misorientations above 125.6^o shows an initial increase, then either a brief decrease or a plateau region associated with the nucleation of short ISF facets and dislocations

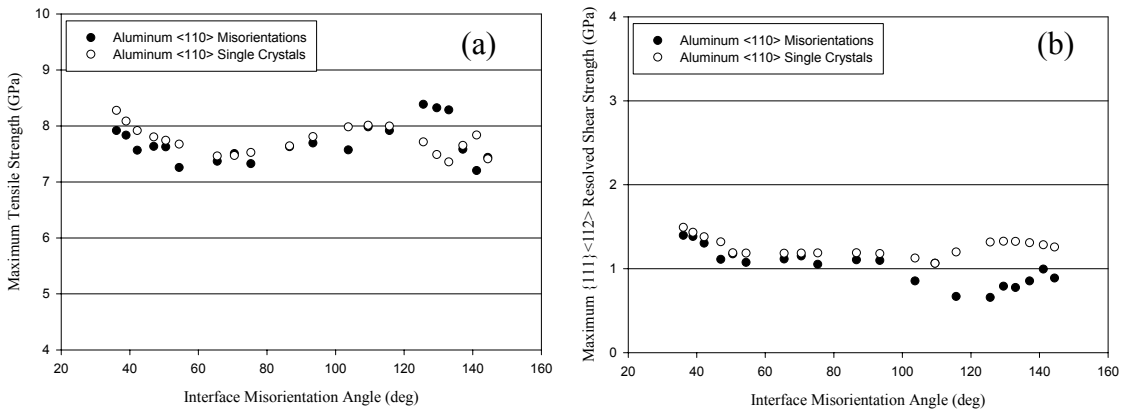

Figure V.34. (a) Maximum tensile strength and (b) {111}<112> critical resolved shear stress as a function of orientation for bicrystal interface models and single crystal models in aluminum subjected to constrained tension boundary conditions.

from the interface and then an increase once the displacement associated with the maximum tensile strength is reached.

Figure V.34(a) shows the maximum tensile stress and the {111}<112> critical resolved shear stress during constrained tensile deformation of the aluminum <110> interface models as a function of the misorientation angle of the interface. For comparison, several single crystal calculations are also performed to determine the role of the lattice orientation on the maximum interface strength. Here, the peak tensile strength follows a form mildly similar to that of the single crystal calculations. Recall that the peak tensile strength for the constrained tension boundary conditions is associated with the nucleation of voids from the interface plane. Thus, the abrupt drop in the nucleation stress is not observed in Fig. V.34(a). However, the drop in the stress required for dislocation nucleation can be easily observed in Fig. V.34(b) for boundaries with misorientations greater than 109.5^{o}. The {111}<112> critical resolved shear stress is calculated using the initial peak in the tensile stress-displacement response. This peak is

associated with the dislocation nucleation event. Finally, note that the variation in the critical resolved shear stress for single crystal models in Fig. V.34(b) is relatively minor over the range of interface misorientations considered. A similar observation is noted in Fig. V.30 for aluminum single crystal models deformed in uniaxial tension. Thus, is appears that non-Schmid behavior is more prevalent in copper for this orientation.

V.4.5 [111] Twist Interfaces

Figures V.35(a) and V.35(b) show the tensile stress-displacement response and the evolution of the nanoporosity measure, respectively, for copper bicrystal interface models subjected to a uniaxial tensile deformation for a range of <111> twist misorientations. Tensile stress, nanoporosity and displacement are calculated over a region around the bicrystal interface, as defined in Section V.2. In Fig. V.35(a), the maximum tensile stress corresponds to the nucleation of partial dislocations. The bicrystal boundary serves as the source for partial dislocations in all cases expect for the $\Sigma 3$ (111) coherent twin interface. For example, Fig. V.36 shows images of the $\Sigma 7$ (111) 38.2^{o} interface model in copper at 300 K subjected to uniaxial tension boundary conditions. All images are colored according to the centrosymmetry parameter (Kelchner *et al*., 1998). In Fig. V.36, atoms with a centrosymmetry parameter close to zero are removed to facilitate viewing of the defect structures. Images in Fig. V.36 indicate that partial dislocations with both edge and screw character are nucleated from the bicrystal interface as a result of the applied mechanical deformation. Specifically, the centrosymmetry parameter identifies the intrinsic stacking fault that connects the partial dislocation core back to the interface. For each of the [111] twist orientations, six slip

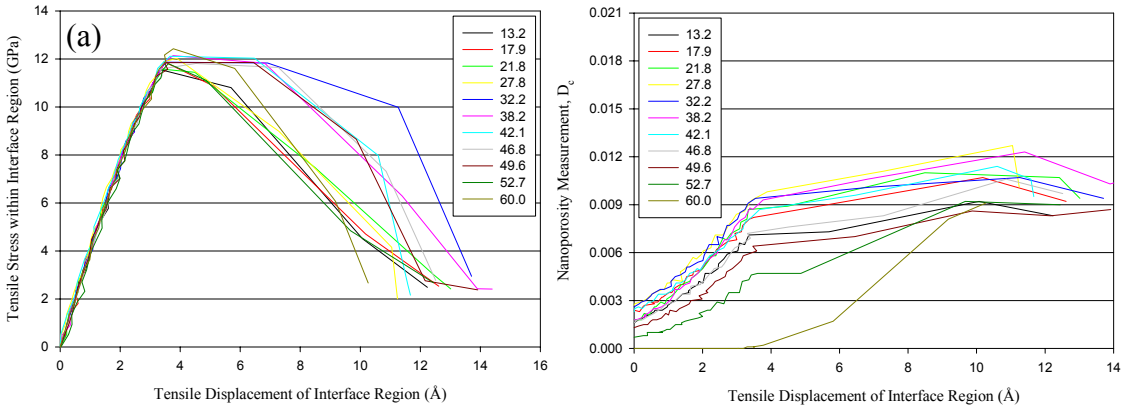

Figure V.35. (a) Tensile stress versus tensile displacement of the interface region and (b) evolution of the nanoporosity measure during uniaxial tension of <111> twist bicrystal interface models in copper.

systems should be simultaneously activated during the uniaxial tensile deformation, according to a Schmid factor analysis (*cf.* Hosford, 1993). Analysis of the defect configurations in Fig. V.36 reveals that partial dislocations are nucleated nearly simultaneously on all six of the activated slip systems in each lattice region. Consequently, the density of dislocation in the system increases rapidly after the nucleation event, as shown in Fig. V.36(c).

The evolution of the nanoporosity measure during uniaxial tensile deformation of the copper <111> bicrystal interface models is shown in Fig. V.35(b). In agreement with results presented previously in this chapter, the nanoporosity measure appears to be a unique way to initially differentiating between interfaces with different misorientations. The boundaries with the lowest porosity are those with small twist misorientations, i.e. those boundaries closest to the screw dislocation regime. The nanoporosity measure shows a similar evolution for each of the <111> boundaries examined in copper. In general, the porosity within the interface region initially increases during elastic

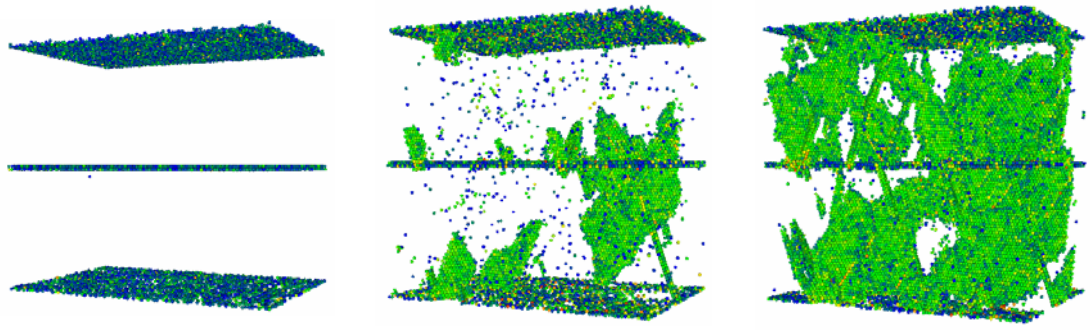

(a) ε = 0.00 (b) ε = 0.077 (c) ε = 0.078

Figure V.36. Nucleation of partial dislocations from a Σ7 (111) 38.2° copper bicrystal interface at increasing levels of strain using the uniaxial tension boundary conditions.

deformation. At a given tensile displacement, the time rate of change of the porosity evolution changes. This displacement corresponds to the displacement associated with the peak tensile strength, as shown in Fig. V.35(a). Apparently, coarsening of the interface plane does not appear to play a role for these boundaries. This is also evident from Figs. V.36(a) and V.36(b) as the bicrystal boundary is approximately the same width before and after the dislocation nucleation event.

Figures V.37(a) and V.37(b) show the maximum tensile stress as a function of the misorientation angle of the interface during uniaxial and constrained tensile deformation, respectively, for copper <111> twist interface models. For comparison, several single crystal calculations are also reported in Fig. V.37 to evaluate the role of lattice orientation on the magnitude of the peak tensile strength. Calculations on <111> twist boundaries allow for unique analysis of the interface structure as the orientation of the primary slip planes with respect to the load is identical for each <111> twist misorientation considered. Accordingly, the maximum tensile yield strength for each of the single

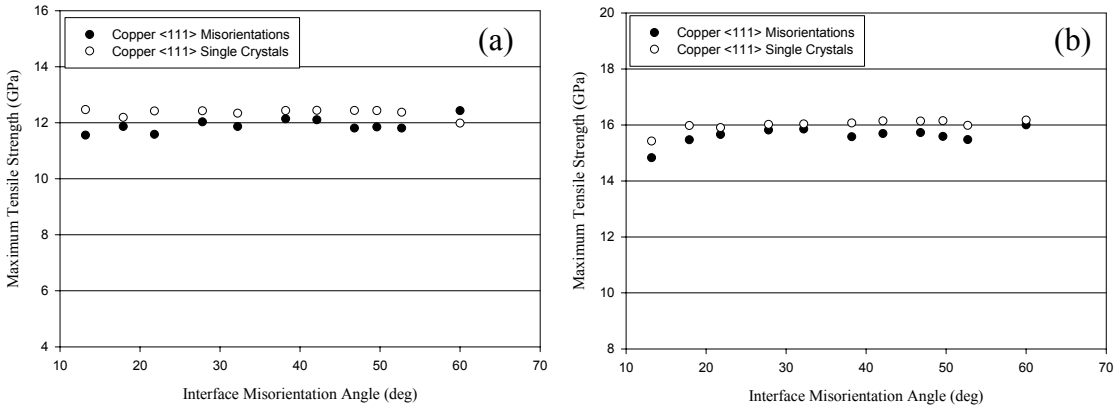

Figure V.37. Maximum tensile strength as a function of orientation for <111> copper interface and single crystal models deformed using the (a) uniaxial and (b) constrained tension boundary conditions.

crystal models reported in Fig. V.37 is approximately constant. Again, the maximum yield strength using the constrained tension boundary conditions is larger than that of the uniaxial case due to the presence of tensile stresses parallel to the boundary plane. For interface models, the relationship between maximum tensile strength and interface misorientation angle follows a form very similar to that of the single crystal models. In general, the maximum tensile stress required for dislocation emission for single crystal models is always greater than that for the bicrystal interface models, except in the case of the $\Sigma 3$ (111) 60.0^{o} perfectly coherent twin interface. This provides addition evidence that the interface is the root of failure in these calculations.

CHAPTER VI

RELATIONSHIP BETWEEN ATOMISTIC SIMULATIONS AND CONTINUUM INTERFACE SEPARATION POTENTIALS

VI.1 Introduction

Molecular dynamics simulation results in Chapters IV and V indicate that for ductile FCC metallic interfaces deformed in tension, nucleation and propagation of dislocations from the bicrystal interface is the predominant mode of failure. Depending on interface misorientation and the boundary conditions, partial dislocation nucleation may be accompanied by structural rearrangement and void nucleation, both of which play a powerful role in the deformation process. In general, integration of atomic level characteristics, such as those highlighted in the previous chapters, into a continuum description of interface behavior is highly desirable, as its inclusion allows for a fundamental characterization of dissipative mechanisms during fracture. Accordingly, the objectives of this chapter are to (i) briefly review existing methods in the literature designed to couple descriptions of material behavior over multiple material length scales, (ii) discuss in detail the use of continuum interface separation potentials (Needleman, 1987) to model decohesion, highlighting the work of Hao *et al*. (2003; 2004) and (iii) propose a general formulation based on internal state variable (ISV) theory which allows for the incorporation of nanoscale interface attributes, such as interface porosity, into a continuum description of interface separation. The parameters within the set of ISVs are intended to be derived from MD calculations and relate topological parameters associated

with the interface structure to the interface separation process. The goal is to obtain a more realistic description of ductile material separation, using nanoscale level details from atomistic simulation results as the building block.

Simulations in this thesis provide additional evidence that atomistic calculations allow for a unique analysis of material behavior on the nanoscale, notwithstanding inherent limitations, such as the accuracy of the interatomic potential and application of boundary conditions. Nevertheless, it is still impractical to model material behavior on the macroscale using molecular dynamics simulations. Even with modern computing hardware and programming techniques, to the author's knowledge the current record for the largest number of atoms in a molecular dynamics simulation is on the order of 10^9 (Buehler *et al*., 2004), reaching length scales on the micron level. Two restrictions still limit massively large-scale atomistic calculations. One, the immense amount of data produced during simulation requires complex analysis tools in order to interpret the results. For example, Zhou *et al*. (1998) monitored the formation of dislocation loops during dynamic fracture in copper. Individual dislocations are identified during the early stages of emission; however, quantitative analysis becomes quite difficult once a large number of dislocations accumulate in front of the crack tip. Two, while length scales at the micron level are an impressive display of computational power, these dimensions still fall short of the scale at which continuum theory would typically be applied for structural analysis (Horstemeyer and Baskes, 1999).

To alleviate some of the computational demand, hybrid-matching techniques have been developed to extend the simulation domain by approximating the motion of atoms far away from an atomic level defect with a continuum constitutive model, such as linear

elasticity (*cf.* Cleri *et al*., 1998). The coupling between atomistic and continuum regions greatly reduces the number of atoms explicitly modeled in the atomistic simulation; however, these methods often require some prescribed 'hand-shaking' region between the two domains. For instance, original multi-region techniques (Sinclair, 1971; 1975, Hoagland *et al*., 1976; Sinclair *et al*., 1978) coupled forces and displacements between two regions through an iterative process. More advanced methods (Yang *et al*., 1994; Gumbsch, 1995; Rafii-Tabar *et al*., 1998) allow for a smoother coupling between the atomic and continuum domains via transition zones or intermediate regions. Unfortunately, the models of Gumbsch (1995) and Rafii-Tabar *et al*. (1998) are unable to deal with displacement discontinuities that must be passed between the atomistic and finite element regions, such as a dislocation. Thus, these multi-region techniques are typically restricted to static or dynamic relaxation of nanoscale defects.

Further reducing the atomistic degrees of freedom, the quasicontinuum (QC) method represents another technique to couple between length scales (Tadmor *et al*., 1996; Miller *et al*., 1998a; 1998b). In this method, a finite element mesh is refined from a coarse level in areas of small deformation to the atomic level around a nanoscale defect. In the coarsely refined regions, atoms are constrained to move by user-defined shape functions, as in traditional finite elements, while the energy of each crystal region and the corresponding finite element stiffness matrix are calculated from the interatomic potential. Initially, the QC method was employed to study the interaction between a crack and a grain boundary (Miller *et al*., 1998a; 1998b). More recently, Sansoz and Molinari (2004; 2005) used the QC method to study the nucleation of defects during shear deformation of a bicrystal interface, which has been discussed at length in the

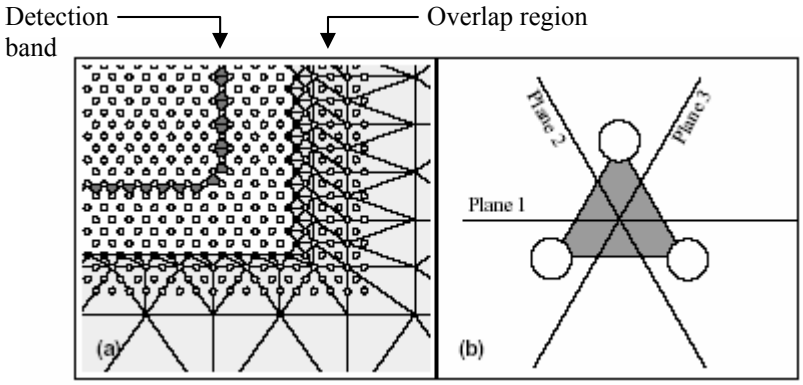

Figure VI.1. (a) Coupling (overlap) region between atomistic and continuum domains; (b) close-up view of a 'detection' element, used to identify nucleated dislocations and appropriate slip systems. Reproduced from Shilkrot *et al*. (2002).

preceding chapters. To address dislocation nucleation and glide, Shilkrot *et al*. (2002; 2004) devised a method to couple the QC method with dislocation dynamics (DD). Their formulation includes the capability to pass defects (such as vacancies or dislocations) between QC and DD domains. The coupling occurs through an overlap region between the two computational domains, as shown in Fig. VI.1. This method is successful for defects that possess an analytic solution for the elastic displacement field and has been used to study the nucleation and glide of dislocations under a nanoindenter (Shilkrot *et al*., 2002; 2004).

Potentially the most promising method to bridge between length scales is the constitutive relationship (CR) approach. This approach will essentially be adopted in this work. In general, a constitutive law relates the individual response of a material body to the input processes (Haupt, 1993). In this approach, a specific constitutive model (that describes the atomic process of interest) is used in the area around a defect; while a classical constitutive model is used to describe material behavior far away from the

defect. Thus, atomic information is embedded within the continuum bulk response without prescribing an explicit atomic-continuum coupling as done in the hybrid-matching techniques discussed above.

The critical step in the CR approach is the selection or development of constitutive equations that mimic atomic scale phenomena. For example, to study the brittle-ductile transition in crystalline solids, Rice (1992) developed a constitutive model for dislocation nucleation and motion at a crack tip, based on the Peierls concept for mobile dislocations (Peierls, 1940). To model interfacial debonding, Needleman (1987) developed a phenomenological description of separation across an interface based on the concept of a cohesive process zone at a crack tip (Dugdale, 1960; Barenblatt, 1962). A phenomenological interface separation potential was proposed, which served as an analogue to the atomic separation processes. When combined with traditional finite elements, a multiscale computational formulation is attained, which allows for a predictive model of fracture in the sense that fracture initiation and propagation criteria need not be introduced. Section VI.2 will provide an in-depth review of interface separation potentials which are based on the Needleman (1987) formulation.

VI.2 Continuum Interface Separation Potentials

VI.2.1 Phenomenological Interface Separation Laws

To model void nucleation by interfacial decohesion, Needleman (1987) introduced a phenomenological methodology to relate the traction vector $\mathbf{T}$ on a crack

surface to the displacement jump vector $\boldsymbol{\Delta}$ across that crack surface via an interface separation potential ϕ, i.e.,

$$\mathbf{T} = -\frac{\partial \phi}{\partial \boldsymbol{\Delta}} \quad . \tag{VI.1}$$

This methodology, which accounts for large deformation and mimics the phenomena of interatomic separation, is based on the concept of a crack tip cohesive zone (Dugdale, 1960; Barenblatt, 1962). In general, the equation for the interface separation potential is chosen to be consistent with the work of separation and interface strengths in the normal and tangential directions, while using normal and tangential coupling parameters to serve as an analogue to atomic separation at an interface. For example, the two-dimensional form of the interface separation potential introduced by Zhai and Zhou (1999) is given by

$$\phi(\boldsymbol{\Delta}) = \phi_o - \phi_o \left(1 + \frac{\Delta_n}{\delta_n}\right) \exp\left(-\frac{\Delta_n}{\delta_n}\right) \exp\left(-\frac{\Delta_t^2}{\delta_t^2}\right) \quad . \tag{VI.2}$$

Here Δ_n and Δ_t are the normal and tangential displacement jumps across the interface and ϕ_o is the work of separation for the interface. The work of separation is defined as the area under the traction-displacement curve that results from inserting Eq. (VI.2) into Eq. (VI.1) (Needleman, 1987). The parameters δ_n and δ_t are introduced as characteristic lengths that normalize the physical interface displacements so that peak

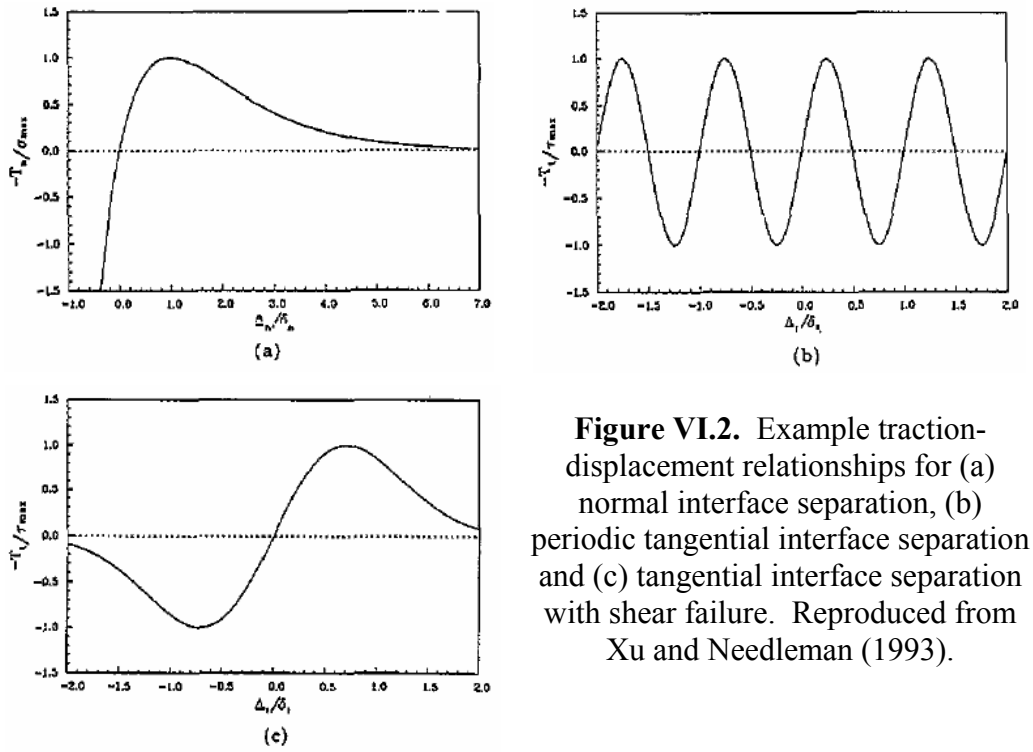

Figure VI.2. Example traction-displacement relationships for (a) normal interface separation, (b) periodic tangential interface separation and (c) tangential interface separation with shear failure. Reproduced from Xu and Needleman (1993).

normal and shear traction occur at specific displacement ratios ($\Delta_n/\delta_n = \Delta_t/\delta_t = 1$). Essentially, Eq. (VI.2) is an equivalent nonlinear elastic separation law for given parameters ϕ_o, δ_n and δ_t. Based on the form of Eq. (VI.2), the maximum interface strength in the normal direction (for example) can be calculated in terms of the work of separation and the characteristic length, i.e., $\sigma_{max} = \phi_o / e\delta_n$ (Zhai and Zhou, 1999).

In general, the form of the traction-displacement relationship is not regarded as being critical to the overall interface separation process; although recent work has argued that certain forms are more appropriate for specific materials (Chandra *et al*., 2002; Li and Chandra, 2003). Several authors have assumed a bilinear or piecewise linear shape for the interface separation potential for simplicity (*cf*. Tvergaard and Hutchinson, 1992; Ortiz and Pandolfi, 1999). Often, an exponential form is chosen to model the normal

interface separation response, as shown in Fig. VI.2(a), to maintain analogy to atomistic calculations of the universal binding energy relationship by Rose *et al.* (1983). The shear response may be modeled using either a periodically repeating dependence of the traction on displacement, as suggested by Beltz and Rice (1991), or using a shear interface separation potential that allows for failure at the interface (Xu and Needleman, 1993). Examples of each traction-displacement response for separation in shear are shown in Figs. VI.2(b) and VI.2(c), respectively.

Combining Eq. (VI.1) with traditional finite elements, the cohesive finite element method (CFEM) has been introduced, which allows for a non-restrictive model of fracture in the sense that fracture initiation and propagation criteria need not be introduced, nor is the concept of a dominant crack essential. Early CFEM studies were aimed at utilizing Eq. (VI.1) to study void nucleation between a ductile matrix and a rigid inclusion or substrate (Needleman, 1987; 1990a; 1990b; Xu and Needleman, 1993; 1994; 1995). Several authors have studied the effect of decohesion strength by altering the parameters that define the form of the constitutive relationship for the interface (Needleman, 1990a; Tvergaard and Hutchinson, 1992; 1993; Xu and Needleman, 1995). More recent work has concentrated on predictive modeling using the CFEM method (Ortiz, 1996; Camacho and Ortiz, 1996; Zhai and Zhou, 1999; 2000). In these formulations, the boundary between each of the traditional finite elements is regarded as a cohesive surface and serves as a possible crack path during the simulation. When combined with bulk constitutive laws, these cohesive models provide a unified framework for simulation of fracture processes over multiple length scales.

VI.2.2 Limitations of Existing Separation Laws

Even though the cohesive finite element is a major advance in fracture simulation, because it allows for the analysis of material fracture without the *a priori* prescription of a crack path, there are several aspects of continuum interface separation potentials that limit its predictive capabilities. First, while allowing features of fracture on the microscopic and macroscopic scales to be captured and quantified, previously developed continuum interface separation potentials do not account for details of nonlocal effects over smaller length scales, structural rearrangement and other dissipative mechanisms. They are not necessarily material specific in their form. Calculations in Chapter V indicate that for interfaces between two ductile FCC metallic constituents, the total work of separation is composed of both the work of cleavage fracture along the boundary plane plus plastic dissipation due to dislocation nucleation. These dissipative effects require the use of additional variables to define the internal state or structure of the system during deformation (Needleman, 1992; Ortiz and Pandolfi, 1999). The role of plasticity in the vicinity of the interface has been studied by several authors (Arata and Needleman, 1998; Wei and Hutchinson, 1999; Evans *et al*., 1999); however, the interface separation potential in these works is still specified as elastic.

Second, interface separation potentials in the sense of Needleman and others lack the ability to reflect heterogeneity at the nanoscale, resulting in nondescript interfaces. Thus, they do not incorporate detailed interface information necessary to distinguish among continuum potentials for interfaces with differing degrees of coherency, roughness or with the inclusion of impurity atoms, for example. Calculations in Chapter V clearly show that interface structure plays a role in the deformation response,

especially for boundaries with <110> misorientations greater than 109.5^{o}. Here, the favorable orientation of the interface structure with respect to the primary slip systems leads to a dramatic drop in the interface strength and work of separation. Needleman (1990a) investigated the effect of an imperfect interface by embedding both bonded and non-bonded cohesive elements between a rigid substrate and ductile material. Still, this only estimated the effect of initially broken bonds at the interface.

It must be recognized that interfaces, in reality, are often complex structures with potentially a spectrum of topological length scales. The simplest is that of a perfectly coherent planar interface between crystals; this kind of interface has intrinsic scales only at nanometer level dimensions. On the other hand, interfaces in most structural materials have a range of characteristic length scales associated with roughness, variations of composition, second phases, etc. For such complex interfaces, presumption of continuum separation laws involves considerable idealization and empiricism, for example along the lines of Eq. (VI.1). Any convolution of length scales ultimately leads to the nanoscale as a starting point; hence, this is the fundamental scale considered in this thesis.

Recently, several authors have introduced measures of irreversibility into continuum interface separation potentials (Tvergaard, 1990; Camacho and Ortiz, 1996; Geubelle and Baylor, 1998; Zhou and Zhai, 1999; Ortiz and Pandolfi, 1999; Raous *et al*., 1999; de-Andres *et al*., 1999; Tomar *et al*., 2004). Essentially, the elastic unloading response of the interface is prescribed such that the interface incorporates a measure of damage in the traction-displacement relationship. Typically, most authors assume that upon unloading, the interface traction-displacement response returns to a state of zero stress and zero displacement for both normal and tangential deformations. Often, a

parameter is defined that characterizes the state of the interface upon unloading. This parameter may be considered as an internal state variable (ISV) (Ortiz and Pandolfi, 1999). The irreversible separation law of Raous *et al*. (1999) is unique in that the tangential separation includes a permanent displacement upon unloading, i.e., the tangential displacement does not return to zero as the shear stress vanishes. While these interface separation potentials begin to address real material separation by estimating the effect of broken bonds at the interface, further advancements are still required to account for other dissipative mechanisms, such as the effects of dislocation generation and glide on the magnitude of the yield stress and work of separation.

VI.3 Multiscale Interface Separation Law for Ductile Constituents

Hao *et al*. (2003; 2004) proposed a multi-scale computational framework for the design of high strength and toughness steels. Interfacial debonding between the ductile iron matrix and rigid titanium carbide inclusions was accounted for through Needleman-type interface separation potentials (Eq. (VI.1)). However, the interface separation potential in their work was designed to account for the effect of dislocation emission on the strength of the Fe-TiC interface. Quantum mechanical calculations were used to determine the critical parameters required to predict if dislocation nucleation or cleavage fracture is favorable for a given interface and to determine the form of the energy-separation relationships for pure normal and tangential deformations.

VI.3.1 Interface Separation Potential Formulation

In their formulation, Hao *et al*. began by splitting the interface separation potential into normal and tangential parts,

$$\mathbf{T}_{\mathrm{n}} = -\frac{\partial \phi_{\mathrm{n}}}{\partial \mathbf{\Delta}_{\mathrm{n}}} \quad \text{and} \quad \mathbf{T}_{\mathrm{t}} = -\frac{\partial \phi_{\mathrm{t}}}{\partial \mathbf{\Delta}_{\mathrm{t}}} \quad . \tag{VI.3}$$

Then, Hao *et al*. proposed that the normal and tangential interface separation potentials take the respective forms:

$$\phi_{\mathrm{n}} = E_{\mathrm{n}} + \kappa_{slide} \sum E_{\mathrm{s}} \tag{VI.4}$$

and

$$\phi_{\mathrm{t}} = E_{\gamma} \quad . \tag{VI.5}$$

Here, E_{n} is the energy required for cleavage fracture of the interface, E_{γ} is the energy for sliding along the interface and $\sum E_{\mathrm{s}}$ is the summation of the sliding energy for all slip systems that are not aligned parallel to the interface plane and κ_{slide} is a coefficient that provides a weight to each slip system. In their formulation, the normal interface separation potential is posed to account for normal separation due to dislocation nucleation at the interface. For example, Fig. VI.3(a) shows the case where no dislocations are nucleated from the boundary. The separation energy is simply taken as the energy required to 'create' the fracture surfaces. On the other hand, Fig. VI.3(b) shows the case where dislocations are nucleated from the interface during the normal

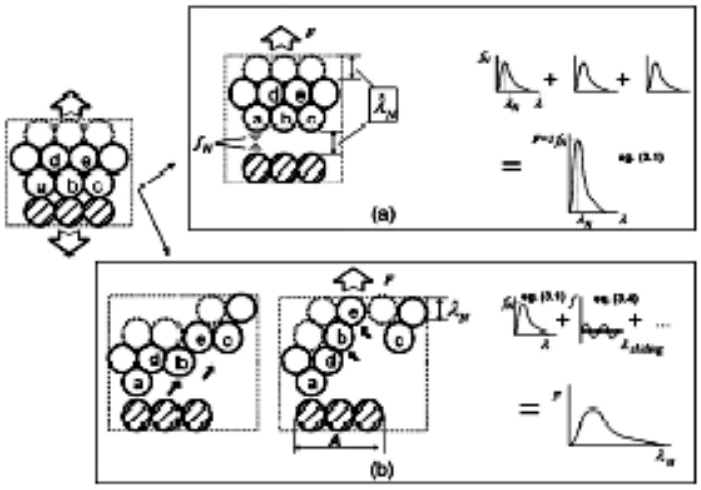

Figure VI.3. (a) Normal separation of the interface through cleavage fracture; (b) normal separation due to cleavage fracture and dislocation glide. Reproduced from Hao *et al*. (2004).

separation process. Here, the total normal separation is written as a function of the cleavage separation plus the normal component of the dislocation induced gliding separation. Dislocation emission at the interface results in the creation of voids along the interface plane. Note in Eq. (VI.5), the total tangential component of the dislocation induced gliding separations is assumed to be negligible.

The term $\kappa_{slide}\sum E_{\mathrm{s}}$ is difficult to compute because the energy of sliding on each slip plane and the contribution of the sliding energy to the normal separation energy would need to be determined from *ab initio* or molecular dynamics simulations. Thus, Hao *et al*. (2003; 2004) introduce a simplified renormalized form,

$$E_{\mathrm{n}} + \kappa_{slide}\sum E_{\mathrm{s}} = 2\gamma_F E_{\mathrm{n}}^{*}\left(\kappa\left[\frac{\Delta_{\mathrm{n}} - \Delta_{\mathrm{n0}}}{\delta_{\mathrm{n}}}\right]\right) \tag{VI.6}$$

In Eq. (VI.6), γ_F is the cleavage surface energy, κ is a recalling factor, Δ_{n0} is the equilibrium spacing across the interface at zero normal separation, δ_n is a normalizing length similar to those in Eq. (VI.2) and E_n^* is the 'universal relation' of Rose *et al*. (1983). Recall that the universal relationship was used by Needleman (1987) as the basis for an exponential form for the interface traction-displacement relationship. Apparently, the effect of dislocation emission on the interface in Eq. (VI.6) is addressed through a linear rescaling of the universal binding energy relationship. In effect, dislocation emission lowers the peak interface strength and the work of separation from that which would be predicted by cleavage fracture. From a classical fracture and plasticity perspective, dislocation emission is associated with the 'toughening' of a material, thereby increasing the work of separation. Recall, the interface separation laws here are written specifically for the interfacial region; thus, far-field effects of dislocations are not included. These effects should be account for through an appropriate constitutive law for the material away from the interface. The *ad hoc* estimate of the rescaling parameter in the work of Hao *et al*. is taken as $\kappa = 0.2$ based on calculations by Alber *et al*. (1992) of the variation in the elastic constants in the vicinity of Σ3 and Σ5 interfaces. In general, κ describes the thickness of the interface zone relative to the interatomic spacing.

Finally, quantum mechanical calculations are employed in Hao *et al*. to estimate the cleavage surface energy, γ_F, the equilibrium separation between atomic layers across the interface, Δ_{n0}, the barrier for dislocation nucleation, γ_{US}, and the form of the normal energy-separation relationship, E_n^*. The boundary considered in their work exists between $\{001\}_{bcc}^{Fe}$ and $\{001\}_{fcc}^{TiC}$, with both Fe-C and Fe-Ti sites important in the

characterization of the interface. To determine if dislocation nucleation occurs at a given interface, Hao *et al*. utilized the brittle-ductile criterion of Rice (1992),

$$\kappa_{\mathrm{R}} \frac{\gamma_F}{\gamma_{US}} > 1 \tag{VI.7}$$

Here, κ_{R} is a scalar function that reflects the effects of slip plane orientation with respect to the interface and the loading conditions (Rice, 1992). Recall from Chapter II that γ_{US} is the unstable stacking fault energy. For the material system of interest in the work of Hao *et al*., only coherent {001} interfaces exist between the iron matrix and the rigid TiC inclusions; thus $\kappa_{\mathrm{R}} \approx 0.3$ for every interface in the system. Hao *et al*. report that dislocation nucleation occurs at the Fe-C site of the Fe-TiC interface and in the bcc Fe matrix. Inserting the computed energies from quantum mechanical calculations into the separation relationships in Eqs. (VI.3)-(VI.6), they obtained normal and tangential traction-separation relations for the interface between the iron matrix and the titanium carbide inclusions. These separation relations were taken as the interface constitutive model and incorporated in their multi-scale computational framework.

VI.3.2 Applicability of the Hao *et al*. Formulation to Interfaces in Cu and Al

The interface separation potentials of Hao *et al*. (2003; 2004) represent an advance relative to existing continuum interface separation relations because they address modifications to the work of separation and the tensile strength due to dislocation nucleation. However, there are several limitations to the formulation proposed by Hao *et*

al. if one wishes to extend the interface separation relations to model decohesion between two ductile FCC metallic constituents (*e.g.* grain boundaries).

First, Hao *et al*. only consider interfaces with fixed orientation. Specifically, the quantum mechanical calculations in their work consider interfaces between $\{001\}_{\text{bcc}}^{\text{Fe}}$ and $\{001\}_{\text{fcc}}^{\text{TiC}}$ crystallographic planes. Accordingly, the cleavage surface energy, γ_F, and the orientation parameter, κ_{R}, are both taken as constants (they assume that the change in surface energy due to dislocation emission is negligible). The value of κ_{R} and the ratio between surface energy and the unstable stacking fault energy of the ductile constituent are used to determine if dislocation nucleation occurs at a given interface. In copper and aluminum polycrystals, on the other hand, interfaces exist with a wide range of orientations and configurations, including both tilt and twist components. The orientation parameter, κ_{R}, should be used to provide a dependence of slip system orientation on the prediction of dislocation nucleation for a given loading condition. Recall that calculations presented in Chapters IV and V indicate that the orientation of the slip systems with respect to the interface plane and the direction of the load is potentially the most important parameter (or set of parameters) required to characterize the interface traction-displacement relationship. For two-phase alloys with ductility in both phases the problem is further complicated due to differences in dislocation nucleation between the two phases. Regardless, Rice's ductile-brittle criterion may not be necessary to determine the mode of failure (except perhaps at cryogenic temperatures or with the addition of embrittling impurity atoms) because in Cu and Al the surface energy is typically much larger than the unstable stacking fault energy, dictating that dislocation nucleation is the primary mode of failure.

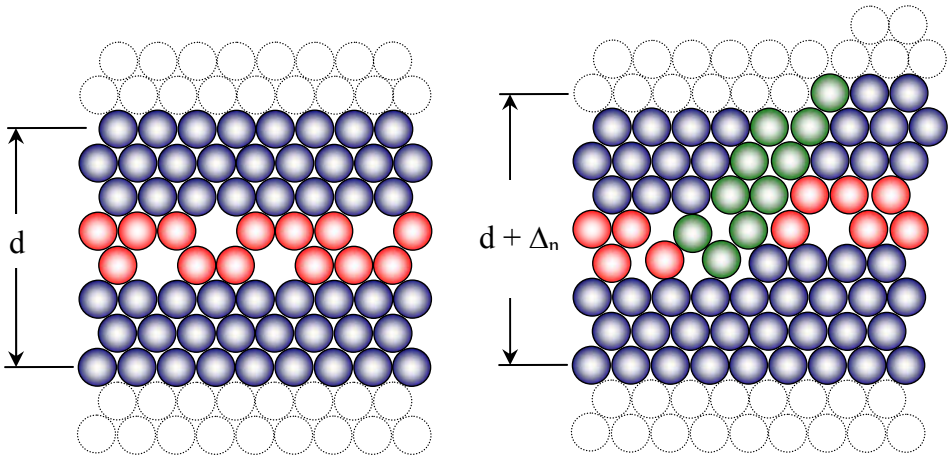

Figure VI.4. (a) Example interface structure in ductile materials showing inherent interface porosity due to the interface misorientation and (b) normal separation due to dislocation glide.

Second, this study finds that dislocation nucleation from interfaces between two ductile materials does not necessarily lead directly to void nucleation at the interface. This is shown repeatedly for a range of interface misorientations in Chapters IV and V. Typically, the interface structure is altered after the nucleation of the trailing partial dislocation. This distortion may result in the formation of ledges, as in the case of an aluminum Σ5 (310) 36.9^{o} interface subjected to uniaxial tensile deformation. On the other hand, the nucleation of dislocations may result in improved interface coherency, as shown in Chapter V with the formation of ISF facets for a range of <110> high-angle boundaries. Regardless, the formulation of Hao *et al*. is applicable for ductile constituents because the interface separation relation is written explicitly to include both the interface and a finite amount of crystalline lattice, as shown in Fig. VI.3. A schematic of dislocation nucleation in ductile systems is shown in Figs. VI.4(a) and VI.4(b). Here, the bicrystal interface retains approximately the same porosity after the dislocation

nucleation event as it had prior to dislocation emission. However, the normal separation of the interface region, Δ_n, consists of components from the elastic stretch and the dislocation glide, as shown in Fig. VI.4(b).

Third, the rescaling parameter κ must include a dependence on the orientation of the interface to properly address the reduction in interface strength due to plastic deformation. In Hao *et al*., the rescaling parameter is taken as $\kappa = 0.2$ based on calculations of the variation in the elastic constants around Σ3 and Σ5 interfaces by Alber *et al*. (1992). In effect, dislocation emission lowers the peak interface strength and the work of separation from that which would be predicted by cleavage fracture. Thus, rescaling of the interface traction-displacement form by a constant value of κ implies that the ratio between the work of separation for cleavage fracture and the work of separation for ductile failure does not vary as a function of orientation. While molecular dynamics calculations in this thesis do not explicitly refute this assumption, because cleavage fracture calculations are not performed, it is unlikely that a constant linear rescaling of the universal binding energy relationship is sufficient to describe the effect of dislocation nucleation on ductile interface separation. For example, the cleavage energies of the copper and aluminum boundaries with <110> misorientations greater than 109.5^o are not that different from those with misorientations less than 109.5^o (as evident from the interface energy calculations from Chapter III); however, there is clearly a discrepancy in the nucleation stress for dislocations between these two sets of boundaries.

VI.4 ISV Model for Ductile Interface Separation

In this section, a general methodology is presented in which a set of interface attributes that characterize the interface structure and morphology is incorporated into a constitutive law for interface separation. The proposed continuum formulation is based on internal state variable (ISV) theory for non-equilibrium behavior and is described in Section VI.4.2. The parameters that compose the set of ISVs are intended to be derived from MD calculations and relate the topology and morphology of the interface structure to the interface separation process. An elastic separation potential is used to account for the nonlinear elastic relation of traction to displacement across an interface. To account for separation associated with irreversible processes, defined as 'plastic' separation, the rate of change of the constituents that characterize the internal structure of the interface is tracked by a set of evolution equations over the course of the deformation. The goal is to obtain a more realistic description of material separation processes, using atomic level detail as the building block.

VI.4.1. Continuum Thermodynamics of Irreversible Processes

During plastic deformation of crystalline solids, the processes of nucleation, motion and interaction of dislocations take place away from thermodynamic equilibrium. To account for nonequilibrium material dissipation, Onsager (1931) first introduced the concept of classical linearized irreversible thermodynamics. Kestin and Rice (1970) later introduced the 'constrained equilibrium' approximation, which assumes a sequence of local, constrained equilibrium states along a non-equilibrium process trajectory. Only the

thermodynamic state of the system is characterized, requiring a much lower order description than that of the full dynamical state. Temperature and entropy are defined using equilibrium concepts with their values extended to the non-equilibrium state space through the introduction of a set of internal state variables (ISVs) (Coleman and Gurtin, 1967; Kestin and Rice, 1970; Rice, 1971) that represent evolving material microstructure attributes. ISV theory assumes a dependence of the material response on a set of independent variables, $\mathbf{\Lambda}_q$, that essentially prescribe the current state of the material. The kinetics of microstructure evolution over the course of a non-equilibrium process are represented by a set of evolution equations for the ISVs, which depend on the temperature and instantaneous values of the full set of ISVs. In the non-equilibrium state space, each ISV is independent of external work variables (Rice, 1971). Thus, the form of these rate equations cannot be altered through external work, even though the values of the internal state variables may change if the process includes irreversible dissipation during cohesive separation, such as dislocation nucleation.

The major assumption behind the constrained equilibrium approximation is that the material state relaxation processes are either very rapid or very slow compared to the duration of loading increments considered (Kestin and Rice, 1970). The characteristic relaxation times of dislocation structures for the calculations in this study tend to be shorter than the total times of observation. Of course, dislocation dynamics is a significantly non-equilibrium set of processes; however, previous atomistic studies have shown that for interface scales on the order of those considered in this work, MD simulations and molecular statics produce similar results with regard to interfacial separation energy and peak tensile stress (Gall *et al.*, 2000).

VI.4.2 Internal State Variable Model

The following section presents a general methodology for embedding results of molecular dynamics simulations, similar to those presented in Chapter IV and V, into traction-displacement relations for interface separation. Molecular dynamics simulations presented in this dissertation dictate that alterations to existing interface separation relations are necessary to account for nanoscale attributes, such as the underlying dissipative mechanisms that occur during fracture. First, the total displacement of the interface region during fracture Δ_n and Δ_t is decomposed into elastic and inelastic (plastic) contributions, i.e.,

$$\Delta_n = \left(\tilde{\Delta}_n + \Delta_n^p\right)\Big|_L \quad \text{and} \quad \Delta_t = \left(\tilde{\Delta}_t + \Delta_t^p\right)\Big|_L \quad . \tag{VI.8}$$

Here $\tilde{\Delta}_n$ and $\tilde{\Delta}_t$ are the elastic portions of the total boundary displacement while Δ_n^p and Δ_t^p are the plastic contributions to the total boundary displacment associated with the generation and motion of point and line defects. The characteristic length normal to the interface, L, generally exceeds the process zone width for cohesive separation and may be related to the physical dimensions of the interface region, as defined in Chapter V. The decomposition of the total displacement into elastic and plastic contributions is common in elastic-plastic fracture mechanics for the calculation of the J-Integral, for example (Rice *et al.*, 1973). The plastic contributions to the total boundary displacement,

Δ_n^p and Δ_t^p, can be determined by measuring the permanent displacement after normal and tangential elastic relaxations, respectively (Spearot *et al*., 2004).

In order to incorporate realistic interface attributes over a range of length scales, a nonlinear elastic separation potential $\tilde{\phi}$ is introduced that includes a dependence on a set of parameters that characterizes the role of the interface structure and morphology on separation. An elastic potential is introduced for interface separation, as it may be assumed that the elastic displacement drives the rearrangement of the underlying microstructure. This potential admits a dependence on a set of ISVs (for the isothermal case) that characterize the interface structure and morphology. Further, $\tilde{\Delta}_n$ and $\tilde{\Delta}_t$ are generalized nonlinear elastic displacements, dictating that the interface separation parameters, σ_{max}, δ_n and δ_t are to depend solely on the set of ISVs, $\mathbf{\Lambda}_q$, i.e.,

$$\tilde{\phi} = \hat{\phi}\left(\sigma_{max}, \frac{\tilde{\Delta}_n}{\delta_n}, \frac{\tilde{\Delta}_t}{\delta_t}, \mathbf{\Lambda}_q \right) \tag{VI.9}$$

with

$$\sigma_{max} = \hat{\sigma}\left(\mathbf{\Lambda}_q\right) \quad , \quad \delta_n = \hat{\delta}_n\left(\mathbf{\Lambda}_q\right) \quad \text{and} \quad \delta_t = \hat{\delta}_t\left(\mathbf{\Lambda}_q\right) \quad . \tag{VI.10}$$

The evolution of the interface attributes is described through

$$\frac{D\mathbf{\Lambda}_p}{Dt} = \dot{\mathbf{\Lambda}}_p = f_p\left(\mathbf{\Lambda}_q, \tilde{\Delta}_n, \tilde{\Delta}_t; \nabla^k \mathbf{\Lambda}_q, \nabla^k \tilde{\Delta}_n, \nabla^k \tilde{\Delta}_t\right) \tag{VI.11}$$

The dependence of the maximum interface strength and the interface normalizing parameters on the interface structure and morphology is evident from the atomistic calculations presented in Chapters IV and V. As before, the elastic potential $\tilde{\phi}$ naturally introduces coupling between the normal and tangential components of elastic interface separation. In this framework, the set of ISVs, $\boldsymbol{\Lambda}_q$, accounts for the non-equilibrium, path-dependent nature of cohesive separation for ductile systems. Each ISV, $q = 1,2,...,Q$, allows for a description of the interface structure and morphology over the course of separation. In accordance with ISV theory, the underlying dissipative mechanisms that change the structure of the interface are described through a set of differential equations for each evolving parameter in the set of ISVs. In Eq. (VI.11), $p = 1,2,...,P$ with $P \le Q$ and ∇^k is the del operator of order k. A dependence on the gradients of separation of order k within the separation boundary layer is incorporated in the evolution equations to facilitate a weakly nonlocal description (Eringen, 1966). For small cut-off radii, k may be reduced to lower order, i.e., k = 1 or k = 2, corresponding to first or second order gradient characterizations of the evolution of the internal structure. While the current work uses Eq. (VI.11), in lieu of explicitly tracking the rate of change of each individual ISV over time, the evolution of the inelastic displacement associated with microstructure rearrangement may be evaluated. In general, the inelastic boundary displacements Δ_n^p and Δ_t^p are not regarded as ISVs themselves, because they evolve in accordance with the set $\boldsymbol{\Lambda}_p$. However, for practical purposes they may be identified with the evolving $\boldsymbol{\Lambda}_p$.

Table VI.1. List of ISVs required to characterize the interface structure and morphology during deformation.

Active ISVs	
D_c	Nanoporosity within the interface region
ρ	Dislocation density within interface region apart from that inherent to the boundary structure
Passive ISVs	
$\boldsymbol{\kappa}_{s,i}$, $\boldsymbol{\kappa}_{n,i}$, $\boldsymbol{\kappa}_{p,i}$ $\quad i = 1, n_{slip}$	Tensor description of slip system orientation
$\bar{\omega}$	RMS characterization of the interface roughness
χ	Impurity atom parameter
C	Composition parameter

VI.4.3 Nanoscale Interface Attributes

To effectively address the dependence of separation on interface structure and morphology, the set of ISVs incorporates parameters that describe the topology of the interface, including a description of physical attributes such as roughness, composition, impurities and porosity. Motivated by the molecular dynamics calculations in the preceding chapters and by research presented in the literature (*cf.* Howe, 1997), Table VI.1 presents a list of ISVs that are deemed critical to characterize the interface strength and work of separation in ductile materials. Each of these ISVs will be defined later in Section VI.4.4. It is proposed that the set of ISVs be classified into subsets of active and passive variables. Passive ISVs are defined as parameters that do not significantly evolve over the course of separation, yet affect the shape of the traction-displacement curve for the interface. For example, previous MD and experimental studies have shown that

impurity atoms adversely affect the yield and fracture strengths of a material (*cf*. Hirth, 1980; Daw and Baskes, 1983). In a closed system, the number of impurity atoms within the interface region remains constant, dictating that an impurity atom parameter be included in the set of passive ISVs. By virtue of their essentially stationary nature, passive ISVs do not significantly contribute to dissipation through their own evolution – they are more akin to 'order parameters' that affect the datum of the free energy state of the original interface and the separation energy during deformation. Active ISVs, on the other hand, are defined as parameters that both affect the stress-displacement response of the interface and evolve significantly over the course of interface deformation, such as a measure of interface porosity. Active ISVs related to dislocation generation and other dissipative structure evolutions may begin to change even at the onset of elastic stretching of the interface, as a means of accommodating the misfit under an applied stress, as shown in Chapter V. Note, that the composition parameter may be considered as an active ISV if diffusion occurs on the same time scale as separation.

The introduction of a set of ISVs to quantify the interface structure during separation requires the introduction of the notion of a 'statistical volume' (SV) associated with the length scale of the MD domain analyzed. Due to the scale of these calculations, in general, this statistical volume is too small to be considered as statistically representative in the continuum sense (Ostoja-Starzewski, 1998). ISVs included in Eqs. (VI.9) – (VI.11) represent averaged values over the SV (Rice, 1971). Such boundary layer effects must be understood from MD calculations. For the case considered here, if the size of the interface region, d, shrinks to the limit of a few interatomic spacings around the boundary, the elastic potential would represent the nonlinear elastic relation for the stretching of interatomic

bonds across the interface. It is nonlinear due to the large local displacements of atoms from their equilibrium spacing within this deformed strip. If the interface region extends further away from the grain boundary interface, the interface potential would lead to more weakly nonlinear force-displacement relations because bonds away from the interface are perturbed only slightly from their equilibrium positions. This separation boundary layer effectively serves to dissipate much of the work of separation via generation of point and line defects. Incorporation of interface-normalizing parameters that are dependent on the interface volume will address length scale dependence, while preserving the basic structure of the interface constitutive equations.

Further, it may be necessary to include terms in the set of ISVs that address the variation of the interface attributes within the interface region, to establish whether gradients of composition, damage or dislocation density are sufficiently strong at the scale of the SV to warrant consideration of nonlocal interactions. These gradients may be formulated on the atomic level by analyzing how the composition and damage measures change over the statistical volume. Then, partial derivatives of these expressions may be taken with respect to position along the interface. Consideration of parameters that are associated with the atomic level discreteness of the interface, as in the set of ISVs, with parameters that are associated with gradients across the interface layer is key to developing continuum interface separation potentials that may be used at both atomistic and higher length scales.

Two caveats are in order with regard to the use of nanoscale ISVs derived from MD simulations. First, the proposed list of ISVs is not a complete set. Atomistic simulations can shed light on combinations of parameters that have a significant effect on

interface separation behavior, as shown in Chapter V. Detailed information that relates to interface separation at the atomic scale is still inaccessible to most physical experiments. From a practical standpoint, it will be assumed that $\mathbf{\Lambda}_q$ is the minimum set of ISVs required to address nanoscale effects on interface separation from a thermodynamic standpoint (Rice, 1971). Second, atomistic calculations of interfaces may not precisely conform to all material arrangements observed in nature. The EAM has been proven as a means to match potentials to certain aspects of mechanical behavior in FCC materials (Daw and Baskes, 1983; 1984; Foiles *et al.*, 1986; Mishin *et al*., 1999; 2001); however, potentials developed by different researchers may not precisely agree with *ab initio* results for some material properties (Zimmerman *et al.*, 2000). To accurately model fracture at the atomic level, quantum mechanical (electronic structure) calculations must be performed. However, computing limitations still restrict *ab initio* calculations from being used at length scales where dislocation nucleation can be studied (especially in the case where a perfect dislocation is split into two partials with extended separation). With this in mind, the focus of this chapter is on the formulation for a general framework in which results of atomistic calculations can inform continuum separation laws.

VI.4.4 Calculation of Interface Attributes

The following subsections present a brief overview of how each of the internal state variables may be calculated during a molecular dynamics simulation. Note that the calculations presented in this dissertation are performed on planar (or nearly planar) homogeneous interfaces with initially defect free crystalline lattices. Thus, the influence of initial dislocation density in the vicinity of the interface, interface roughness,

composition and impurity atom content on the interface separation response is not explicitly studied in this work. Nonetheless, the calculation of these parameters is discussed in the following subsections for completeness.

VI.4.4.1 Nanoporosity

A measure of nanoporosity is developed in Chapter V of this thesis. Recall that this measure is developed by examining the first-order coordination number of each atom, $\mathbb{Z}_1^i$. Atoms with $\mathbb{Z}_1^i$ less than that of the perfect crystal arrangement are defined as 'damaged' in that they have partially ineffective bonding or that they lie at newly created free surfaces. Using this concept, an expression for the damage parameter on a per atom basis is formulated, i.e.,

$$D^i = 1 - \left\langle \frac{\mathbb{Z}_1^i - \mathbb{Z}_{1,th}}{\mathbb{Z}_{1,ref} - \mathbb{Z}_{1,th}} \right\rangle \quad . \tag{VI.12}$$

Equation (VI.12) allows for the i^{th} atom to have partial damage ($0 \le D^i \le 1$) depending on its local environment. Angle brackets define that atoms with $\mathbb{Z}_1^i < \mathbb{Z}_{1,th}$ have $D^i = 1$ and atoms with $\mathbb{Z}_1^i > \mathbb{Z}_{1,ref}$ have $D^i = 0$. By averaging the point-wise damage measure over a set of atoms within the statistical volume, a cumulative measure of damage D_c is defined as

$$D_c = \frac{1}{N'}\left[\sum_{i=1}^{N'} D^i\right] = \frac{1}{N'}\left[\sum_{i=1}^{N'}\left(1 - \left\langle \frac{\mathbb{Z}_1^i - \mathbb{Z}_{1,th}}{\mathbb{Z}_{1,ref} - \mathbb{Z}_{1,th}} \right\rangle\right)\right] \quad . \tag{VI.13}$$

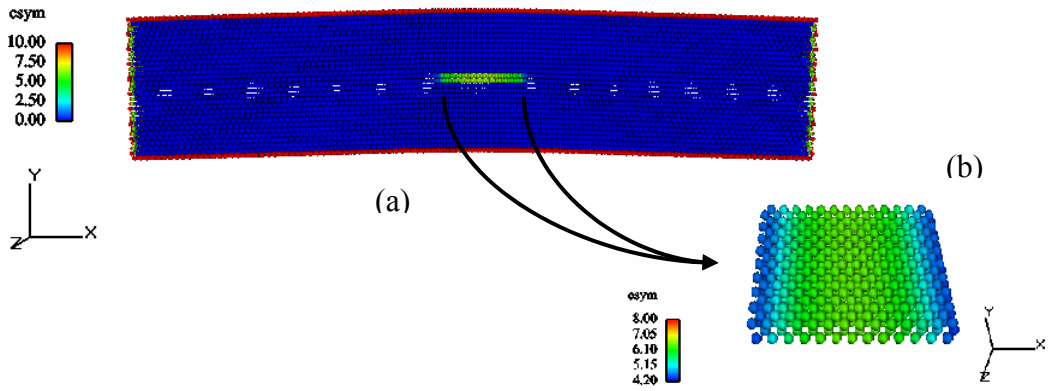

Figure VI.5. Calculation of dislocation density in the molecular dynamics framework at 0 K. The Shockley partial dislocation cores are separated from the stacking fault region using the centrosymmetry parameter.

Numerically, Eq. (VI.13) may be evaluated at each timestep simply from the atomic positions and requires no preconceived knowledge of the void content within the system at fracture. If free volume is created during the deformation process, the nanoporosity measure will increase from its initial value to some critical value less than one. Note that calculations in Chapter V show that structural rearrangement during elastic stretch of the interface region sometimes dictates that the interface porosity decreases prior to void nucleation.

VI.4.4.2 Dislocation Density

Experimentally, dislocation density, ρ, may be calculated by summing the total line length of the dislocation cores and dividing by the total volume of material sampled (Hirth and Lothe, 1982; Hull and Bacon, 2001), i.e.,

$$\rho = \frac{\ell_c}{V_{int}} \tag{VI.14}$$

Here, ℓ_c represents the total line length of the dislocation cores and V_{int} is the volume of the interface region. Previously, this volume definition (Rudd and Belak, 2002) as well as an alternative area definition (Fournet and Salazar, 1995) have been used to calculate dislocation density during atomistic calculations, an example of which is shown in Fig. VI.5 for a dissociated dislocation in copper at 0 K. Areas of local lattice distortion are identified using the centrosymmetry parameter (Kelchner *et al*., 1998). Figure VI.5(a) shows that the centrosymmetry parameter can distinguish between atoms that reside between the partial dislocations (stacking fault region) and those that are within the bulk lattice. To separate the partial dislocation cores from the stacking fault region, the centrosymmetry calculation may be 'banded' as shown in Fig. VI.5(b). Geometrically, atoms positioned at the leading and trailing edges of the stacking fault region have a slightly different local lattice environment than atoms within the stacking fault. The total length of all dislocations within the interface region may be found by summing the individual partial dislocation core lengths and dividing by two. It is important to divide by two as only one of the Shockley partials should be included in the dislocation density calculation. Dislocation density may then be calculated by dividing the total dislocation core line length by the volume of the interface region. It is noted that images in Fig. VI.5 are taken at 0 K. Adjustments must be made to the above methodology to handle simulations at elevated temperatures. Calculations in (Li *et al*., 2003) show that the discrete identification of individual dislocation cores at temperatures above approximately 100 K is very difficult due to thermal vibrations.

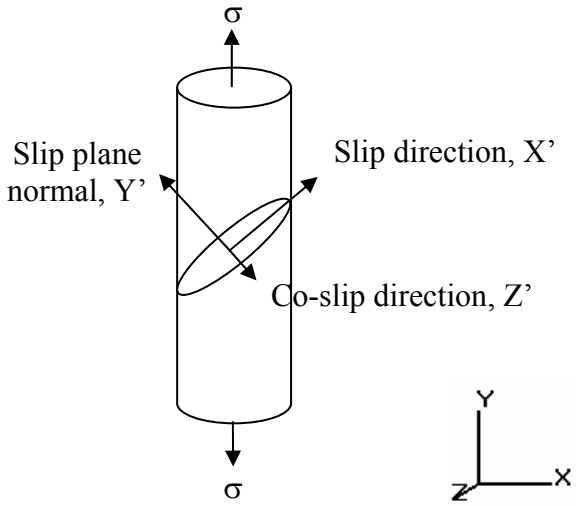

Figure VI.6. Stress elements that act upon the slip plane during a tensile deformation in the Y-direction. Orientation parameters in the set of ISVs project the local stress state onto the slip plane.

VI.4.4.3 Orientation

In general, three orientation tensors are required for each slip system in each phase across an interface between ductile constituents to admit a dependence of the interface separation potential on the directionality of the adjoining lattice regions. In Table VI.1, $\boldsymbol{\kappa}_{s,i}$ projects the local stress tensor in the vicinity of the interface onto the slip plane in the slip direction, $\boldsymbol{\kappa}_{n,i}$ projects the stress tensor onto the slip plane normal and $\boldsymbol{\kappa}_{p,i}$ projects of the stress tensor onto the slip plane in the co-slip direction. The co-slip direction is defined as the vector that lies within the slip plane perpendicular to the slip direction. Let X, Y, and Z be the orientation vectors associated with the applied load and X', Y' and Z' denote the slip direction, the slip plane normal and the co-slip direction

within the slip plane, respectively, as shown schematically in Fig. VI.6. Then, the linearly independent orientation tensors are defined as (Hosford, 1993)

$$\boldsymbol{\kappa}_{s,i} = \begin{bmatrix} \ell_{y'x}\ell_{x'x} & \ell_{y'x}\ell_{x'y} & \ell_{y'x}\ell_{x'z} \\ \ell_{y'y}\ell_{x'x} & \ell_{y'y}\ell_{x'y} & \ell_{y'y}\ell_{x'z} \\ \ell_{y'z}\ell_{x'x} & \ell_{y'z}\ell_{x'y} & \ell_{y'z}\ell_{x'z} \end{bmatrix} , \tag{VI.15}$$

$$\boldsymbol{\kappa}_{n,i} = \begin{bmatrix} \ell_{y'x}\ell_{y'x} & \ell_{y'x}\ell_{y'y} & \ell_{y'x}\ell_{y'z} \\ \ell_{y'y}\ell_{y'x} & \ell_{y'y}\ell_{y'y} & \ell_{y'y}\ell_{y'z} \\ \ell_{y'z}\ell_{y'x} & \ell_{y'z}\ell_{y'y} & \ell_{y'z}\ell_{y'z} \end{bmatrix} , \tag{VI.16}$$

and

$$\boldsymbol{\kappa}_{s,i} = \begin{bmatrix} \ell_{y'x}\ell_{z'x} & \ell_{y'x}\ell_{z'y} & \ell_{y'x}\ell_{z'z} \\ \ell_{y'y}\ell_{z'x} & \ell_{y'y}\ell_{z'y} & \ell_{y'y}\ell_{z'z} \\ \ell_{y'z}\ell_{z'x} & \ell_{y'z}\ell_{z'y} & \ell_{y'z}\ell_{z'z} \end{bmatrix} . \tag{VI.17}$$

Here, $\ell_{y'x}$ is the direction cosine between the Y' and X directions, for example. Because direction cosines are used in Eqs. (VI.15) – (VI.17), it is not critical that the director vectors associated with the applied load or the slip systems be unit vectors. Apparently, each component of each orientation tensor is defined from the scalar product of two direction cosines. If perfect Schmid behavior was observed for the single crystal calculations in Chapter V, $\boldsymbol{\kappa}_{s,i}$ would be the only tensor required to characterize the relationship between maximum tensile strength and orientation. However, non-Schmid behavior is prominent for some orientations and thus the non-Schmid tensors in Eqs. (VI.16) and (VI.17) must be included.

In this work, the shear stress on the boundaries of each interface or single crystal model is approximately zero. Thus, using the orientation tensors, the resolved shear stress in the slip direction, slip plane normal and co-slip direction are,

$$\begin{aligned}\tau_{y'x'} &= \ell_{y'x}\ell_{x'x}\sigma_{xx} + \ell_{y'y}\ell_{x'y}\sigma_{yy} + \ell_{y'z}\ell_{x'z}\sigma_{zz} \\ \sigma_{y'y'} &= \ell^2_{y'x}\sigma_{xx} + \ell^2_{y'y}\sigma_{yy} + \ell^2_{y'z}\sigma_{zz} \\ \tau_{y'z'} &= \ell_{y'x}\ell_{z'x}\sigma_{xx} + \ell_{y'y}\ell_{z'y}\sigma_{yy} + \ell_{y'z}\ell_{z'z}\sigma_{zz}\end{aligned} \quad . \tag{VI.18}$$

Recall that for uniaxial tension boundary conditions, $\sigma_{xx} \approx \sigma_{zz} \approx 0$; while for constrained tension boundary conditions, $\sigma_{xx}, \sigma_{zz} > 0$.

VI.4.4.4 Roughness

Interface roughness may be accounted for by calculating the root-mean-squared (RMS) of the amplitude of the individual roughness peaks, $\omega_{a,i}$, i.e.,

$$\bar{\omega} = \sqrt{\frac{1}{l}\sum_{i}\left(\omega_{a,i}\right)^2} \quad . \tag{VI.19}$$

Here, l is an arbitrary length along the interface plane. The magnitude of each peak is defined from an arbitrary reference line over this length. This formulation accounts for both the frequency and magnitude of the undulations within the boundary layer of separation. Note that there are many other ways to account for interface or surface roughness in a continuum formulation. The RMS characterization of interface roughness,

included in the list of ISVs, is postulated for simplicity and potential ease of calculation during an atomistic simulation. The interfaces in this work are considered planar and thus surface or interface roughness effects are not explicitly addressed.

VI.4.4.5 Composition / Impurity Content

Impurity atom and composition parameters are related, in that they involve a description of separation behavior for interfaces with more than one elemental constituent. In the set of ISVs, impurity atom content is used to describe interfaces that contain interstitial atoms within the interface region that do not correspond to the material on either side of the interface. The impurity atom parameter may be defined as an atomic fraction over the statistical volume, i.e.,

$$\chi = \frac{N_{imp}}{N} \quad . \tag{VI.20}$$

Here, N is the total number of atoms and N_{imp} is the number of impurity atoms within the statistical volume. Clearly, in the event of a pure interface (single material), χ reduces to zero. Realistically, the impurity atom parameter will never approach unity. The composition parameter, which is associated with elemental intermixing, describes the progression of the interface within the boundary layer, admitting a description of either sharp or diffuse interfaces. For the description of bimaterial interfaces, the phase-field method utilizes order parameters to characterize the state of the entire microstructure (Langer, 1991). Typically, an order parameter is chosen to vary between zero and one. For example, order parameter values of zero may represent regions of element A, while

values of one may correspond to regions of element B. Regions with both A and B constituents will have an order parameter value between zero and one, allowing for a description of the 'thickness' of the interface between two elements. Here, the discussion is limited to two elemental constituents; thus, compositional order parameters are defined, $c_{\mathrm{A}}^{\mathrm{i}}$ and $c_{\mathrm{B}}^{\mathrm{i}}$, as the atomic fraction between the number of like atoms and the number of total atoms around a particular atom i, i.e.,

$$c_{\mathrm{A}}^{\mathrm{i}} = \left(\frac{\mathbb{Z}_{\mathrm{j,A}}}{\mathbb{Z}_{\mathrm{j}}} \right)^{\mathrm{i}} \quad \text{and} \quad c_{\mathrm{B}}^{\mathrm{i}} = \left(\frac{\mathbb{Z}_{\mathrm{j,B}}}{\mathbb{Z}_{\mathrm{j}}} \right)^{\mathrm{i}} \quad . \tag{VI.21}$$

Here, $\mathbb{Z}_{\mathrm{j}}$ is the total number of neighbors to a particular atom, which is a function of the cut-off distance of the chosen interatomic potential. Thus, $\mathbb{Z}_{\mathrm{j,A}}$ and $\mathbb{Z}_{\mathrm{j,B}}$ are the number of A and B atoms, respectively, within the sphere of EAM influence around the i^{th} atom. For the development of the nanoporosity measure, it was only necessary to account for first nearest neighbors to which a particular atom is directly bonded. If both metallic and non-metallic elemental constituents are to be modeled, Eq. (VI.21) may have to be altered to address the affect of bond directionality, for example. As a mathematical convenience, an additional variable, c^{i}, is created as the product of the order parameters, i.e.,

$$c^{\mathrm{i}} = c_{\mathrm{A}}^{\mathrm{i}} \cdot c_{\mathrm{B}}^{\mathrm{i}} \quad . \tag{VI.22}$$

If an atom only interacts with atoms of an identical material, $c^{i} = 0$. Atoms that interact with an equal number of both type A and B atoms will have $c^{i} = 0.25$. All other variations of composition will lie between these two bounding values. Equation (VI.22) represents an atom-by-atom measure of the composition variable. If c^{i} is averaged over the total number of atoms within the interface region, a single measure of composition is developed for use in the set of ISVs, i.e.,

$$C = \frac{1}{N}\left[\sum_{i=1}^{N} c^{i}\right] = \frac{1}{N}\left[\sum_{i=1}^{N}\left(c_{A}^{i} \cdot c_{B}^{i}\right)\right] \quad . \tag{VI.23}$$

Equations (VI.21)-(VI.23) allow for a single, scalar measure of composition, for use in the set of ISVs, which accounts for both the 'thickness' of the elemental mixing region and the 'sharpness' of the region between elements A and B. If composition were symmetric across the interface region, an interface with a large intermixing zone (diffuse interface) will have a larger C value than an interface with a small intermixing zone (sharp interface). However, the elemental intermixing region may not be symmetric within the SV. Equation (VI.23) provides a distinction between two interfaces with identical 'thicknesses', but with different mixing characters. Clearly, for single material interfaces, such as those studied in this work, $C = 0$.

VI.4.5 Application of the ISV Model to [001] Interfaces

To illustrate the utility of the internal state variable formulation, recall the simulation results presented in Sections V.4.1 and V.4.2 for uniaxial tensile deformation

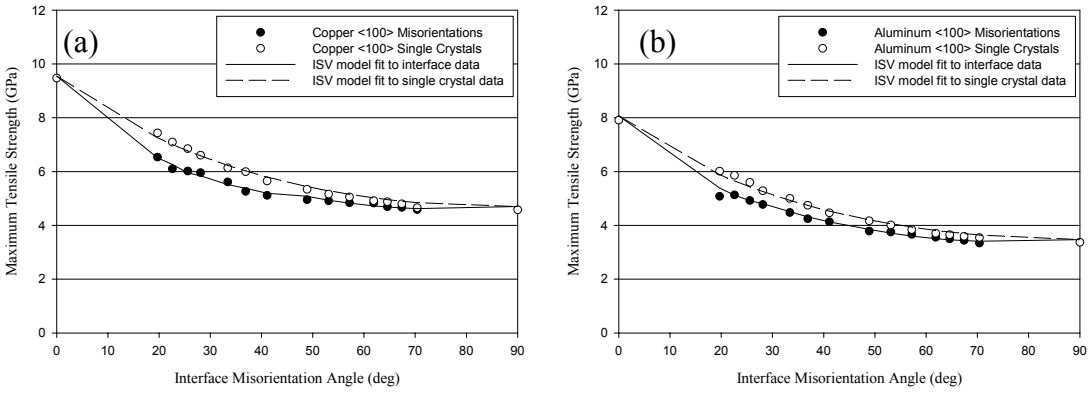

Figure VI.7. Application of the ISV interface separation model to [001] interface and single crystal samples in (a) copper and (b) aluminum.

of copper and aluminum [001] single crystal and interface models. For convenience, the maximum tensile strength for each atomistic model is repeated in Figs. VI.7(a) and VI.7(b). Simulation results in Chapter V indicate that for the [001] misorientation axis, the orientation of the adjoining lattice regions and the porosity in the vicinity of the interface play a strong role in defining the maximum tensile strength. The nanoporosity measure proved capable of capturing the initial porosity within the interface region and the evolution character of the interface structure; however, porosity alone did not appear to be the only factor contributing to the tensile strength of the interface.

To develop a correlation between the tensile strength of the interface and a characterization of the interface structure (orientation and porosity), the following two step process is adopted. First, atomistic simulation results for uniaxial tensile deformation of single crystal models are used to isolate the influence of lattice orientation on the maximum tensile stress. As discussed in Chapter V, atomistic simulations in this work show that non-glide stresses appear to play a strong role in defining the stress

associated with the nucleation of dislocations. Several phenomenological theories have been introduced to address the influence of non-glide stresses on the yield of single crystals (Qin and Bassani, 1992; Dao and Asaro, 1993; Steinmann *et al*., 1998). Motivated by these methodologies, the following relationship is proposed to describe the correlation between lattice orientation and maximum tensile strength during a uniaxial tensile deformation in the Y-direction,

$$\sigma_{\max} = \frac{\sigma_{\text{ideal}}}{\mu_s SF + \mu_n NF^2 + \mu_p PF^2} \tag{VI.24}$$

where,

$$SF = \ell_{y'y}\ell_{x'y} \tag{VI.25}$$

$$NF = \ell_{y'y}^2 \tag{VI.26}$$

$$PF = \ell_{y'y}\ell_{z'y} \quad . \tag{VI.27}$$

Recall that $\ell_{x'y}$ is the direction cosine between the X' and Y axes (for example); consequently, SF, NF and PF are individual components of the $\boldsymbol{\kappa}$ tensors that provide a dependence on the orientation of the adjoining lattice regions. Recall from Section VI.4.4.3 that SF projects the uniaxial stress onto the slip plane in the slip direction, NF projects the uniaxial stress onto the slip plane normal and PF projects of the uniaxial stress onto the slip plane in the co-slip direction. The ideal shear strength, σ_{ideal}, is defined as the shear strength required to nucleate a dislocation when all other stresses applied to the slip plane are zero. *Ab initio* calculations by Ogata *et al*. (2002) calculate the ideal shear strength as $\sigma_{\text{ideal}}^{\text{Cu}} = 2.16$ GPa and $\sigma_{\text{ideal}}^{\text{Al}} = 2.84$ GPa. The scalar

parameters μ_s, μ_n and μ_p are used to characterize the degree of non-Schmid behavior, i.e., the influence of stresses exerted on the slip plane in non-glide directions. Note that Eq. (VI.24) is written specifically for a uniaxial tensile stress normal to the interface plane. If the interface is subjected to a multiaxial state of stress (constrained tension boundary conditions), additional scalar parameters, μ, and a more complex relationship may be required to model the influence of lattice orientation on the peak tensile strength. Clearly, if $\mu_s = 1$ and $\mu_n = \mu_p = 0$, Eq. (VI.24) reduces to traditional Schmid behavior,

$$\sigma_{\max} = \frac{\sigma_{\text{ideal}}}{SF} \quad . \tag{VI.28}$$

The quadratic dependence on NF and PF in Eq. (VI.24) is motivated by the *ab initio* calculations in Ogata *et al*. (2002). Although their analysis is limited due to the range of the non-glide stresses evaluated, they showed that the effect of the normal and co-slip direction stresses on the maximum <112> shear stress is nonlinear. In this work, as the orientation of the lattice region is increased from 0^o to 90^o around the [001] axis, NF and PF will vary disproportionately. In general, the exponential factors on NF and PF may be used as additional fitting parameters if higher-order accuracy is desired. Nonetheless, Figs. VI.7(a) and VI.7(b) show that the proposed relationship in Eq. (VI.24) correlates well with the single crystal data collected from MD simulations. For single crystal copper, the factors that characterize the non-Schmid behavior are taken as $\mu_s = 0.32$, $\mu_n = 0.70$ and $\mu_p = 0.32$. For single crystal aluminum, the non-Schmid factors are taken as $\mu_s = 0.4$, $\mu_n = 1.4$ and $\mu_p = 0.6$.

Once the effect of lattice orientation on the maximum tensile interface strength has been determined, the influence of the bicrystal interface is incorporated into Eq. (VI.24) by adding a dependence on the porosity within the interface region, i.e.,

$$\sigma_{\max} = \left(1 - \xi \mathrm{D_c}\right) \frac{\sigma_{\text{ideal}}}{\mu_s SF + \mu_n NF^2 + \mu_p PF^2} \quad . \tag{VI.29}$$

Here, ξ is an amplification factor for the cumulative damage measure. Essentially, Eq. (VI.29) represents a Kachanov (1986) type damage implementation. Figures VI.7(a) and VI.7(b) show that the proposed relationship in Eq. (VI.29) is capable of modeling the influence of interface structure and orientation on the maximum tensile strength reported from MD simulations. The magnification factor on the nanoporosity is taken as $\xi = 6.0$ in copper and $\xi = 3.0$ in aluminum. The interface model data in Fig. VI.6 is correlated using the value of nanoporosity at the tensile interface displacement associated with the maximum tensile stress calculated from molecular dynamics simulations for each interface model. A specific expression to characterize the evolution of the interface porosity is not developed in this dissertation, as it would require additional simulations (beyond those presented in Chapter IV) to characterize the individual mechanisms that occur at the interface prior to the dislocation nucleation event. In particular, a more detailed understanding of the interface coarsening process during elastic stretch of the interface is required to properly pose such an expression for the porosity evolution.

Molecular dynamics simulation results for uniaxial tension of copper and aluminum [001] interface models are used to test the utility of the ISV formulation as it is

clear that the orientation of the adjoining lattice regions and the porosity along the interface plane are the two primary factors which influence the maximum tensile stress. However, molecular dynamics simulation results for uniaxial tension of [110] interface models in copper and aluminum in Sections V.4.3 and V.4.4 indicate that this observation is not universally valid for all interface misorientations. Here a significant drop is observed in the maximum tensile stress for boundaries with <110> interface misorientations greater than 109.5^{o}. As discussed at length in Chapter V, boundaries within this misorientation range contain the E structural unit, which has increased free volume (as compared with other structural features) and is favorably aligned with the coplanar slip systems. Unfortunately, the nanoporosity measure by itself is unable to characterize the role of the E structural unit. As a result, the functional form proposed in Eq. (VI.29) will be unable to capture the severe drop in the tensile strength and work of separation for these boundaries.

Two possible solutions are hypothesized to address this range of boundary misorientations. First, additional internal state variables may be included to admit a dependence of the interface separation potential on the distribution (or gradient) of damage within the interface region. Second, the amplification factor for the nanoporosity measure, ξ, may be posed as a function of the distribution of interface structural units present within each boundary. The latter solution represents a phenomenological approach and would require a detailed description of each boundary prior to the deformation event, which may be extremely complicated in the case of real interfaces between grains. The former solution requires additional analysis of the molecular dynamics results to define the relationship between porosity distribution and dislocation

nucleation. It is likely that the localized 'pockets' of porosity, characteristic of interfaces with the E structural unit, result in high stress concentrations which contribute to the drop in tensile strength.

Finally, the effect of scale on the forms of the relationships proposed in this section must be considered. From the definition of the nanoporosity measure, it is clear that the magnitude of this parameter will be dependent on the volume over which the per atom damage measure is averaged. Consequently, the magnitude of the amplification factor for the nanoporosity measure, ξ, will be scale dependent. However, based on arguments presented in Chapter IV, regarding the effect of scale on the character of the nucleated dislocations and the stress levels at which dislocations are emitted from the bicrystal interfaces, the form of Eq. (VI.29) is not believed to be scale dependent.

CHAPTER VII

CONCLUSIONS AND RECOMMENDATIONS

VII.1 Summary of Significant Contributions

The focus of the work presented in this dissertation is on the exploration of structure-property relationships on the nanoscale for homogeneous interfaces in ductile materials. Recall that the four main objectives to this thesis are: (i) to efficiently determine the minimum energy equilibrated structure of homogeneous copper and aluminum bicrystal interfaces; (ii) to provide a characterization of atomic scale inelastic behavior at an interface, including both dislocation and void nucleation activities which lead to interfacial failure; (iii) to investigate potential relationships between interface structure (occurrence of CSL boundaries) and interface properties; and (iv) to utilize the results of the atomistic calculations to motivate improved forms for continuum interface separation potentials, contributing eventually to a more predictive multiscale model of fracture. It is clear that each of these objectives is addressed by the work presented in this dissertation. In particular, the significant contributions of this work are summarized as follows:

- Numerical schemes are developed and/or implemented into an existing molecular dynamics code in order to perform the calculations presented in this dissertation. As discussed in Chapter II, the original MD code was authored by Dr. Steve Plimpton (Sandia National Laboratories / Albuquerque, NM). To address the

requirements of this work, several algorithms have been added to the code including the capabilities to perform energy minimization calculations with a nonlinear conjugate gradient algorithm and the ability to perform simulations in the constant pressure or constant stress ensembles. In addition, new output subroutines have been added to calculate different interface measures, such as nanoporosity.

- Algorithms are developed in this dissertation to assist in the isobaric-isothermal equilibration procedure and to deform atomistic models using a mixed set of boundary conditions (constant strain rate simulations). Both algorithms are critical to the accuracy of the results presented in this work. Specifically, an extra damping term is added to the equation for the isobaric 'friction' constant, $\boldsymbol{\eta}$, that critically damps the pressure or stress equilibration. Feller *et al.* (1995) showed that the additional boundary 'drag' term reduces the influence of the value of the damping constant, v_P. For solids, it is desirable to have the system equilibrate in a reasonable amount of time without large pressure or stress fluctuations. The mixed set of boundary conditions combines displacement-controlled and stress-controlled boundary prescriptions. Here, the aim is to be able to apply a constant strain rate in one direction, while having the motion of the boundaries transverse to the loading direction be controlled via the imbalance between the system stress and the desired value.

- Energy minimization calculations with a nonlinear conjugate gradient algorithm are used to refine the initial interface structures. Recall that one of the primary goals of this thesis is to quantify the role of specific interface features in the inelastic response of the interface. Thus, it is critical that the initial interface structures be described accurately to meet the computational objectives of this work. In agreement with previous results in the literature, it is found that a number of starting configurations must be used to increase the probability that the global minimum energy configuration is attained. As expected, the optimum starting configuration (lateral shift and separation normal to the interface plane) varies depending on the orientation of the lattice regions and the characteristics of the material. This thesis represents an advancement over previous energy minimization calculations of interface structures in FCC metallic systems due to the accuracy of the interatomic potential used for these calculations.

- The interface energy versus misorientation angle relationships reported in this work are in qualitative agreement with those presented previously in the literature (Wolf, 1990; Rittner and Seidman, 1996). The energies of the Σ3 and Σ5 boundaries in this work are in agreement with those reported by Mishin *et al.* (1999; 2001). It is found that cusps appear in the energy at certain low-order CSL boundaries. For the <001> misorientation axis, small cusps occur at the Σ5 (310) and Σ5 (210) interfaces, which are the two lowest-order CSL boundaries for this misorientation axis. For the <011> misorientation axis, cusps occur in the energy versus misorientation angle relationship at the Σ3 (111) and Σ11 (113)

boundaries. Note that these boundaries are not the two lowest-order CSL boundaries around the <110> misorientation axis. For instance, a 70.5^{o} rotation around the <110> axis creates the Σ3 (112) boundary. However, this boundary does not show a cusp in the energy according to the calculations performed in this work.

- The interface structures presented in this work are in qualitative agreement with those presented in the literature using either computational or experimental techniques (*cf*. Mills *et al*., 1992; Medlin *et al*., 1993; Rittner and Seidman, 1996). In this work, it is found that the structural unit model (Sutton and Vitek, 1983a) is accurate only for materials with high-stacking fault energies. For materials with low-stacking fault energies, the interface dislocations tend to dissociate, leading to more diffuse interface structures. Regardless, the dissociated interface structures can still be classified using structural units, i.e., the interface structure is not amorphous. Interface structures in aluminum predicted using the Mishin *et al*. EAM potentials are in agreement with published high-resolution transmission electron microscopy results in the literature (Medlin *et al*., 1993).

- Molecular dynamics simulations are used to study the atomic scale mechanisms that occur at bicrytal boundaries in copper and aluminum with a range of interface misorientations as a result of an applied mechanical deformation. This thesis goes beyond the previous atomistic calculations in the literature that investigate the mechanisms associated with dislocation nucleation using either bicrystal or

nanocrystalline geometries by (i) addressing interface evolution and dislocation nucleation at finite temperature (as opposed to 0 K) and (ii) considering larger bicrystal samples (by an order of magnitude in some cases) than the previous studies.

- Molecular dynamics simulations of tensile interface separation indicate that dislocations are nucleated directly from the interface structural units during the deformation process. Particular attention is paid to the structure of the interface before and after the dislocation nucleation event. It is found that dissimilar interface features play different roles during dislocation emission. For instance, in aluminum, the trailing partial dislocation is commonly observed to be nucleated from the boundary. The interface structural units at the site of the dislocation nucleation event are distorted as a result. After emission of the trailing partial dislocation a ledge is left within the interface plane for <001> boundaries. Interfaces with dissociated structure show more complex evolution prior to the dislocation nucleation by comparison, as in the case of the 59.0^{o} <110> boundary. In general, interface distortion may be discussed in terms of partial dislocation or disclination positions.

- Molecular dynamics simulations in Chapters IV and V indicate that the interface structure may evolve prior to the dislocation nucleation event. This structural evolution occurs through two mechanisms: (i) coarsening or thickening of the interface region on non-primary slip plane or (ii) through the nucleation of short

intrinsic stacking fault facets on primary slip systems. Such dissipative structural evolution occurs at the onset of elastic stretching of the interface, as a means of accommodating the misfit under an applied stress. The nanoporosity measure appears capable of identifying the onset of the structural evolution prior to the dislocation nucleation event.

- The role of boundary prescription is considered in this dissertation. Specifically, molecular dynamics simulations are performed using either 'uniaxial' or 'constrained' tension boundary conditions, which may be considered as limiting cases for deformation in nanoscale systems. Uniaxial tension boundary conditions involve the application of deformation at a constant strain rate normal to the interface plane, while the lateral boundaries are prescribed as stress free (and thus allowed to contract during the deformation process). Constrained tension boundary conditions involve the application of deformation at a constant strain rate normal to the interface plane, while the lateral periodic boundaries are prescribed with a zero strain condition. Thus, these simulations consider stresses parallel to the boundary plane during the tensile deformation process. It is found that the presence of tensile stress lateral to the loading direction promotes a more brittle mode of failure than the uniaxial case. In addition, certain low-order coincident site lattice (CSL) interfaces have increased strength (relative to other boundaries with misorientations within a few degrees) in cases where lateral confinement causes stresses parallel to the interface plane.

- Molecular dynamics simulations indicate that the orientation of the load with respect to the crystallographic slip systems is one of the primary factors that influences the tensile strength of the interface, especially for uniaxial tension boundary conditions. Only in the case of dissociated interfaces, where ISF facets are sufficiently spaced apart along the interface plane, does the interface structure promote dislocation nucleation on non-primary slip systems. Dislocation activity does not appear to be affected by the applied boundary conditions, i.e., the same slip systems are activated for both uniaxial and constrained tensile deformation.

- Certain <110> boundaries, which contain the E structural, unit show a severe drop in the tensile strength and tensile work of separation as compared with other boundaries for the same misorientation axis. Here, the character of the interface structure and the orientation of the primary slip systems with respect to the load both contribute to this significant drop in the interface strength. Sansoz and Molinari (2005) reported that the E structural unit has increased free volume as compared with the other structural features for the <110> misorientation axis. In their work, the increased free volume inherent to the E structural unit triggered a change in the shear deformation mode. In addition, boundaries with misorientations greater than 109.5^{o} deform by dislocation emission on one slip plane only, with two directions active within that slip plane, i.e., coplanar slip systems. Thus, the favorable orientation of the E structural unit with respect to the coplanar slip systems results in the drop in tensile strength.

- A critical review of the multiscale constitute relationship for interface separation proposed by Hao *et al*. concludes that their methodology may be extended to model ductile interface separation between FCC materials if orientation of the adjoining lattice regions is properly addressed. Specifically, the rescaling parameter κ must include a dependence on the orientation of the interface to properly account for the reduction in interface strength due to plastic deformation. Molecular dynamics simulations in this work show that lattice orientation is a key factor in defining the strength of the interface. In their formulation, the total normal separation is written as a function of the cleavage separation plus the normal component of the dislocation induced gliding separation.

- A general formulation is introduced, based on internal state variable (ISV) theory, which allows for the incorporation of nanoscale interface attributes, such as interface porosity, into a continuum description of interface separation. This formulation addresses some of the limitations of phenomenological interface separation potentials by including detailed interface information necessary to distinguish among continuum potentials for interfaces with differing degrees of coherency, roughness or with the inclusion of impurity atoms, for example. The parameters within the set of ISVs are intended to be derived from MD calculations and relate topological parameters associated with the interface structure to the interface separation process. The interface separation relation is written explicitly to include both the interface and a finite amount of crystalline lattice around the boundary.

- Atomistic calculations are used to identify the key interface attributes for use in set of internal state variables. It is found that orientation of the adjoining lattice regions and the interface porosity are key factors in the description of the tensile interface strength, tensile work of separation and the form of the interface traction-displacement relation. Although their influence is not investigated via molecular dynamics simulations in this dissertation, other internal state variables are introduced, which are designed to account for dislocation density in the vicinity of the interface, interface roughness, interface composition and impurity atom content. Numerical schemes are introduced to calculate each of the ISVs 'on the fly' during a MD simulation.

- The set of ISVs is divided into subsets of active and passive variables. Passive ISVs are defined as parameters that do not significantly evolve over the course of separation, yet affect the shape of the traction-displacement curve for the interface. By virtue of their essentially stationary nature, passive ISVs do not significantly contribute to dissipation through their own evolution – they are more akin to 'order parameters' that affect the datum of the free energy state of the original interface and the separation energy during deformation. Active ISVs, on the other hand, are defined as parameters that both affect the stress-displacement response of the interface and evolve significantly over the course of interface deformation. Active ISVs related to dislocation generation and other dissipative structure evolutions may begin to change even at the onset of elastic stretching of

the interface, as a means of accommodating the misfit under an applied stress, as shown in Chapter V with the nanoporosity measure.

VII.2 Recommendations for Future Work

Atomistic calculations in this work provide a wealth of information regarding the mechanisms associated with dislocation nucleation from copper and aluminum bicrystal interfaces on the nanoscale. The homogeneous bicrystal interface geometry was chosen for this dissertation so that predicted interface structures may be compared to previous theoretical and experimental descriptions in the literature. Thus, definite conclusions can be drawn regarding the accuracy of the initial interface structures in this dissertation, from both energetic and geometric perspectives. Molecular dynamics simulations in the literature using nanocrystalline geometries (*cf*. Schiøtz *et al*., 1998; Van Swygenhoven *et al*., 1999a; Yamakov *et al*. 2001) make no guarantee regarding the accuracy of the initial interface configurations. Further, symmetric tilt and twist interfaces are chosen for this dissertation to allow for the application of periodic boundaries at reasonable length scales. Consequently, there are a number of issues that are not addressed in this work that potentially play a strong role in real microstructures, which are certainly more complex:

- Inelastic deformation of asymmetric tilt and twist boundaries should be performed to gain further insight into the role of lattice orientation on dislocation emission. In this case, the orientation of the slip systems in each lattice region would be

different, as is commonly the case for polycrystalline materials. Recent molecular dynamics simulations have showed that at the structural unit model does not hold for asymmetric tilt boundaries and that the energy of tilt boundaries may increase as the angle of the interface plane deviates from that which creates a perfectly symmetric interface structure (Zhang *et al*., 2005). In these cases, the internal state variable model may require a more complex description of the orientation dependence of the slip systems with respect to the interface and the loading direction.

- Molecular dynamics simulations should be performed to study the influence of impurity atoms on the properties of the interface and the form of the traction-displacement separation relation. Previous MD and experimental studies have shown that impurity atoms adversely affect the yield and fracture strengths of a material (*cf*. Hirth, 1980; Daw and Baskes, 1983). In general, the inclusion of impurity atoms promotes a more brittle fracture mode, potentially reducing the dependence of orientation and increasing the influence of porosity in the internal state variable model of ductile material separation. Further, Millett *et al*. (2005) showed that the inclusion of dopant atoms can dramatically change the local interface structure, potentially activating different dislocation nucleation mechanisms during the deformation process.

- Bimaterial or dual-phase interfaces should be studied using molecular dynamics simulations to determine if the scalar parameter included in the list of internal

state variables is sufficient to capture the role of interface composition on the traction-displacement relationship.

- Finally, some of the details of the computational procedure should be examined, such as strain rate and the application technique for the deformation. In general, both of these are commonly considered as limitations to the molecular dynamics method. Here, the very high strain rate potentially plays a role in the extent that non-Schmid behavior influences the dislocation nucleation stress. Further, recall that atomistic models are deformed using either the standard Melchionna *et al*. (1993) equations of motion or a modified version of the same equations, developed in this dissertation. The motion of the simulation cell is driven by the imbalance between the internal and prescribed systems pressures, while the positions of the atoms are also redistributed around the system center of mass. The consequence of this redistribution on the nucleation and motion of dislocations is not well understood in the literature.

REFERENCES

Alber, I., Bassani, J.L., Khantha, M., Viter, V. and Wang, G.J. (1992). Grain boundaries as heterogeneous systems: atomic and continuum elastic properties. Philosophical Transactions of the Royal Society A, **339**, 555-586.

Allen, M.P. and Tildesley, D.J. (1987). Computer Simulations of Liquids, Clarendon Press, Oxford.

Andersen, H.C. (1980). Molecular dynamics simulations at constant pressure and/or temperature. Journal of Chemical Physics, **72**, 2384-2393.

Arata, J.J.M. and Needleman, A. (1998). Effect of plasticity on dynamic crack growth across an interface. International Journal of Fracture, **94**, 383-399.

Ashurst, W.T. and Hoover, W.G. (1976). Microscopic fracture studies in the two-dimensional triangular lattice. Physical Review B, **14**, 1465-1473.

Bachurin, D.V., Murzaev, R.T. and Nazarov, A.A. (2003). Atomistic computer and disclination simulation of [001] tilt boundaries in nickel and copper. Fizika Metallov i Metallovedenie, **96**, 11-17.

Barenblatt, G.I. (1962). The mathematical theory of equilibrium cracks in brittle fracture. Advances in Applied Mechanics, Vol. VII, Academic Press, 55-129.

Baskes, M.I. (1992). Modified embedded-atom potentials for cubic materials and impurities. Physical Review B, **46**, 2727-2742.

Baskes, M.I., Hoagland, R.G. and Tsuji, T. (1998). An atomistic study of the strength of an extended-dislocation barrier. Modelling and Simulation in Materials Science and Engineering, **6**, 9-18.

Beltz, G.E. and Rice, J.R. (1991). Dislocation nucleation versus cleavage decohesion at crack tips. Modeling the Deformation of Crystalline Solids presented at the Annual Meeting of the Minerals, Metals, and Materials Society, Feb 17-21 1991, New Orleans, LA, USA.

Bozzolo, G., Ferrante, J. and Smith, J.R. (1991). Universal behavior in ideal slip. Scripta Metallurgica et Materialia, **25**, 1927-1931.

Brandon, D.G. (1966). The structure of high-angle grain boundaries. Acta Metallurgica, **14**, 1479-1484.

Buehler, M.J., Hartmaier, A., Gao, H., Duchaineau, M. and Abraham, F.F. (2004). Atomic plasticity: Description and analysis of a one-billion atom simulation of ductile materials failure. Computer Methods in Applied Mechanics and Engineering, **193**, 5257-5282.

Byun, T.S. (2003). On the stress dependence of partial dislocation separation and deformation microstructure in austenitic stainless steels. Acta Materialia, **51**, 3063-3071.

Cahn, J.W. and Hilliard, J.E. (1958). Free energy of a nonuniform system. I. Interfacial free energy. Journal of Chemical Physics, **28**, 258-267.

Camacho, G.T. and Ortiz, M. (1996). Computational modelling of impact damage in brittle materials. International Journal of Solids and Structures, **33**, 2899-2938.

Carlsson, A.E. (1990). Beyond pair potentials in elemental transition metals and semiconductors. Solid State Physics, 43, Academic Press, New York, 1-91.

Carter, C.B. and Ray, I.L.F. (1977). On the stacking-fault energies of copper alloys. Philosophical Magazine, **35**, 189-200.

Caturla, M.-J., Nieh, T.G. and Stolken, J.S. (2004). Differences in deformation processes in nanocrystalline nickel with low- and high-angle boundaries from atomistic simulations. Applied Physics Letters, **84**, 598-600.

Chandra, N. and Dang, P. (1999). Atomistic simulation of grain boundary sliding and migration. Journal of Materials Science, **34**, 655-666.

Chandra, N., Li, H., Shet, C. and Ghonem, H. (2002). Some issues in the application of cohesive zone models for metal-ceramic interfaces. International Journal of Solids and Structures, **39**, 2827-2855.

Chapra, S.C. and Canale, R.P. (1988). Numerical Methods for Engineers, McGraw-Hill, New York.

Cheung, K.S. and Yip, S. (1991). Atomic-level stress in an inhomogeneous system. Journal of Applied Physics, **70**, 5688-5690.

Cleri, F., Phillpot, S.R., Wolf, D. and Yip, S. (1998). Atomistic simulations of materials fracture and the link between atomic and continuum length scales. Journal of the American Ceramic Society, **81**, 501-516.

Coleman, B.D. and Gurtin, M.E. (1967). Thermodynamics with internal state variables. Journal of Chemical Physics, **47**, 597-613.

Cormier, J., Rickman, J.M. and Delph, T.J. (2001). Stress calculation in atomistic simulations of perfect and imperfect solids. Journal of Applied Physics, **89**, 99-104.

Dao, M. and Asaro, R.J. (1993). Non-Schmid effects and localized plastic flow in intermetallic alloys. Materials Science & Engineering A, **A170**, 143-160.

Daw, M.S. and Baskes, M.I. (1983). Semiempirical, quantum mechanical calculation of hydrogen embrittlement in metals. Physical Review Letters, **50**, 1285-1288.

Daw, M.S. and Baskes, M.I. (1984). Embedded-atom method: derivation and application to impurities, surfaces, and other defects in metals. Physical Review B, **29**, 6443-6453.

Daw, M.S. (1989). Model of metallic cohesion: the embedded-atom method. Physical Review B, **39**, 7441-7452.

De-Andres, A., Perez, J.L. and Ortiz, M. (1999). Elastoplastic finite element analysis of three-dimensional fatigue crack growth in aluminum shafts subjected to axial loading. International Journal of Solids and Structures, **36**, 2231-2258.

Derlet, P.M. and Van Swygenhoven, H. (2002). Length scale effects in the simulation of deformation properties of nanocrystalline metals. Scripta Materialia, **47**, 719-724.

Derlet, P.M., Van Swygenhoven, H. and Hasnaoui, A. (2003). Atomistic simulation of dislocation emission in nanosized grain boundaries. Philosophical Magazine, **83**, 3569-3575.

Dugdale, D.S. (1960). Yielding in steel sheets containing slits. Journal of the Mechanics and Physics of Solids, **8**, 100-104.

Ercolessi, F. and Adams, J.B. (1994). Interatomic potentials from first-principles calculations: the force-matching method. Europhysics Letters, **26**, 583-588.

Eringen, A.C. (1966). Unified theory of thermomechanical materials. International Journal of Engineering Science, **4**, 179-202.

Evans, A.G., Hutchinson, J.W. and Wei, Y. (1999). Interface adhesion: Effects of plasticity and segregation. Acta Materialia, **47**, 4093-4113.

Evans, D.J. (1983). Computer `experiment' for nonlinear thermodynamics of Couette flow. Journal of Chemical Physics, **78**, 3297-3302.

Feller, S.E., Zhang, Y., Pastor, R.W. and Brooks, B.R. (1995). Constant pressure molecular dynamics simulation: The Langevin piston method. Journal of Chemical Physics, **103**, 4613.

Field, D.P. and Adams, B.L. (1992). Interface Cavitation damage in polycrystalline copper. Acta Metallurgica et Materialia, **40**, 1145-1157.

Foiles, S.M., Baskes, M.I. and Daw, M.S. (1986). Embedded-atom-method functions for the FCC metals Cu, Ag, Au, Ni, Pd, Pt, and their alloys. Physical Review B, **33**, 7983-7991.

Fournet, R. and Salazar, J.M. (1995). Computer simulations on dislocation patterning. Diffusion and Defect Data Part B, **42-43**, 205-216.

Frederiksen, S.L., Jacobsen, K.W. and Schiotz, J. (2004). Simulations of intergranular fracture in nanocrystalline molybdenum. Acta Materialia, **52**, 5019-5029.

Froseth, A.G., Derlet, P.M. and Van Swygenhoven, H. (2004). Dislocations emitted from nanocrystalline grain boundaries: Nucleation and splitting distance. Acta Materialia, **52**, 5863-5870.

Gall, K., Horstemeyer, M.F., Van Schilfgaarde, M. and Baskes, M.I. (2000). Atomistic simulations on the tensile debonding of an aluminum-silicon interface. Journal of the Mechanics and Physics of Solids, **48**, 2183-2212.

Gertsman, V.Y., Nazarov, A.A., Romanov, A.E., Valiev, R.Z. and Vladimirov, V.I. (1989). Disclination-structural unit model of grain boundaries. Philosophical Magazine A, **59**, 1113-1118.

Gertsman, V.Y. and Tangri, K. (1995). Computer simulation study of grain boundary and triple junction distributions in microstructures formed by multiple twinning. Acta Metallurgica et Materialia, **43**, 2317-2324.

Geubelle, P.H. and Baylor, J.S. (1998). Impact-induced delamination of composites: a 2D simulation. Composites Part B, **29B**, 589-602.

Greiner, W., Neise, L. and Stocker, H. (1995). Thermodynamics and Statistical Mechanics, Springer-Verlag, New York.

Grigoriadis, P., Karakostas, T., Komninou, P. and Pontikis, V. (1999). Low-energy configurations of the Σ5 (210)[001] tilt grain boundary in FCC crystals. Materials Science Forum, **294-296**, 177-180.

Grujicic, M. and Lai, S.G. (1998). Effect of martensitic transformation in Ti-15 at % V beta-phase particles on lamellar boundary decohesion in gamma-TiAl. Journal of Materials Science, **33**, 4389-4400.

Gumbsch, P. (1995). An atomistic study of brittle fracture: toward explicit failure criteria from atomistic modeling. Journal of Materials Research, **10**, 2897-2907.

Haile, J.M. (1992). Molecular Dynamics Simulation: Elementary Methods, Wiley, New York.

Hao, S., Moran, B., Liu, W.K. and Olson, G.B. (2003). A hierarchical multi-physics model for design of high toughness steels. Journal of Computer-Aided Materials Design, **10**, 99-142.

Hao, S., Liu, W.K., Moran, B., Vernerey, F. and Olson, G.B. (2004). Multi-scale constitutive model and computational framework for the design of ultra-high strength, high toughness steels. Computer Methods in Applied Mechanics and Engineering, **193**, 1865-1908.

Hartford, J., von Sydow, B., Wahnstrom, G. and Lundqvist, B.I. (1998). Peierls barriers and stresses for edge dislocations in Pd and Al calculated from first principles. Physical Review B, **58**, 2487-2496.

Haupt, P. (1993). Thermodynamics of Solids. Non-Equilbrium Thermodynamics with Applications to Solids, Springer - Verlag, New York,

Heino, P., Hakkinen, H. and Kaski, K. (1998). Molecular-dynamics study of copper with defects under strain. Physical Review B, **58**, 641-652.

Hertzberg, R.W. (1996). Deformation and Fracture Mechanics of Engineering Materials, John Wiley & Sons, New York.

Hirth, J.P. (1980). Effects of hydrogen on the properties of iron and steel. Metallurgical Transactions A, **11A**, 861-890.

Hirth, J.P. and Lothe, J. (1982). Theory of Dislocations, John Wiley & Sons, New York.

Hoagland, R.G., Hirth, J.P. and Gehlen, P.C. (1976). Atomic simulation of the dislocation core structure and Peierls stress in alkali halide. Philosophical Magazine, **34**, 413-439.

Holian, B.L., Posch, H.A. and Hoover, W.G. (1990). Nonequilibrium free energy, coarse-graining, and the Liouville equation. Physical Review A, **42**, 3196-3206.

Hoover, W.G., Ladd, A.J.C. and Moran, B. (1982). High-strain-rate plastic flow studied via nonequilibrium molecular dynamics. Physical Review Letters, **48**, 1818-1820.

Hoover, W.G. (1985). Canonical dynamics: equilibrium phase-space distributions. Physical Review A, **31**, 1695-1697.

Horstemeyer, M.F. and Baskes, M.I. (1999). Atomistic finite deformation simulations: A discussion on length scale effects in relation to mechanical stresses. Journal of Engineering Materials and Technology, **121**, 114-119.

Horstemeyer, M.F., Baskes, M.I. and Plimpton, S.J. (2001). Length scale and time scale effects on the plastic flow of FCC materials. Acta Materialia, **49**, 4363-4374.

Horstemeyer, M.F., Baskes, M.I. and Plimpton, S.J. (2001). Computational nanoscale plasticity simulations using embedded atom potentials. Theoretical and Applied Fracture Mechanics, **37**, 49-98.

Horstemeyer, M.F., Baskes, M.I., Godfrey, A. and Hughes, D.A. (2002). A large deformation atomistic study examining crystal orientation effects on the stress-strain relationship. International Journal of Plasticity, **18**, 203-229.

Hosford, W.F. (1993). The mechanics of crystals and textured polycrystals, Oxford University Press, New York.

Howe, J.M. (1997). Interfaces in materials: Atomic structure, thermodynamic and kinetics of solid-vapor, solid-liquid and solid-solid interfaces, Wiley, New York.

Hull, D. and Bacon, D.J. (2001). Introduction to Dislocations, Butterworth Heinemann, Oxford.

Hurtado, J.A., Elliott, B.R., Shodja, H.M., Gorelikov, D.V., Campbell, C.E., Lippard, H.E., Isabell, T.C. and Weertman, J. (1995). Disclination grain boundary model with plastic deformation by dislocations. Materials Science & Engineering A, **190**, 1-7.

Ishida, Y. and McLean, M. (1973). Burgers vectors of boundary dislocations in ordered grain boundaries of cubic metals. Philosophical Magazine, **27**, 1125-1134.

Jacobsen, K.W., Norskov, J.K. and Puska, M.J. (1987). Interatomic interactions in the effective-medium theory. Physical Review B, **35**, 7423-7442.

Johnson, R.A. (1972). Relationship between two-body interatomic potentials in a lattice model and elastic constants. Physical Review B, **6**, 2094-2100.

Kachanov, L.M. (1986). Introduction to Continuum Damage Mechanics, Dordrecht-Nijhoff Publishers, Boston.

Kaxiras, E. and Duesbery, M.S. (1993). Free energies of generalized stacking faults in Si and implications for the brittle-ductile transition. Physical Review Letters, **70**, 3752-3755.

Kelchner, C.L., Plimpton, S.J. and Hamilton, J.C. (1998). Dislocation nucleation and defect structure during surface indentation. Physical Review B, **58**, 11085-11088.

Kestin, J. and Rice, J.R. (1970). Paradoxes in the application of thermodynamics to strained solids. A Critical Review of Thermodynamics, Mono Book Corp., Baltimore, 275-298.

Khan, A.S. and Huang, S. (1995). Continuum Theory of Plasticity, John Wiley & Sons, New York.

Kitamura, T., Yashiro, K. and Ohtani, R. (1997). Atomic simulation on deformation and fracture of nano-single crystal of nickel in tension. JSME International Journal A, **40**, 430-435.

Klein, P.A., Bammann, D.J., McFadden, S.X., Antoun, B.R. and Foulk, J.W. (2003). A mechanism-based themomechanical cohesive zone approach for modeling ductile fracture. US National Congress on Computational Mechanics VII, Albuquerque, NM.

Komanduri, R., Chandrasekaran, N. and Raff, L.M. (2001). Molecular Dynamics simulation of uniaxial tension of some single-crystal cubic metals at nanolevel. International Journal of Mechanical Sciences, **43**, 2237-2260.

Langer, J.S. (1991). An introduction to the kinetics of first-order phase transitions. Solids Far From Equilibrium, Cambridge University Press, Cambridge, 311-322.

Lennard-Jones, J.E. (1924a). The determination of molecular fields. I. From the variation of the viscosity of a gas with temperature. Proceedings of the Royal Society of London A, **106**, 441.

Lennard-Jones, J.E. (1924b). The determination of molecular fields. II. From the equation of state of a gas. Proceedings of the Royal Society of London A, **106**, 463.

Li, H. and Chandra, N. (2003). Analysis of crack growth and crack-tip plasticity in ductile materials using cohesive zone models. International Journal of Plasticity, **19**, 849-882.

Li, J.C.M. (1972). Disclination Model of High Angle Grain Boundaries. Surface Science, **31**, 12-26.

Li, M. (2003). EAM potential for aluminum, personal communication.

Li, M., Chu, W.Y., Qian, C.F., Gao, K.W. and Qiao, L.J. (2003). Molecular dynamics simulation of dislocation intersections in aluminum. Materials Science and Engineering A, **363**, 234-241.

Lim, L.C. (1987). Surface intergranular cracking in large strain fatigue. Acta Metallurgica et Materialia, **35**, 1653-1662.

Lutsko, J.F. (1988). Stress and elastic constants in anisotropic solids: Molecular dynamics techniques. Journal of Applied Physics, **64**, 1152-1154.

Martyna, G.J., Tuckerman, M.E., Tobias, D.J. and Klein, M.L. (1996). Explicit reversible integrators for extended systems dynamics. Molecular Physics, **87**, 1117-1157.

McDowell, D.L. (2001). Materials design: A useful research focus for inelastic behavior of structural metals. Theoretical and Applied Fracture Mechanics, **37**, 245-259.

Medlin, D.L., Mills, M.J., Stobbs, W.M., Daw, M.S. and Cosandey, F. (1993). HRTEM observations of a Σ3 {112} bicrystal boundary in aluminum. Symposium on Atomic-scale Imaging of Surfaces and Interfaces, Nov 30-Dec 2 1992, Boston, MA, USA.

Mehl, M.J., Papaconstantopoulos, D.A., Kioussis, N. and Herbranson, M. (2000). Tight-binding study of stacking fault energies and the Rice criterion of ductility in the fcc metals. Physical Review B (Condensed Matter), **61**, 4894-4897.

Melchionna, S., Ciccotti, G. and Holian, B.L. (1993). Hoover NPT dynamics for systems varying in shape and size. Molecular Physics, **78**, 533-544.

Miller, R. and Phillips, R. (1996). Critical analysis of local constitutive models for slip and decohesion. Philosophical Magazine A, **73**, 803-827.

Miller, R., Ortiz, M., Phillips, R., Shenoy, V. and Tadmor, E.B. (1998). Quasicontinuum models of fracture and plasticity. Engineering Fracture Mechanics, **61**, 427-444.

Miller, R., Tadmor, E.B., Phillips, R. and Ortiz, M. (1998). Quasicontinuum simulation of fracture at the atomic scale. Modelling and Simulation in Materials Science and Engineering, **6**, 607-638.

Millett, P.C., Selvam, R.P., Bansal, S. and Saxena, A. (2005). Atomistic simulation of grain boundary energetics - Effects of dopants. Acta Materialia, **53**, 3671-3678.

Mills, M.J., Daw, M.S., Thomas, G.J. and Cosandey, F. (1992). High-resolution transmission electron microscopy of grain boundaries in aluminum and correlation with atomistic calculations. Ultramicroscopy, **40**, 247-257.

Mishin, Y., Farkas, D., Mehl, M.J. and Papaconstantopoulos, D.A. (1999). Interatomic potentials for monoatomic metals from experimental data and ab initio calculations. Physical Review B, **59**, 3393-3407.

Mishin, Y., Mehl, M.J., Papaconstantopoulos, D.A., Voter, A.F. and Kress, J.D. (2001). Structural stability and lattice defects in copper: Ab initio, tight-binding, and embedded-atom calculations. Physical Review B, **63**, 224106-224101.

Murr, L.E. (1975). Interfacial Phenomena in Metals and Alloys, Addison-Wesley, Reading, MA.

Nagata, N. and Yoshida, S. (1972). Deformation of copper single crystals and polycrystals at high strain rates. Transactions of the Japan Institute of Metals, **13**, 332-338.

Nazarov, A.A., Shenderova, O.A. and Brenner, D.W. (2000). On the disclination-structural unit model of grain boundaries. Materials Science & Engineering A, **A281**, 148-155.

Needleman, A. (1987). Continuum model for void nucleation by inclusion debonding. Journal of Applied Mechanics, **54**, 525-531.

Needleman, A. (1990a). An analysis of decohesion along an imperfect interface. International Journal of Fracture, **42**, 21-40.

Needleman, A. (1990b). An analysis of tensile decohesion along an interface. Journal of the Mechanics and Physics of Solids, **38**, 289-324.

Needleman, A. (1992). Micromechanical modelling of interfacial decohesion. Ultramicroscopy, **40**, 203-214.

Norskov, J.K. (1982). Covalent effects in the effective-medium theory of chemical binding: hydrogen heats of solution in the 3d metals. Physical Review B, **26**, 2875-2885.

Nose, S. (1984). A molecular dynamics method for simulations in the canonical ensemble. Molecular Physics, **52**, 255-268.

Ogata, S., Li, J. and Yip, S. (2002). Ideal pure shear strength of aluminum and copper. Science, **298**, 807-811.

Olson, G.B. (2000). Designing a new material world. Science, **288**, 993-998.

Onsager, L. (1931). Reciprocal relations in irreversible processes. I. Physical Review, **37**, 405-426.

Ortiz, M. (1996). Computational micromechanics. Computational Mechanics, **18**, 321-338.

Ortiz, M. and Pandolfi, A. (1999). Finite-deformation irreversible cohesive elements for three-dimensional crack-propagation analysis. International Journal for Numerical Methods in Engineering, **44**, 1267-1282.

Ostoja-Starzewski, M. (1998). Random field models of heterogeneous materials. International Journal of Solids and Structures, **35**, 2429-2455.

Palumbo, G. and Aust, K.T. (1990). Structure-dependence of intergranular corrosion in high purity nickel. Acta Metallurgica et Materialia, **38**, 2343-2352.

Pan, Y., Adams, B.L., Olson, T. and Panayotou, N. (1996). Grain-boundary structure effects on intergranular stress corrosion cracking of Alloy X-750. Acta Materialia, **44**, 4685-4695.

Parrinello, M. and Rahman, A. (1981). Polymorphic transitions in single crystals: a new molecular dynamics method. Journal of Applied Physics, **52**, 7182-7190.

Peierls, R.E. (1940). The size of a dislocation. Proceedings of the Physical Society, **52**, 34-37.

Qin, Q. and Bassani, J.L. (1992). Non-Schmid yield behavior in single crystals. Journal of the Mechanics and Physics of Solids, **40**, 813-833.

Rafii-Tabar, H., Hua, L. and Cross, M. (1998). A multi-scale atomistic-continuum modelling of crack propagation in a two-dimensional macroscopic plate. Journal of Physics: Condensed Matter, **10**, 2375-2387.

Randle, V. (1993). The Measurement of Grain Boundary Geometry, Institute of Physics Publishing, Bristol.

Randle, V. (1996). The role of the coincidence site lattice in grain boundary engineering, Institute of Materials, London.

Raous, M., Cangemi, L. and Cocu, M. (1999). A consistent model coupling adhesion, friction, and unilateral contact. Computer Methods in Applied Mechanics and Engineering, **177**, 383-399.

Read, W.T. and Shockley, W. (1950). Dislocation models of crystal grain boundaries. Physical Review, **78**, 275-289.

Rice, J.R. (1971). Inelastic constitutive relations for solids: an internal-variable theory and its application to metal plasticity. Journal of the Mechanics and Physics of Solids, **19**, 433-455.

Rice, J.R., Paris, P.C. and Merkle, J.G. (1973). Some further results of J-integral analysis and estimates. Progress in Flaw Growth and Fracture Toughness Testing, ASTM STP 536, American Society of Testing and Materials, Philadelphia, 231-245.

Rice, J.R. (1992). Dislocation nucleation from a crack tip: an analysis based on the Peierls concept. Journal of the Mechanics and Physics of Solids, **40**, 239-271.

Rittner, J.D. and Seidman, D.N. (1996). <110> symmetric tilt grain-boundary structures in fcc metals with low stacking-fault energies. Physical Review B, **54**, 6999.

Rittner, J.D., Seidman, D.N. and Merkle, K.L. (1996). Grain-boundary dissociation by the emission of stacking faults. Physical Review B, **53**, 4241-4244.

Romanov, A.E. (1993). Screened disclinations in solids. Materials Science & Engineering A, **A164**, 58-68.

Rose, J.H., Smith, J.R. and Ferrante, J. (1983). Universal features of bonding in metals. Physical Review B, **28**, 1835-1845.

Rudd, R.E. and Belak, J.F. (2002). Void nucleation and associated plasticity in dynamic fracture of polycrystalline copper: An atomistic simulation. Computational Materials Science, **24**, 148-153.

Sansoz, F. and Molinari, J.F. (2004). Incidence of atom shuffling on the shear and decohesion behavior of a symmetric tilt grain boundary in copper. Scripta Materialia, **50**, 1283-1288.

Sansoz, F. and Molinari, J.F. (2005). Mechanical behavior of Σ tilt grain boundaries in nanoscale Cu and Al: A quasicontinuum study. Acta Materialia, **53**, 1931-1944.

Schiotz, J., Di Tolla, F.D. and Jacobsen, K.W. (1998). Softening of nanocrystalline metals at very small grain sizes. Nature, **391**, 561-563.

Schiotz, J., Vegge, T., Di Tolla, F.D. and Jacobsen, K.W. (1999). Atomic-scale simulations of the mechanical deformation of nanocrystalline metals. Physical Review B, **60**, 11971-11983.

Schuh, C.A., Kumar, M. and King, W.E. (2003). Analysis of grain boundary networks and their evolution during grain boundary engineering. Acta Materialia, **51**, 687-700.

Shewchuk, J.R. (1994). An introduction to the conjugate gradient method without the agonizing pain. Carnegie Mellon University.

Shih, K.K. and Li, J.C.M. (1975). Energy of grain boundaries between cusp misorientations. Surface Science, **50**, 109-124.

Shilkrot, L.E., Curtin, W.A. and Miller, R.E. (2002). A coupled atomistic/continuum model of defects in solids. Journal of the Mechanics and Physics of Solids, **50**, 2085-2106.

Shilkrot, L.E., Miller, R.E. and Curtin, W.A. (2004). Multiscale plasticity modeling: coupled atomistics and discrete dislocation mechanics. Journal of the Mechanics and Physics of Solids, **52**, 755-787.

Sinclair, J.E. (1971). Improved atomistic model of a bcc dislocation core. Journal of Applied Physics, **42**, 5321-5329.

Sinclair, J.E. (1975). The influence of the interatomic force law and of kinks on the propagation of brittle cracks. Philosophical Magazine, **31**, 647-671.

Sinclair, J.E., Gehlen, P.C., Hoagland, R.G. and Hirth, J.P. (1978). Flexible boundary conditions and nonlinear geometric effects in atomic dislocation modeling. Journal of Applied Physics, **49**, 3890-3897.

Smith, C.S. (1981). A Search for Structure: Selected Essays on Science, Art and History, MIT Press, Cambridge, MA.

Spearot, D.E., Jacob, K.I. and McDowell, D.L. (2004). Non-local separation constitutive laws for interfaces and their relation to nanoscale simulations. Mechanics of Materials, **36**, 825-847.

Spearot, D.E., Jacob, K.I., McDowell, D.L. and Plimpton, S.J. (2005). Effect of deformation path sequence on the behavior of nanoscale copper bicrystal interfaces. Journal of Engineering Materials and Technology, **127**, accepted for publication.

Steinmann, P., Kuhl, E. and Stein, E. (1998). Aspects of non-associated single crystal plasticity: influence of non-Schmid effects and localization analysis. International Journal of Solids and Structures, **35**, 4437-4456.

Stott, M.J. and Zaremba, E. (1980). Quasiatoms: An approach to atoms in nonuniform electronic systems. Physical Review B, **22**, 1564-1533.

Sutton, A.P. and Vitek, V. (1983a). On the structure of tilt grain boundaries in cubic metals. I. Symmetrical tilt boundaries. Philosophical Transactions of the Royal Society of London A, **309**, 1-36.

Sutton, A.P. and Vitek, V. (1983b). On the structure of tilt grain boundaries in cubic metals. II. Asymmetrical tilt boundaries. Philosophical Transactions of the Royal Society of London A, **309**, 37-54.

Sutton, A.P. and Vitek, V. (1983c). On the structure of tilt grain boundaries in cubic metals. III. Generalizations of the structural study and implications for the properties of grain boundaries. Philosophical Transactions of the Royal Society of London A, **309**, 55-68.

Sutton, A.P. and Balluffi, R.W. (1987). On geometric criteria for low interfacial energy. Acta Metallurgica, **35**, 2177-2201.

Sutton, A.P. and Balluffi, R.W. (1990). Rules for combining structural units of grain boundaries. Philosophical Magazine Letters, **61**, 91-94.

Swope, W.C., Andersen, H.C., Berens, P.H. and Wilson, K.R. (1982). A computer simulation method for the calculation of equilibrium constants for the formation of physical clusters of molecules: application to small water clusters. Journal of Chemical Physics, **76**, 637-649.

Tadmor, E.B., Ortiz, M. and Phillips, R. (1996). Quasicontinuum analysis of defects in solids. Philosophical Magazine A, **73**, 1529-1563.

Tomar, V., Zhai, J. and Zhou, M. (2004). Bounds for element size in a variable stiffness cohesive finite element model. International Journal for Numerical Methods in Engineering, **61**, 1894-1920.

Tsai, D.H. (1979). The virial theorem and stress calculation in molecular dynamics. Journal of Chemical Physics, **70**, 1375-1382.

Tuckerman, M., Berne, B.J. and Martyna, G.J. (1992). Reversible multiple time scale molecular dynamics. Journal of Chemical Physics, **97**, 1990-2001.

Tuckerman, M.E. and Martyna, G.J. (1999). Comment on "Simple reversible molecular dynamics algorithms for Nose-Hoover chain dynamics" [J. Chem. Phys. 107, 9514 (1997)]. Journal of Chemical Physics, **110**, 3623-3625.

Tvergaard, V. (1990). Effect of fibre debonding in a whisker-reinforced metal. Materials Science & Engineering A: Structural Materials: Properties, Microstructure and Processing, **A125**, 203-213.

Tvergaard, V. and Hutchinson, J.W. (1992). The relation between crack growth resistance and fracture process parameters in elastic-plastic solids. Journal of the Mechanics and Physics of Solids, **40**, 1377-1397.

Tvergaard, V. and Hutchinson, J.W. (1993). Influence of plasticity on mixed mode interface toughness. Journal of the Mechanics and Physics of Solids, **41**, 1119-1135.

Valiyev, R.Z., Vladimirov, V.I., Gertsman, V.Y., Nazarov, A.A. and Romanov, A.Y. (1990). Disclination-structural model and grain-boundary energy in metals with FCC lattice. Physics of Metals and Metallography, **69**, 30-37.

Van Swygenhoven, H. and Caro, A. (1998). Plastic behavior of nanophase metals studied by molecular dynamics. Physical Review B, **58**, 11246-11251.

Van Swygenhoven, H., Spaczer, M., Caro, A. and Farkas, D. (1999a). Competing plastic deformation mechanisms in nanophase metals. Physical Review B, **60**, 22-25.

Van Swygenhoven, H., Spaczer, M., Farkas, D. and Caro, A. (1999b). The role of grain size and the presence of low and high angle grain boundaries in the deformation mechanism of nanophase Ni: A molecular dynamics computer simulation. Nanostructured Materials, **12**, 323-326.

Van Swygenhoven, H., Spaczer, M. and Caro, A. (1999c). Microscopic description of plasticity in computer generated metallic nanophase samples: A comparison between Cu and Ni. Acta Materialia, **47**, 3117-3126.

Van Swygenhoven, H., Caro, A. and Farkas, D. (2001). A molecular dynamics study of polycrystalline fcc metals at the nanoscale: Grain boundary structure and its influence on plastic deformation. Materials Science and Engineering A, **309-310**, 440-444.

Van Swygenhoven, H., Derlet, P.M. and Hasnaoui, A. (2002). Atomic mechanism for dislocation emission from nanosized grain boundaries. Physical Review B, **66**, 024101-024101.

Van Swygenhoven, H., Derlet, P.M. and Froseth, A.G. (2004). Stacking fault energies and slip in nanocrystalline metals. Nature Materials, **3**, 399-403.

Voter, A.F. and Chen, S.P. (1987). Accurate interatomic potentials for Ni, Al and Ni/sub 3/Al. Characterization of Defects in Materials Symposium, 1-2 Dec. 1986, Boston, MA, USA.

Wang, G.J., Sutton, A.P. and Vitek, V. (1984). A computer simulation study of <001> and <111> tilt boundaries: the multiplicity of structures. Acta Metallurgica, **32**, 1093-1104.

Warrington, D.H. and Grimmer, H. (1974). Dislocation Burgers vectors for cubic metal grain boundaries. Philosophical Magazine, **30**, 461-468.

Watanabe, T. (1984). Approach to grain boundary design for strong and ductile polycrystals. International Journal of Structural Mechanics and Materials Science, **11**, 47-84.

Watanabe, T., Yamada, M. and Karashima, S. (1991). Grain boundary strengthening associated with Σ9 near-coincidence boundary in <1010> twist zinc bicrystals at high temperatures. Philosophical Magazine A, **63**, 1013-1022.

Watanabe, T. (1994). Impact of grain boundary character distribution on fracture in polycrystals. Materials Science & Engineering A, **A176**, 39-49.

Watanabe, T. and Tsurekawa, S. (1999). The control of brittleness and development of desirable mechanical properties in polycrystalline systems by grain boundary engineering. Acta Materialia, **47**, 4171-4185.

Wei, Y. and Hutchinson, J.W. (1999). Models of interface separation accompanied by plastic dissipation at multiple scales. International Journal of Fracture, **95**, 1-17.

Wolf, D. (1989). Structure-energy correlation for grain boundaries in F.C.C. metals. I. Boundaries on the (111) and (100) planes. Acta Metallurgica, **37**, 1983-1993.

Wolf, D. (1990). Structure-energy correlation for grain boundaries in F.C.C metals. III. Symmetrical tilt boundaries. Acta Metallurgica, **38**, 781-790.

Xu, X.-P. and Needleman, A. (1993). Void nucleation by inclusion debonding in a crystal matrix. Modelling and Simulation in Materials Science and Engineering, **1**, 111-132.

Xu, X.-P. and Needleman, A. (1994). Numerical simulations of fast crack growth in brittle solids. Journal of the Mechanics and Physics of Solids, **42**, 1397-1434.

Xu, X.-P. and Needleman, A. (1995). Numerical simulations of dynamic interfacial crack growth allowing for crack growth away from the bond line. International Journal of Fracture, **74**, 253-275.

Yamakov, V., Wolf, D., Salazar, M., Phillpot, S.R. and Gleiter, H. (2001). Length-scale effects in the nucleation of extended dislocations in nanocrystalline Al by molecular-dynamics simulation. Acta Materialia, **49**, 2713-2722.

Yamakov, V., Wolf, D., Phillpot, S.R. and Gleiter, H. (2002). Deformation twinning in nanocrystalline Al by molecular-dynamics simulation. Acta Materialia, **50**, 5005-5020.

Yamakov, V., Wolf, D., Phillpot, S.R. and Gleiter, H. (2003). Dislocation-dislocation and dislocation-twin reactions in nanocrystalline Al by molecular dynamics simulation. Acta Materialia, **51**, 4135-4147.

Yang, W., Tan, H. and Guo, T. (1994). Evolution of crack tip process zones. Modelling and Simulation in Materials Science and Engineering, **2**, 767-782.

Zhai, J. and Zhou, M. (1999). Micromechanical modeling of mixed-mode crack growth in ceramic composites. ASTM Special Technical Publication, 174-200.

Zhai, J. and Zhou, M. (2000). Finite element analysis of micromechanical failure modes in a heterogeneous ceramic material system. International Journal of Fracture, **101**, 161-180.

Zhang, H., Mendelev, M.I. and Srolovitz, D.J. (2005). Mobility of Σ5 tilt grain boundaries: Inclination dependence. Scripta Materialia, **52**, 1193-1198.

Zhou, M. (2003). A New Look at the Atomic Level Virial Stress -- On Continuum-Molecular System Equivalence. Proceedings of the Royal Society of London A, **459**, 2347-2392.

Zhou, S.J., Lomdahl, P.S., Voter, A.F. and Holian, B.L. (1998). Three-dimensional fracture via large-scale molecular dynamics. Engineering Fracture Mechanics, **61**, 173-187.

Zimmerman, J.A., Gao, H. and Abraham, F.F. (2000). Generalized stacking fault energies for embedded atom FCC metals. Modelling and Simulation in Materials Science and Engineering, **8**, 103-116.

Zimmerman, J.A., Kelchner, C.L., Klein, P.A., Hamilton, J.C. and Foiles, S.M. (2001). Surface step effects on nanoindentation. Physical Review Letters, **87**, 165507-165501.

Zimmerman, J.A., Webb III, E.B., Hoyt, J.J., Jones, R.E., Klein, P.A. and Bammann, D.J. (2004). Calculation of stress in atomistic simulation. Modelling and Simulation in Materials Science and Engineering, **12**, S319-S332.